Charge and Magnetic X-ray Scattering

Philip David Spencer

A thesis submitted in fulfilment of the requirements for the degree of Doctor of Philosophy

University of Durham

Department of Physics 2004

Abstract

The hole doped transition metal oxides show remarkable properties that are related to the influence of charge and spin correlations. In this thesis charge correlations in hole doped manganite and nickelate systems are studied using soft (< 2 keV), normal (10 keV) and high energy x-ray scattering (100 keV).

The charge and Jahn-Teller (JT) order is studied in the bi-layer manganite $La_{2-2x}Sr_{1+2x}Mn_2O_7$ for $x = 0.5$, 0.55 and 0.60 using high energy x-ray scattering. In the $x = 0.55$ sample the charge ordered state existed in the same checkerboard pattern as observed in the $x = 0.5$ sample with no change in behaviour. However, in the $x = 0.6$ doped sample the charge ordered state entered a new regime characterised by incommensurate JT and charge order. The magnitude of the incommensurability was inversely proportional to the intensity of the JT and charge peaks.

High resolution x-ray measurements of the charge stripe order in the $La_{2-x}Sr_xNiO_4$ system in the doping range $0.20 \leq x \leq 0.50$ are presented. As the doping was moved away in either direction from the commensurate $x = 0.33$ the charge stripes changed from a highly correlated state to an increasingly disordered charge glass state. At the commensurate 0.5 composition there was no increase in the intensity or correlation of the charge order despite a significantly higher transition temperature than in the lower doped compositions.

Finally the first measurements of the orbital order in $La_{0.5}Sr_{1.5}MnO_4$ using soft x-ray scattering at the manganese L edges are presented. The measurements directly probe the orbital order unlike the previously reported measurements at the manganese K-edge. Energy scans were carried out on the orbital order and compared with theoretical predictions. From this it was determined that both the Jahn-Teller distortions and direct orbital ordering contribute to the observed scattering.

Acknowledgements

I would firstly like to thank my supervisor Prof. Peter Hatton for his support, patience and encouragement over the last three years. I would like to express my thanks to the other members of the research group; Stuart Wilkins for his computing expertise, and Tom Beale and Mohammed Ghazi for their support during my study. I have also appreciated the help of other members of the x-ray and magnetism research group in particular Sean Giblin for the magnetisation measurements he carried out, James Buchanan, Tom Hase, Neil Parkinson, Ian Terry and Brian Tanner. My thanks go to John Dobson for his technical support and expertise throughout my PhD and to Wayne Dobby and Ian Manfren for the loan of equipment and support when demonstrating. I would also like to thank Mike Lee, Vicki Dobby and Pauline Russell of the audio-visual department and the support staff of Penny Carse, Claire Davies, Dave Stockdale and others.

This thesis would not have been possible without the collaboration with other research groups. I would like to thank Dr Andrew Boothroyd and Dr D. Prabhakaran of the Physics Department Oxford University for the high quality crystals they provided. In addition I would like to thank Paul Freeman of Oxford for the magnetisation measurements he carried out. I would like Dr David Fort of Birmingham University for providing a high quality Holmium crystal at short notice.

The results in this thesis were obtained at central scientific facilities and I would like to thank the following for their valuable assistance. Firstly, to Simon Brown, Paul Thompson, Danny Mannix, David Paul and Sandra Beaufoy from the XMaS beamline at the ESRF Grenoble. I would like to thank Martin Zimmermann of HASYLAB Hamburg for his help with the high energy experiments. I would like to thank Dr Mark Roper of Daresbury laboratory for his development of the soft x-ray diffractometer that made the soft x-ray measurements possible and Dr Steve Collins of Daresbury for his assistance during the beamtime on station 16.3

Finally, I would like to thank my parents and my sister Jill for their continual support and encouragement throughout my studies.

Declaration

The work in this thesis is that of the author unless stated otherwise and no part of the thesis has been submitted to this or any other university.

Philip D. Spencer

Publication List

1. Wilkins, S.B., Spencer, P.D. *et al.*, *Charge Ordering and structural distortions at low temperature in* $La_{2-2x}Sr_{1+2x}Mn_2O_7$. Physical Review B, 2003. **67**(20): p. 205110.
2. Hatton, P.D., S.B. Wilkins, and P.D. Spencer, *High energy x-ray scattering studies of strongly correlated oxides.* Journal of Physics D-Applied Physics, 2003. **36**(10A): p. A157-A161.
3. Spencer, P.D., *et al.*, *Charge Stripe Glasses in* $La_{2-x}Sr_xNiO4$ *for* $0.20 < x < 0.25$. Journal of Physics - Condensed Matter, 2003: Submitted.
4. Spencer, P.D., *et al.*, *Stripe and Checkerboard Order in the High doped nickelates.* Physical Review B, 2003: In preparation.
5. Spencer, P.D., *et al.*, *Incommensurate structural distortions in the higher doped bilayer manganite* $La_{2-2x}Sr_{1+2x}Mn_2O_7$. Journal of Physics - Condensed Matter, 2003: p. in preparation.
6. Wilkins, S.B., Spencer, P.D. *et al.*, *Direct Observation of orbital ordering in* $La_{0.5}Sr_{1.5}MnO_4$. Physical Review Letters, 2003. **91**(16): p. 167205.
7. Spencer, P.D., *et al.*, *Soft X-ray study of the magnetic order in Holmium.* Journal of Physics - Condensed Matter, 2004: In preparation.

Contents

Chapter 1 Introduction and Thesis Outline

The 3*d* transition metal oxides have been studied intensively in recent years after the discovery of high temperature superconductivity in the cuprates and colossal magnetoresistance (CMR) in the manganites. These studies have shown that the transition metal oxides demonstrate remarkable phenomena including superconductivity, CMR, metal-insulator transitions and charge, spin and orbital ordering. Extensive studies have been carried out on the charge, spin and orbital order using a variety of techniques to determine their relationship with the electronic and physical properties. By doping holes into the transition metal oxides the physical properties are changed dramatically. These holes can order at low temperature and this charge ordering is usually accompanied by spin ordering and in the manganites orbital ordering. X-ray scattering is ideal for the study of charge modulations and the development of high intensity third generation synchrotron sources has allowed high resolution measurements to be carried out on very weak phenomena.

In chapter 2 there is a general review of the theory and studies to date in the manganites, nickelates and cuprates. The theory of resonant x-ray scattering for charge and orbital ordering in the manganites at the manganese *K*-edge is discussed. There is a discussion of the high energy x-ray scattering technique and the advantages over the use of conventional x-ray scattering. There is also a brief discussion of the experimental stations used at the ESRF, HASYLAB and SRS and the D3 laboratory diffractometer where all samples were pre-aligned.

The bi-layer manganite $La_{2-2x}Sr_{1+2x}Mn_2O_7$ shows the largest CMR effect observed in all the manganites for the $x = 0.4$ doping but by substituting La for Sr and hence, increasing the hole doping level the physical and electronic properties of the bi-layer can be changed drastically and for a doping of $x > 0.47$ it enters a charge ordered state. It is intended to study the charge ordered state within the bi-layer in the doping range $0.475 \leq x \leq 0.60$ using high energy and resonant x-ray scattering techniques. These will be the first single crystal x-ray diffraction measurements carried out over this doping range.

This will provide significantly more detailed data than the previous powder diffraction studies and reconcile any differences in those studies and overall, should increase the understanding of the bi-layer manganite system.

Chapter 3 discusses the high energy x-ray and resonant x-ray scattering studies of the Jahn-Teller, charge and orbital order on the $La_{2-2x}Sr_{1+2x}Mn_2O_7$ for doping levels of $x = 0.5$ and 0.475. The differences between the behaviour of the Jahn-Teller and charge order in the two systems are discussed. These results are compared with earlier studies to resolve any differences in the interpretation of the results. In chapter 4 the high energy x-ray scattering study of the Jahn-Teller and charge order is extended to single crystal studies of the $x = 0.55$ and 0.60 doped samples. These are the first single crystal studies of the bi-layer system at these doping levels using any technique. The behaviour of the Jahn-Teller and charge order is compared with that in the $x = 0.5$ and 0.475 doped samples and with the neutron and x-ray powder diffraction results to determine the behaviour of the charge ordered state as a function of doping in the bi-layer system.

The $La_{2-x}Sr_xCuO_4$ system is of great interest because it shows high temperature superconductivity. However, at the $x = 1/8$ doping level a suppression in the superconducting temperature was observed and it was postulated that this could occur due to the stabilisation of charge stripes at the commensurate wavevector. There has been considerable debate as to a possible relationship between charge stripes and superconductivity and it is still not known what if any the relationship is. The $La_{2-x}Sr_xNiO_4$ nickelate system has the same structure as the cuprate system but does not show superconductivity. However, the charge stripes within the nickelate system are intense and stable whereas those in the cuprate system are weak and dynamic. Due to its similarity with the high T_C cuprates the nickelate system has been a central focus for the study of charge and spin stripes.

In chapter 5 the results of a high resolution x-ray study of the charge ordering in the nickelate system $La_{2-x}Sr_xNiO_4$ for doping levels of $x = 0.20$, 0.225 and 0.25 are presented. The results are discussed and compared with earlier neutron and high energy x-ray work on the 0.20 and 0.225 doping levels and with earlier results x-ray results

obtained on the x = 0.33, 0.30 and 0.275 doping levels in order to determine how the charge order in the nickelates behaves in the doping region $0.20 \leq x \leq 0.33$.

In chapter 6 the study of the charge ordering in the nickelate system in the x = 0.40, 0.48 and 0.50 doped levels using high resolution x-ray scattering is presented. From the measurements on the 0.50 system the nature of the charge order rearrangement is determined and secondly, if there is a stabilisation of the charge order pattern at the commensurate 0.50 doping as there is in the 0.33 doping level. Finally, from these results the behaviour of the charge order in the doping regime $0.20 \leq x \leq 0.50$ is discussed.

Very recently the use of resonant soft magnetic diffraction has been extended into the soft x-ray region (500 – 2000 eV) to allow the study of the magnetic order in the transition metal oxides at the L edges. The prototypical system for the study of magnetic order by resonant x-ray scattering is holmium and the magnetic structure is extremely well known. By a comparison of the results with earlier studies the validity of the results of the soft x-ray scattering technique is determined. In chapter 7 there is a review of the studies carried out on holmium using neutron diffraction and resonant and non-resonant x-ray scattering and the theory of resonant x-ray magnetic scattering is discussed. There is a description of the 5U.1 experimental station and the soft x-ray in-vacuum diffractometer used for the experiments. The first soft x-ray study of magnetic order in holmium at the M_{IV} and M_V edges is discussed and the results are compared with those from earlier neutron and x-ray work to determine the validity of the soft x-ray scattering technique.

In Chapter 8 the first studies of the orbital order using soft x-ray diffraction at the manganese (Mn) L edges in the manganite system $La_{0.5}Sr_{1.5}MnO_4$ are presented. This is the only technique that can directly probe the orbital degree of freedom and there is a review of the theoretical predictions for the behaviour of the orbital order at the Mn L edges. The results obtained are compared with these theoretical predictions to determine the nature and mechanism behind the orbital order in the manganites.

Chapter 2

General Background

The $3d$ transition metal oxides have been studied extensively in recent years due to the remarkable physical properties that they display. The most remarkable of these is the colossal magnetoresistance (CMR) in the manganites and the high temperature superconductivity in the cuprates. A significant amount of this research has been directed to the study of the charge, spin and orbital degrees of freedom and the interplay between these degrees of freedom to determine how they affect the physical and electronic properties.

The major focus of this thesis is a study of correlated electron systems. Transition metal oxides are typical correlated electron systems in which the electron interactions strongly determine the electronic properties. Charge ordering has attracted significant interest due to its possible relationship with superconductivity in the high temperature cuprates. The charge ordering is strongly correlated with structural distortions, which are related to orbital ordering and also to spin ordering, which changes the magnetic properties. Indeed all of the different electron correlations (charge, spin, orbital) are strongly interlinked in the $3d$ transition metal oxides and are the root cause of their complex behaviour.

In this chapter the basic properties of the manganites, cuprates and nickelates will be discussed. The theory of resonant x-ray scattering in the manganites for both charge and orbital order with respect to the manganites will be discussed. Finally the experimental instruments and equipment used to carry out the experiments will be discussed

2.1 Manganites – General Theory

The perovskite manganites have been studied extensively during the recent years due to the discovery of colossal magnetoresistance (CMR) in $Nd_{0.5}Pb_{0.5}MnO_3$[1] and $La_{0.67}Ba_{0.33}MnO_3$ [2]. The manganites were actually first studied in the 1950s but the discovery of this effect generated great interest due to the possible technological applications. These applications are still years away but the perovskite manganites are ideal materials for studying the physics of strongly correlated electron systems. The physical properties and phenomena in the manganites vary significantly depending on the doping level x of the system, and in addition to the CMR effect they display charge and orbital order states and metal – insulator transitions. Extensive studies have been carried out into how the interplay of the charge, spin and orbital degrees of freedom are related to the remarkable phenomena shown.

The general formula of the perovskite manganites is $R_{1-x}A_xMnO_3$ where R is a rare earth ion such as La, Nd, Pr and A is a Group II divalent ion such as Ca or Sr. The parent compounds $RMnO_3$ are all antiferromagnetic insulators and the manganese (Mn) ions present are all Mn^{3+}. By substituting a divalent ion into the lattice the physical properties of the system are dramatically changed. In the parent compound all the manganese ions present are Mn^{3+} ions but by substituting in a divalent ion the valence of the Mn^{3+} ions is changed to Mn^{4+} and the ratio of Mn^{3+} to Mn^{4+} ions is dependent on the doping level x. Mn^{3+} has 4 electrons in the $3d$ shell and due to Hund's rules the spins are aligned in the same direction. If the Mn^{3+} existed as a lone ion the levels would not be split but the Mn^{3+} ion is surrounded six oxygen ions and it exists in a $Mn^{3+}O_6$ octahedron. The crystal field causes the $3d^4$ levels to split into a triply degenerate t_{2g} state and a doubly degenerate e_g state which is higher in energy. A schematic of this is shown in Figure 2.1 The t_{2g} orbitals point 45° away from the $2p$ oxygen orbitals. There is only very weak hybridisation with the O $2p$ orbitals and the electrons in the t_{2g} orbitals can therefore be considered to be localised. However, the e_g orbitals point towards the oxygen $2p$ orbitals and are therefore strongly hybridised and cannot be considered to be localised, and it is these delocalised states that are thought to be responsible for conduction.[3]

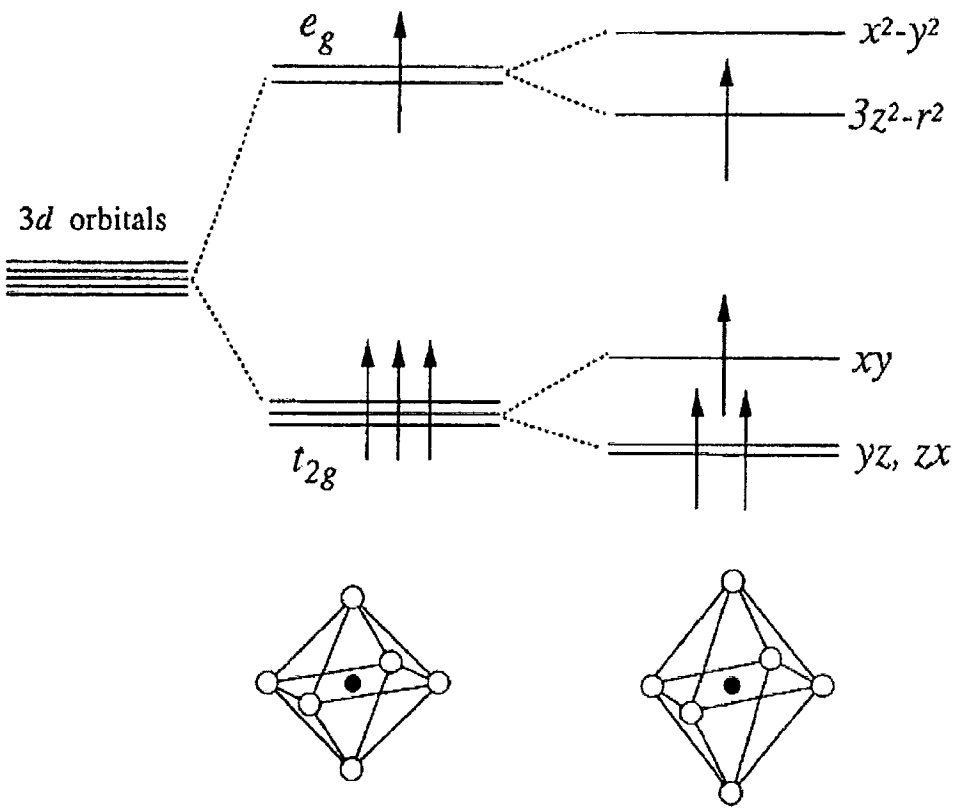

Figure 2.1: *Schematic of the 3d energy levels for a lone ion, under the crystal field and under a crystal field distorted due to the Jahn-Teller effect.* [4]

There is also an additional splitting in the 3*d* band that is caused by the Jahn-Teller effect, which is a distortion of the octahedron around the Mn^{3+} ions. The distortion lowers the energy of the system and lifts the degeneracy of the e_g energy level, and this distortion consists of an elongation of the octahedra along one particular direction. The size of the distortion is often measured as the *c/a* ratio where an undistorted octahedron has a ratio of 1.00 and hence, the larger the distortion the larger the ratio.

The substitution of a divalent element such as Ca or Sr introduces mobile charge carriers (holes) into the system and the valence state of the Mn ions is found to exist in an intermediate state between Mn^{3+} and Mn^{4+} and in this region a number of different spin states can be observed that affect the spin degree of freedom. In the ferromagnetic (FM) state the double exchange process is favoured and this requires mobile electrons, and

hence the charge density on each Mn site is identical. However there are states in which the charge order can segregate into different regions which have Mn^{3+} and Mn^{4+} valence. This charge ordered state was actually first observed in 1955 by Wollan and Koehler [5] and in the charge ordered state the dominant mechanism is the super-exchange interaction. These superexchange interactions are ferromagnetic (FM) or antiferromagnetic (AFM) depending on the orbital in which the mobile electron is present.

The charge ordered state would most likely be favoured for a doping level of $x = 0.5$, in which there is a 1:1 ratio of Mn^{3+} and Mn^{4+} ions and a checkerboard-type ordering pattern would be expected. There would be no Jahn-Teller distortions associated with the Mn^{4+} ions because it has no electron in the e_g orbital, and is hence Jahn-Teller inactive. There will however, be Jahn-Teller order associated with the Mn^{3+} ions and as shown in Figure 2.1 this lifts the degeneracy of the e_g orbital and this causes the e_g orbital to order – the orbitally ordered state. This was predicted by Goodenough in 1955 [6] and in his model the e_g orbitals form a zigzag pattern within the $a - b$ plane.

Figure 2.2 illustrates the predicted schematic of the charge and Jahn-Teller order in the *a-b* plane. The Mn^{3+} ions are shown by the blue circles with the direction of the e_g orbital. The Mn^{4+} ions are represented with red circles. The Jahn-Teller distorted unit cell is shown by the dotted blue box and the charge order unit cell by the red dotted line with the Jahn-Teller order and orbital order having a modulation double that of the charge order. In addition the basic perovskite unit cell is shown by the green dotted line. In this model the Jahn-Teller and the orbital order occur at the same modulation in reciprocal space. They can however, be differentiated using resonant x-ray scattering and polarisation analysis which will be discussed in section 2.6. The suggested movement of the Mn^{4+} ions is shown by the black arrows. The Jahn-Teller effect causes an elongation in the Mn-O bond length along the occupied e_g orbital and this causes a cooperative movement of the Mn^{4+} ions within the lattice in the directions as shown by the arrows. This causes a difference in the electron density and it is this that is referred to as the Jahn-Teller order.

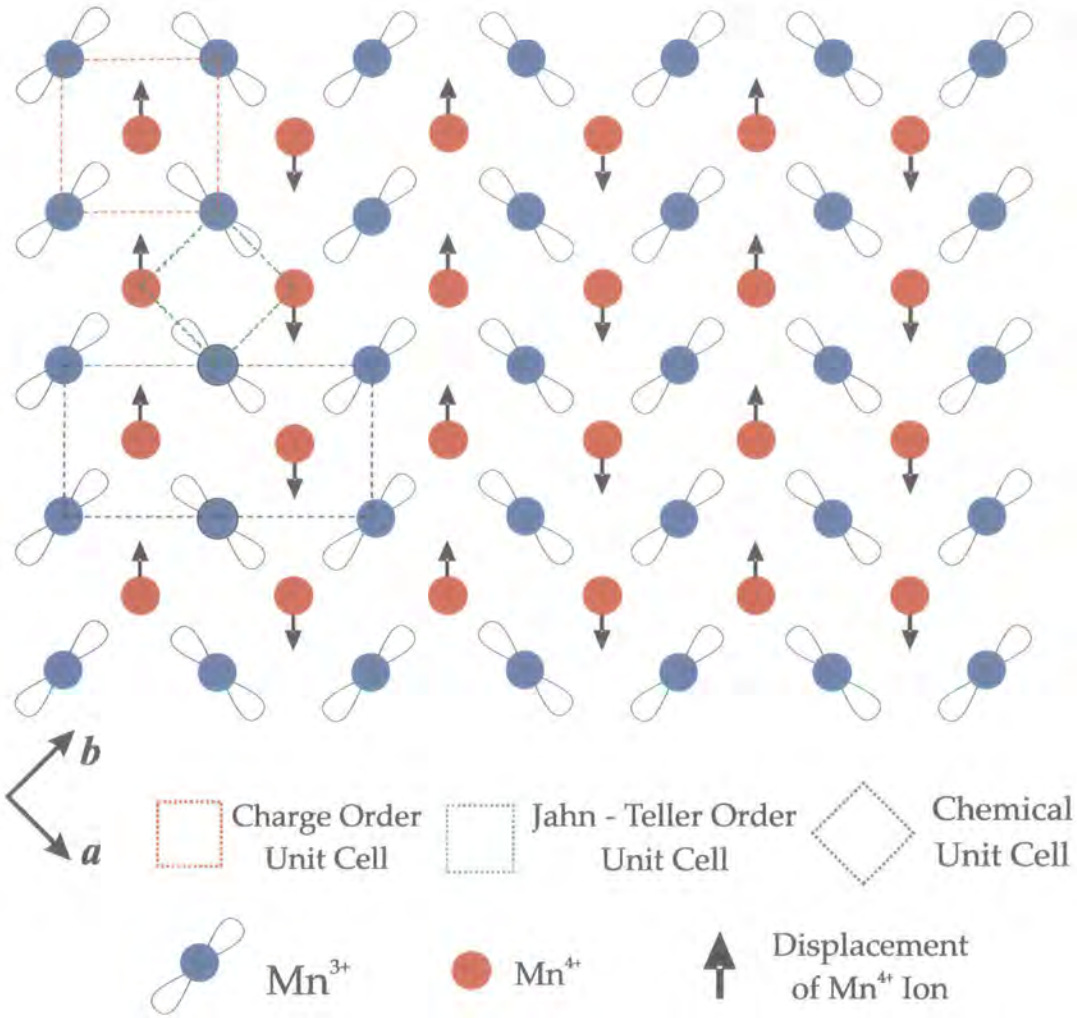

Figure 2.2: *Schematic of the charge and Jahn-Teller ordering in the manganites. The charge order, Jahn-Teller and chemical unit cells are outlined.*

The first system in which the above Jahn-Teller/charge ordered state was studied and confirmed in was $La_{1-x}Ca_xMnO_3$ and the phase diagram is shown in Figure 2.3 [7]. The system shows a huge range of electronic states depending on the doping level and the temperature. In the doping region $0.18 < x \leq 0.5$ the system shows a transition from a paramagnetic state to a ferromagnetic state and it is charge ordered in the doping region $0.5 < x < 0.8$. However, in the half doped system it shows both ferromagnetic and antiferromagnetic charge ordered regimes. $La_{0.5}Ca_{0.5}MnO_3$ is a paramagnetic insulator at

room temperature and on cooling undergoes a transition into a ferromagnetic state at approximately 225 K and then on further cooling undergoes a first order transition into a CE-type AFM ordered state at 165 K. The variety of phases shown is postulated to be due to the competition between the double exchange and superexchange associated with the ferromagnetic and antiferromagnetic ordering.

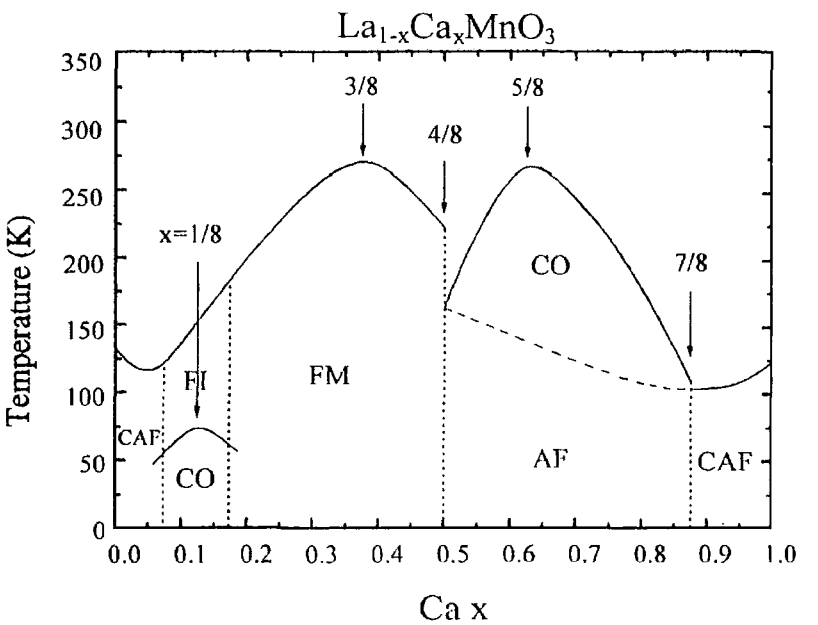

***Figure 2.3**: Phase diagram of the $La_{1-x}Ca_xMnO_3$ system*

The charge order pattern obtained using electron diffraction by Chen and Cheong [8] and the proposed charge/orbital schematic is shown in Figure 2.4. Superlattice peaks were observed at a wavevector of $\boldsymbol{q} = (2\pi/a)(\frac{1}{2}-\varepsilon, 0, 0)$ with $\varepsilon = 0.013$. This was attributed to be due to charge order, but an x-ray and neutron powder diffraction study by Radaelli *et. al.* [9] found that the superlattice reflections were actually caused by the motion of the Mn^{4+} ions and in early studies there had been confusion in regard to which reflection were associated with the charge and Jahn-Teller order.

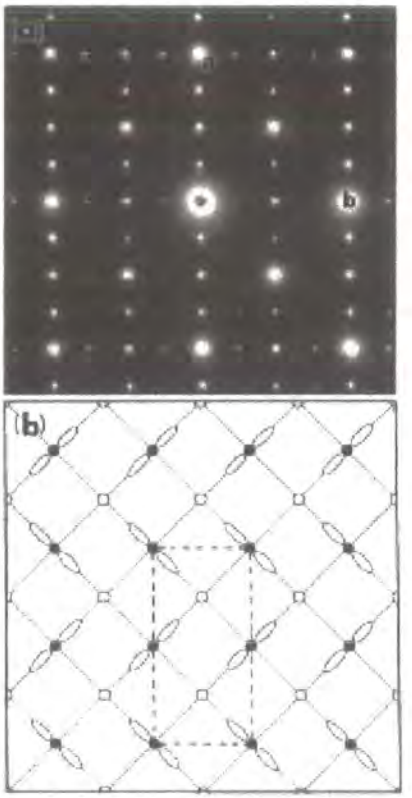

Figure 2.4: *[001] Zone-axis diffraction pattern from $La_{0.5}Ca_{0.5}MnO_3$ (top). The bottom panel shows the proposed charge orbital order pattern.* [8]

It is difficult to synthesise single crystal samples of $La_{0.5}Ca_{0.5}MnO_3$ and, due to this, studies of the system have been restricted to powder diffraction. Powder diffraction is a very useful technique but single crystal x-ray diffraction provides much more detailed and accurate information on the charge ordered state. It is possible to synthesise single crystals of $Nd_{0.5}Sr_{0.5}MnO_3$ [10] which shows similar phase transitions to $La_{0.5}Ca_{0.5}MnO_3$ and single crystals of $Bi_{1-x}Ca_xMnO_3$ which is isostructural with $La_{1-x}Ca_xMnO_3$ and shows a very similar phase diagram.

The phase diagram for $Nd_{1-x}Sr_xMnO_3$ is shown in Figure 2.5. From the phase diagram it can be seen that the system shows a wide variety of phases but the charge ordering only exists in a very narrow doping level around $x = 0.5$. However, the half doped system $Nd_{0.5}Sr_{0.5}MnO_3$ behaves in a similar way to the $La_{0.5}Ca_{0.5}MnO_3$ system. $Nd_{0.5}Sr_{0.5}MnO_3$ is paramagnetic at room temperature and on cooling it undergoes a transition into a

ferromagnetic state at ~ 250 K. Upon further cooling below 160 K it undergoes a transition into a charge ordered, antiferromagnetic state and in this system the charge and spin order occur at the same temperature *i.e.* $T_{CO} = T_N \sim 160$ K.

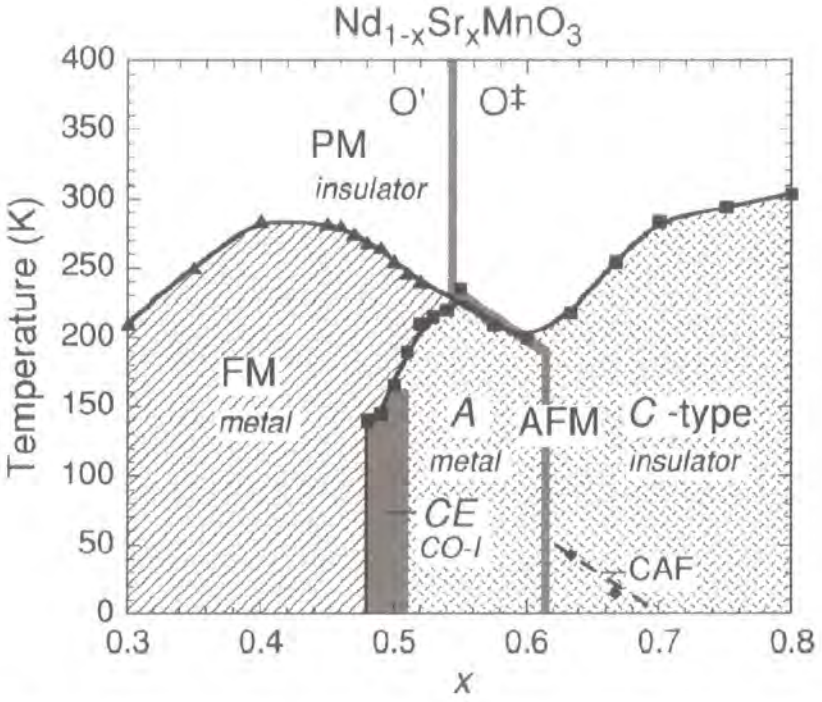

***Figure 2.5**: Phase diagram of $Nd_{1-x}Sr_xMnO_3$. PM – paramagnetic; FM – Ferromagnetic; AFM – Antiferromagnetic; CE – CE type charge magnetic ordering; A- A-type antiferromagnetic; C- C-type antiferromagnetic; CAF-canted antiferromagnetic order taken from Kajimoto et al.* [10]

It has been shown that resonant x-ray scattering at the Mn *K*-edge (which will be described in the section 2.6) could successfully probe the charge and orbital order in $La_{0.5}Sr_{1.5}MnO_4$[11]. $La_{0.5}Sr_{1.5}MnO_4$ has the same charge/orbital order arrangement in the *a* – *b* plane as $La_{0.5}Ca_{0.5}MnO_3$ and $Nd_{0.5}Sr_{0.5}MnO_3$ and the technique was also used to probe the charge and orbital order in $Nd_{0.5}Sr_{0.5}MnO_3$. Nakamura *et al.*[12] found reflections at the Mn *K*-edge corresponding to charge order below 140 K at a modulation of (0, *k*, 0) and orbital order reflections at a modulation of (0, *k*/2, 0). The orbital ordering could not be observed away from the Mn *K*-edge and the charge order showed a clear increase in

the scattered intensity at the Mn *K*-edge The charge ordering reflection fitted a model expected of an alternating pattern of Mn^{3+} and Mn^{4+} ions and the orbital order reflection was attributed to the alternating $3x^2-r^2/3y^2-r^2$ orbital pattern and this is in agreement with the pattern shown in Figure 2.2.

Studies were carried out on the $Pr_{1-x}Ca_xMnO_3$ system which shows charge order over a larger doping range for doping levels of $x = 0.4$ and 0.5.[13] Von Zimmermann *et al.* reported the presence of charge and orbital order similar to that observed in the $Nd_{0.5}Sr_{0.5}MnO_3$ system. Even in the $x = 0.4$ doped system where there are not equal numbers of Mn^{3+} and Mn^{4+} ions, the same charge/orbital order pattern was observed as in the $x = 0.5$ doped sample. Evidence of charge /orbital order was also reported by Wakabayashi *et al.* in the half-doped bi-layer $LaSr_2Mn_2O_7$ [14] which will be discussed in greater detail in section 2.5. The $Bi_{1-x}Ca_xMnO_3$ system is of significant interest because it shows the same phase diagram as $La_{0.5}Ca_{0.5}MnO_3$ with it displaying charge order in the doping range $0.5 \leq x \leq 0.875$. Recently, the $x = 0.76$ doped $Bi_{0.24}Ca_{0.76}MnO_3$ was studied at the Mn *K*-edge by Hatton *et al.*[15, 16] At this doping level in the system there are three times more Mn^{4+} ions than Mn^{3+} ions. In this study the charge order was observed at a modulation of (0.5, 0, 0) and the orbital order at a modulation of (0.25, 0, 0) which is double the direct space modulation seen in the half doped samples. This is consistent with one Mn^{3+} ion per four Mn sites and is an indication in the $Bi_{1-x}Ca_xMnO_3$ system that the charge/orbital order state has another stable configuration at the ¾ doping level. It was postulated that the charge order formed a pattern of Mn^{3+} 'stripes' separated by Mn^{4+} regions in contrast to the checkerboard charge ordered pattern observed in the half doped samples.

The two manganite systems that are studied within this thesis are the $n = 1$ and $n = 2$ members of the Ruddlesden-Popper $(La,Sr)_{n+1}Mn_nO_{3n+1}$ series. This corresponds to the single layer $La_{1-x}Sr_{1+x}MnO_4$ system and the bi-layer $La_{2-2x}Sr_{1+2x}Mn_2O_7$ system and a review of the studies carried out on these systems follows in the next section.

2.2 The Ruddlesden-Popper $(La,Sr)_{n+1}Mn_nO_{3n+1}$ Series

The cubic perovskite system $La_{1-x}Sr_xMnO_3$ was reported to show colossal magnetoresistance at 350 K [17] but a very large magnetic field was required to produce the CMR effect. There are two possible methods of changing the physical and electronic methods in the system, the first is to change the doping levels of La and Sr and the second method is to change the dimensionality of the system. The magnetoresistance properties are very sensitive to the dimensionality of the manganese oxide lattice and by inserting rock salt blocker layers between manganese sheets it is possible to greatly vary the electronic and magnetic properties of the system. This group of compounds is known as the Ruddlesden-Popper (RP) series and they have the general formula $(La,Sr)_{n+1}Mn_nO_{3n+1}$ where n is an integer. Figure 2.6 shows a diagram of the structure in the single layered ($n = 1$), bi-layered ($n = 2$) and cubic ($n = \infty$) systems

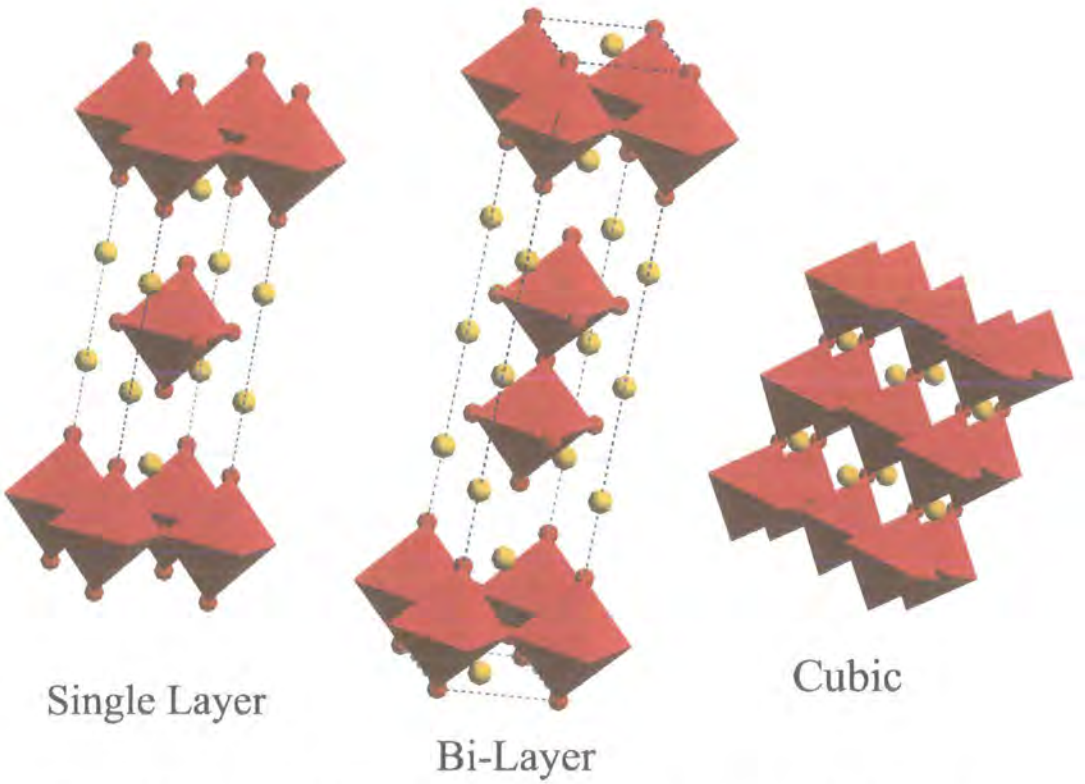

***Figure 2.6**: Structures of the, single layered, bi-layered manganites and cubic manganites*

The first member of this series is the single layered system which corresponds to $n = 1$ and has the general formula $La_{1-x}Sr_{1+x}MnO_4$ and its structure is shown in Figure 2.6. It has one rock salt blocker layer between the MnO_2 planes and a longer c-axis than the cubic system of approximately 12.5 Å. In contrast to the cubic system the single layered system does not show the CMR effect for any doping level or at any temperature; instead the system shows a transition into an antiferromagnetically ordered insulating state with a variation in T_N with doping and in the half doped system $La_{0.5}Sr_{1.5}MnO_4$ at the charge ordering temperature of 220 K there is a significant increase in the resistivity. [18] It should be noted that the $n = \infty$ member of the Ruddlesden-Popper series corresponds to the cubic perovskite system $La_{1-x}Sr_xMnO_3$. By varying the value of n the properties of the system are dramatically changed and they should eventually approach those of the cubic system as n is increased towards infinity. The $n = 2$ member of the Ruddlesden Popper series is known as the bi-layer system and is shown in Figure 2.6 and it is characterized by a very long c-axis of approximately 20 Å. The long c-axis reduces the dimensionality of the system and in the $x = 0.4$ doped system the largest CMR effect observed in the manganites was reported.[19] It was significantly larger than seen previously in the three dimensional (3-D) system and required a smaller magnetic field to produce this effect; i.e. at 1 Tesla the CMR effect is ~ 20 times larger in the bi-layer compared to that of the 3-D system. However, this larger effect is at the cost of a lower transition temperature at approximately 126 K compared to the 3-D system where the transition occurs at 350 K. In theory this system could have possible technical applications as a magnetic sensor. The properties of the cubic system will be discussed briefly before discussing the single layered manganite system and the bi-layer system which are the two manganite systems understudy in this thesis.

2.3 $La_{1-x}Sr_xMnO_3$

$LaMnO_3$ is an insulator but substituting Sr for La dopes holes into the system. It shows a large range of physical properties depending on the doping level and the phase diagram as a function of temperature and doping is shown in Figure 2.7.

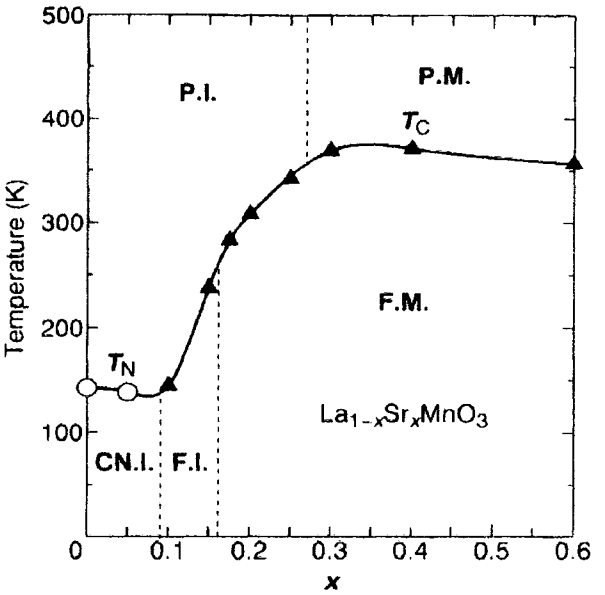

***Figure 2.7**: Phase diagram of the $La_{1-x}Sr_xMnO_3$ system taken from Urushibara et al.*[17]

The half doped system does not show the charge order state, instead below 350 K the system exists in ferromagnetic metallic state. However, in the low doped region between $0 \leq x \leq 0.17$ the system shows some interesting properties. The parent compound $LaMnO_3$ was found to be orbitally ordered with a resonance at a wavevector of (1, 0, 0) at the Mn *K*-edge. This is the expected modulation for the orbital ordering because the system only contains Mn^{3+} ions and hence, the orbital order unit cell will be at half the real space cell compared to that in the half-doped systems. It is not charge ordered because only the Mn^{3+} species are present in the system. The $x = 0.12$ system doped was studied using resonant x-ray scattering technique by Endoch *et al.*[20] At 291 K the system undergoes a transition into a Jahn-Teller distorted phase and on cooling below 145 K the system undergoes a transition into an orbitally ordered state. For $x > 0.18$ the system only shows a transition into the ferromagnetic state.

2.4 $La_{1+x}Sr_{1-x}MnO_4$

The $La_{1-x}Sr_{1+x}MnO_4$ system is indexed with the *I4/mmm* space group with $a = b =$ 3.86Å and $c = 12.4$ Å. The single layered system is often indexed with $a = b = a_P$ as

opposed to the 3-D systems which are indexed with $a \sim b \sim \sqrt{2}a_p$. This corresponds to a rotation of the a and b axes by 45°. The $La_{1-x}Sr_{1+x}MnO_4$ system was studied using electron diffraction and resistivity and susceptibility measurements on single crystal samples in the doping region $0 \leq x \leq 0.7$ by Moritomo *et al.*.[18] The electron diffraction measurements at low temperature showed superlattice reflections surrounding the Bragg peaks at a modulation of (¼, ¼, 0). Figure 2.8 shows the electron diffraction images obtained at 300 K and 110 K.

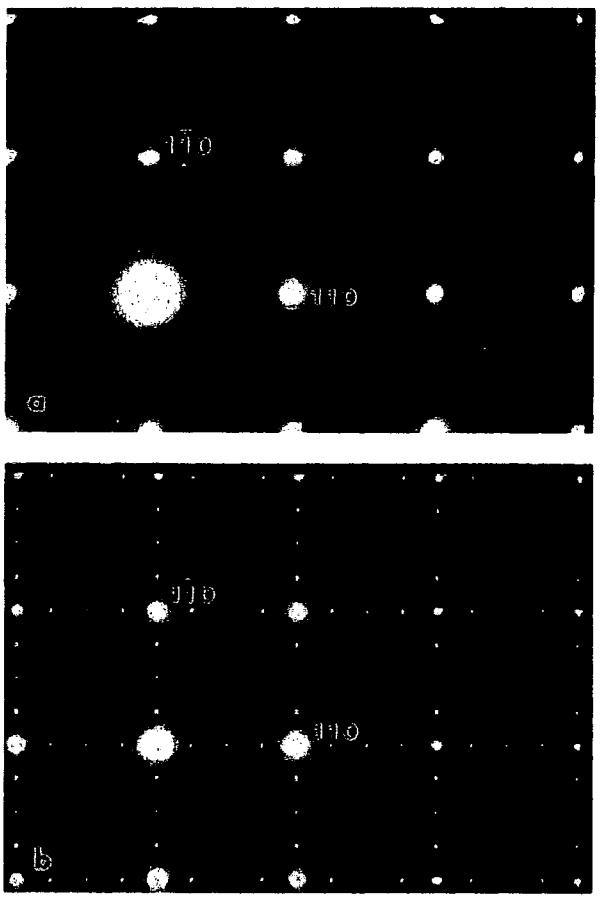

***Figure 2.8**: [001] zone electron diffraction images at 300 K(top) and 110 K (bottom)* [18]

It can be clearly seen that there are two sets of reflections running along the [1 1 0] and [1 $\bar{1}$ 0] directions which suggests the presence of two charge ordered domains. The reflections appeared at 220 K and the resistivity measurements showed this was accompanied by a steep increase in the resistivity. This study was the first to suggest the

existence of a charge ordered phase in $La_{0.5}Sr_{1.5}MnO_4$ but the modulations of (¼, ¼, 0) did not agree with the Goodenough model.

Sternlieb *et al.* [21] carried out a neutron diffraction study on the half doped single layered $La_{0.5}Sr_{1.5}MnO_4$. They reported the observation of superlattice reflections at a wavevector of (½,½, 0) which is attributed to the charge ordering of the Mn^{3+}/Mn^{4+} species and this modulation is in agreement with the model predicted by Goodenough *et al.* The charge order temperature T_{CO} was determined as 217 K which is in agreement with the measurements of Moritomo *et al.*[18] Below the Neél temperature of 110 K superlattice reflections were located at a modulation of (¼, ¼, ½) and these reflections were attributed to the magnetic ordering. The temperature dependence of the charge and magnetic order reflections is shown in Figure 2.9 with the inset showing the resistivity data where a significant increase is seen at the charge ordering temperature. This modulation of the charge order agreed with the Goodenough model.

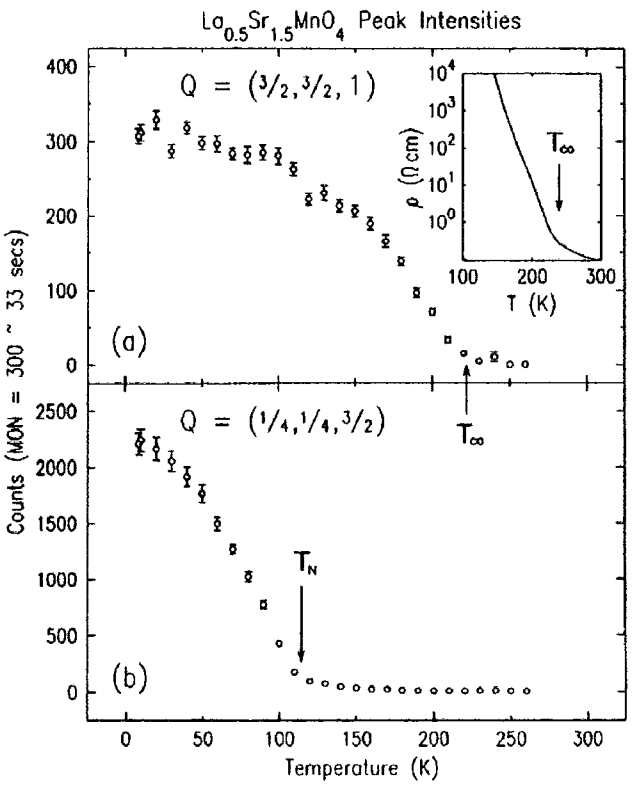

***Figure 2.9**: Temperature dependence of the charge and magnetic order in $La_{0.5}Sr_{1.5}MnO_4$ measured by Sternlieb et al.*[21]

The Goodenough model also predicted order of the e_g orbitals on the Mn^{3+} and this orbital ordering would accompany the charge ordering. In 1998 Murakami *et al.* performed a resonant x-ray scattering study on $La_{0.5}Sr_{1.5}MnO_4$ and this was in fact the first resonant study carried out on any of the manganite systems.[11] In this study they report the first direct evidence of the alternating pattern of the Mn^{3+} and Mn^{4+} ions and claimed the first evidence of the orbital ordering pattern of the e_g electrons on the Mn^{3+} ions. The energy scans for the charge and orbital order are shown in Figure 2.10. A temperature dependence measurement carried out on the charge and orbital order is shown in Figure 2.11 and from this it can be seen that the charge and orbital order appear at the same temperature at approximately 220 K.

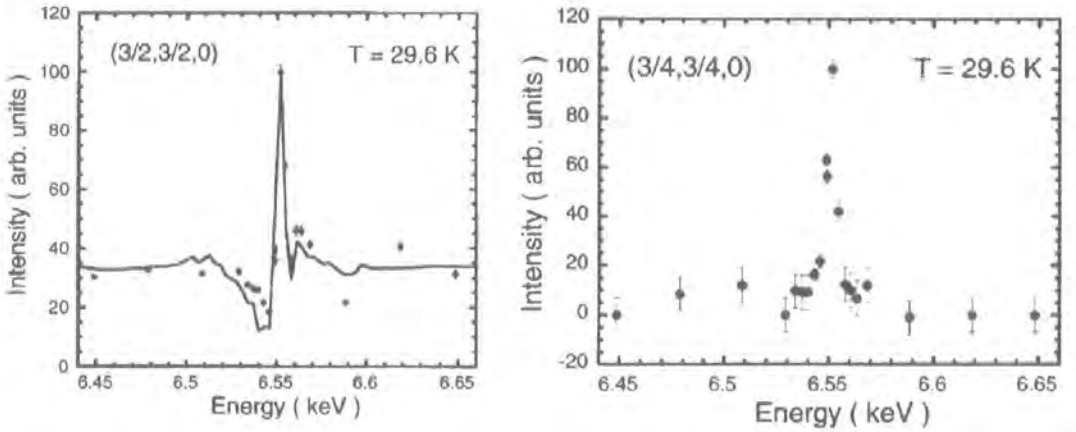

***Figure 2.10**: Energy scans for the (3 2, 3 2, 0) charge order (left) and (3 4, 3 4, 0) orbital order reflections (right) taken from Murakami et al.[11]*

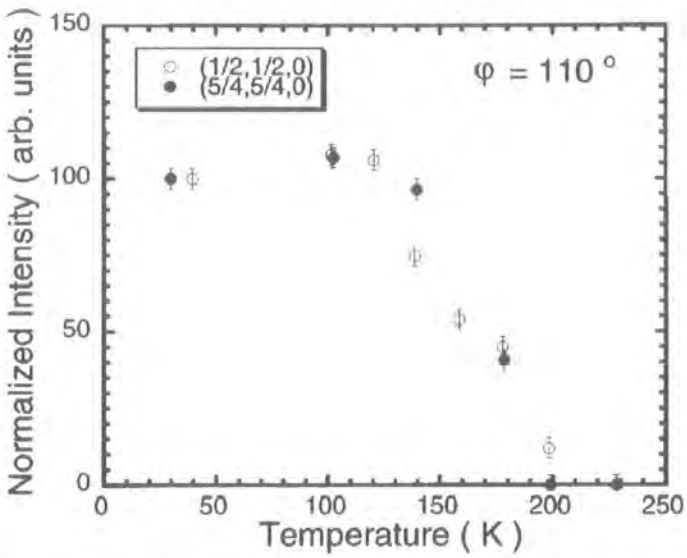

***Figure 2.11**: Temperature dependence of the (1/2,1/2, 0) and (5/4, 5/4, 0) reflections*

If we refer to section 2.7 to discuss the charge order it can be seen that the resonance confirms the Mn^{3+}/Mn^{4+} pattern. Resonant x-ray scattering is the only technique that can confirm this pattern as the electron and neutron techniques are only sensitive to distortions of the crystal lattice. In the study it was claimed this technique was the first to directly measure the orbital order. However, this claim has caused considerable debate as the *K*-edge measurements are sensitive to a splitting in the 4*p* orbitals caused by the orbital ordering in the 3*d* orbitals. This is discussed in greater detail in Chapter 8. The study did confirm the charge and orbital ordering occurs at the same temperature.

2.5 $La_{2-2x}Sr_{1+2x}Mn_2O_7$

The bi-layer system corresponds to the $n = 2$ member of the Ruddlesden – Popper series and has the general formula $La_{2-2x}Sr_{1+2x}Mn_2O_7$. The bi-layer manganite has the *I4/mmm* space group with $a = b = 3.87$ Å and $c \sim 20$ Å. The presence of the rock salt blocker layer has the effect of reducing the dimensionality of the system. As mentioned the $x = 0.4$ doped system shows a huge CMR effect but by substituting La for Sr and hence increasing the hole doping level, the physical and electronic properties of the bi-layer can be changed drastically. The half-doped bi-layer system $LaSr_2Mn_2O_7$ has the

same structure within the *a-b* plane as that in the perovskite manganites and the single layered $n = 1$ $La_{0.5}Sr_{1.5}MnO_4$. The half doped bi-layer would therefore be expected to display the same charge/orbital order checkerboard arrangement seen in $La_{0.5}Sr_{1.5}MnO_4$, $Nd_{0.5}Sr_{0.5}MnO_3$ [12] and $Pr_{0.5}Ca_{0.5}MnO_3$[13]. Figure 2.12 shows a comparison of resistivity measurements carried out on a series of half doped manganite compounds. It can be seen that there is a significant difference in the behaviour of the single layered and bi-layered systems. The bi-layer system shows significantly lower resistivity and on cooling below 160 K actually shows a decrease in resistivity before recovering at low temperatures.

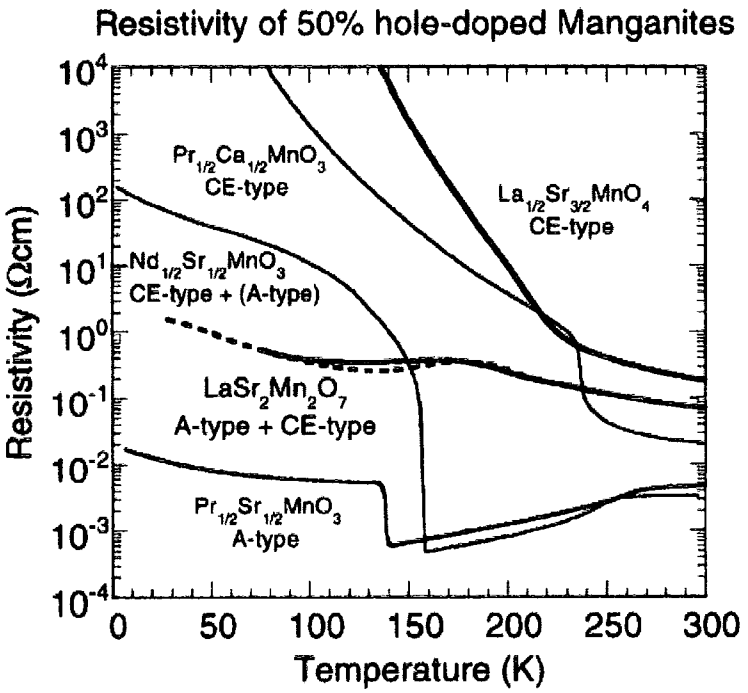

***Figure 2.12**: Temperature dependence of the resistivity in various half doped manganites taken from Kubota et al.* [22]

As in the single layered system the bi-layer system is often indexed with $a = b = a_P$ and in this model the charge and orbital reflections occur at a modulation of

$$\boldsymbol{Q}_{CO} = (\tfrac{1}{2}, \tfrac{1}{2}, 0)$$

$$\boldsymbol{Q}_{OO} = (\tfrac{1}{4}, \tfrac{1}{4}, 0)$$

The half doped system was first studied using electron diffraction and image simulation by Li *et al.* [23] They reported the appearance of reflections at low temperature around the

Bragg peaks with a modulation of (¼, ¼, 0) and they attributed these to charge ordering. They obtained electron diffraction images from the sample at 300 K and 110 K and they reported the observation of two sets of satellites along the [110] and [1 $\bar{1}$ 0] directions which was suggested to be two charge ordered domains. These results were also observed by Kimura *et al.*[24] by electron and x-ray diffraction. The electron diffraction image obtained by Kimura *et al.* is shown in Figure 2.13. The figure illustrates that the superlattice reflections are only observed in the intermediate temperature region between 100 K and 200 K.

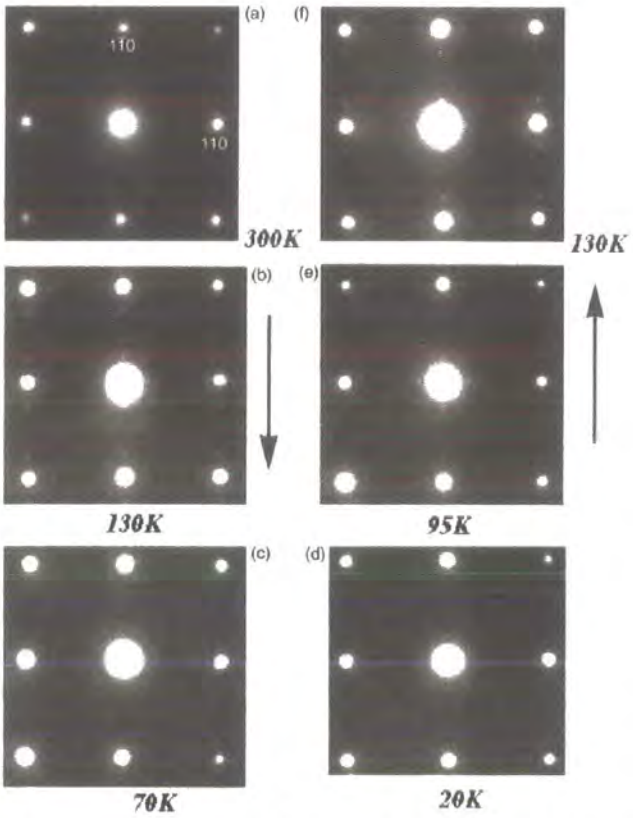

***Figure 2.13**: [001] zone-axis electron diffraction measurements observed at 300, 130, 70, 20 and 95 K taken from Kimura et al.*[24]

In both studies the superlattice reflections appeared below 210 K and increased sharply in intensity reaching a maximum at 180 K. Li *et al.* reported that the charge ordering showed re-entrant behaviour, with the system ordering antiferromagnetically at 180 K, causing the charge ordered state to collapse and the superlattice reflections to

decrease in intensity and to be not observable below 100 K. This was also reported by Kimura *et al.* and from x-ray imaging they obtained the temperature dependence of intensity for the (7/4, -1/4, 0) and (7/4, 1/4 0) reflections and this is shown in Figure 2.14. In these studies they found no evidence of the charge order reflections below 100 K.

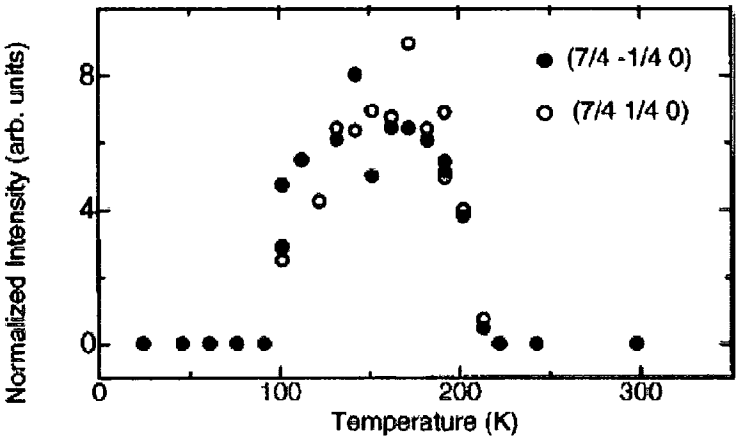

***Figure 2.14**: Temperature dependence of the charge order reflections observed using x-ray imaging taken from Kimura et al.*[24]

However, the observation of charge order at a modulation of (¼, ¼, 0) does not agree with the Goodenough model which predicts the charge order to occur at (½, ½, 0) and orbital order at (¼, ¼, 0). Chatterji *et al.* [25] carried out both a high energy and resonant x-ray diffraction on an $x = 0.5$ sample. At high energy they observed the appearance of the charge ordered state below 220 K at a modulation of (-0.25, 0.25, 0) around the Bragg peaks and this was again attributed to charge order. The satellites reached a maximum in intensity at 180 K and decreased until a minimum was reached at 100 K and this is shown in Figure 2.15. However, unlike the electron diffraction they reported that the reflections always had non-zero intensity and below 50 K the reflection displayed a recovery in intensity reaching a value of 9% at base temperature of 9 K. This reflection was observed at a high energy well away from the Mn *K*-edge so it cannot be orbital order and is therefore in disagreement with the Goodenough model. Chatterji *et al.* suggest a model in which there is an alternate stacking of Mn^{3+} - Mn^{3+} - Mn^{4+} - Mn^{4+} along the *b*-axis, a type of narrow stripe ordering. They also performed resonant X-ray scattering experiments at the Mn *K*-edge on the same sample. They report the observation of a

reflection at (0.25, 0.25, 10) which was observed away from resonance and when the scattering geometry was $\sigma - \pi'$ and this is shown in Figure 2.16.

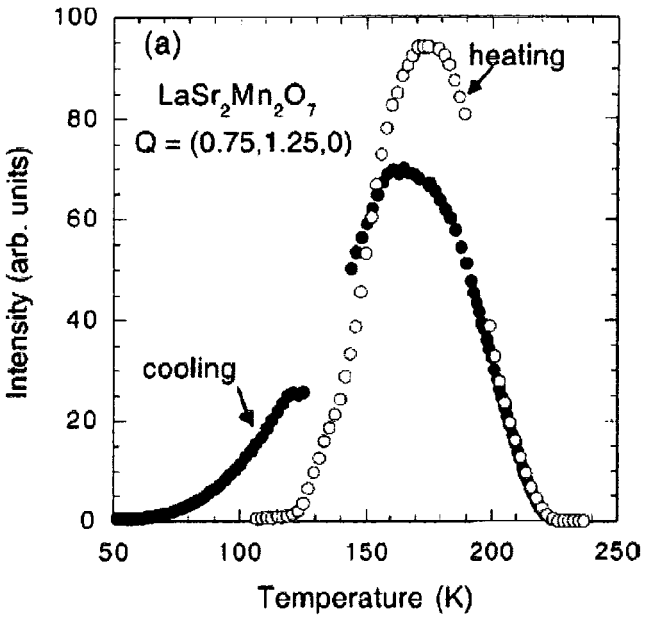

***Figure 2.15**: Temperature dependence of the (0.75, 1.25, 0) reflection as reported by Chatterji et al.*[25]

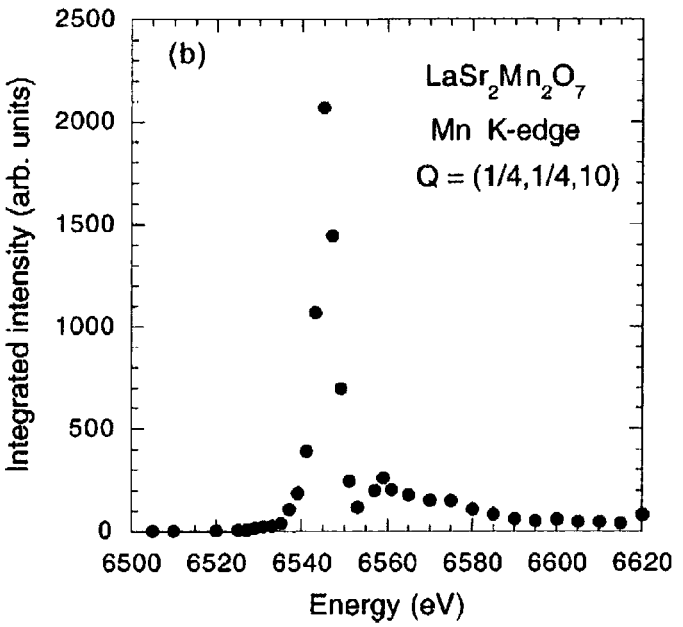

***Figure 2.16**: Energy scan of the (0.25, 0.25, 10) reflection at the Mn K-edge. Taken from Chatterji et al.*[25]

The reflection was not observed away from the Mn-*K* edge and they did not speculate on the cause of this reflection but its behaviour is consistent with the orbital order that would be observed in the Goodenough model. A resonant X-ray study by Wakabayashi *et al.* [14] concentrated on the charge and orbital order within the half doped bilayer manganite. They utilised the Anisotropy of the Tensor Susceptibility (ATS) technique which had previously been used to study $La_{0.5}Sr_{1.5}MnO_4$ and $Nd_{0.5}Sr_{0.5}MnO_3$. Unlike Chatterji they reported the presence of the charge order at a modulation of (0.5, 0.5, 0) and the orbital order at (0.25, 0.25, 0) which is consistent with the modulations predicted by the Goodenough model. Polarisation analysis determined that the charge order signal scattered $\sigma - \sigma$ and the orbital order signal scattered σ - π and Figure 2.17 shows the energy resonances obtained on the charge and orbital order.

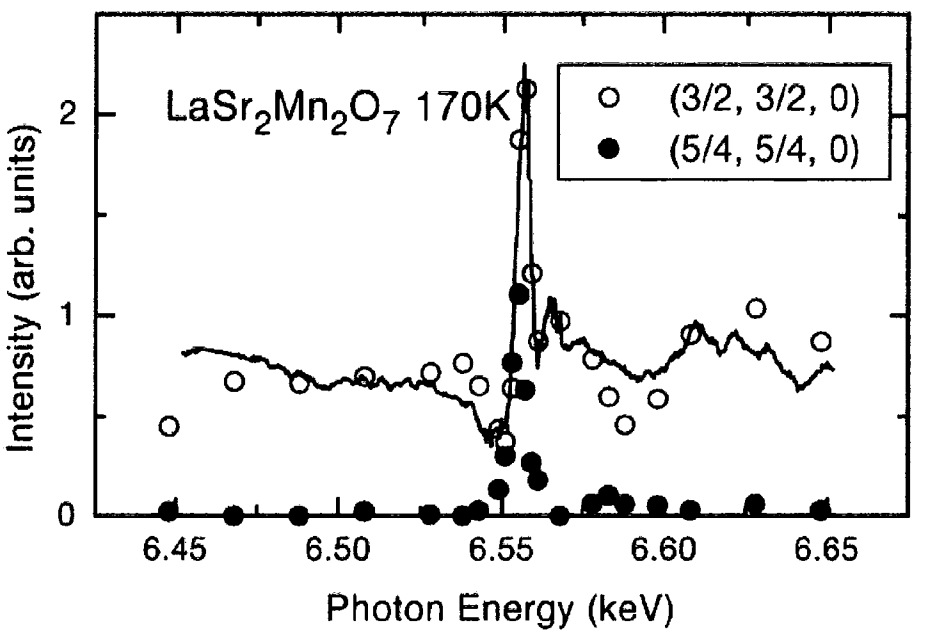

***Figure 2.17**: Energy Scan of the (3/2, 3/2, 0) charge order and (5/4, 5/4, 0) orbital order reflections taken from Wakabayashi et al.* [14]

The behaviour of the charge and orbital order is consistent with that seen in other manganites using resonant x-ray scattering. A similar temperature dependence to that seen by Chatterji *et al.*[25] was observed but they did not observe the reappearance below 50K. Originally the charge ordered state was though to only exist in a very narrow

doping region around x = 0.5. However, magnetotransport and powder diffraction measurements carried out by Dho *et al.* [26] showed that the charge order existed in a much larger doping regime. The measurements indicated that the re-entrant charge order existed in the doping regime $0.47 < x < 0.62$ and a non-re-entrant charge ordered state existed for $x > 0.62$. However, this was powder diffraction data and to gain more information about the charge ordered state it is necessary to carry out single crystal x-ray diffraction studies to understand the evolution of the charge ordered state.

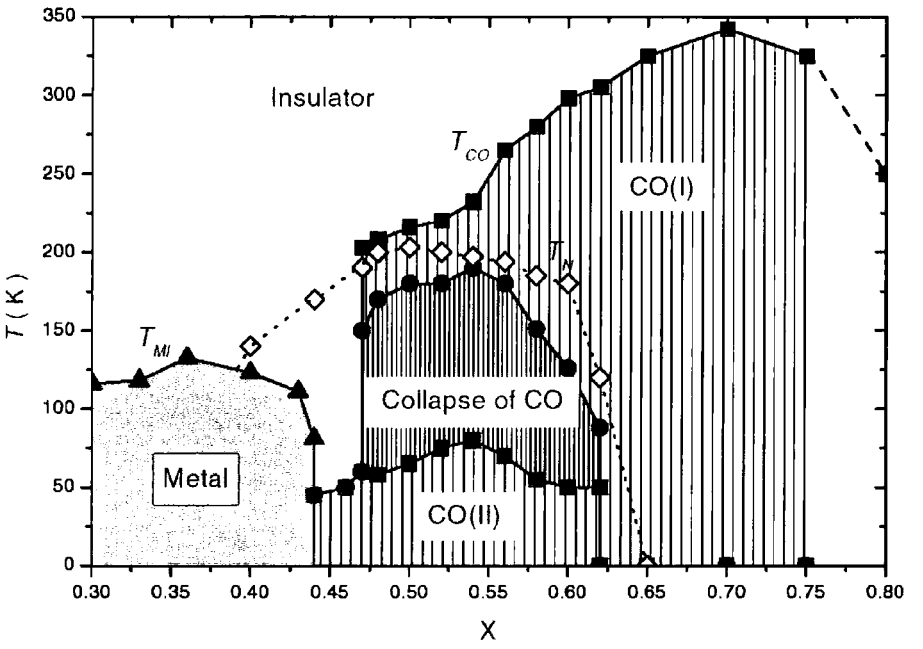

***Figure 2.18**: Phase diagram of the $La_{2-2x}Sr_{1+2x}Mn_2O_7$ system in the doping region $0.3<x<0.8$. The filled symbols show the transport data and the open symbols are from previously reported values. The squares show T_{CO} and the triangles T_{MI}*

In Chapter 3 the results from the x = 0.5 and x = 0.475 bi-layer manganites using high energy x-ray scattering at HASYLAB Hamburg and resonant x-ray scattering at the Mn *K*-edge at beamline BM28 ESRF Grenoble are discussed. In Chapter 4 we discuss the results from high energy x-ray scattering studies on the x = 0.55 and 0.60 doping in which no previous single crystal studies of any type have been carried out.

2.6 Resonant X-ray scattering

2.6.1 Charge Ordering

With neutron scattering and non-resonant x-ray scattering techniques it is not possible to determine whether reflections originate from structural modulations associated with the Jahn-Teller order or charge order or if they originate from the electron density difference between the charge order pattern of the Mn^{3+} and Mn^{4+} ions. The technique suitable for differentiating between them is resonant x-ray scattering. Structural modulations will be expected to show a decrease in intensity at an absorption edge. Due to increased absorption a smaller volume is probed and hence, the scattered intensity decreases. However, reflections associated with the Mn^{3+}/Mn^{4+} pattern would be expected to show a resonance at the Mn *K*-edge.

The total scattering factor is given by the equation

$$f(Q,\hbar\omega) = f_0(Q) + f^{|}(\hbar\omega) + if^{||}(\hbar\omega) \qquad \textbf{(2.1)}$$

where f_0 is the non-resonant scattering factor and $f^{|}$ and $if^{||}$ are the real and imaginary parts of the anomalous scattering factor.

At an absorption edge there is a significant increase in the anomalous scattering factors. For the half-doped charge order unit cell the Mn^{3+} and Mn^{4+} ions scatter out of phase, hence the intensity of the charge order reflection is proportional to the difference in the scattering between the Mn^{3+} and Mn^{4+} ions. Away from the absorption edges this difference is very small and only due to differences in the oxygen octahedra around the Mn^{3+} and Mn^{4+} ions. The absorption edges of the Mn^{3+} and Mn^{4+} ions are at slightly different positions due to the effects of the chemical shift. Figure 2.19 shows XAFS data from $LaMnO_3$ and $SrMnO_3$ which contain only Mn^{3+} and Mn^{4+} ions respectively obtained at Daresbury station 2.3 by Stuart Wilkins.

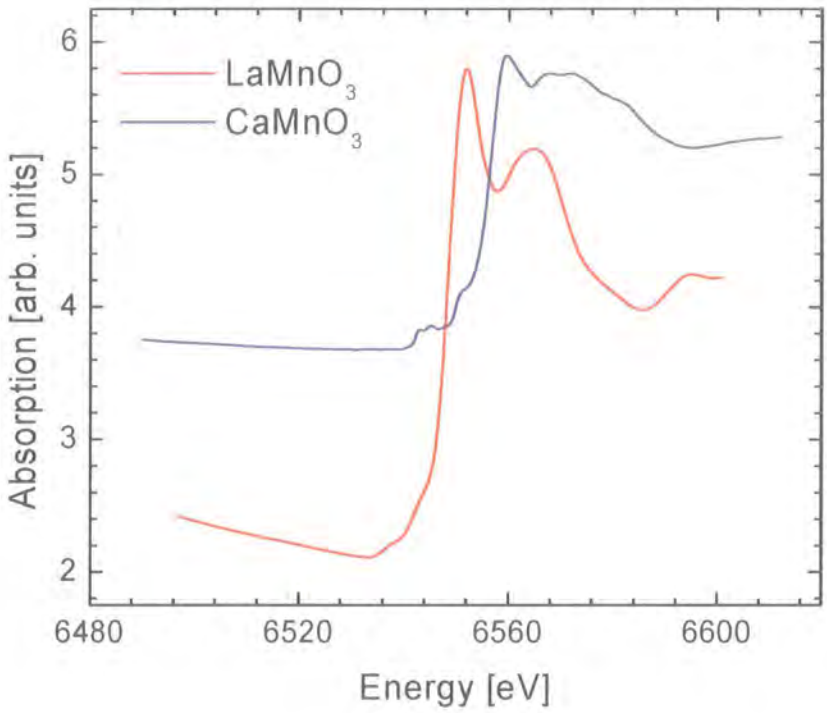

***Figure 2.19**: XAFS data for $LaMnO_3$ and $CaMnO_3$*

From this figure it can be determined that there is a difference in the absorption edges of approximately 8 eV. From this it can therefore be concluded that there will be an increase in the anomalous scattering factors of the Mn^{3+} ions at a slightly lower energy than the Mn^{4+}ions. The total scattering factor for the charge ordering is given by the equation : -

$$f_{CO}(Q,\hbar\omega) = (f_0^{3+} + f'^{3+}(\hbar\omega) + if''^{3+}(\hbar\omega)) - (f_0^{4+} + f'^{4+}(\hbar\omega) + if''^{4+}(\hbar\omega)) \quad \textbf{(2.2)}$$

Therefore, if the x-ray energy is tuned to an energy between the two edges there will be a large contrast in the scattering factors of the Mn^{3+} and Mn^{4+} ions and a resonance in the scattered intensity will be observed. Therefore, the resonant x-ray scattering technique can differentiate between structural modulations and the Mn^{3+}/Mn^{4+} pattern.

2.6.2 Orbital Ordering

The orbital ordering is associated with differences in the charge density between neighbouring Mn^{3+} ions caused by the two possible orientations of the e_g electron on the Mn^{3+} ions. Away from an absorption edge this effect is negligible, but by tuning to an absorption edge there will be a resonant enhancement in the scattered signal.

At the Mn *K* edge the transition occurring is from the $1s$ – $4p$ orbitals and in manganese the $4p$ shell is unoccupied. However, one theory suggested that the interaction with the ordered $3d$ e_g orbitals caused a splitting in the unoccupied $4p_{x,y,z}$ states. Figure 2.20 shows a schematic of the orbital ordering in $LaMnO_3$ and the associated energy level schematic in the $4p$ band in the orbitally ordered state proposed by Murakami *et al.*[27]

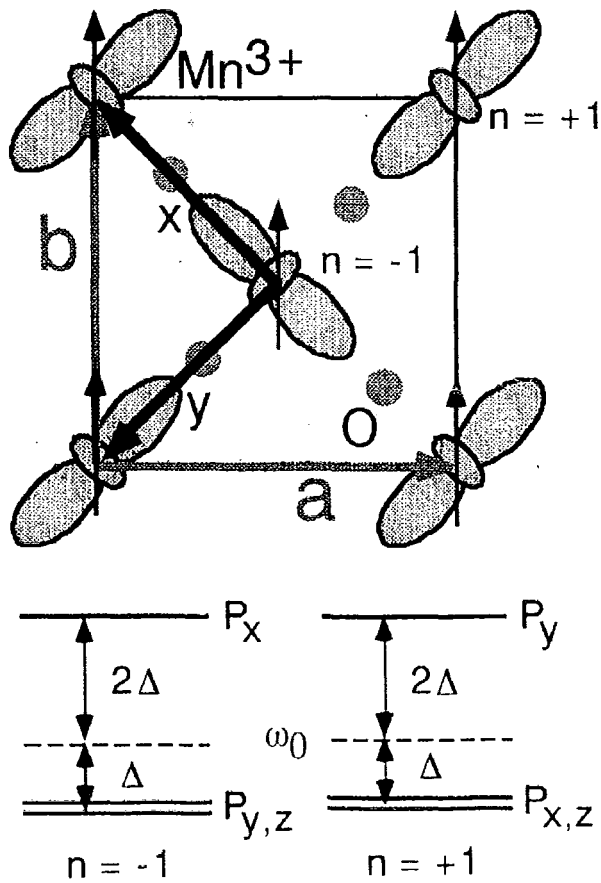

***Figure 2.20**: Schematic of the energy level splitting in the 4p band associated with the 3d orbital order*

The intensity of the x-ray scattering depends upon the size of the splitting Δ. In this co-ordinate system the *x*, *y* axes are along the direction in which the ordered e_g orbital extends and *z* is perpendicular to the *a*-*b* plane. The two different directions of the e_g orbital are given by the value of *n* where *n* = + 1 when the orbital extends along the *y* axis and *n* = -1 along the *x* axis. The intensity from the difference between the two split 4*p* states is given by the equation

$$I^{res} = \langle \sum_{m=x,y,z,n=\pm 1} n \frac{< s \mid P^{\alpha} \mid p_m >< p_m \mid P^{\beta} \mid s >}{\omega - \omega_0 - \delta\omega_m^n + i\Gamma/2} \varepsilon'^{\alpha} \varepsilon^{\beta} \rangle^2 \quad \textbf{(2.3)}$$

Where $\mid s >$ and $\mid p >$ are the wavefunctions of the 1*s* and 4*p* orbitals. P^{α} and P^{β} are the dipole operators. ω is the incident photon angular frequency, ω_0 is the angular frequency of the unperturbed 4*p* levels. The polarisation of the incoming photons is ε and that of the emitted photons ε'. Γ is the lifetime of the excited state and *n* has been defined previously. $\hbar\delta\omega_m^1 = 2\Delta$ for $m = y$ and -Δ for $m = x, z$ and similarly $\hbar\delta\omega_m^{-1} = 2\Delta$ for $m = x, z$ and -Δ for $m = y$. Δ is the energy.

However, Murakami *et al.* did not specify the origin of the splitting within the 4*p* band in their model. There has been a great deal of debate as to whether the *K* edge experiments are a direct probe of the orbital order and it has been suggested in a paper by Castleton and Altarelli [28] that the only technique to directly probe the orbital degree of freedom would be resonant x-ray scattering studies at the Mn L_{II} and L_{III} edges which would directly probe the e_g level. Two models have been proposed to explain the splitting in the 4*p* levels. The first model proposed was that the Jahn-Teller distortion of the oxygen octahedra would lower the 4*p* levels along the direction of the elongation and raise them in the direction of the compression. The second possible method is through Coulomb interactions between the 4*p* states and the orbitally ordered 3*d* levels suggested by Ishihara *et al.*[29] In a re-examination of the data by Benfatto *et al.* [30] they suggested that the *K*-edge experiment would be 100 times more sensitive to the associated Jahn-

Teller ordering and this will be discussed in greater detail in Chapter 8. It should be noted that the *K*-edge resonant technique cannot distinguish between the two mechanisms, it is only sensitive to the splitting not the origin and a reflection is observed for non-zero Δ.

The first system in which the resonant x-ray scattering technique at the Mn *K* edge was used was the single layered $La_{0.5}Sr_{1.5}MnO_4$. [11] It should be noted that the related cubic perovskite $La_{0.5}Sr_{0.5}MnO_3$ does not show charge order. In $La_{0.5}Sr_{1.5}MnO_4$ there is a 1:1 ratio of Mn^{3+} and Mn^{4+} ions and this doping is the most stable configuration for a charge ordering pattern. In the $a - b$ plane it shows the same charge and orbital pattern as that in cubic perovskite manganites. It undergoes a metal insulator transition at approximately 220 K and below this temperature charge and orbital order were observed at the expected modulations predicted by Goodenough.

2.7 Cuprates

Superconductivity was first discovered in the layered copper oxides system $La_{2-x}Ba_xCuO_4$ in 1986 by Bendnorz and Müeller [31] and this provoked intensive research into the layered cuprates. The parent compound La_2CuO_4 is an antiferromagnetic Mott insulator and has the layered K_2NiF_4 structure but by substituting Ba for La holes are doped into the system and in the doping region $0.05 \leq x \leq 0.20$ the system displays superconductivity. Superconductivity was later reported in the related Sr doped system $La_{2-x}Sr_xCuO_4$ over a similar doping range. [32] One of the major areas of investigation in understanding the properties of the layered cuprates is the relationship between charge stripes and superconductivity. In both the $La_{2-x}Ba_xCuO_4$ and $La_{2-x}Sr_xCuO_4$ systems a suppression of the superconductivity was observed when the doping level was approximately equal to 1/8. Figure 2.21 shows susceptibility measurements carried out on the $La_{2-x}Sr_xCuO_4$ system by Radaelli *et al.* [33] that show a clear suppression of the superconductivity temperature at approximately $x = 0.125$ and similar behaviour was also observed in $La_{2-x}Ba_xCuO_4$. It was clear from these measurements that there was something significant occurring in the doping level of $x = 1/8$.

There has been a great deal of discussion about the origin of the suppression at the 1/8 doping level and one strongly debated idea is the holes doped into the system ordering into charge stripes. It has been postulated that the charge stripes are stabilised at the 1/8 position because it is commensurate with the lattice and the coupling between the charge and the lattice stabilises any charge stripe order.

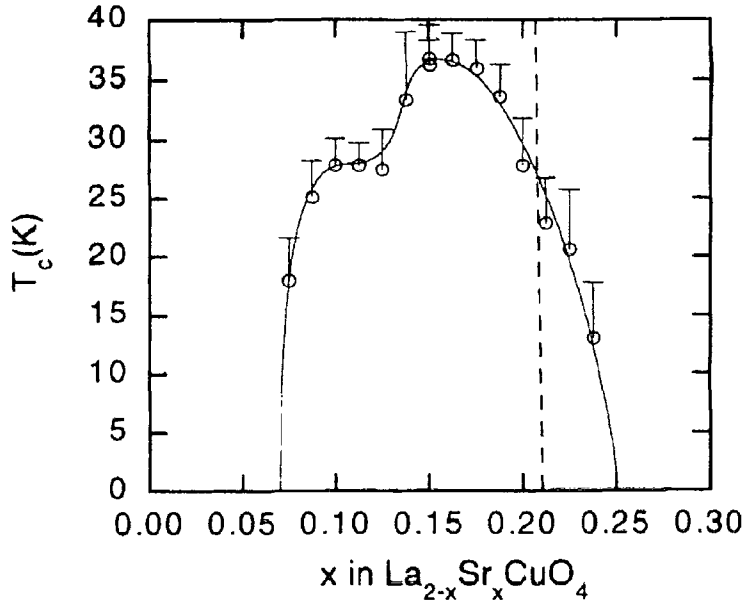

***Figure 2.21**: Onset (top of error bars) and midpoint (circle) critical temperature as a function of doping from a.c susceptibility measurements. The dotted line shows the orthorhombic to tetragonal phase transition from neutron diffraction measurements.*[33]

Neutron scattering measurements carried out by Cheong *et al.* on $La_{2-x}Sr_xCuO_4$ for doping levels of x = 0.075 and 0.14 provided the first evidence of incommensurate magnetic fluctuations in this system.[34] A later study on the x = 0.12 doped system by Suzuki *et al.* [35] showed that below the superconductivity temperature of 31.5 K a splitting occurred around the (½, ½, 0) position and very weak peaks were located at modulations of (½ ± ε, ½, 0) and (½, ½ ± ε, 0) with ε = 0.126. The peaks were interpreted as being evidence of long range magnetic order. Measurements carried out by Kimura [36] on the same doping level determined an in-plane correlation length of 200 Å, again indicative of long range magnetic order. Interestingly in work carried out by Wakimoto *et al.*[37]

incommensurate magnetic peaks were also located in the non-superconducting $x = 0.05$ doping level. This was initially thought to show that the spin order was not strongly related to the superconductivity but a more detailed study in the doping range 0.03 – 0.12 [38] revealed that in the superconducting samples the spin stripes were rotated by 45° compared to those in the insulating phase. The spin stripes in the insulating phase ran diagonally in the plane and in that respect existed in a similar state to those observed in the nickelate system which does not show superconductivity. The second difference was that in the superconducting phase there were four satellites whereas in the insulating phase only two satellites were observed. Evidence of one dimensional spin order was found in doping levels as low as 0.024 by Matsuda *et al.*[39] and the data from that study and that of Wakimoto is shown in Figure 2.22 that shows the incommensurability as a function of doping.

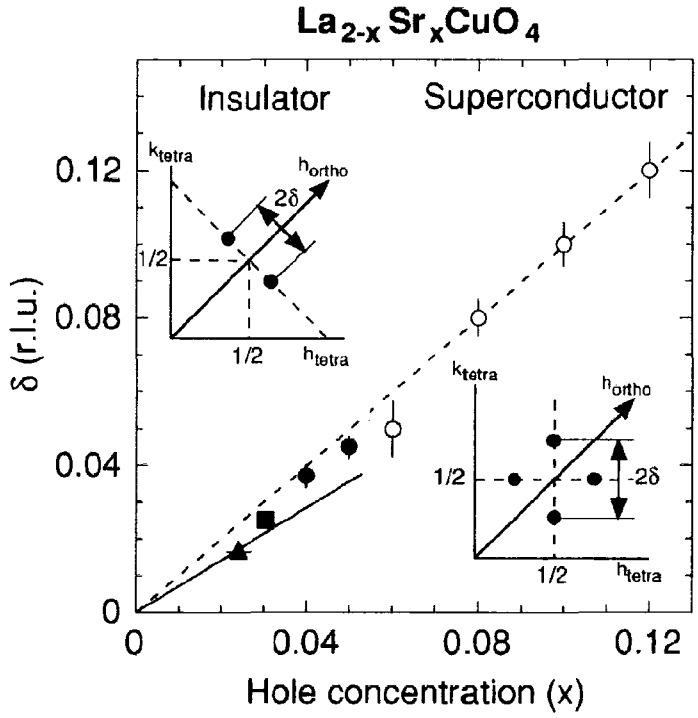

***Figure 2.22**: Incommensurability dependence as a function of hole concentration taken from Matsuda et al.*[39]

The first evidence of static charge stripes in the cuprate system was observed in neodymium doped $La_{1.6-x}Nd_{0.4}Sr_xCuO_4$ in which there is a partial substitution of La for Nd.[40] Studies of the cuprate system showed that the suppression phenomenon in addition to a commensurate doping level of ~ 1/8 also requires a distortion of the lattice from a low-temperature orthorhombic (LTO) phase to a low temperature tetragonal (LTT) phase and this is stabilised by the substitution of Nd for La. Nd has the same valence as La but Nd^{3+} has a slightly smaller radius than the La^{3+} (1.15 Å compared to 1.22 Å for La^{3+}) and the substitution of Nd stabilises the LTT phase necessary for stable charge and spin order. It has been suggested that this causes a pinning of the stripes and hence, static charge stripes are observed. In the $x = 0.12$ doped sample $La_{1.48}Nd_{0.4}Sr_{0.12}CuO_4$ Tranquada *et al.* observed the magnetic superlattice peaks at a modulation of ($\frac{1}{2} \pm \varepsilon$, $\frac{1}{2} \pm \varepsilon$, 0) and the charge superlattice peaks at a modulation of (2ε, 0, 0). The magnetic order peaks were observed to be more intense than those in the in undoped system. The magnetic order was found to be two dimensional in nature with an in-plane correlation length of 170 Å, but poorly correlated between planes. The temperature dependence of the charge and magnetic order is shown below in Figure 2.23.

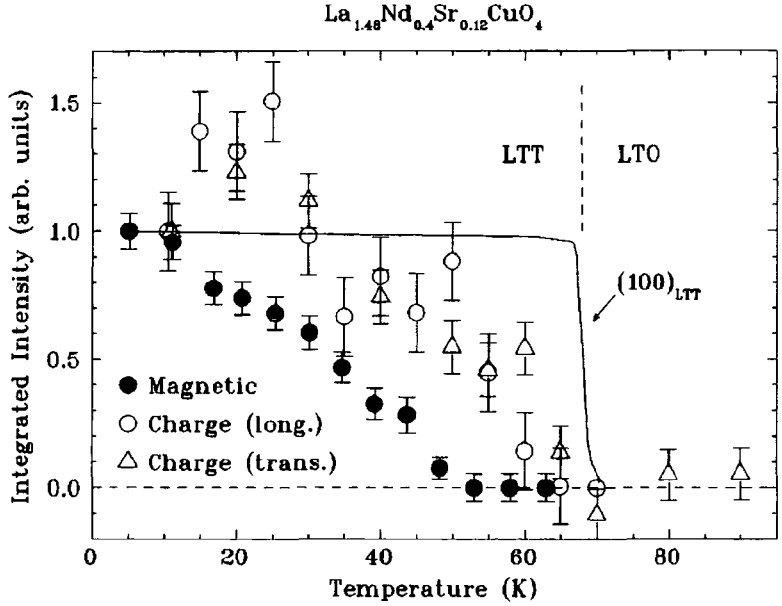

***Figure 2.23**: Temperature dependence of the charge and magnetic order in $La_{1.48}Nd_{0.4}Sr_{0.12}CuO_4$ taken from Tranquada et al.*[40]

On heating the charge order disappeared at approximately 60 K and the magnetic order at 50 K and the structural transition from LTT – LTO was determined to be at 70 K which was in line with the LTT structure favouring the charge ordering. High energy x-ray scattering studies by von Zimmermann *et al.* [41] confirmed that the reflections observed at the (2-2ε, 0, 0) originated from charge order but they did not observe the spin order peaks due to the weak interaction of x-rays with magnetic order. The relationship between charge stripes and superconductivity has been strongly debated and at present, despite many studies, there is no definite proof that the two are related.

2.8 The $La_{2-x}Sr_xNiO_{4+\delta}$ Nickelate System

The nickelate system $La_{2-x}Sr_xNiO_4$ is isostructural to the $La_{2-x}Sr_xCuO_4$ system and for this reason attracted much interest after the discovery of high-temperature superconductivity in the cuprate system. The nickelate system unlike the cuprate system does show strong well correlated charge stripe ordering but it does not show superconductivity for any doping level. Like La_2CuO_4 the parent compound La_2NiO_4 is an antiferromagnetic Mott insulator with the layered perovskite K_2NiF_4 structure. By substituting strontium for lanthanum, holes are doped into the system, and this changes the properties of both systems from insulating to metallic behaviour. However, the critical hole concentrations are considerably different between the two systems. As discussed in the previous section the cuprate system displays weak, diffuse charge stripes whereas the nickelate system displays strong well correlated charge stripes. In the nickelates, metallic behaviour does not occur until approximately $x = 1$ [42] and at no doping level does the material displays superconductivity, whereas $La_{2-x}Sr_xCuO_4$ becomes metallic and display superconductivity for x as small as 0.05. The nickelates are model stripe systems and are ideal for an investigation of the interplay between the charge and lattice. The difference in the electrical and magnetic properties has been attributed to the stronger electron-lattice coupling in nickelates [43] which causes much stronger localisation effects than that observed in the cuprates.

When strontium is substituted into the system for lanthanum, holes are doped into the system. The holes doped into the lattice are mobile and drastically change the properties

of the $La_{2-x}Sr_xNiO_4$ system. In resistivity measurements carried out by Cheong *et al.* [44] on $La_{2-x}Sr_xNiO_{4+\delta}$ in the doping region $0.2 \leq x \leq 0.4$ shown in Figure 2.24 an anomaly was observed at 240 K and this was most significant in the $x = 0.33$ doped sample. The susceptibility in the bottom panel also shows an anomaly at 240 K with it again being most significant in the $x = 0.33$ doped sample.

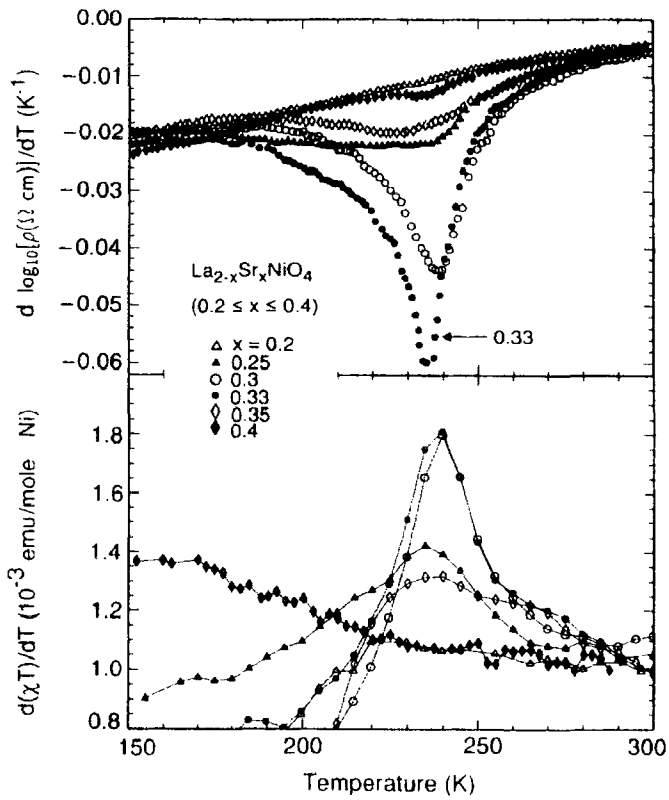

***Figure 2.24**: Temperature derivative of the logarithmic resistivity (top panel) and susceptibility multiplied by temperature as a function of temperature in the doping range $0.2 \leq x \leq 0.4$ taken from Cheong et al.* [44]

At high temperatures the holes are mobile and have a random distribution throughout the lattice. Below the charge ordering temperature, T_{CO}, the holes segregate to form stripes and below T_N, the spins order in the region between the charge stripes. The spacing between the stripes is dependent on the hole concentration n_h. The hole-rich stripes act as π domain walls for the local antiferromagnetic order, existing in the hole deficient regions with nickel moments parallel to the stripe propagation direction. Such

charge and spin stripes form within the $a - b$ plane of the material, and are found to be two dimensional in nature with poor correlation between planes. A schematic view of the charge stripes is shown in Figure 2.25. The charge stripes are at 45° to the a and b axes in the tetragonal $I4/mmm$ setting.

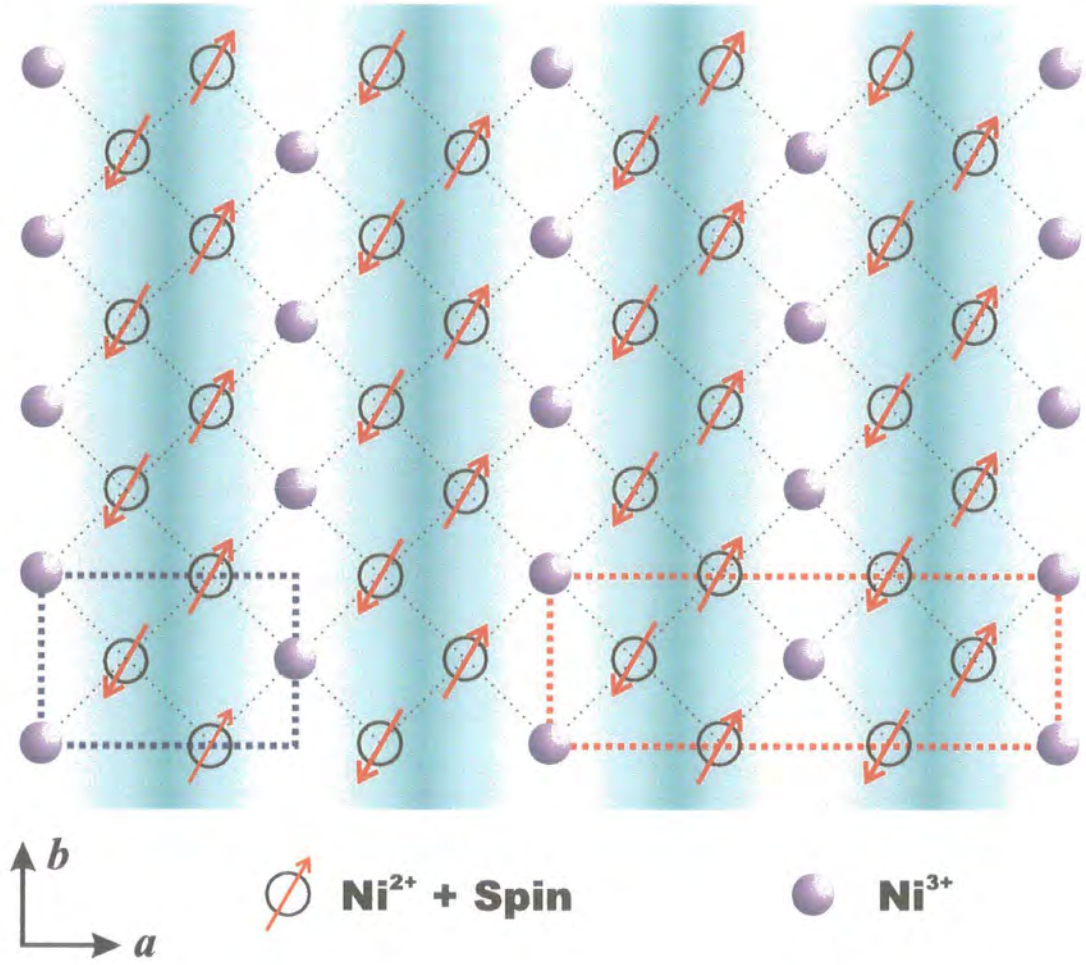

***Figure 2.25**: A schematic representation of the charge and spin stripes in $La_{1.67}Sr_{0.33}NiO_4$. Ni^{3+} ions are shown as filled circles and the Ni^{2+} ions are represented as open circles with the associated spin vector. The spins are believed to be canted away from the stripe direction. The dotted lines show the spin and charge supercells respectively and the shading shows the charge density distribution.* [45]

The system was initially studied using neutron diffraction by Lee *et al.* [46] and the wavevectors for the charge and spin ordering were found to be $Q_{CO} = (2\varepsilon, 0, 1)$ and $Q_{SO} = (\varepsilon, 0, 1)$ respectively. The commensurability approximately follows the law $\varepsilon = n_h$ law with $n_h = x + 2\delta$. δ is the amount of excess oxygen in the stoichiometry where the chemical formula for the system is $La_{2-x}Sr_xNiO_{4+\delta}$. The $x = 0.33$ composition is unique because the charge and spin stripes occur at the same point in reciprocal space which is not the case for any other doping level. Figure 2.26 shows the position of the charge and spin stripes with doping and it can be clearly determined that at a doping level of $x = 0.33$ the charge and spin stripes are coincident in reciprocal space.

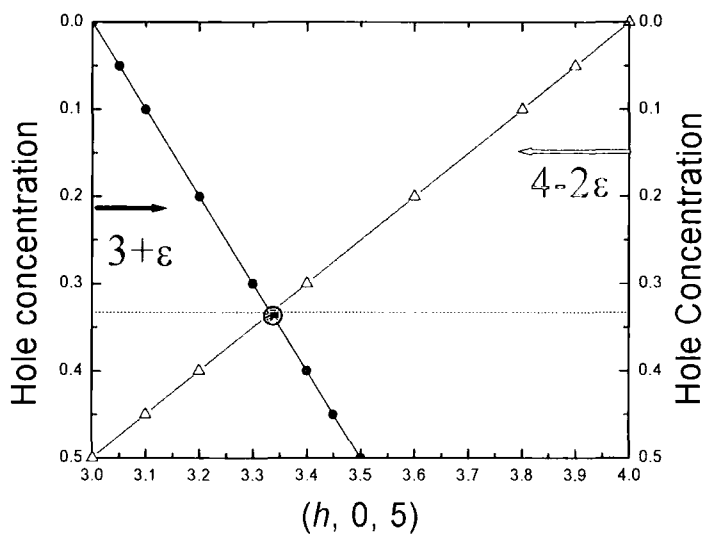

***Figure 2.26**: A schematic representation of how the spin (circles) and charge order (triangles) positions vary with doping. The large circle marks the doping level where the charge and spin ordering coincide at the same point in reciprocal space for the x = 0.33 doping level*

In a neutron study by Lee *et al.* [46] the charge and spin ordering temperatures were measured to be T_{CO} = 239 K and T_{SO} = 190 K respectively. Their measurements of the charge and spin order revealed that the charge order was approximately three times more correlated than the spin order leading them to the conclusion that the charge ordering drives the spin ordering. The measurements of the commensurability determined that it remained constant at $\varepsilon = 0.33$ throughout the whole temperature range. This modulation is a commensurate with the lattice i.e. a charge stripe occurs every three unit cells. Originally it was thought that the stripe ordering was restricted to commensurate values such as 1/3 and ½ etc.[44] However, charge and spin stripes have been confirmed in a large range of Sr concentrations from $0.135 \leq x \leq 0.50$.[47-49] A neutron scattering study for the doping range $0.289 \leq x \leq 0.50$ was carried out by Yoshizawa *et al.* [50] and they found the transition temperatures for the charge stripes and spin stripes T_{CO} and T_{SO} respectively to maximise in the x = 0.33 sample. Figure 2.27 shows T_{CO} and T_{SO} and the incommensurability as a function of hole concentration n_h with $n_h = x + 2\delta$ where x is the strontium concentration and δ is the excess oxygen concentration. It can be clearly seen that with deviations in the stoichometry from 0.33 in either direction there is a decrease in T_{CO} and T_{SO} and there is also a divergence from the $\varepsilon = n_h$ law away from the stable n_h = 0.33 value. It was concluded by Yoshiwawa *et al.* that because the charge stripes and spin stripes occur at the same point in reciprocal space the strong electron lattice coupling stabilises the charge stripes.

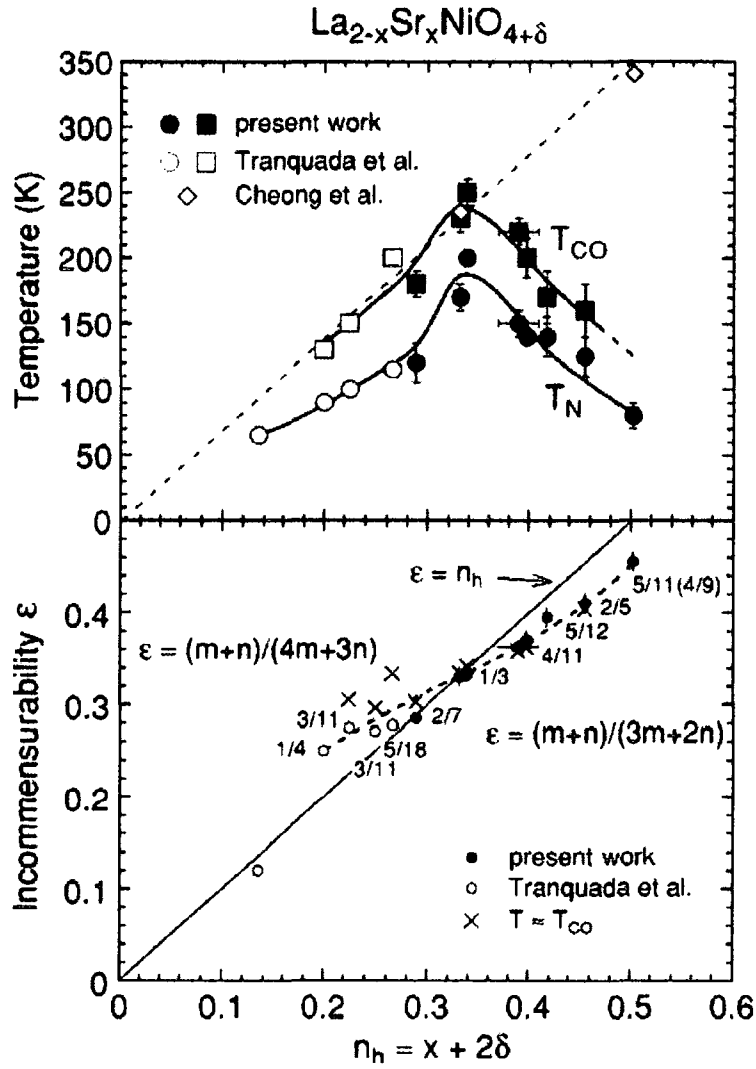

***Figure 2.27**: T_{CO}, T_N transition temperatures as a function of doping (top panel) and commensurability as a function of doping bottom panel taken from Yoshizawa et al.*[50]

High resolution X-ray measurements have been carried on doping levels between $0.275 \leq x \leq 0.33$ by Du *et al.* [51] and Ghazi *et al.* [52] X-rays have the advantage over neutrons in that they are scattering directly from the charge order as opposed to neutrons which only scatter from structural modulations associated with charge order. This has the advantage of obtaining higher intensities and resolution where the charge order is concerned. In the x-ray studies carried out by Ghazi *et al.*, on the $x = 0.33$, 0.30 and 0.275 doped systems the charge order becomes weaker, less correlated, incommensurate

and there is a decrease in the charge ordering temperature as the doping is decreased away from the stable doping position of $x = 0.33$. This behaviour is in agreement with the neutron scattering studies, however there was a significant difference reported in the behaviour of the integrated intensity in the neutron and x-ray scattering results. In the neutron diffraction results a gradual decrease in the integrated intensity from base temperature was reported in both the studies of the 1/3 doped system by Cheong *et al.* and the $x = 1/3$ doped and $x = 0.275$ doped systems by Lee *et al.* [53] In the x-ray measurements a gradual increase in intensity is observed on heating from base temperature. This is shown in Figure 2.28 in the x = 0.33 sample where the intensity actually peaks at 190 K which corresponds to T_N and shows that there is a factor of four increase in the intensity on heating from base temperature to 190 K.

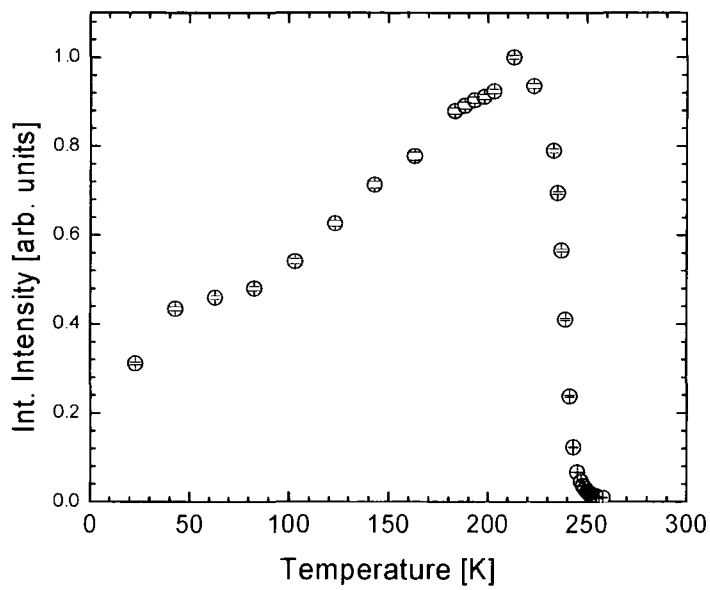

***Figure 2.28**: Integrated intensity as a function of temperature in the 0.33 doped system from x-ray diffraction measurements taken from Ghazi*[54]

This effect was most dramatic in the 0.33 sample but it was also observed in the $x = 0.30$ and 0.275 samples. The increase in intensity is indicative of an increase in the contrast of the charge stripes and it was postulated that at low temperatures the spin

exchange interactions favour a uniform distribution of the holes on the charge stripes and this lowers the contrast in electron density between the hole rich and hole poor areas. As the temperature is increased the holes gain thermal energy and can overcome the effects of the spin exchange interactions and to minimise the Coulomb repulsion the holes maximise the distance between each other. Why this effect is not observed in the neutron measurements is not known, but it is possible that x-ray diffraction observes this effect due to its greater sensitivity to charge than neutrons. However, more investigation is needed to confirm the reason for this difference. The other significant result obtained from the x-ray measurements was that the position of the charge ordering in all samples favours the stable $x = 0.33$ position. The temperature dependence of the commensurability of the three samples is shown in Figure 2.29.

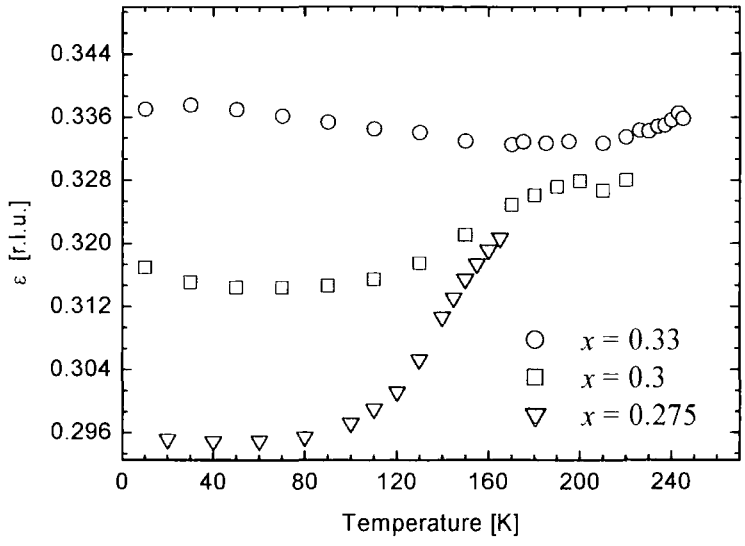

***Figure 2.29**: Commensurability as a function of temperature in the $x = 0.33$, 0.30 and 0.275 systems from x-ray measurements by Ghazi et al.*[52]

It can be clearly seen that as the temperature is increased the commensurability moves towards the stable $x = 0.33$ position which is known to stabilise the charge order pattern due to the coupling between the lattice and the charge order. In the $x = 0.33$ sample the commensurability actually "locked in" to the 1/3 position and this was accompanied by a

decrease in the inverse correlation length i.e. the charge order became more stable. In the x = 0.30 and 0.275 samples the change in commensurability was significantly larger but the charge order disappeared before reaching the stable $\varepsilon = 0.33$ position.

In Chapter 6 the results from a high resolution x-ray study of the x = 0.25, 0.225 and 0.20 doping levels will be discussed. To date the x = 0.20 doped system has only been studied by the use of neutron diffraction by Sachan *et al.* [47] In the study they report the presence of weak, diffuse charge stripes *i.e.* the charge order exists in a charge glass in contrast to the strong well correlated charge stripes observed in the $x \geq 0.275$ doping level and above. The x = 0.225 system has been studied using neutron diffraction [49] and x-ray scattering using energies of 100 keV by Vigilante *et al.*[48] As discussed in the next section this allowed the bulk of the system to be probed. The charge order was found to again exist in a charge glass. By studying the x = 0.20, 0.225 and 0.25 doping levels and comparing the result with earlier studies it was hoped to build up a complete understanding of the behaviour of the charge order in the doping region $0.20 \leq x \leq 0.33$.

2.9 High Energy X-ray Scattering

The vast majority of x-ray diffraction studies have been carried out in the energy region from 4 – 20 keV. Energies in this region only probe the top few microns and it was only possible to probe the bulk of a system using neutron diffraction techniques which are not directly sensitive to the charge distributions. A relatively new technique involves the use of very high energy x-ray scattering to probe the bulk properties. This technique utilises energies of approximately 100 keV or greater and has considerable advantages over normal x-ray scattering techniques.

Firstly, as the energy is increased into the 100 keV regime there is a huge decrease in the sample absorption. The absorption is given by the equation

$$I(\omega) = I_0 e^{-\mu(\omega)x} \qquad \textbf{(2.4)}$$

where I and I_0 are the final and initial intensities. $\mu(\omega)$ is the linear absorption co-efficient and x is the sample thickness. This large decrease in absorption leads to a dramatic increase in penetration depth where the penetration depth is defined as being equal to $1/\mu(\omega)$. An example of this is shown in Figure 2.30 for elemental manganese in the energy range 1-500 keV.

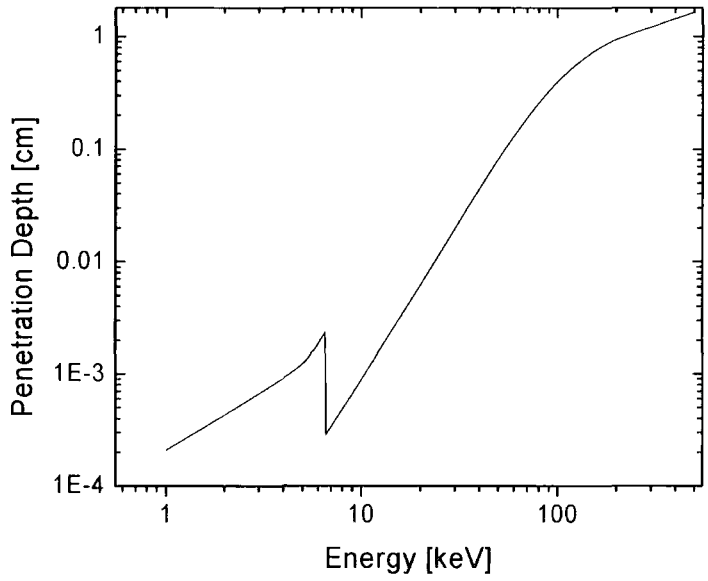

***Figure 2.30**: Penetration depth as a function of energy in Manganese*

It can be clearly seen that the penetration depth is at least two orders of magnitude greater at 100 keV compared to 10 keV and this leads to a massive increase in the scattering volume. This in turn leads to an increase in the scattered intensity of the system making the high energy technique ideal for observing and measuring weak phenomena. The high energy x-ray scattering technique allows the bulk properties of a system to be probed where previously only a few microns at the surface was probed using x-rays in the conventional region. Neutron diffraction techniques also probe the bulk properties of the sample but neutrons do not scatter directly from the charge, instead they scatter from structural modulations associated with the charge order and suffer from low resolution and scattered intensities. X-rays scatter directly off the charge density and high energy x-

ray scattering allows significantly higher resolution and intensities to be obtained. The high energy x-ray experiments can be performed in Laue transmission geometry which allows access to significantly more Bragg planes than when working in reflection geometry. In addition the radius of the Ewald sphere probed is equal to $2\pi/\lambda$ where λ is the wavelength of the incoming beam. The volume of reciprocal space that can be probed is governed by the size of the Ewald sphere and hence, the higher the energy the larger the volume of reciprocal space probed. Given the volume of reciprocal space probed is proportional to the radius cubed, in theory at 100 keV it is possible to access a volume of reciprocal space 1000 times greater than at 10 keV.

The second advantage of this technique is the increase in resolution available. For perfect crystals the Darwin width of the reflection is given by the equation which is derived in [55]

$$\kappa_{darwin}^{FWHM} = \left(\frac{6d^2 r_0}{\sqrt{2}\pi n^2 v_c} \right) \tan(\theta) |F| \quad \textbf{(2.5)}$$

where θ is the Bragg angle and d is the lattice spacing and n is the order of the reflection given in Bragg's law ($n\lambda = 2d\sin\theta$). r_0 is the Thomson scattering length and v_c is the volume of the unit cell. |F| is the structure factor for the unit cell which is given by the equation.

$$|F| = F(Q,\omega) = \sum_{r_j} f(\omega) e^{iQ \bullet r_j} \quad \textbf{(2.6)}$$

As the energy is increased then firstly, the Bragg angle becomes smaller and secondly the resonant scattering factor $f(\omega)$ decreases as the energy is increased away from an absorption edge. Therefore it can be concluded that the angular Darwin width also decreases. For example in silicon when the energy is increased to 130 keV from 10 keV there is a huge decrease in the Darwin width by a factor of approximately six for the silicon (113) reflection. For these reasons very high energy x-ray scattering is ideal for the study of weak phenomena because it allows high intensity, high resolution bulk measurements to be obtained.

2.10 Experimental Stations

2.10.1 D3 Laboratory Diffractometer

***Figure 2.31**: Picture of the D3 diffractometer*

All preliminary measurements and alignment work was carried out on the Bede D3 Laboratory diffractometer shown above in Figure 2.31. The system was designed to maximise flux but to still have the resolution to obtain valid measurements on transition metal oxide crystals. The transition metal oxide crystals studied usually have a mosaic width no better than 0.05°. This is significantly larger than semiconductor crystals such as silicon and germanium which are often used as monochromator or analyser crystals. Silicon has a wavevector resolution of ~ 10^{-4} $Å^{-1}$ and is used as a monochromator on synchrotron sources because the mosaic width is close to the natural beam divergence. However, from a laboratory source the x-rays produced from the target have a large

divergence and the use of a silicon monochromator produces a well focussed beam but a huge intensity loss. This occurs because the silicon or germanium monochromator allows only a fraction of the x-rays from the source to be passed.

The use of traditional wider band pass monochromators such as pyrolytic graphite (0001) increases the flux considerably. However, the rocking curve width is 0.3° which is too large to measure the intrinsic inverse correlation lengths. Instead any measurements are dominated by the instrumental resolution of the monochromator and not that of the sample. The D3 diffractometer uses 2 graded parabolic mirrors shown in Figure 2.32 one mounted vertically the other horizontally to collimate the x-ray beam into a spot size of ~ 1 mm^2 at 500 mm from the second mirror.

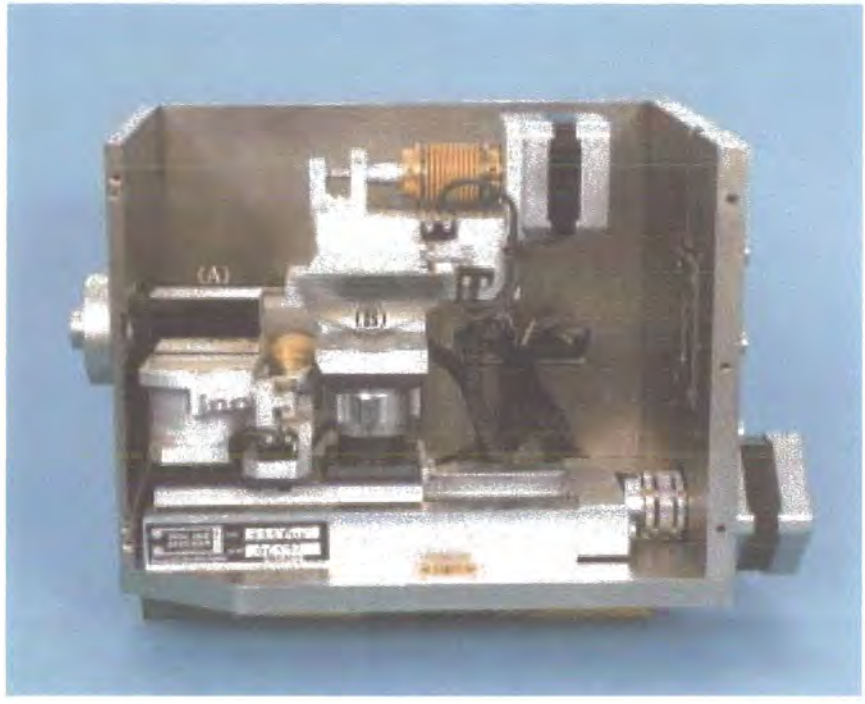

***Figure 2.32**: The D3 mirror box The horizontal and vertical mirrors are labelled (A) and (B) respectively. The unfocused beam enters from the left and a focused beam leaves from the right.*

The motorised arms of the two mirrors can be observed which allow for intensity optimisation. The mirrors focus the x-rays generated from an Enraf-Nonius FR571 rotating anode generator with an electron beam spot size of 3 mm × 30 μm impinging on

a copper target. The system uses a cut double bounce germanium (220) analyser crystal for triple axis measurements. The Bede D3 system consists of a four circle triple axis diffractometer. The θ and 2θ axes are controlled by a Unidex motor controller unit and driven by encoded servo-motors which in theory allows for movements to an accuracy of 1.53×10^{-5} degrees. All other axes are controlled by a Minicam 3 control unit and driven by four and five phase stepper motors. A cryostat sample stage can be mounted on the diffractometer. It uses a microminature refrigerator developed by MMR Ltd which can reach temperatures of 90 K cooling with high pressure argon gas using Joule-Thomson expansion. The system cools to 90 K in approximately 30 minutes and can be controlled to an accuracy of ± 0.1 K. To detect the scattered x-rays usually a Bede EDRa scintillation detector is used. The scintillation detector has a high dynamic range but suffers from a relatively high noise level and also have poor energy resolution leading to harmonic contamination from $\lambda/2$, $\lambda/3$ etc from Bragg peaks. However, it is also possible to mount an Amptek solid state detector which reduces the noise by a factor of 10 and has an energy resolution accurate to 186 eV. This makes it ideal for detecting weak phenomena as it removes contamination from fluorescence and harmonics. The system is controlled using in-house software. The system has an increase by a factor of 10 in intensity coupled with an increase in resolution by 7.5 over the previous optical system. Further details of the D3 can be obtained from Wilkins *et al.*[56]. The D3 system was used to pre-align samples but because of the weak phenomena under study synchrotron sources were required for all of the experiments described in this thesis.

2.10.2 XMaS Beamline

The XMaS (X-ray Magnetic Scattering) beamline is situated in Grenoble France at the ESRF synchrotron source. The ESRF synchrotron source is a 6 GeV ring and has a maximum current of 200 mA. The beamline[57] is situated on the "soft" sector of the BM28 bending magnet giving a critical photon energy of 9.8 keV and has been designed to access an energy range from 3 - 15 keV. The beam is focussed using 2 water cooled silicon (111) monochromator crystals followed by a platinum coated Zeiss focussing mirror. The mirror is bent pneumatically to provide 1:1 focusing at the sample position. The mirror is set at a grazing incidence angle of 4.5 mrad giving an energy cut-off of approximately of 15 keV. The optical elements are kept under an ultra high vacuum at all times and flight paths from the optics hutch to the experimental hutch are evacuated. The phenomena studied are very weak and it is necessary to eliminate contamination from incident beam harmonics. This is done by the use of 2 pyrex harmonic rejection mirrors. The diffractometer is a four circle 11-axis Huber diffractometer and is shown in Figure 2.33. The four circles have a resolution of 1 arcsecond and absolute accuracy of 20-30 arcseconds. It is possible to mount a closed circle helium displex cryostat with two beryllium (Be) shrouds on the Eulerian cradle. This allows a base temperature of 10 K to be accessed with both Be shields and approximately 15 K with one Be shield in place. Recently a closed cycle He cryofurnace has been developed which can be mounted within the cradle and allows a temperature range from 10 K – 800 K to be accessed. On the 2θ arm it is possible to mount a polarisation analyser stage which can be evacuated or a two-circle conventional analyser stage. The system used to detect the X-rays is a NaI scintillation detector which can be electronically gated to a limited degree. The diffractometer is controlled using SPEC software.

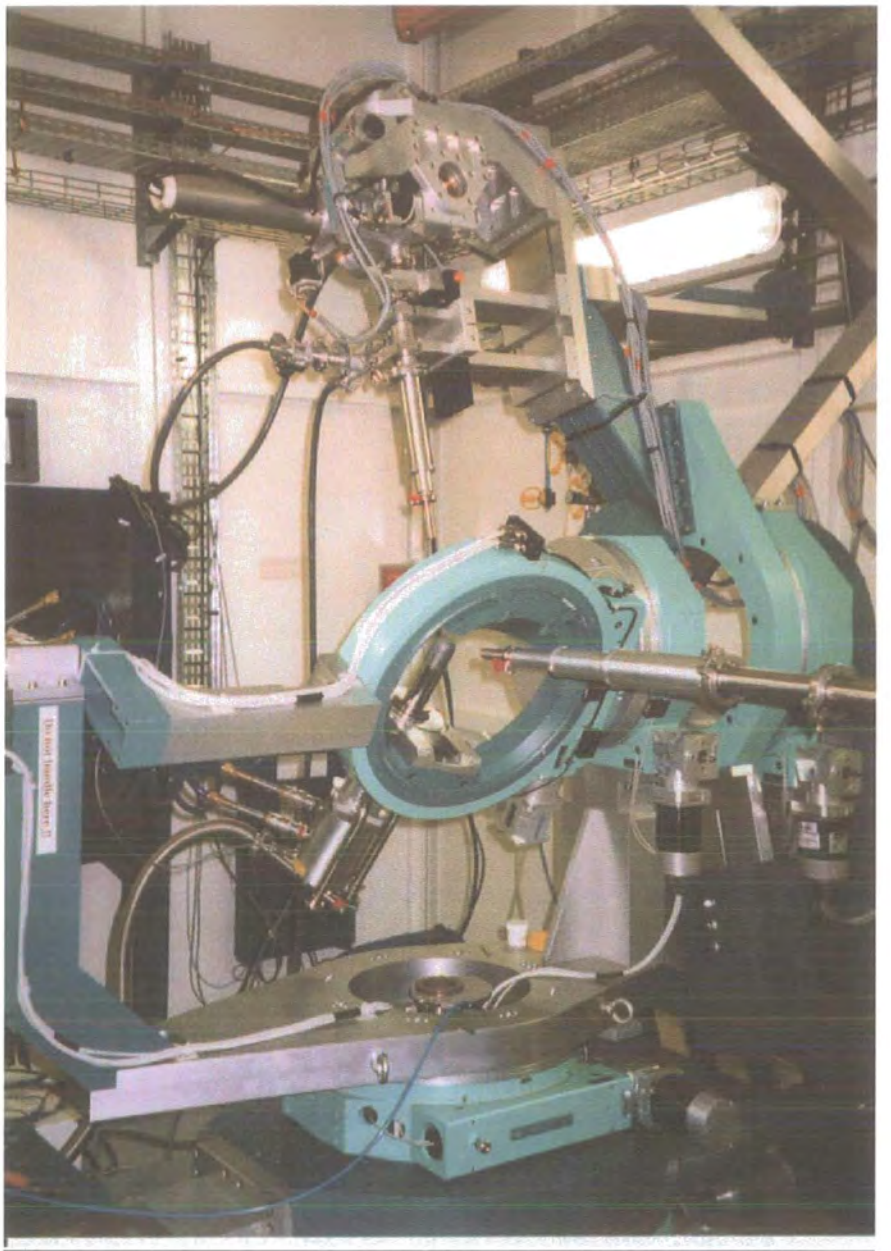

***Figure 2.33**: Picture of the Huber diffractometer at BM28 with the polarisation analyser mounted on the 2θ arm.*

2.10.3 Station 16.3 SRS

The 16.3 beamline is situated at the Synchrotron Radiation Source (SRS) at Daresbury in the United Kingdom. Station 16.3 is the central beamline on Wiggler 16 – a 6 Tesla superconducting wavelength-shifter - on the 2 GeV SRS ring. The beamline is designed to carry out high resolution single crystal and material studies. It is possible to access a broad range of incident energies from 5 keV to 50 keV with a critical energy of 16 keV and a flux of approximately 1.2×10^{10} photons s^{-1} at this energy. The incoming white X-ray beam is monochromated by using one or two channel-cut Silicon (111) and (311) single crystals. The crystals are water cooled to dissipate the heat load from the incoming white beam. Samples are mounted within a closed cycle displex cryostat that allows a temperature range of 10 – 300 K to be accessed. The cryostat was in turn mounted on a Huber 512 Eulerian cradle. An energy gated solid state MCA detector or a Bede EDRa detector could be used to detect the scattered X-rays. A single or triple bounce silicon (111) crystal was utilised as an analyser to provide high resolution measurements. The motion of the diffractometer was controlled using PINCER software.

2.10.4 Station BW5 Hasylab

High energy experiments were performed on the BW5 beamline situated on the 4.5 GeV DORIS storage ring at HASYLAB and is designed for x-ray scattering experiments above 60 keV and the wiggler has a critical energy of 26.5 keV. A schematic of the beamline is shown in Figure 2.34

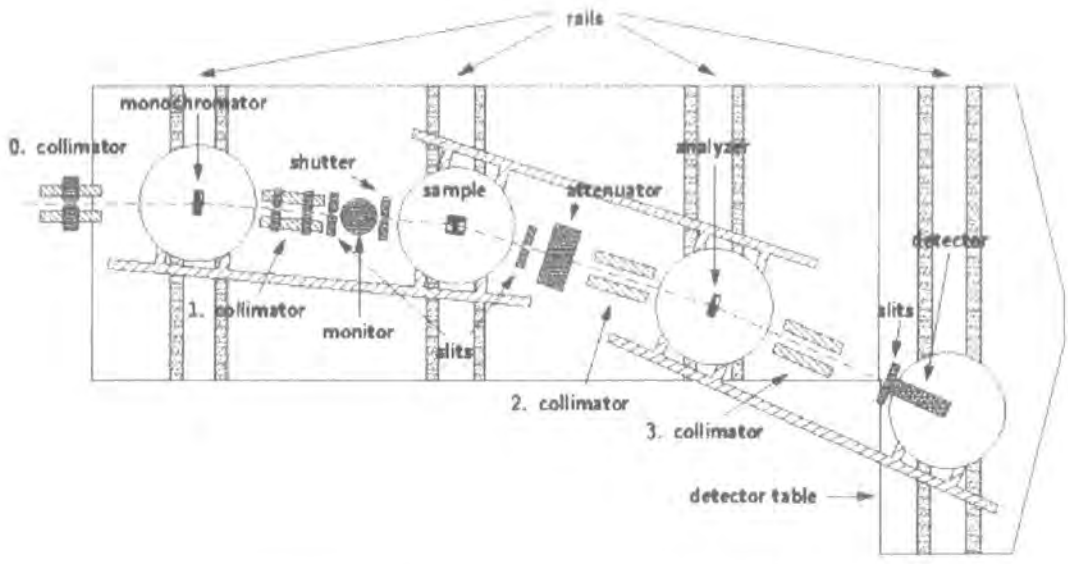

Figure 2.34: *Schematic of the BW5 beamline.*[58]

A water-cooled 1.5 mm thick copper plate is used as a high-pass filter to reduce the heat load on the optical elements that follow and together the wiggler and filter select a spectral range from approximately 60 – 200 keV. It is possible to mount different monochromators depending on the resolution required. The monochromator used in our experiments is a graded silicon/germanium $Si_{1-x}Ge_x$ crystal which is operated in Laue geometry. It can be translated horizontally to alter the bandpass and hence the resolution and flux of the system. The mosaic width varies from 15 – 70 arcseconds. This allows the resolution of the system to be matched to the rocking curve width of the sample and the intensity is maximised while still having the required resolution to obtain valid peak widths. For triple-axis measurements a matching $Si_{1-x}Ge_x$ crystal is used as an analyser crystal. It is possible to mount either a 512.1 Eulerian cradle for four circle diffraction or a ± 15° double tilt goniometer for mounting a cryomagnet or furnace on. A closed circle displex cryostat can be mounted in the Eulerian cradle and can access a temperature range from 10-300 K and a picture of this experimental set up is shown in Figure 2.35.

***Figure 2.35**: Picture of the BW5 Diffractometer when the Eulerian cradle is in use*

A full description of the beamline was made by Bouchard *et al.*[59]

2.11 References

1 R. M. Kusters, J. Singleton, D. A. Keen, R. McGreevy and W. Hayes Physica B **155**, 362 (1989).

2 R. von Helmholt, J. Wecker, and B. Holzapfel, Physical Review Letters **71**, 2331 (1993).

3 D. S. Dessau and Z. X. Shen, *Colossal Magnetoresistive Oxides* (Gordon and Breach Science Publishers, 2000).

4 E. Dagotto, T. Hotta, and A. Moreo, Physics Reports **344**, 1 (2001).

5 E. O. Wollan and W. C. Koehler, Physical Review **100**, 545 (1955).

6 J. B. Goodenough, Physical Review **100**, 564 (1955).

7 S. W. Cheong, *Colossal Magnetoresistive Oxides* (Gordon and Breach Science Publishers, 2000).

8 C. H. Chen and S. W. Cheong, Physical Review Letters **76**, 4042 (1996).

[9] P. G. Radaelli, D. E. Cox, M. Marezio, *et al.*, Physical Review B-Condensed Matter **55**, 3015 (1997).
[10] R. Kajimoto, H. Yoshizawa, H. Kawano, *et al.*, Physical Review B-Condensed Matter **60**, 9506 (1999).
[11] Y. Murakami, H. Kawada, H. Kawata, *et al.*, Physical Review Letters **80**, 1932 (1998).
[12] K. Nakamura, T. Arima, A. Nakazawa, *et al.*, Physical Review B-Condensed Matter **60**, 2425 (1999).
[13] M. von Zimmermann, J. P. Hill, D. Gibbs, *et al.*, Physical Review Letters **83**, 4872 (1999).
[14] Y. Wakabayashi, Y. Murakami, I. Koyama, *et al.*, Journal of the Physical Society of Japan **69**, 2731 (2000).
[15] P. D. Hatton, S. B. Wilkins, P. D. Spencer, *et al.*, International Journal of Modern Physics B **16**, 1661 (2002).
[16] S. B. Wilkins, P. D. Spencer, P. D. Hatton, *et al.*, Physica B **318**, 295 (2002).
[17] A. Urushibara, Y. Moritomo, T. Arima, *et al.*, Physical Review B **51**, 14103 (1995).
[18] Y. Moritomo, Y. Tomioka, and A. Asamitsu, Physical Review B **51**, 3297 (1995).
[19] Y. Moritomo and A. Asamitsu, Nature **380**, 141 (1996).
[20] Y. Endoch, K. Hirota, S. Ishihara, *et al.*, Physical Review Letters **82**, 4328 (1999).
[21] B. J. Sternlieb, J. P. Hill, U. C. Wildgruber, *et al.*, Physical Review Letters **76**, 2169 (1996).
[22] M. Kubota, H. Yoshizawa, T. Moritomo, *et al.*, Journal of the Physical of Japan **68**, 2202 (1999).
[23] J. Q. Li, Phys. Rev. B. **57**, R3205 (1998).
[24] T. Kimura, R. Kumai, Y. Tokura, *et al.*, Physical Review B-Condensed Matter **58**, 11081 (1998).
[25] T. Chatterji, G. J. McIntyre, W. Caliebe, *et al.*, Physical Review B **61**, 570 (2000).
[26] J. Dho, W. S. Kim, H. S. Choi, *et al.*, Journal of Physics - Condensed Matter **13**, 3655 (2001).
[27] Y. Murakami, J. P. Hill, D. Gibbs, *et al.*, Physical Review Letters **81**, 582 (1998).
[28] C. W. M. Castleton and M. Altarelli, Physical Review B **62**, 1033 (2000).
[29] S. Ishihara, Phys. Rev. B. **58**, 13442 (1998).
[30] M. Benfatto, Y. Joly, and C. R. Natoli, Physical Review Letters **83**, 636 (1999).
[31] J. G. Bednorz and K. A. Muller, Zeitschrift fur Physik B **64**, 189 (1986).
[32] R. J. Cava, R. B. van Dover, B. Batlogg, *et al.*, Physical Review B **58**, 408 (1987).
[33] P. G. Radaelli, Phys. Rev. B. **49**, 4163 (1994).
[34] S.-W. Cheong, G. Aeppli, T. E. Mason, *et al.*, Physical Review Letters **67**, 1791 (1991).
[35] T. Suzuki, Phys. Rev. B **57**, R3229 (1998).
[36] H. Kimura, H. Matsushita, K. Hirota, *et al.*, Physical Review B **61**, 14366 (2000).
[37] S. Wakimoto, R. J. Birgeneau, M. A. Kastner, *et al.*, Physical Review B **61**, 3699 (2000).
[38] S. Wakimoto, R. J. Birgeneau, Y. S. Lee, *et al.*, Physical Review B **63**, 172501 (2001).
[39] M. Matsuda, K. Fujita, and K. Yamada, Physical Review B **62**, 9148 (2000).

[40] J. M. Tranquada, J. D. Axe, N. Ichikawa, *et al.*, Physical Review B-Condensed Matter **54**, 7489 (1996).
[41] M. von Zimmermann, A. Vigliante, T. Niemoller, *et al.*, Europhysics Letters **41**, 629 (1998).
[42] R. J. Cava, B. Batlogg, T. T. Palstra, *et al.*, Physical Review B **43**, 1229 (1991).
[43] P. Wochner, J. M. Tranquada, and D. J. Buttrey, Phys. Rev. B. **57**, 1066 (1998).
[44] S. W. Cheong, H. Y. Hwang, C. H. Chen, *et al.*, Physical Review B **49**, 7088 (1994).
[45] P. D. Hatton, S. B. Wilkins, P. D. Spencer, *et al.* Journal of Physics D-Applied Physics **36**, A157 (2003).
[46] S.-H. Lee and S.-W. Cheong, Physical Review Letters **79**, 2514 (1997).
[47] V. Sachan, D. J. Buttrey, J. M. Tranquada, *et al.*, Physical Review B Condensed Matter **51**, 12742 (1995).
[48] A. Vigliante, M. von Zimmermann, J. R. Schneider, *et al.*, Physical Review B **56**, 8248 (1997).
[49] J. M. Tranquada, D. J. Buttrey, and V. Sachan, Physical Review B Condensed Matter **54**, 12318 (1996).
[50] H. Yoshizawa, T. Kakeshita, R. Kajimoto, *et al.*, Physical Review B **61**, R854 (2000).
[51] C.-H. Du, M. E. Ghazi, Y. Su, *et al.*, Physical Review Letters **84**, 3911 (2000).
[52] M. E. Ghazi, P. D. Spencer, S. B. Wilkins, *et al.*, Physical Review B submitted (2004).
[53] S.-H. Lee, S.-W. Cheong, K. Yamada, *et al.*, cond-mat/0002348 (2000).
[54] Ghazi M.E, PhD Thesis, Department of Physics, University of Durham, (2002).
[55] J. Als-Nielsen and D. McMorrow, *Elements of Modern X-ray Physics* (John Wiley & Sons Ltd., Chichester, 2001).
[56] S. B. Wilkins, S. P. D. Spencer, P. D. Hatton, *et al.*, Review of Scientific Instruments **73**, 2666 (2002).
[57] S. Brown, L. Bouchenoire, D. Bowyer, *et al.*, Journal of Syncrotron Radiation **8**, 1172 (2001).
[58] http://www-hasylab.desy.de/facility/experimental_stations/stations/BW5.htm.
[59] R. Bouchard, R. Hupfeld, D. Lippmann, *et al.*, Journal of Synchrotron Radiation **5**, 90 (1998).

Chapter 3

Jahn-Teller and Charge ordering in the bilayer manganite $La_{2-2x}Sr_{1+2x}Mn_2O_7$ $x = 0.5$ and 0.475

3.1 Introduction

In this chapter we discuss the Jahn-Teller and charge ordering in $La_{2-2x}Sr_{1+2x}Mn_2O_7$ in the $x = 0.5$ and 0.475 doped systems. It was originally thought that, as in the $Nd_{0.5}Sr_{0.5}MnO_3$ system the charge ordered state in the bi-layer system was restricted to a very narrow doping window around the half doped level. However, the powder diffraction and magnetotransport measurements in the doping range $0.3 \leq x \leq 0.8$ provided strong evidence that the charge ordered state existed over a significantly greater doping range and that a 're-entrant' charge ordered phase in the doping region $0.47 \leq x \leq 0.62$ existed as shown below in Figure 3.1.

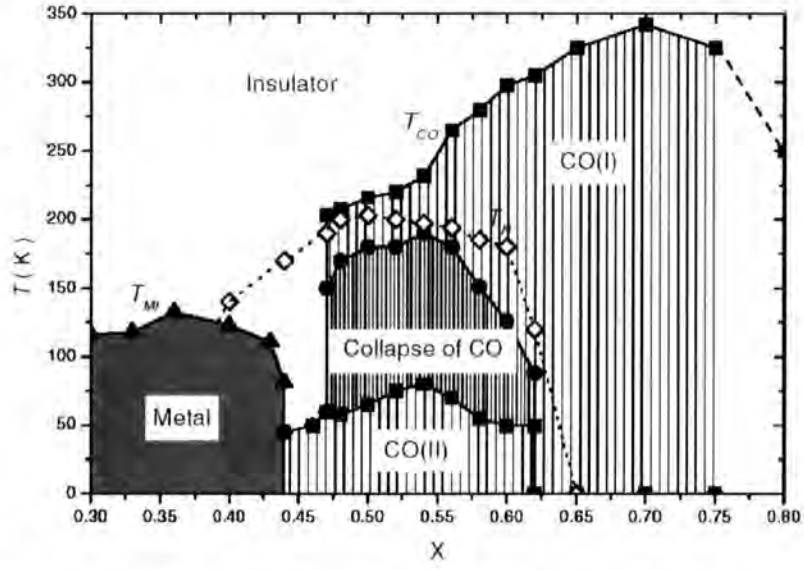

***Figure 3.1**: Phase diagram of the $La_{2-2x}Sr_{1+2x}Mn_2O_7$ system in the doping region $0.3 \leq x \leq 0.8$. The filled symbols show the transport data and the open symbols are from previously reported values. The squares show T_{CO} and the triangles T_{MI} taken from Dho et al.[1]*

By carrying out single crystal diffraction measurements it was hoped it would be possible to obtain significantly more detailed and accurate measurements about the nature of the charge ordered state. Dho *et al.* reported the onset of the charge ordered state for doping levels of $x > 0.47$. For this reason the 0.475 doped system was studied in order to obtain information about the charge ordered state close to the boundary of the charge ordered regime. Previously, no single crystal studies had been carried out on the 0.475 doping or indeed any other doping except $x = 0.5$. By comparing the results with those from the 0.5 doped sample it was hoped that information could be obtained on the doping dependence of the charge ordered state and see if there was any stabilization in the charge ordered state as the doping was increased to the half doped value. The second objective of this study was to determine the modulations of the Jahn-Teller, charge and orbital order. As discussed in the previous chapter in the studies carried out by Kimura,[2] Chatterji[3] and Wakabayashi[4] there were disagreements over the wavevectors of the charge and orbital modulations. The Goodenough model[5] predicted the charge order to occur at a modulation of (½, ½, 0) and the orbital order at (¼, ¼, 0). This model was in agreement with the results of Wakabayashi *et al.* but strongly disagreed with the x-ray results obtained by Chatterji *et al.* and the electron diffraction results by Kimura *et al.* which claimed the charge order existed at a modulation of (¼, ¼, 0). In this study we wished to determine, through resonant x-ray scattering studies at the Mn *K*-edge and high energy x-ray scattering studies, the correct modulations of the Jahn-Teller, charge and orbital order.

In this chapter we report the study of the $x = 0.5$ and $x = 0.475$ bi-layer manganites using high energy x-ray scattering at HASYLAB Hamburg and resonant x-ray scattering at the Mn *K*-edge at beamline BM28 ESRF Grenoble. Additionally high resolution structural measurements on the Bragg peaks were performed at station 16.3 at the SRS Daresbury to determine if there was any type of structural change associated with the transition into the Jahn-Teller/charge order state.

The bi-layer system corresponds to the n = 2 member of the Ruddlesden – Popper series and has the general formula $La_{2-2x}Sr_{1+2x}Mn_2O_7$. The bi-layer system has the *I4/mmm* tetragonal space group with lattice parameters $a = b = 3.87$ Å and $c \sim 19.90$ Å and the structure is shown in Figure 3.2.

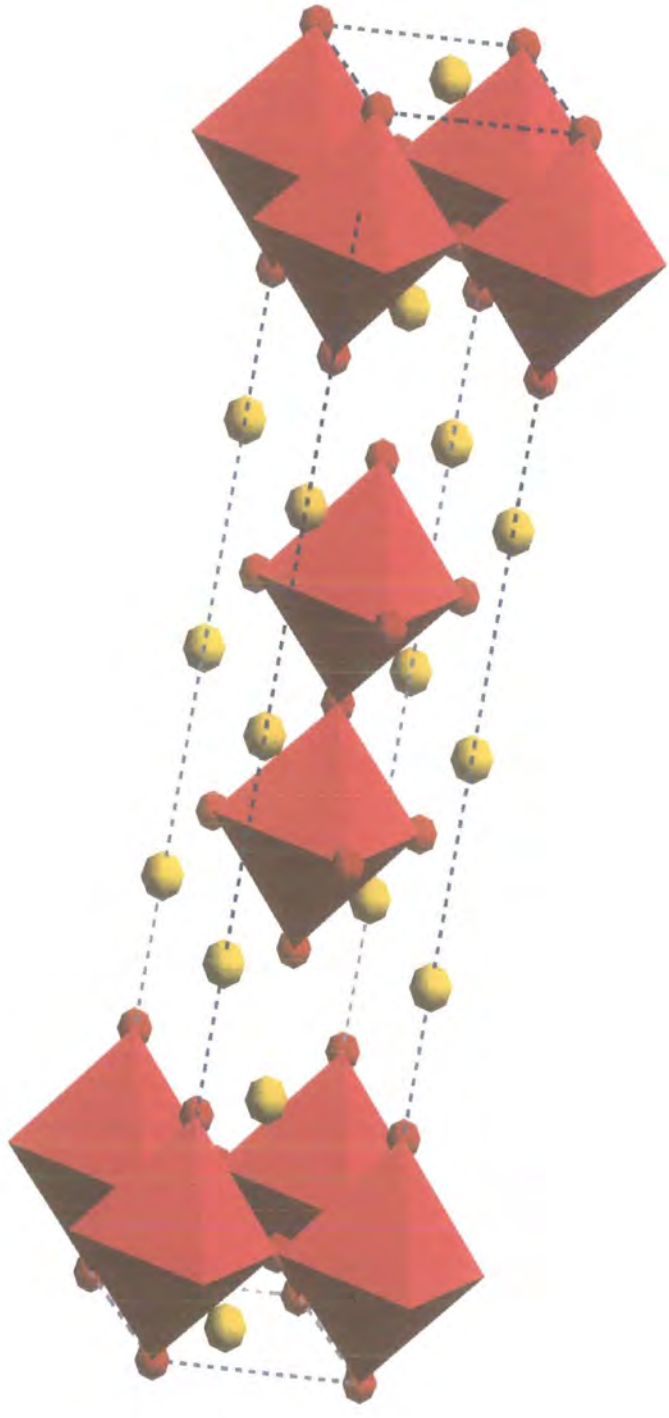

***Figure 3.2**: Crystal structure of the $La_{2-2x}Sr_{1+2x}Mn_2O_7$ bi-layer manganite*

3.2 High Energy Study

3.2.1 Experimental Procedure

The high energy X-ray experiments were carried out on beamline BW5 at HASYLAB, Hamburg Germany. The incident beam was monochromated using a graded silicon/germanium $Si_{1-x}Ge_x$ crystal in transmission geometry. A second $Si_{1-x}Ge_x$ crystal was used as an analyser to provide triple-axis measurements. The use of a graded crystal allows the bandpass of the monochromator to be adjusted to match the system under study. The crystals have a constant compositional gradient and the bandpass can be adjusted by simply translating the crystal horizontally. This allows the resolution to match the mosaic width of the sample and hence, maximise the flux. The transition metal oxide crystals studied are of relatively poor quality compared to silicon or germanium and for this reason the monochromator could be adjusted to maximise flux while still providing the required resolution. A solid state Ge detector was used to detect the diffracted x-rays and higher order harmonics were removed by pulse height analysis. A closed cycle displex cryostat was used and this allowed a temperature range from 10 – 300 K to be accessed.

A high quality sample of $La_{2-2x}Sr_{1+2x}Mn_2O_{7+\delta}$ with $x = 0.5$ was grown at the University of Oxford by the floating zone method. The doping was determined using electron probe microanalysis (EPMA) as $x = 0.50 \pm 0.01$. The excess oxygen content was determined using thermo-gravimetric analysis (TGA) as $\delta = 0.00 \pm 0.01$. The crystal was indexed in the *I4/mmm* setting with lattice parameters of $a = b = 3.87$ Å and $c = 19.90$ Å. An incident energy of 100.7 keV was used. The $x = 0.5$ sample was of relatively high quality for a transition metal oxide crystal with a rocking curve width of 0.03°. More than one crystallite was observed in the sample, so in order to ensure that only one crystallite was measured a 1mm × 1mm beam was used. The beamsize was sufficiently small that, by translating the sample only one crystal was observed. The sample was aligned by rocking the sample in θ and using a fluorescent screen to observe diffracted peaks. The long axis in the c direction allowed it to be easily identified and the (0, 0, 10) reflection was located and entered into the **UB** matrix (see Busing and Levy[6]). The sample was

rotated and the orthogonal (1, 1, 0) reflection located and entered into the UB matrix. The matrix was calculated using the two reflections allowing the positions of other peaks to be calculated.

3.2.2 High Energy $x = 0.5$ Studies

The $x = 0.5$ sample was cooled to 170 K which corresponded to the temperature where the charge order reflections had been reported to be at their maximum intensity from previous studies. A search was carried out for superlattice reflections corresponding to the Jahn-Teller and charge ordering at modulations of (±0.25, ±0.25, 0) and (±0.5, ±0.5, 0) respectively.

Reflections were located around the (1, 0, *L*) type Bragg peaks with the strongest satellites located around the (1, 0, 5) Bragg peak. Superlattice reflections at a wavevector of (-0.25, -0.25, 0) were observed which was consistent with the high energy results seen by Chatterji *et. al.* These reflections are clearly not from orbital order which can only be observed at the Mn *K*-edge. Additionally weaker superlattice peaks were seen at a wavevector of (-0.5, -0.5, 0) which had not been observed by Chatterji *et. al.* but had been observed by Wakabayashi *et. al* in studies at the Mn *K*-edge. From this we postulated that the reflections observed at (0.25, 0.25, 0) are due to the Jahn-Teller ordering and the reflections at a modulation of (0.5, 0.5, 0) are from the charge ordering of the Mn^{3+} and Mn^{4+} pattern which is consistent with the Goodenough model and the results observed by Wakabayashi *et. al.*

The (0.75, -0.25, 5) reflection corresponding to Jahn-Teller order and the (0.5, -0.5, 5) reflection corresponding to the charge order were studied as a function of temperature. At 170 K the peak intensities were 34.2×10^3 counts per second (cps) for the Jahn-Teller reflection and 1.2×10^3 cps for the charge ordering reflection. The sample was cooled to 10 K and the intensity of the superlattice reflections decreased significantly, but both the Jahn-Teller and charge order were still observable at low temperatures. The peak intensities were 5.1×10^3 cps for the Jahn-Teller order and 147 cps for the charge order. Scans were taken along the *H, K* and *L* directions of reciprocal space in triple-axis geometry on both the Jahn-Teller and charge order. The Jahn-Teller and charge order were both found to fit the Lorentzian squared lineshape in all directions.

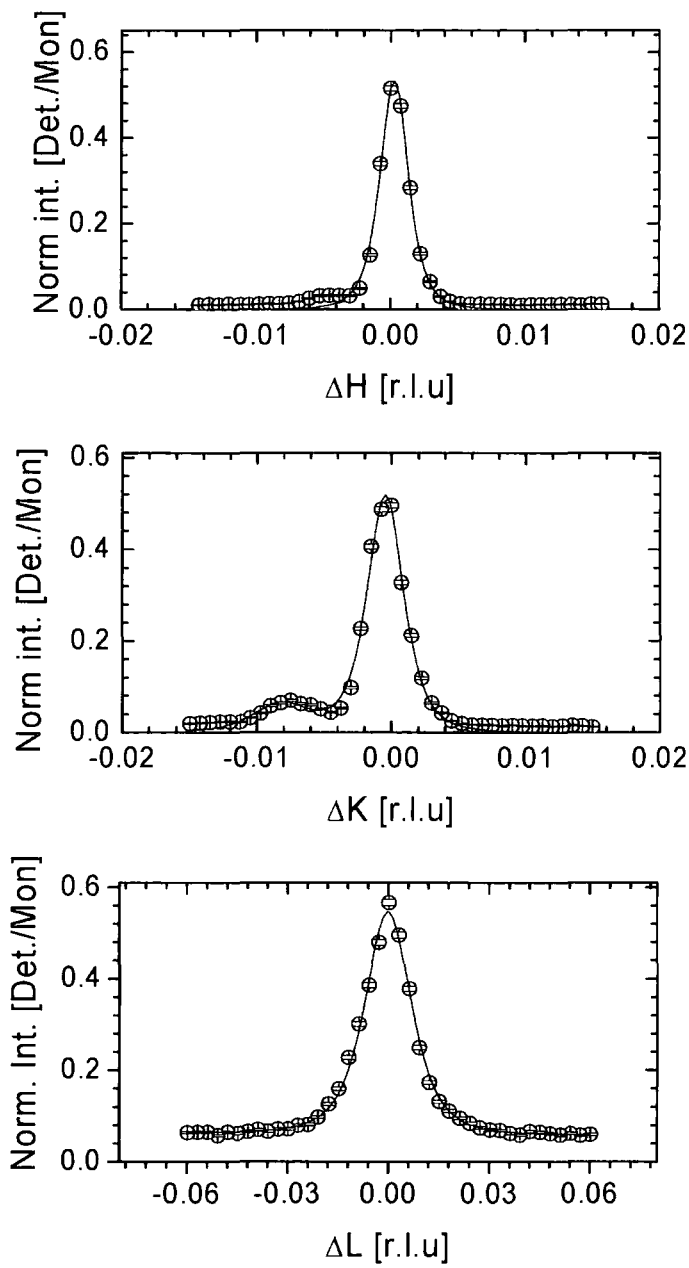

***Figure 3.3**: Scans through H, K and L directions of the (0.75, -0.25, 0) JT order peak at 170 K. The solid line is the fit to the experimental data using a Lorentzian squared lineshape. The detector [Det] counts are normalised to the monitor counts [Mon]*

The scans and fits for the Jahn-Teller order peak are shown in Figure 3.3 at 170 K. The scan in the K direction is fitted with two Lorentzian squared lineshapes.

The sample was cooled to 10 K and the Jahn-Teller order peak was again located and fitted using the parameters from the fits at 170 K. The Jahn-Teller peak order again fitted the Lorentzian squared lineshape in all three principal reciprocal space directions at 10 K. The inverse correlation length ξ^{-1} was calculated in each direction using the equation

$$\xi^{-1} = \kappa \times \left(\frac{2\pi}{d} \right) \qquad \textbf{(3.1)}$$

where κ is the half width at half maximum of the peak and d is the Bragg plane spacing normal to the scattering vector.

	H [Å^{-1}]$\times 10^{-3}$	K [Å^{-1}]$\times 10^{-3}$	L [Å^{-1}]$\times 10^{-3}$
170 K	1.90 ± 0.03	2.25 ± 0.06	2.57 ± 0.08
10 K	1.64 ± 0.05	2.15 ± 0.06	2.56 ± 0.04
Ratio $\xi^{-1}_{10}/\xi^{-1}_{170}$	0.86 ± 0.03	0.96 ± 0.04	0.99 ± 0.04

***Table 3.1**: Inverse correlation lengths measured on the (0.75, -0.25, 5) Jahn- Teller ordering peak at 10 K and 170 K*

Table 3.1 shows a comparison of the inverse correlation lengths in the H, K and L directions at 170 K and 10 K and from this it can be seen clearly that there is no significant change in the inverse correlation length between the high temperature state and the low temperature state despite the large decrease in intensity at low temperatures. The temperature dependence of the Jahn-Teller order reflection were measured as a function of temperature in the range 10 – 230 K The temperature dependence of the integrated intensity of the Jahn-Teller order is shown in Figure 3.4 in the H and K directions.

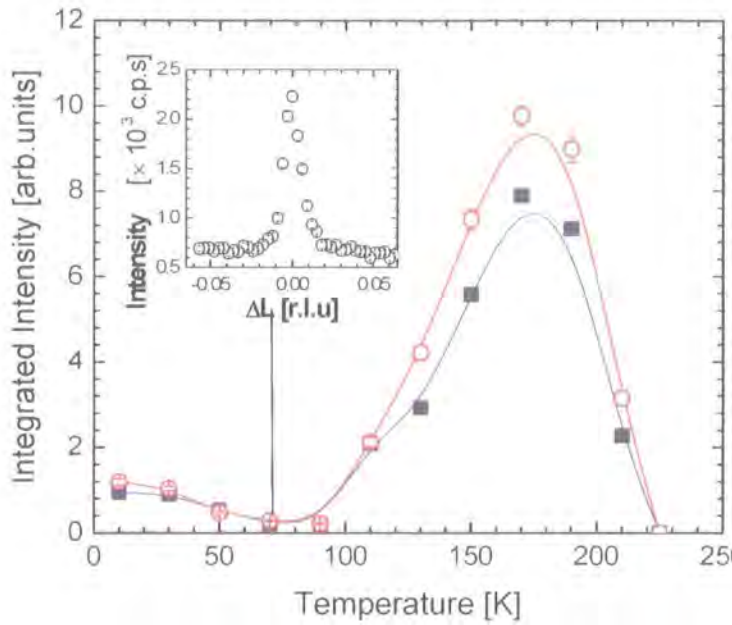

***Figure 3.4**: Temp. dependence of the (0.75 -0.25 5) JT peak in the H and K directions shown by the squares and circles respectively. The solid lines are a guide to the eye. The inset shows a scan through the L direction at 70 K.*

The integrated intensity is a measure of the magnitude of the Jahn-Teller distortion on the Mn^{3-} octahedra. The Jahn-Teller distortion of the Mn^{3-} ions causes movement of the Mn^{4-} ions which changes the charge density distribution. A larger distortion of the $Mn^{3+}O_6$ octahedra produces a larger displacement of the Mn^{4-} and hence a greater intensity. On heating from 10 K there is an initial decrease in the integrated intensity and this decrease continues until 70 K. However, the Jahn-Teller order is still observable and the inset in Figure 3.4 shows a scan in the *L* direction at 70 K which clearly demonstrates that the Jahn-Teller distortion is observable at all temperatures. This provides evidence that the Jahn-Teller order is not re-entrant, as previously believed, but instead the Jahn-Teller order exists in a weaker state with an intensity of 1.5×10^3 cps above background. On further heating the intensity stayed approximately constant until 90 K at which point the intensity began to rapidly increase reaching a maximum at 170 K. This maximum coincides with the antiferromagnetic ordering temperature which is consistent with

previous results with the onset of AFM order causing the charge ordered state to collapse. Further heating causes the integrated intensity to decrease until at 225 K it is not observable above background. The integrated intensity in the L direction demonstrates the same behaviour and this is shown in Figure 3.5.

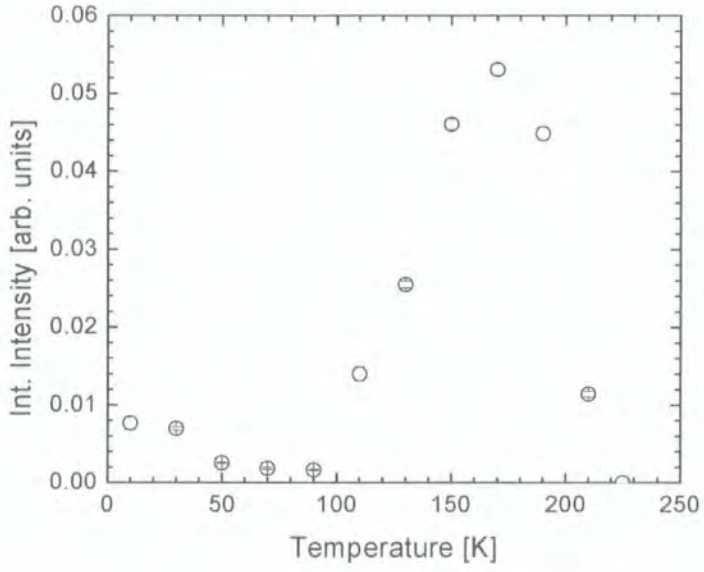

***Figure 3.5**: Temperature dependence of the (0.75, -0.25, 5) J-T peak in the L direction*

The inverse correlation length was measured as a function of temperature in each of the three principal reciprocal space directions and the temperature dependence in the H direction is shown in Figure 3.6. It should be noted that the behaviour in the K and L directions is the same as that in shown in the H direction

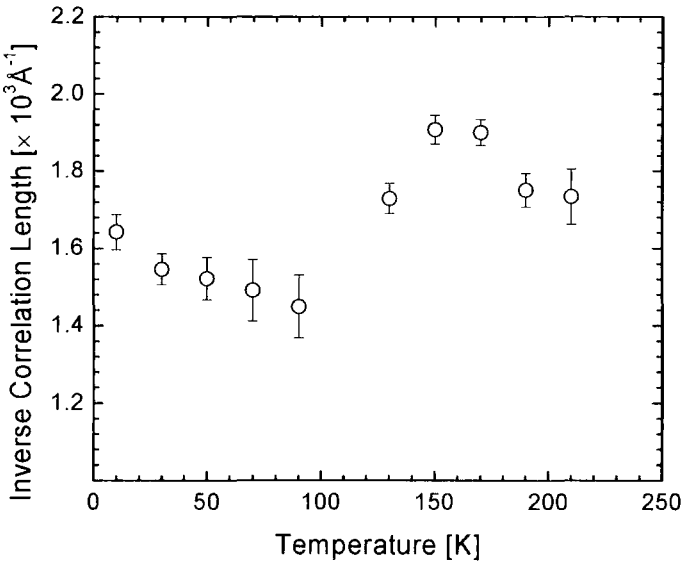

Figure 3.6: *Temperature dependence of the inverse correlation length in the H direction.*

The results indicate that the inverse correlation length has a weak dependence with temperature with it following the same pattern as the integrated intensity. However, the change in the inverse correlation length with temperature is significantly smaller than that of the intensity. The change in the inverse correlation length across the temperature range is small and the measurements demonstrate that the Jahn-Teller order exists in a highly correlated state in both the high and low temperature phase. The Jahn-Teller ordering showed similar inverse correlation lengths in the H, K and L directions and provides clear evidence of the three dimensional nature of the Jahn-Teller order. The measurements of the inverse correlation length in the L direction demonstrate that the Jahn-Teller order remains three dimensional in nature in both the high temperature and low temperature phases.

The position of the Jahn-Teller order peak was measured as a function of temperature to determine the commensurability of the structural modulation. No change was noted in the position of the Jahn-Teller peaks beyond that expected due to thermal expansion. To summarise, the Jahn-Teller order in the 0.5 system exists in a well correlated and commensurate state at all temperatures. However, the magnitude of the Jahn-Teller

ordering shows a significant variation with temperature. The onset of the AFM order at 170 K cause the charge ordered state to collapse and it shows a recovery below 50 K. The behaviour of the integrated intensity agrees with the high energy results obtained by Chatterji *et al.*, but there was no mention of the behaviour of the inverse correlation length in their study. Chatterji *et al.* state that this reflection is due to charge order but we suggest that this reflection is actually due to Jahn-Teller order and our observation of reflections at a modulation of (0.5, 0.5, 0), which we ascribe to the charge order, supports this idea.

The strongest charge order reflection was the (0.5, -0.5, 5) peak and the temperature dependence of this peak was measured. The (0.5, -0.5, 5) charge order reflection was measured at 170 K in the *H*, *K* and *L* directions where the intensity like the Jahn-Teller order was found to be at its maximum. Due to the additional crystallites present in the sample it was very difficult to fit the charge order in the *H* and *K* directions. However, it was possible to fit the charge order peak in the *L* direction and it was found to fit a Lorentzian squared lineshape. The sample was cooled to 10 K and the charge order peak was still observable with a much reduced intensity. It could only be fitted in the *L* direction as at 170 K but again it fitted the Lorentzian squared lineshape. A comparison of the inverse correlation lengths in the *L* direction is shown in Table 3.2 and similar to the Jahn-Teller order there is no difference in the inverse correlation length between the high and low temperature regimes. The integrated intensity of the charge order was measured in the *L* direction as a function of temperature in the temperature range 10 – 230 K. Scans carried out in the *H* and *K* directions insured that the same crystallite was measured at all temperatures and hence, provide valid measurements. The integrated intensity of the (0.5, -0.5, 0) in the *L* direction is shown in Figure 3.7 and from this it can be seen that the charge order exhibits a similar temperature dependence to the Jahn-Teller order.

	L [Å^{-1}]$\times 10^{-3}$
170 K	2.93 ± 0.11
10 K	2.69 ± 0.18
Ratio $\xi^{-1}_{10}/\xi^{-1}_{170}$	0.92 ± 0.04

***Table 3.2**: Inverse Correlation length of the (0.5, -0.5, 5) Charge order peak*

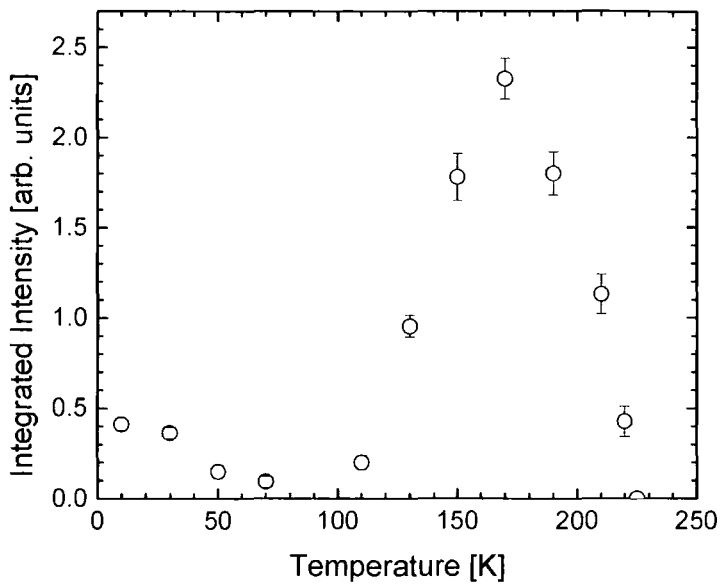

***Figure 3.7**: Temperature dependence of the (0.5, -0.5, 5) charge order (CO) reflection in the L direction*

On warming from 10 K the charge order decreased in intensity and reached a minimum at 70 K where it was very weak but could still be observed above the background. This was clear evidence that charge order continued to exist in the low temperature regime albeit in a significantly weaker state and did not show re-entrant behaviour as had been reported by Wakabayashi *et al.*.[4] Above 90 K the intensity of the charge order reflection began to increase sharply and it reached its maximum intensity at 170 K as expected and this followed exactly the behaviour of the Jahn-Teller order peak. Further heating above 170K causes the charge order integrated intensity to decrease rapidly and it is not observable above background at approximately 230 K. The inverse correlation length of the charge order peak was measured in the *L* direction and this is shown in Figure 3.8.

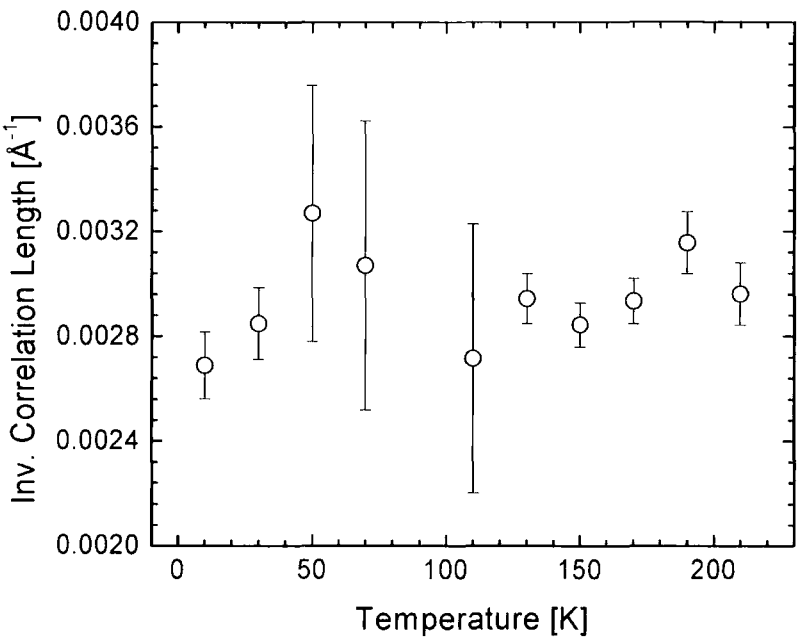

Figure 3.8: *Inverse correlation length as a function of temperature in the L direction for the (0.5, -0.5, 5) charge order peak.*

Unlike the Jahn-Teller order the charge order did not show a variation with temperature beyond error. A possible explanation for this is that the inverse correlation length of the charge order was higher than that of Jahn-Teller order. Due to this it may not have been possible to observe the small changes in the inverse correlation length that were seen in the Jahn-Teller order. Similar to the Jahn-Teller order the charge ordered state shows no significant change in correlation despite the decrease in intensity and it remained highly correlated at all temperatures. No change in the commensurability of the charge order peak was measured beyond thermal expansion, indicating that the charge order remains at a fixed position in reciprocal space below the transition temperature. To summarise, the charge order exists in a commensurate, well correlated state below the transition temperature of 230 K. The results from this section will be discussed in section 3.4 in conjunction with the results from the x = 0.475 system.

3.3 Resonant X-ray scattering measurements on the $x = 0.475$

The resonant X-ray scattering studies were carried out on beamline XMaS beamline BM 28 at the ESRF in Grenoble France which was described in the previous chapter. The doping was determined as $x = 0.475 \pm 0.01$ from EPMA and the excess oxygen as $\delta = 0.00 \pm 0.01$. The sample was mounted in a closed cycle He cryostat without a scattering shield that allowed a temperature range from approximately 15 – 300 K to be accessed. The experiments were carried out at the Mn *K*-edge which corresponds to an energy of approximately 6.55 keV. The incident beam was 87% plane polarised and the energy resolution of the monochromator was 2 eV. All the flight paths were evacuated to reduce the effects of absorption and maximise the intensity. A copper (2, 2, 0) crystal was used as an analyser crystal to allow polarisation analysis to be carried out. At the Mn *K*-edge it scattered close to 45° i.e. the Brewster angle and this meant it could scatter into the σ' and π' channels and hence, allow the signal from the orbital order to be separated from the charge ordering.

The crystals naturally cleaved in the *a*-*b* plane due to the long *c*-axis and hence the <001> direction was surface normal. The measurements were carried out in reflection geometry around the manganese *K*-edge and due to geometric restrictions it was not possible to access the reflections around the (1, 1, 0) Bragg peak, for this reason the crystal was remounted with the <001> direction surface normal. The crystal was aligned and a UB matrix obtained using the (0, 0, 10) and (1, 1, 12) reflections as the primary and secondary reflections respectively.

The sample was cooled to 180 K and a search was carried out for satellite reflections at the expected modulations for Jahn-Teller, charge and orbital order. Reflections were located at (0.5, 0.5, 10), (0.25, 0.25, 10) and (2.25, -0.25, 10). Polarisation analysis showed the (0.5, 0.5, 10) and (2.25, -0.25, 10) reflections to be mainly $\sigma^{|}$ polarised with no rotation of the plane of polarisation compared to the incident polarisation, whereas the (0.25, 0.25, 10) reflection was found to be $\pi^{|}$ polarised which corresponds to a 90° rotation in the plane of polarisation with no significant scattering observed in the σ channel.

The energy scan for the (2.25, -0.25, 10) reflection at constant wavevector is shown in Figure 3.9. It shows the same behaviour as the (0, 0, 10) Bragg peak with a decrease in intensity as it is scanned through the Mn *K*- edge. This is due to the decreased sample volume caused by an increase in the absorption at the Mn *K*-edge. This is the behaviour expected from a structural modulation associated with the Jahn-Teller ordering (JTO) and confirms that the scattering observed at (0.25, 0.25, 0) can be ascribed to cooperative Jahn-Teller distortions.

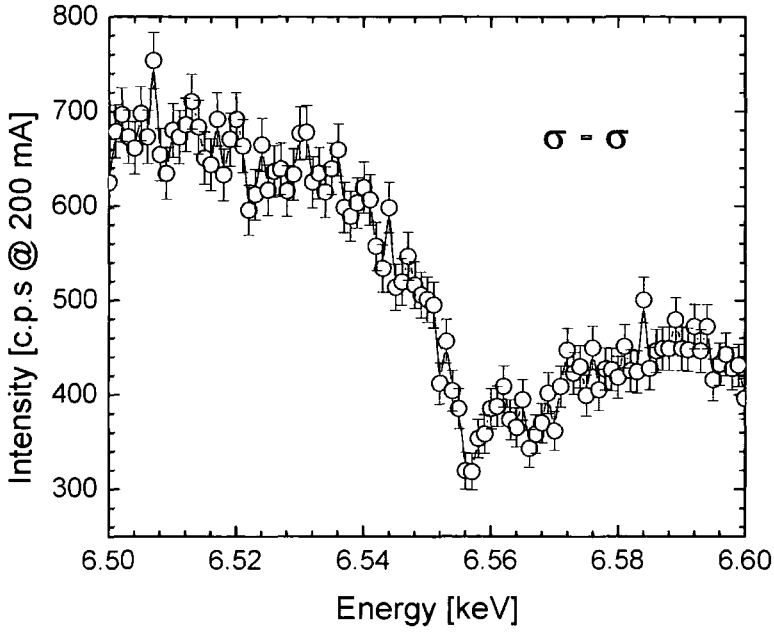

***Figure 3.9**: Energy scan at constant wavevector through the (2.25, -0.25, 10) JT-peak*

Figure 3.10 shows the energy scan through the (0.5, 0.5, 10) peak at a fixed wavevector. The resonance was observed in the σ channel only and peaked at an energy of 6.556 keV with the absorption edge position confirmed by the fluorescence spectrum displayed in the lower panel of Figure 3.10.

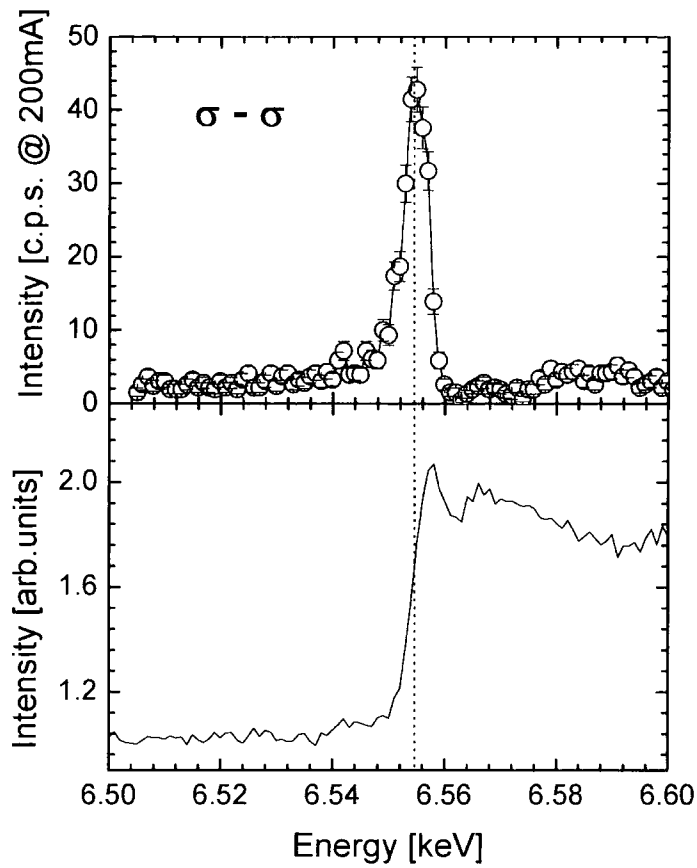

Figure 3.10: *Energy scan at constant wavevector of the (0.5, 0.5, 10) charge order peak. The solid line is a guide to the eye. The fluorescence spectrum on the sample is shown in the lower section confirming the position of the energy resonance.*

This behaviour is consistent with that expected from the Mn^{3+}/Mn^{4+} charge order pattern. Due to the effects of the chemical shift there is a difference in the absorption edge position for the Mn^{3+} and Mn^{4+} ions. At resonance there is an increase in the anomalous scattering factors for the Mn^{3+} ions at a lower energy than the Mn^{4+} ions and this leads to a sharp increase in the contrast between the Mn^{3+} and Mn^{4+} sublattices and hence, a sharp resonance is observed around the Mn *K*-edge. This confirms the charge order modulation as (0.5, 0.5, 0). A comparison of the energy scan with that obtained on the (3/2, 3/2, 0) charge reflection by Wakabayashi *et al.*[4] revealed that the resonant

enhancement for the (0.5, 0.5, 10) charge order peak was larger than that observed in the (3/2, 3/2, 0) charge order peak. It should be noted though that the non-resonant contribution to the (0.5, 0.5, 10) reflection is significantly smaller and the energy scan is close to what would be expected with no structural contribution to the charge order.

Figure 3.11 shows the energy scan through the (0.25, 0.25, 10) peak at a fixed wavevector.

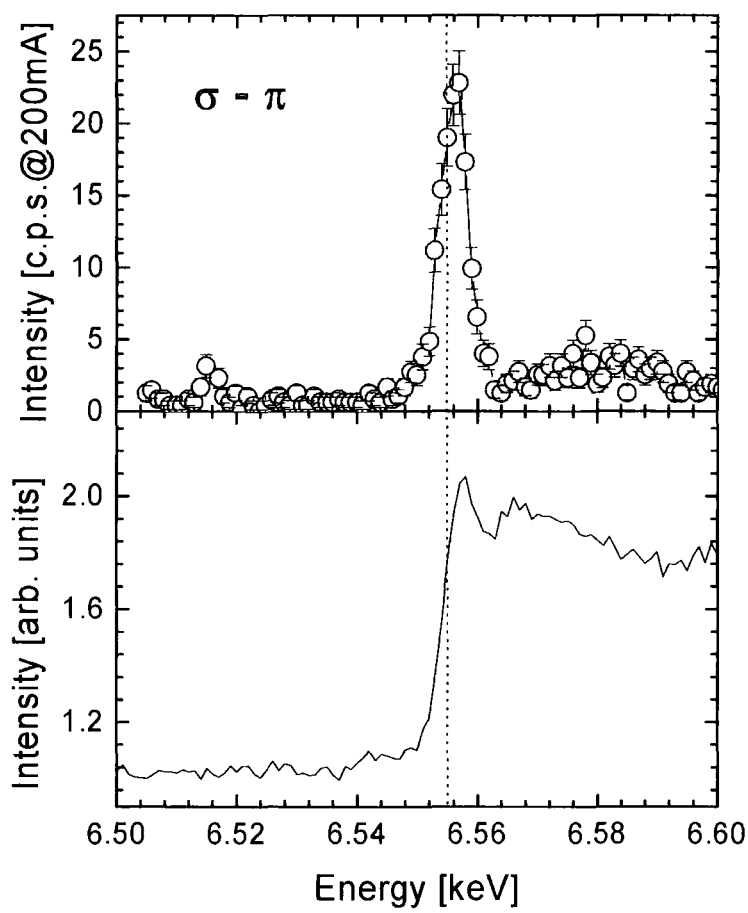

Figure 3.11: *Energy scan at constant wavevector of the (0.25, 0.25, 10) orbital order reflection in the π channel. The fluorescence spectrum on the sample is shown in the lower section confirming the position of the energy resonance*

The reflection at (0.25, 0.25, 10) was observed in the π channel only which is a 90° rotation in the plane of polarisation compared to the incident beam. The reflection was only observed at the Mn *K*-edge and this is consistent with a dipole transition from the 1*s* to the 4*p* state. No signal above background away from the absorption edge was observed. Similar behaviour was observed for the (0.25, -0.25, 10) reflection with the resonance occurring at the same energy. No scattering was observed in the σ channel above background. These results are consistent with the origin of the reflection being due to orbital ordering which causes a splitting in the 4*p* levels when the 3*d* orbitals order. The resonant X-ray scattering technique carried out at the Mn *K*-edge cannot determine the mechanism responsible for the splitting of the 4*p* levels but it does detect the ordering of the orbitals indirectly.

Due to the relatively broad rocking curve width of the copper polarisation analyser crystal it was not possible to carry out high resolution measurements of the width of the peak in reciprocal space. However, it was still possible to measure the temperature dependence of the intensity of the Jahn-Teller order, charge order and orbital order and Q_Z scans were carried out as a function of temperature on the (2.25, -0..25, 10) Jahn-Teller order peak, (0.5, 0.5, 10) charge order peak and the (0.25, 0.25, 10) orbital order peak. The temperature dependence of the Jahn-Teller order is shown in Figure 3.12.

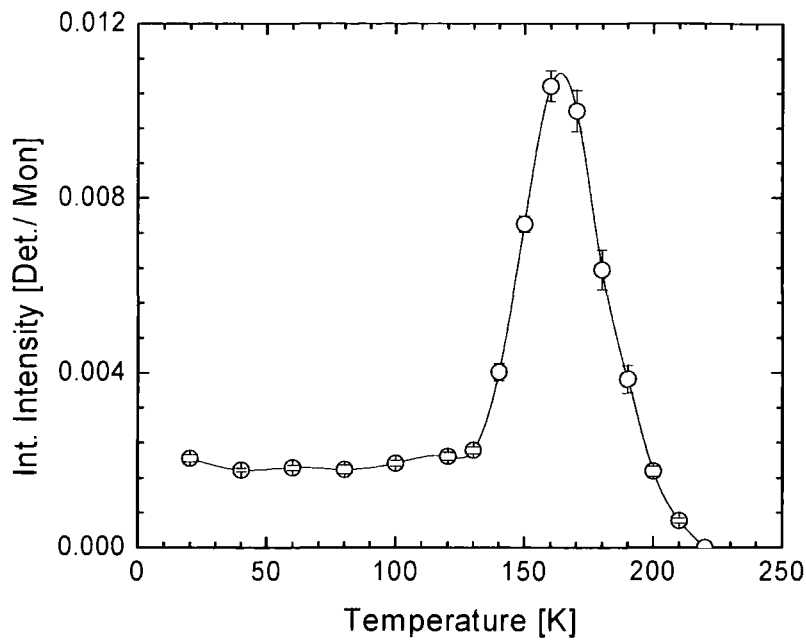

Figure 3.12: *Temp. dependence of the integrated intensity of the (2.25, -0.25, 0) JTO peak. Solid line is guide to the eye.*

At low temperatures the integrated intensity is weak and it remains constant until it reaches a temperature of 100 K. At this temperature the intensity begins to increase sharply and maximises at 180 K. Above this temperature the intensity begins to decrease sharply and it disappears by 220 K. The temperature dependence of the charge and orbital order is shown in Figures 3.13 and 3.14. Neither the charge order (CO) or orbital order (OO) are intense enough to be observed below 120 K. However, the presence of the Jahn-Teller order at low temperatures shows that the system is still charge / orbitally ordered as it could not be Jahn-Teller ordered without being charge ordered. Both the charge and orbital order showed a maximum in intensity at 180 K and above the temperature the intensity decreases sharply and they both disappear at 220 K.

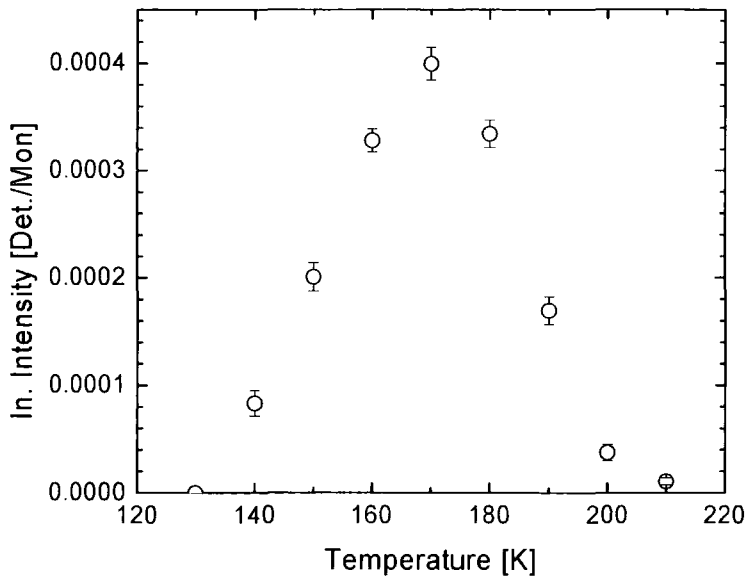

***Figure 3.13**: Temp. dependence of the intensity of the (0.5, 0.5, 10) CO peak*

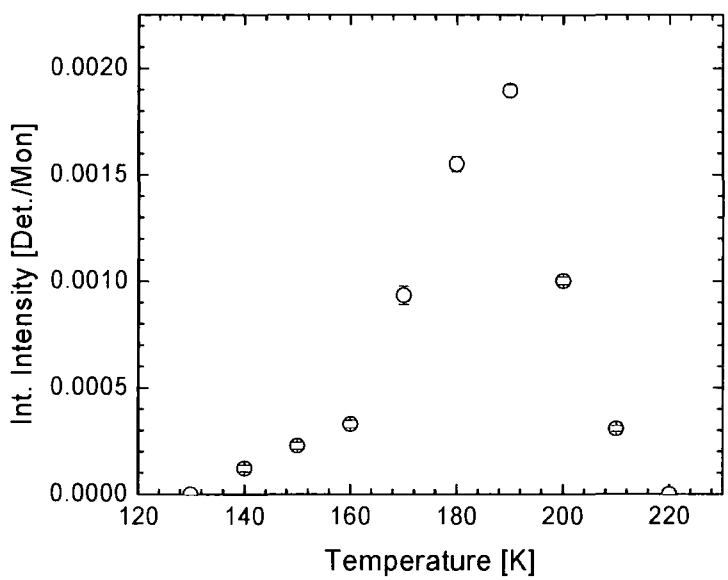

***Figure 3.14:** Temp. dependence of the intensity of the (0.25, 0.25, 10) OO peak*

3.4 Discussion

The x = 0.475 sample was studied with high energy x-rays at HASYLAB and these results are referred to in the discussion and can be found in the thesis of Stuart Wilkins[7]. Figure 3.15 shows a summary of the results obtained on the (1.75, 0.25, 0) Jahn-Teller order peak taken from by Wilkins *et al*[8]

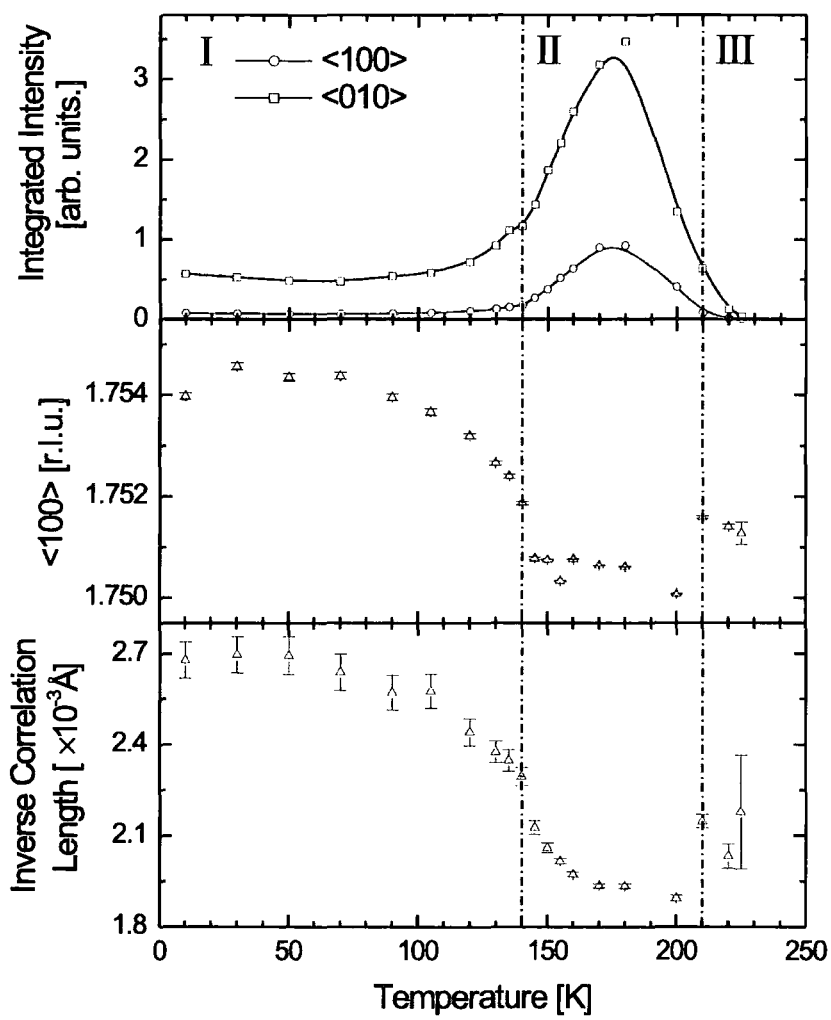

Figure 3.15: *Integrated intensity, position and inverse correlation length of the (1.75, 0.25, 0) Jahn-Teller reflection as a function of temperature taken from Wilkins et al.*[8]

The Jahn-Teller order also demonstrates considerable differences between the two doping levels. In the 0.475 doped system the Jahn-Teller order can be divided into two clear regions below the charge ordering temperature. In region I below 140 K the Jahn-Teller order exists in a weak, poorly correlated and incommensurate state, whereas in region II above 140 K the Jahn-Teller order is strong, well correlated and commensurate with the lattice. This contrasts with the 0.5 doped sample where the Jahn-Teller order remains well correlated and commensurate at all temperatures despite the decrease in intensity. In both samples the intensity of the Jahn-Teller order began to decrease at approximately 180 K which is in agreement with the measurements by Dho *et al.*[1]. The onset of the A-type antiferromagnetic order causes the charge order state to collapse and temperatures are in agreement with those measured by Ling *et al.* [9] in a neutron diffraction study.

The onset of the magnetic ordering causes the collapse of the Jahn-Teller/charge order state in both samples but from these results it is apparent that there is a significantly greater destabilising effect in the 0.475 sample. This is most apparent in the correlation in L direction where the Jahn-Teller order is correlated over a distance twenty times greater at 180 K than at 10 K; i.e. in the low temperature regime of the 0.475 system the Jahn-Teller order exists in a two dimensional state. This is in clear contrast with the half doped system in which the Jahn-Teller remains in a three dimensional state at all temperatures and shows only a small difference between the high and low temperature regimes. In the 0.475 sample the Jahn-Teller order below 140 K is slightly incommensurate with an incommensurability of $\varepsilon = 0.004$. At 140 K the Jahn-Teller order locks in to a commensurate value of 0.25 and this is shown in the middle panel of Figure 3.15 and this coincides with an decrease in the inverse correlation of the Jahn-Teller order. In the 0.5 system, no variation in the Jahn-Teller position was observed beyond thermal expansion and the wavevector was constant at all temperatures. From this it is postulated that at the commensurate position there is a coupling between the lattice and the Jahn-Teller/charge order that stabilises the charge order pattern i.e. a "commensurability effect". In the 0.5 sample the Jahn-Teller/charge order is commensurate at all temperatures and as a consequence is stabilised at all temperatures. In the 0.475 sample the Jahn-Teller/charge order is only commensurate above 140 K and

hence, it is only stabilised by the interaction with the lattice in this region. A possible explanation for this difference is firstly that in the 0.475 sample there is not an exact 1:1 ratio of Mn^{3+} to Mn^{4+} ions and hence the charge order pattern is not as stable as in the 0.5 sample. A second factor is that the 0.475 doping is very close to the phase boundary below which no charge order is observed. It is therefore possible that due to this the transition into the *A*-type antiferromagnetic state leads to increased instability compared to the 0.5 system. In studies carried out on the single layered $La_{1-x}Sr_{1+x}MnO_4$ system by Wakabayashi *et al.* [10] they report a decrease in the correlation of the Jahn-Teller/charge order as the doping is decreased from 0.5 towards the critical concentration for charge order of approximately 0.47. The results for the bi-layer system appear to follow this behaviour with the Jahn-Teller order measured to be slightly more correlated in the 0.5 than 0.475 systems even in the high temperature regime where it stabilises in the x = 0.475 system.

Comparing the results between the x = 0.50 and x = 0.475 there are clear differences in the behaviour of the charge order. In the half doped system the charge order is observable in the low temperature regime below 100 K albeit in a significantly less intense state. In the 0.475 system the charge order was only observed in region II where the Jahn-Teller order was strong and below 120 K the charge order was too weak to be observed above background. The observation of the Jahn-Teller order in the x = 0.475 system is evidence that the system was charge ordered at low temperature but too weak to be observed. The charge order in the 0.475 sample showed an increase in the inverse correlation length in the *L* direction on cooling indicating that the charge order was becoming more two dimensional in nature. In the half doped system the charge order, like the Jahn-Teller order, showed no significant change in correlation with temperature despite the decrease in intensity at low temperature. These results demonstrate that, while in the intermediate temperature range there is little difference in the stability of the charge order, in the low temperature region the Jahn-Teller/charge order state is clearly more stable in the 0.5 doped system.

An examination of the Jahn-Teller order data in the low temperature region 10 – 100 K reveals a further difference in the behaviour of the two samples. In the 0.475 sample the Jahn-Teller order intensity decreases until reaching 100 K and only cooling further to

the base temperature of 10 K there is no significant change in the intensity. In the 0.5 sample the intensity minimises at 90 K but as the temperature is decreased there is a recovery in the intensity with it maximising at 10 K which is in agreement with the half doped results from Chatterji *et al.*[3]. This is in agreement with the resistivity measurements by Dho *et al.* who measured a larger dip in the resistivity in the $x = 0.5$ doped system than that observed in the $x = 0.475$ system. It is not known why there is this difference in the low temperature regime between the two samples. High resolution structural measurements were carried out on both samples to see if there was any difference in the behaviour in the low temperature region and follow in section 3.5.

3.5 High Resolution Bragg Peak Measurements

In the study carried out by Wakabayashi *et. al.* [4] they reported the broadening of the Bragg peaks as the intensity of the charge and orbital order increased in intensity. The Bragg peaks showed the maximum width at the point where the charge and orbital order were at their maximum intensity. This is consistent with the charge and Jahn-Teller ordering causing strain within the lattice. The crystal used by Wakabayashi *et. al.* had a rocking curve width of ~ 0.2°, however, the crystals used in our study were much higher quality with a rocking curve width of 0.03° for the $x = 0.475$ sample and 0.04° for the $x = 0.5$ sample. We carried out high resolution measurements on the Bragg peaks at station 16.3 at the SRS Daresbury which has been described in Chapter 2. The measurements were carried out at an energy of 12.4 keV (1Å) in reflection geometry. An energy gated solid state Ge detector was used to eliminate harmonics. Both samples were mounted with the <001> direction normal to the scattering vector and the <110> direction down the beam. The temperature dependence of the wavevector (position), width and intensity of the Bragg peaks was measured as a function of temperature in the three principal directions of reciprocal space (*H, K,* and *L*). In the $x = 0.475$ sample the (1, 0, 17), (0, 0, 10) and (1, -1, 16) were all measured as a function of temperature $10 < T < 300$ K. However, a clear increase in the inverse correlation length were observed in all directions. This was seen in all Bragg peaks but the cleanest data was observed for the (1, -1, 16) Bragg peak. Figures 3.16, 3.17 and 3.18 show the inverse correlation lengths of the (1, -1, 16) Bragg peak in the *H, K* and *L* directions.

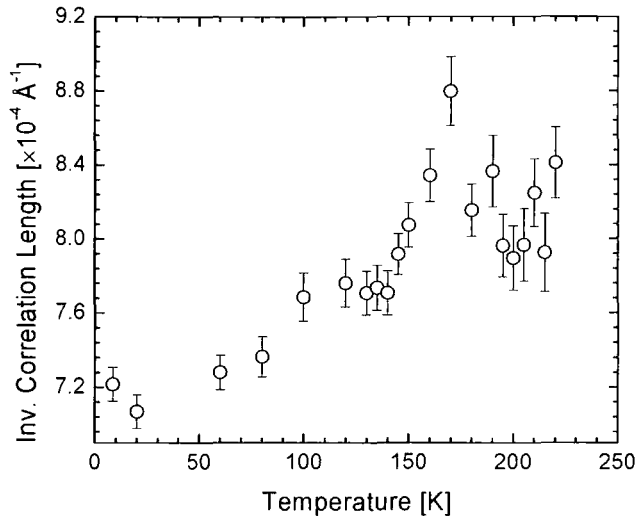

Figure 3.16: *Temperature dependence of the inverse correlation length of the (1, -1, 16) Bragg reflection in the H-direction*

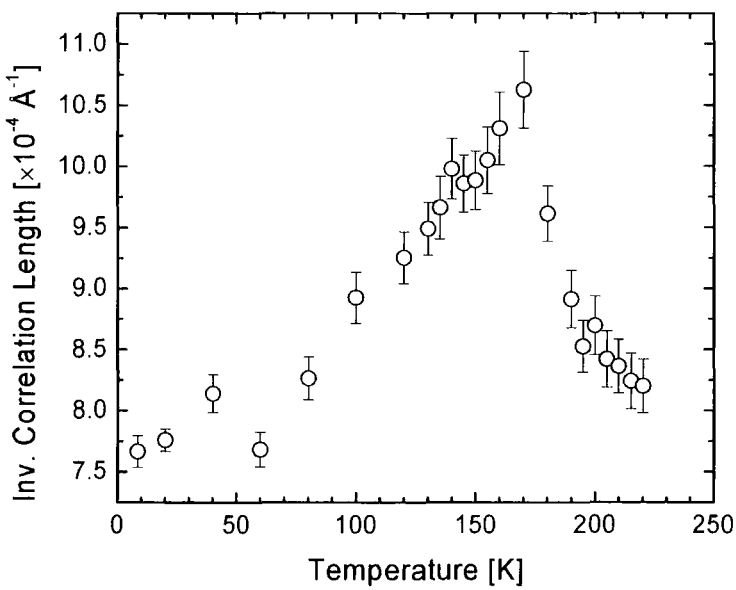

Figure 3.17: *Temperature dependence of the inverse. correlation length of the (1, -1, 16) Bragg reflection in the K-direction*

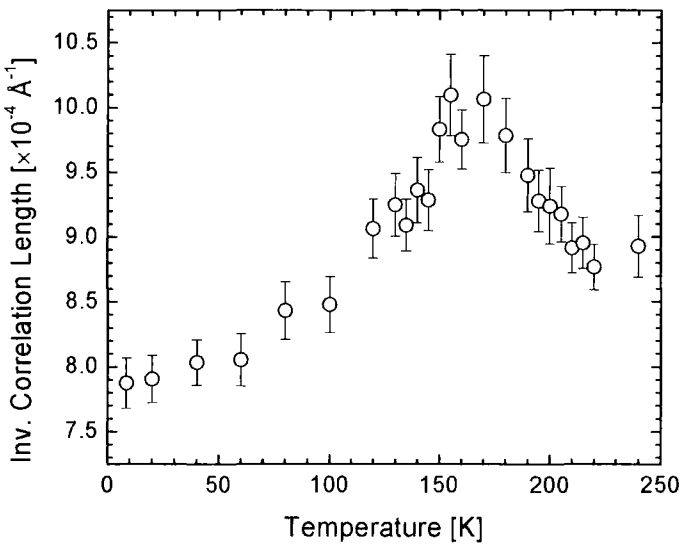

Figure 3.18: *Temperature. dependence of the inverse correlation length of the (1, -1, 16) Bragg reflection in the L-direction*

In all directions there is a clear broadening in the inverse correlation length. This is consistent with the presence of the Jahn-Teller and charge order causing strains within the lattice. The maximum inverse correlation length coincides with the temperature at which the Jahn-Teller distortion is at its maximum value. This broadening is most distinct in the L direction possibly because this corresponds to Q_Z the direction of maximum instrumental resolution. This could also be due to their being more strain within the lattice between planes (L direction) than occurs within the plane (H and K directions). There was no significant change in the integrated intensity or wavevector beyond thermal expansion in any direction of reciprocal space.

The x = 0.5 sample was of poorer quality, with many crystallites which made it difficult to obtain a measure of the inverse correlation lengths in the H and K directions. However, the L direction corresponded to the Q_Z direction and it was possible to accurately measure the intensity, width and wavevector with temperature in the range 10 – 300 K. Similar to the x = 0.475 sample there was no significant change in the integrated intensity or wavevector of the Bragg peaks. Accurate measurements were

carried out in the low temperature regime to determine if there was any difference in the Bragg peak behaviour between the $x = 0.475$ and $x = 0.5$ samples in this range that would explain why the Jahn-Teller order decreases from 10 K -70 K in the 0.5 sample but remains constant in the 0.475 sample. There was a clear broadening in the inverse correlation length of the Bragg peak around the temperature of 180 K as expected because this is the temperature where the strain on the lattice was at its peak. Our measurements at low temperature revealed no difference between the $x = 0.5$ and 0.475 samples with respect to the wavevector. There was no evidence for a structural transition in either sample at the charge ordering temperature T_{CO} or any temperature below T_{CO}.

3.6 Conclusions

The studies of the $x = 0.475$ and 0.5 samples have confirmed the correct modulation for the wave vector for the Jahn-Teller, charge and orbital order as (0.25, 0.25, 0), (0.5, 0.5, 0) and (0.25, 0.25, 0). The resonant x-ray scattering results on the $x = 0.475$ sample provided definite confirmation of the origin of the reflections. This is in agreement with the resonant x-ray scattering studies of Wakabayashi *et. al.* but does not agree with the original results of Chatterji *et. al.*. It is postulated that the charge order reflections observed by Chatterji were Jahn-Teller order and in a recent paper by Di Matteo, Chatterji *et al.*[11] they also conclude that the reflections at the (0.25, 0.25, 0) modulation arise from the Jahn-Teller/orbital order.

The results have determined that the charge/orbitally ordered state is not re-entrant in nature but in fact exists in a significantly weaker state below 100 K in both samples. In the earlier studies performed by Wakabayashi *et al.* and the electron studies by Kimura *et al.* it is postulated that they did not have the incident flux to observe the Jahn-Teller/charge order in the low temperature regime. Evidence for this is the fact that in the $x = 0.5$ sample the charge order reflection is observable at all temperatures below the transition temperature. The presence of long range Jahn-Teller order in the $x = 0.475$ system is indicative that the system is charge ordered, the charge order is too weak to be observed above background

Comparing the results on the $x = 0.5$ sample with those obtained on the $x = 0.475$ at high energy there are clear differences in the charge ordered states between the $x = 0.5$ and the results from the previous study on the $x = 0.475$ samples. Firstly in the 0.5 sample the Jahn-Teller order and charge order remain in a highly correlated state over the whole temperature range. There is a small variation with temperature in the inverse correlation length of the Jahn-Teller with it following the same pattern as the integrated intensity but the effect is small and it remains highly correlated at all temperatures. In the 0.475 sample two clear regions are observed. At low temperature below 140 K the charge order is too weak to be observed and the Jahn-Teller order is weak, poorly correlated and incommensurate. Above 140 K the charge order is visible and the Jahn-Teller order is strong, well correlated and locks into a commensurate value. This 'lock in' behaviour was not seen in the $x = 0.5$ sample. In the $x = 0.475$ sample the intensity is constant between 10 - 100 K, however, in the $x = 0.5$ sample the intensity decreases from 10 K to a minimum at 70 K before dramatically increasing above 90 K. It is not known why there is this difference but investigating higher doped samples may provide a clearer picture of what is occurring in the low temperature regime.

3.7 References

1 J. Dho, W. S. Kim, H. S. Choi, *et al.*, Journal of Physics - Condensed Matter **13**, 3655 (2001).

2 T. Kimura, R. Kumai, Y. Tokura, *et al.*, Physical Review B-Condensed Matter **58**, 11081 (1998).

3 T. Chatterji, G. J. McIntyre, W. Caliebe, *et al.*, Physical Review B **61**, 570 (2000).

4 Y. Wakabayashi, Y. MuraKami, I. Koyama, *et al.*, Journal of the Physical Society of Japan **69**, 2731 (2000).

5 J. B. Goodenough, Physical Review **100**, 564 (1955).

6 W. R. Busing and H. A. Levy, Acta. Cryst. **22**, 457 (1967).

7 S. B. Wilkins, PhD thesis, Physics Department ,University of Durham (2002).

8 S. B. Wilkins, P. D. Spencer, T. A. W. Beale, *et al.*, Physical Review B **67**, 205110 (2003).

9 C. D. Ling, J. E. Millburn, J. F. Mitchell, *et al.*, Physical Review B **62**, 15095 (2000).

10 Y. Wakabayashi, Y. Murakami, Y. Moritomo, *et al.*, Journal of the Physical of Japan **70**, 1194 (2001).

11 S. Di Matteo, T. Chatterji, Y. Joly, *et al.*, Physical Review B **68**, 024414 (2003).

Chapter 4

Jahn-Teller and Charge Ordering in $La_{2-2x}Sr_{1+2x}Mn_2O_7$ for $x = 0.55$ and 0.60

4. 1 Introduction

Experimentally, the $La_{2-2x}Sr_{1+2x}Mn_2O_7$ has been thoroughly described in the doping region $0.3 \leq x \leq 0.5$ where the system displays a dramatic range of electronic and magnetic properties. An antiferromagnetically insulated state was also reported for a doping level of $x = 1.0$ However, in the doping region $0.5 < x < 1.0$ it is very difficult to grow samples and studies carried out on the system have been limited to x-ray powder diffraction studies by Dho *et al.*[1], neutron powder diffraction studies by Ling *et .al.* [2]and Mitchell e*t al.*[3] and electron powder diffraction by Li *et al.*[4]

It was initially thought that the charge ordering in the bilayer system was restricted to a very narrow doping range around $x = 0.5$, similar to that observed in the $Nd_{0.5}Sr_{0.5}MnO_3$ [5]system. However, a study of the bi-layer system by Dho *et al.* in the doping range $0.3 \leq x \leq 0.8$ by means of transport, magnetisation and x-ray powder diffraction measurements reported this not to be the case. They reported the presence of a re-entrant charge ordered state in the doping regime $0.47 \leq x \leq 0.62$ which was a broader range than previously believed for the bi-layer manganites (see Figure 4.1). Our single crystal measurements on the $x = 0.475$ doped sample confirmed that long range Jahn-Teller and charge order were present away from the half doped system.[6] The question that it was hoped to answer in this Chapter is what happens to the charge ordered state for doping levels of $x > 0.5$? X-ray and neutron powder diffraction studies by Mitchell *et al.* for $0.5 < x < 1.0$ also provided evidence that the charge ordering observed at $x = 0.5$ persists well into the Mn^{4+} rich regime. They reported evidence of charge ordering up to a doping level of at least $x = 0.6$. They reported that the charge ordering in the 0.6 system showed similar behaviour to the $x = 0.5$ sample with the intensity of the Jahn-Teller maximising at an intermediate temperature of 160 K and then decreasing in intensity again at low temperatures. This disagreed with TEM measurements by Li *et al.* who reported an

increase in the temperature where the intensity maximised in the 0.60 system compared to the 0.50 system. Li *et al.* carried out TEM measurements on the doping range $0.40 < x < 0.75$. Above 0.5 they reported a gradual decrease in the wavevector from (0.25, 0.25, 0) and in the $x = 0.60$ system the Jahn-Teller order was measured as (0.2, 0.2, 0). The charge ordering temperature was measured as 280 K – a significantly higher temperature than in the lower doped systems. However, the data from powder diffraction is limited compared to that which can be obtained from single crystal studies. The neutron studies by Ling and Mitchell determined a magnetic phase diagram from $0.3 < x < 1.0$ and this is shown in Figure 4.2. Clearly a huge variation in the magnetic phase diagram is observed with doping with ferromagnetic behaviour exhibited below $x = 0.4$ and a transition into a canted antiferromagnetic state between 0.40 and 0.47. This was in agreement with previous studies but this was the first time that the magnetic phase diagram in the doping range $0.5 < x < 1.0$ had been reported. There is a progression of antiferromagnetic insulating phases as the doping is increased from 0.5. In the region $0.5 < x < 0.66$ the system displays the layered *A*-type magnetic order. In the $0.66 < x < 0.75$ no evidence of any long range magnetic order was observed and the reason for this behaviour is as yet unclear. In the doping regime $0.75 < x < 0.90$ the system displays *C*-type antiferromagnetic order and in the doping region $0.90 < x < 1.0$ the system displays *G*-type antiferromagnetic order. It is important to attempt to link the results from Ling *et al.* and Dho *et al.* in order to understand what is occurring within the system. Dho reports that the charge order collapses in the regime $0.47 < x < 0.62$, and this result is consistent with the system showing *A*-type antiferromagnetic order because the onset of *A*-type ordering causes the charge ordered state to collapse. Ling and Mitchell report the absence of any long range magnetic order in the region $0.66 < x < 0.75$ and they postulate that this indicates the presence of a frustrated spin state. Dho *et al.* report the presence of charge order in this regime but it no longer displays the collapse in the charge order seen in samples with $x < 0.62$. This supports the neutron diffraction data because the absence of *A*-type antiferromagnetic order would mean the charge ordered state would not collapse due to competition between the two states. The resistivity measurements indicated that as the doping level was increased the charge ordering temperature increased until reaching a maximum of 340 K at $x = 0.7$.

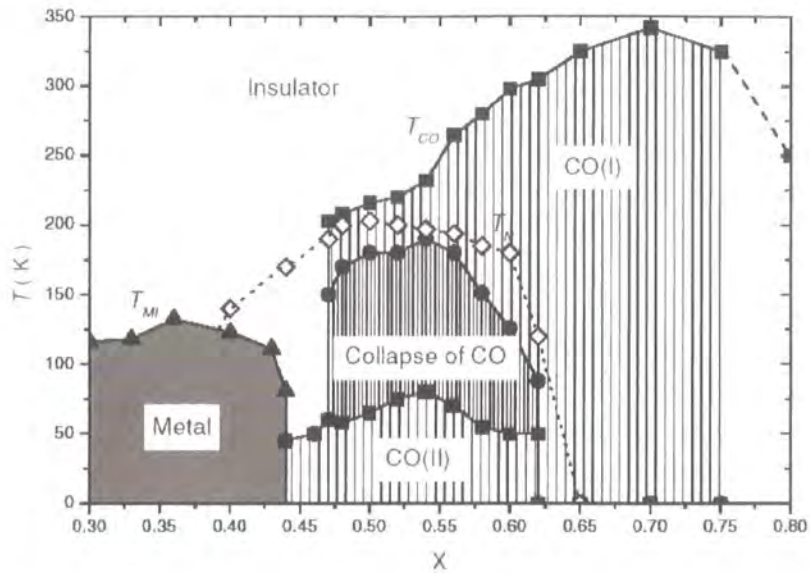

***Figure 4.1**: Phase diagram of the $La_{2-2x}Sr_{1+2x}Mn_2O_7$ system in the doping region 0.3 x 0.8. The charge ordering temperature is shown by the filled squares taken from Dho et al*[1]

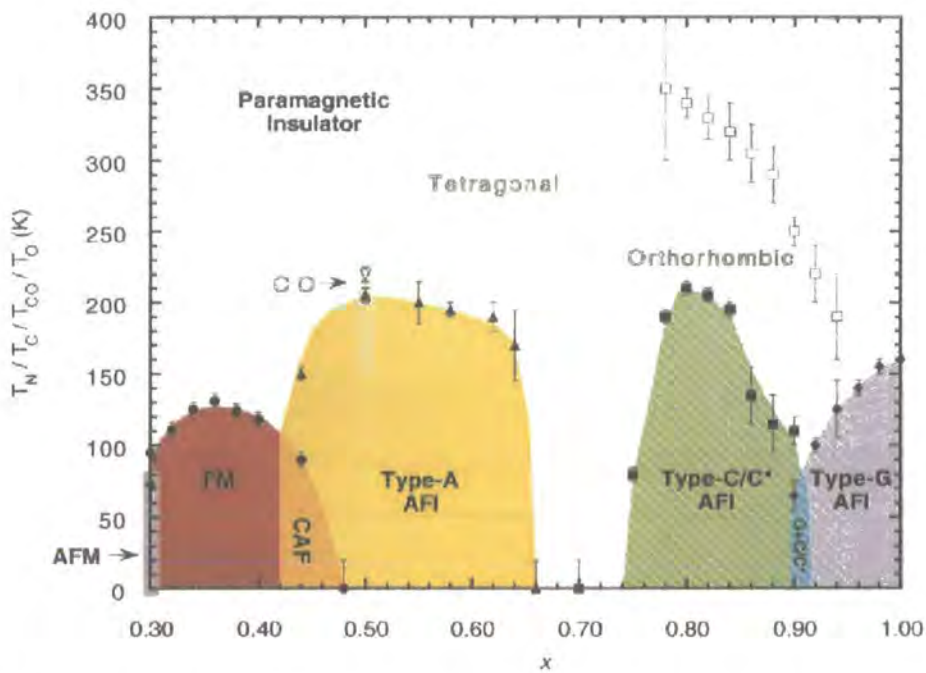

***Figure 4.2:** Magnetic and crystallographic phase diagram for $La_{2-2x}Sr_{1+2x}Mn_2O_7$. Solid points show magnetic transitions from neutron powder diffraction data. Open points show crystallographic transitions taken from Ling et al.*[2]

Above this temperature no long range charge order was observed by Dho *et al.* and the onset of *C*-type magnetic order might not allow the presence of long range charge order. The study by Ling *et. al.* reported no charge order above $x = 0.5$. However, the later study by Mitchell reported the system was charged ordered until at least $x = 0.60$ and this is in agreement with the Dho and Li measurements.

To date no studies have been carried out for doping levels of $x > 0.5$ on single crystal samples due to difficulties in synthesising samples with higher doping levels. Powder diffraction studies do not allow high resolution data about the charge ordered state to be obtained and the Jahn-Teller and charge ordering is too weak to be observed in these studies. We have high quality single crystals grown at the University of Oxford with doping levels of $x = 0.55$ and $x = 0.60$. Single crystal studies will give much more detailed information than powder diffraction studies about the nature of the charge ordering present in the higher doped regime. The crystals were grown using the same conditions as utilised for the $x = 0.475$ and 0.5 samples, so valid comparisons between the charge ordered states within the different doping levels can be made. As discussed in the previous chapter there were considerable differences in the charge ordered state between the $x = 0.475$ and 0.5 doped systems. The Jahn-Teller and charge order was observed to occur in two different regions in the $x = 0.475$ sample; at low temperature the charge ordering was too weak to be observed and the Jahn-Teller ordering was weak, poorly correlated and incommensurate. In region 2 between 140 K and 210 K the charge ordering was observable and the Jahn-Teller ordering was strong and well correlated. In the $x = 0.5$ sample the Jahn-Teller ordering remains well correlated and commensurate down to 10 K and the charge ordering is also observed down to 10 K. The $x = 0.55$ doping corresponds to the centre of the region in which the charge order collapses upon the onset of *A*-type antiferromagnetic order and the $x = 0.60$ sample is close to the boundary of this phase. By studying the $x = 0.55$ and 0.60 samples significant information on the evolution of the charge ordered state with doping will be obtained. In particular such a study will show if increasing the doping from $x = 0.5$ has the same effect on the Jahn-Teller/charge order as decreasing the doping away from $x = 0.5$. In this chapter the high energy scattering results for the Jahn-Teller and charge order in the 0.55 and 0.60 bi-layer samples will be discussed and compared with the lower doped levels

and the powder diffraction measurements for a better understanding of the high doped bi-layer manganites.

4.2 Experimental Procedure

The crystal were grown at the University of Oxford using the floating zone method and were grown under the same conditions as the $x = 0.475$ and $x = 0.5$ doped samples. Both the $x = 0.55$ and $x = 0.60$ samples were indexed in the *I4/mmm* setting with $a = b =$ 3.87 Å and $c = 20$ Å a schematic of which was shown in the previous Chapter. The doping levels were determined as $x = 0.55 \pm 0.01$ and $x = 0.60 \pm 0.01$ respectively from EPMA and the excess oxygen as 0.00 ± 0.01 in both samples from TGA The x-ray scattering studies were carried out on beamline BW5 at HASYLAB and the beamline has been described in a previous Chapter. Graded $Si_{1-x}Ge_x$ crystals were used as the monochromator and analyser to provide high resolution triple axis measurements and allowed the flux to be maximised. The samples were mounted in a closed cycle displex cryostat which allowed a temperature range from 10 – 300 K to be accessed. Both samples were mounted with the <100> direction normal to the scattering plane and the <001> direction corresponding to the direction of the incident beam. The measurements were performed in transmission geometry using an incoming energy of 100 keV and a beam size of 2 × 2 mm.

4.3 Results

4.3.1 $x = 0.55$

The sample was aligned using the (2, 0, 0) and (0, 0, 10) as the *or0* and *or1* reflections and a UB matrix obtained. The $x = 0.55$ sample was cooled to 180 K and a search carried out for the Jahn-Teller and charge ordered peaks at the expected modulations of $\boldsymbol{Q}_{CO}$ = (±½, ±½, 0) and $\boldsymbol{Q}_{JTO}$ = (±¼, ±¼, 0). This was done because the previous experimental work suggested at this temperature the charge and Jahn-Teller ordering would be at their most intense. Since the study was carried out at high energies the signal associated with the orbital order would not be observed and any scattering observed at a modulation of

(0.25, 0.25, 0) would be due to the structural modulation associated with the Jahn-Teller distortion.

Strong reflections were located around the (2, 0, 0) Bragg peak at the expected positions for the Jahn-Teller and charge order. As in the $x = 0.5$ sample strong reflections were observed at modulations of (±0.25, ±0.25, 0) and these corresponded to the Jahn-Teller order reflections and weaker reflections were observed at a modulation of (±0.5, ±0.5, 0) corresponding to the charge order reflections. On cooling to 10 K the Jahn-Teller order and charge order were both still observable, but had a much reduced intensity. At 180 K the peak intensities were ~ 44 × 10^3 counts per second (cps) above background for the Jahn-Teller order and ~ 1.8 × 10^3 cps above background for the charge order. At 10 K the intensity of the Jahn-Teller order had decreased to ~ 11 × 10^3 cps and the charge order was ~ 250 cps above background.

Scans were carried out along the *H*, *K* and *L* directions of reciprocal space for the Jahn-Teller in triple axis mode. At 180 K the Jahn-Teller order reflection fitted a Gaussian lineshape in the *H* direction and two Lorentzian squared lineshape in the *K* direction and these fits are shown in Figures 4.3 and 4.4. The inverse correlation length ξ^{1} was calculated in each direction using the equation

$$\xi^{-1} = \kappa \times \left(\frac{2\pi}{d} \right) \qquad [4.1]$$

where κ is the half width at half maximum of the peak and d is the Bragg plane spacing normal to the scattering vector.

The sample was then cooled to 10 K and a search carried out for the Jahn-Teller order satellites once again. The Jahn-Teller order peak was located and once again it was scanned in the *H*, *K* and *L* directions. Using the parameters from the fitting at 180 K the Jahn-Teller order peak was fitted. The Jahn-Teller order peak fitted a Gaussian lineshape in the *H* direction and two Lorentzian squared lineshapes in the *K* direction and these fits are shown in Figures 4.5 and 4.6. It should be noted that the data in the *L* direction were very difficult to fit due to the presence of more than one crystallite in the scan. However, an attempt was made to fit the data to obtain an approximate comparison of the inverse correlation lengths at 10 K and 180 K.

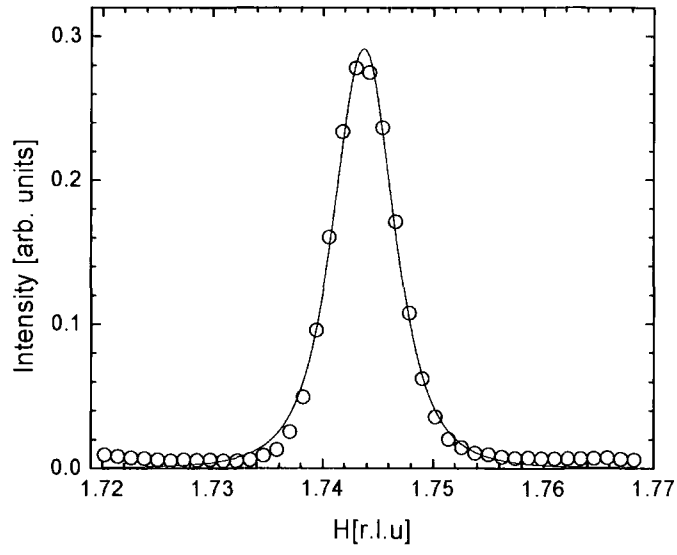

Figure 4.3: *Scan along the H direction of the (1.75, 0.25, 0) Jahn-Teller peak at 180 K. The solid line shows a fitted Gaussian lineshape.*

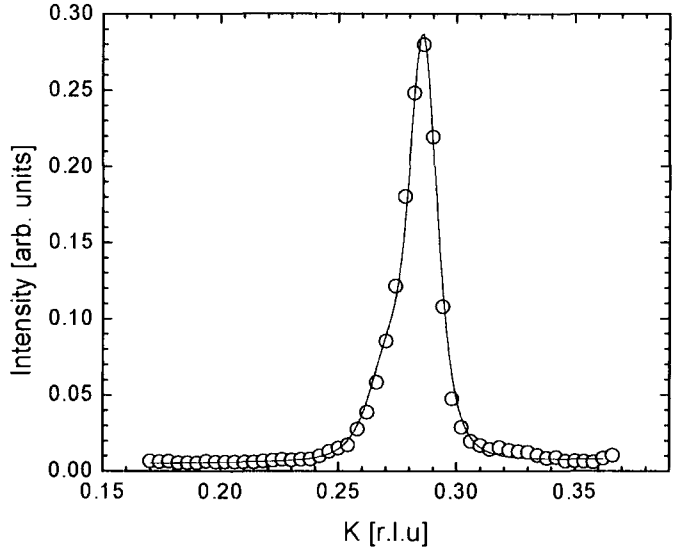

Figure 4.4: *Scan along the K direction of the (1.75, 0.25, 0) Jahn-Teller peak at 180 K. The solid line shows the fitted lineshape of two convoluted Lorentzian squared peaks.*

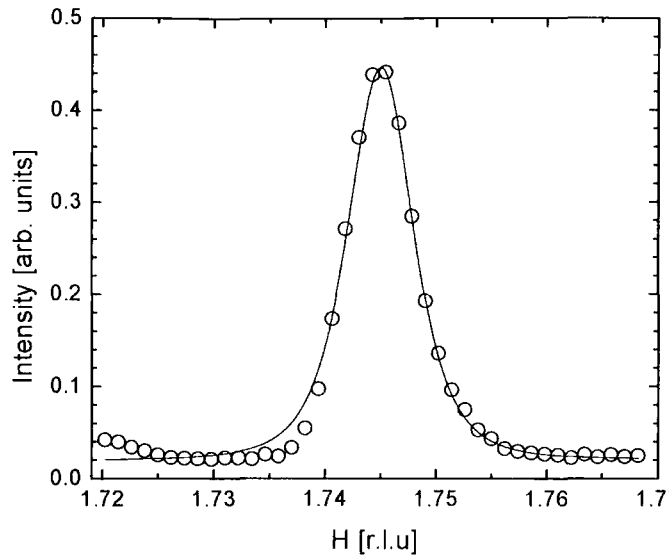

Figure 4.5: *Scan along the H direction of the (1.75, 0.25, 0) Jahn-Teller peak at 10 K. The solid line shows the Gaussian lineshape fitted.*

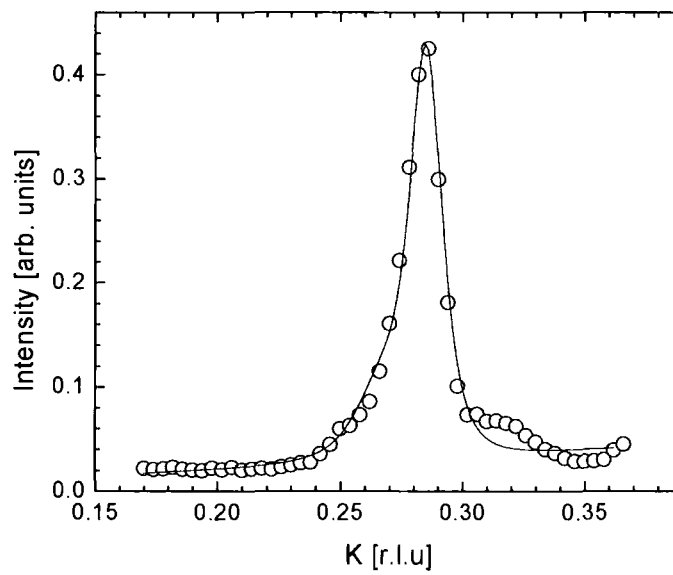

Figure 4.6: *Scan along the K direction of the (1.75, 0.25, 0) Jahn-Teller peak at 10 K. The solid line shows the fitted lineshape of two Lorentzian squared peaks.*

Table 4.1 shows the inverse correlation lengths at 10 K and 180 K for the (1.75, 0.25, 0) Jahn-Teller order peak.

	H [Å^{-1}]×10^{-3}	K [Å^{-1}]×10^{-3}	L [Å^{-1}]×10^{-3}
180 K	5.53 ± 0.03	15.29 ± 0.05	7.43 ± 0.37
10 K	5.84 ± 0.09	16.64 ± 0.06	7.82 ± 0.31
Ratio $\xi^{-1}_{10}/\xi^{-1}_{180}$	1.06 ± 0.02	1.09 ± 0.01	1.05 ± 0.05

Table 4.1: *Inverse Correlation lengths of the (1.75, 0.25, 0) Jahn-Teller order peak at 180 K and 10 K*

From Table 4.1 it can be determined that the inverse correlation lengths at 10 K and 180 K are very similar and there appears to be no significant change in correlation length between the high temperature and low temperature regimes despite the decrease in intensity. This is consistent with the behaviour observed for the Jahn-Teller order in the half doped system in which there is also virtually no change in correlation length between the high and low temperature regimes. The Jahn-Teller order was calculated to have reduced in intensity by a factor of five at 10 K compared to the intensity at 180 K. It should be noted that this reduction is not as great as that observed in the x = 0.5 doped system where there is a reduction in intensity by a factor of six.

The temperature dependence of the (1.75, 0.25, 0) Jahn-Teller order reflection was measured as a function of temperature in the range 10 – 230 K in the H and K directions. It was very difficult to fit the peaks in the L direction due to the presence of more than one crystallite in the sample but at each temperature scans were carried out in the L direction to ensure that the data were taken on the same crystallite throughout the temperature range. The temperature dependence of the integrated intensity in the H and K directions is shown in Figure 4.7.

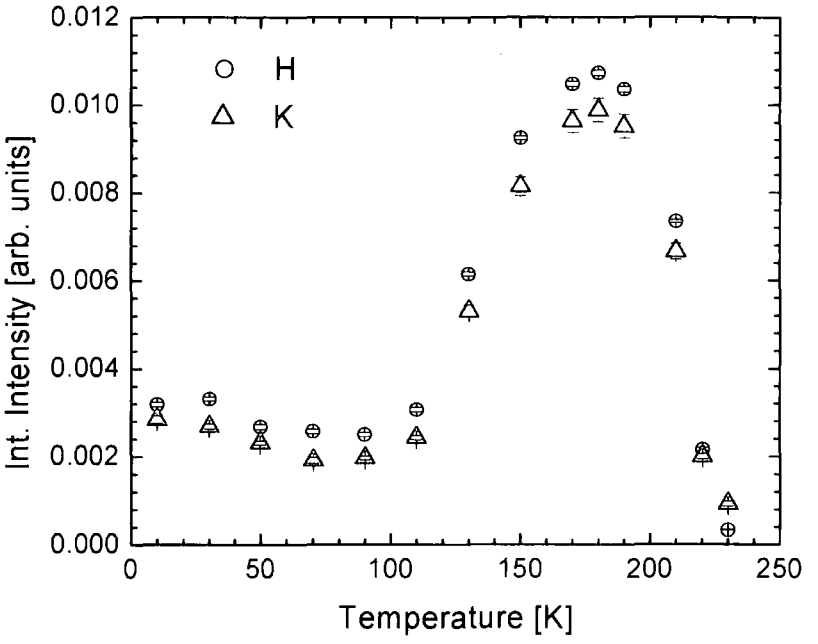

Figure 4.7: *Integrated Intensity as a function of temperature in the H and K directions for the (1.75, 0.25, 0) Jahn-Teller order peak.*

At 10 K the Jahn-Teller order peak is relatively weak indicating that the magnitude of the Jahn-Teller order is small. On heating from 10 K the integrated intensity began to decrease slightly and reached a minimum at 70 K and stayed constant until 90 K. This was similar to the half doped system but it should be noted the reduction in intensity in the low temperature regime was not as significant as that observed in the x = 0.5 system. The Jahn-Teller order was still strong enough to be easily observed throughout the low temperature regime – evidence that, as in the 0.475 and 0.5 samples the charge ordered state is not re-entrant. As the temperature was increased above 90 K the intensity began to increase sharply and this continues until a temperature of 180 K. The maximum in peak intensity corresponds to the antiferromagnetic ordering temperature. As the temperature was increased above 180 K the integrated intensity began to decrease sharply until no long range Jahn-Teller order was observable above background at 230 K, the same transition temperature as in the x = 0.5 sample.

Before discussing the behaviour of the inverse correlation length, the experimental geometry needs to be considered. Table 4.1 shows the inverse correlation lengths. It can be clearly seen that the inverse correlation length is significantly smaller in the H direction than the K direction. However, the greatest instrumental resolution is obtained when scanning through the Q_Z direction and this corresponds to the H direction in the experimental setup utilised. The L direction is equivalent to the Q_X direction in this alignment and the K direction is at 90° to the Q_Z direction. Hence, in this experimental alignment the highest resolution was in the H direction and poorest resolution was in the K direction. For this reason the Jahn-Teller order shows a smaller inverse correlation length in H direction than the K direction and the measurements in this direction are significantly more accurate.

The temperature dependence of the inverse correlation length in the H direction is shown in Figures 4.8.

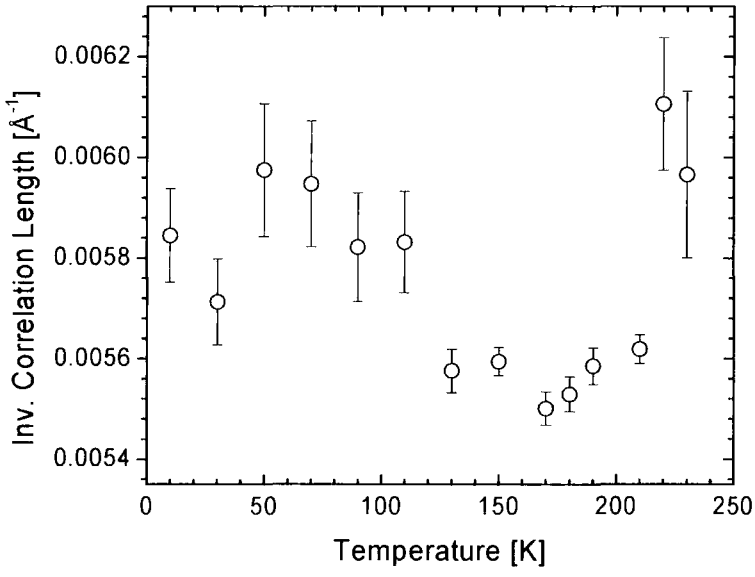

***Figure 4.8**: Inverse correlation length as a function of temperature of the (1.75, 0.25, 0) Jahn-Teller peak in the H direction.*

The error bars shown in Figure 4.8 are 1σ and while there is an overlap between all points when the error bars are increased to 3σ we cannot conclusively determine whether the inverse correlation length shows a variation with temperature or not. If there is a variation in the inverse correlation length with temperature it is small and in the low and high temperature regions the Jahn-Teller order remains highly correlated and in this respect it is similar to the x = 0.5 doped system. In the K direction no change in the inverse correlation length was observed but the instrumental resolution is not good enough to observe any change in inverse correlation length. From the comparison in the L direction at 10 and 180 K and the similarity with the 0.5 system we can postulate that the same behaviour occurs with respect to the inverse correlation length in the L direction as in the H and K directions. These results indicate that while the magnitude of the Jahn-Teller distortion varied significantly with temperature the Jahn-Teller order remains highly correlated in both the high and low temperature regions. This was similar behaviour to that observed in the x = 0.5 doped sample.

The position of the Jahn-Teller order peak was measured as a function of temperature in the H and K directions to determine the commensurability of the structural modulation. The highest resolution was in H and hence, if there was any variation in the commensurability with temperature it would be most observable in this direction. No significant change in position was observed in the K or H directions. This provides evidence that the Jahn-Teller order remains at a fixed commensurate position and shows no variation with temperature and this behaviour is consistent with the half-doped sample.

Charge Order

The charge order was located at the expected modulation of (0.5, 0.5, 0) at 180 K. The strongest reflection was located at a modulation of (1.5, 0.5, 0) and this was measured as a function of temperature. The peak was scanned in the H, K and L directions of reciprocal space at 180 K. The charge order peak fitted a Gaussian lineshape in the H direction and the Lorentzian squared lineshape in the K direction i.e. it fitted the same lineshapes as the Jahn-Teller order. It was not possible to fit the data in the L direction

due to the presence of more than one crystallite but it was ensured that the data was taken on the same crystallite at high and low temperatures. The charge order was located at 10 K and utilising the parameters from the fits at 180 K it was again fitted to the same lineshapes. The inverse correlation lengths of the (1.5, 0.5, 0) charge order peak are shown in Table 7.2 for 10 K and 180 K. Similarly to the Jahn-Teller order there is no difference between the inverse correlation length in either the high or low temperature regimes beyond error. Hence, despite the decrease in the intensity of the charge order in the low temperature regime there is no decrease in the degree of correlation

	H[Å^{-1}]×10^{-3}	K[Å^{-1}]×10^{-3}
180 K	4.39 ± 0.08	13.68 ± 0.29
10 K	4.23 ± 0.31	14.01 ± 0.76
Ratio $\xi^{-1}_{10}/\xi^{-1}_{180}$	0.96 ± 0.07	1.02 ± 0.06

Table 4.2: *Inverse correlation lengths of the (1.5, 0.5, 0) CO peak at 10 K and 180 K*

The behaviour of the integrated intensity, inverse correlation length and position were measured as a function of temperature in the H and K directions. Once again due to crystallites in the sample it was not possible to carry out measurements of the temperature dependence in the L direction but it was ensured measurements were carried out on the same crystallite throughout. The temperature dependence of the integrated intensity in the H and K directions is shown in Figure 4.9. The charge order, like in the x = 0.5 sample, is observable at all temperatures but there is a considerable reduction in the intensity by a factor of five. On heating from 10 K to 70 K it shows a slight decrease in intensity similar to the Jahn-Teller order. This decrease in intensity is not as large as observed in the x = 0.5 doped sample but the overall behaviour is very similar to the x = 0.5 sample. The intensity minimises at 70 K and remains constant to 90 K. As the temperature is increased beyond 90 K the integrated area increases sharply, mirroring the behaviour of the Jahn-Teller ordering and it reached a maximum intensity at 180 K. Above 180 K the charge order decreased sharply and was not observable from the background at 230 K.

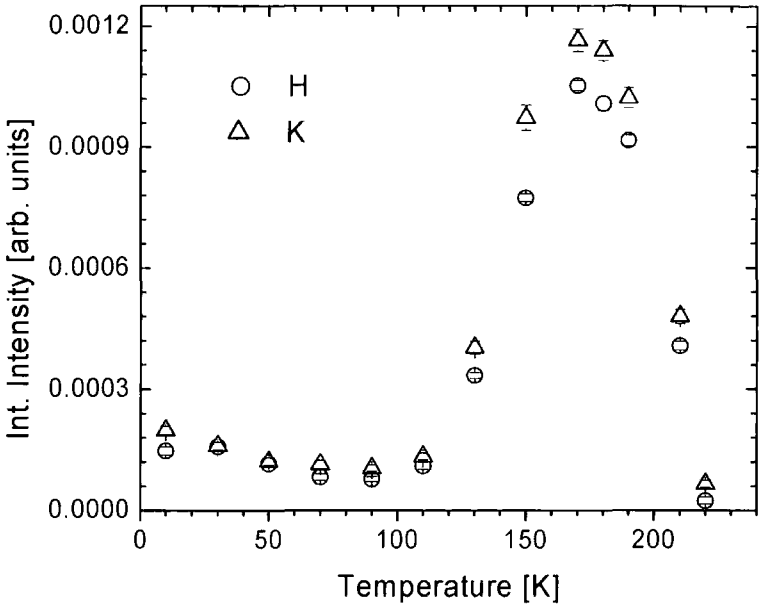

Figure 4.9: *Integrated intensity as a function of temperature in the H and K directions for the (1.5, 0.5, 0) charge order peak.*

The temperature dependence of the inverse correlation length in the *H* and *K* directions was measured for the charge order and Figure 4.10 shows the behaviour of the inverse correlation length in the *H* direction. There does not appear to be any strong variation in the inverse correlation length of the charge order with temperature. Similar to the Jahn-Teller order the charge order remains highly correlated in both the high and low temperature regimes. The inverse correlation length in the *K* direction showed no change with temperature but in the *K* direction the resolution was not good enough to observe any changes in the inverse correlation length..

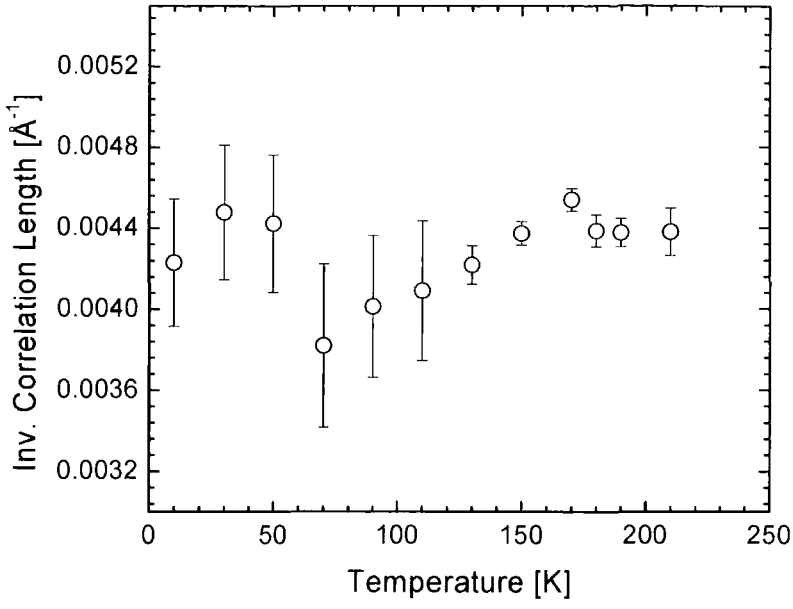

Figure 4.10: *Inverse correlation length as a function of temperature for the (1.5, 0.5, 0) charge order peak.*

The behaviour of the charge order in this sample is similar to that observed for the charge order in the half doped sample where it existed in a highly correlated state in both the high and low temperature regimes. The inverse correlation in the L direction was estimated to be similar in the high and low temperature regimes suggesting that the charge order remains three dimensional at all temperatures. Finally, the commensurability of the charge order was measured and no significant change in the position was observed showing that the charge order remains commensurate throughout the whole charge ordered phase.

To summarise, the Jahn-Teller/charge order state within the x = 0.55 doped system is the same as that in the x = 0.5 doped system. This is characterised by observation of the charge order in the high and low temperature regimes and the JTO/CO remaining commensurate and highly correlated at all temperatures. From the measurements by Dho *et al.* it can be determined that the charge order temperature is the same in the 0.5 and 0.55 systems and from the neutron measurements by Ling *et al.* of T_N it can be

determined to be the same in both systems. Our results are in agreement with these measurements and we conclude from that increasing the doping from 0.5 to 0.55 results in no change in the behaviour of the charge ordered state.

4.3.2 x = 0.60

The study on the x = 0.55 composition showed that the charge and Jahn-Teller order behave in the same way as in the x = 0.5 doped system. The x = 0.6 doped system is close to the 0.62 boundary where Dho *et al.* reported the system to show the collapse of the charge order state.

The sample was aligned and a UB matrix calculated using the (2, 0, 0) and (0, 0, 10) as the *or0* and *or1* reflections respectively. The x = 0.60 sample was cooled to 180 K and a search carried out at the modulations corresponding to the Jahn-Teller and charge order around the (2, 0, 0) Bragg peak. However, the behaviour of the Jahn-Teller and charge order was observed to be considerably different to that in the lower doped samples. Firstly, the Jahn-Teller and charge order peaks differed from the lower doped samples in having their maximum intensity at 210 K instead of approximately 180 K as in the x = 0.475, 0.5 and 0.55 doped systems. The most significant difference from the lower doped systems was that Jahn-Teller order and charge order peaks were observed at incommensurate positions in reciprocal space. At 210 K the Jahn-Teller order peaks were observed at a modulation of (0.215, 0.215, 0) and the charge order at (0.43, 0.43, 0) and not at the commensurate wavevectors of (0.25, 0.25, 0) and (0.5, 0.5, 0) respectively. The wavevector of the Jahn-Teller order is defined as (0.25-ε, 0.25-ε, 0) where ε is the incommensurability. Using this definition it can be determined that at low temperatures the incommensurability is larger than at high temperatures. Scans were carried out in the three principle directions of reciprocal space on the Jahn-Teller order at 210 K. The Jahn-Teller order was found to fit a Gaussian lineshape in the H and K directions and a Lorentzian squared lineshape in the L direction. These fits are shown in Figure 4.11.

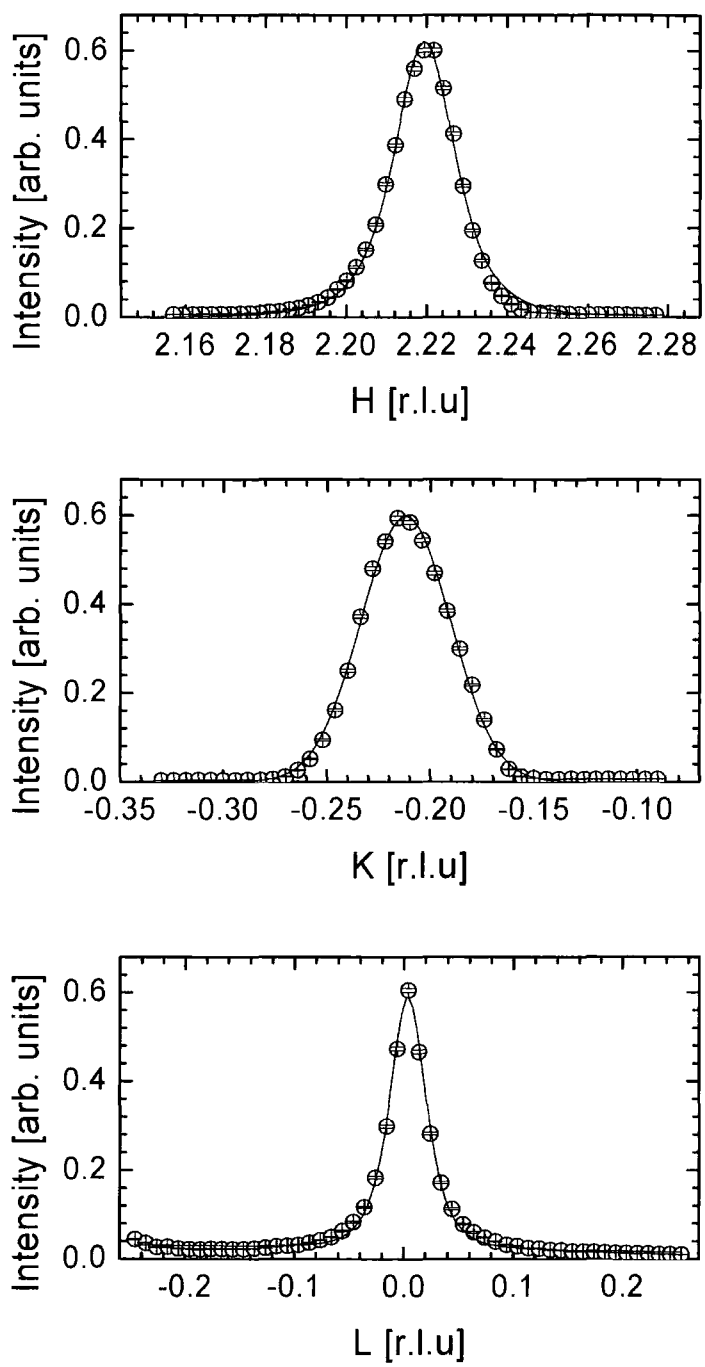

***Figure 4.11**: Scans through H, K and L directions of the (2.25-ε, -0.25+ε, 0) Jahn-Teller peak. The solid lines show the lineshapes fitted to the experimental data.*

The sample was then cooled to 10 K and the Jahn-Teller order peak was again located. The Jahn-Teller order was weaker by a factor of approximately 20 compared to the intensity at 210 K, which was a significantly larger decrease than in the lower doped compositions. Remarkably the wavevector modulation of the Jahn-Teller order had decreased to a modulation of (0.19, 0.19, 0) around the Bragg peaks after correcting for thermal expansion. Scans were again carried out on the Jahn-Teller order in the *H*, *K* and *L* directions of reciprocal space. As at 210 K the Jahn-Teller order was observed to fit the Gaussian lineshape in the *H* direction and the Lorentzian squared lineshape in the *K* and *L* directions. Table 4.3 shows a comparison of the inverse correlation lengths in the *H*, *K* and *L* directions for the (2.25-ε, -0.25+ε, 0) Jahn-Teller peak at 210 K and 10 K.

	$H[Å^{-1}]\times10^{-2}$	$K[Å^{-1}]\times10^{-2}$	$L[Å^{-1}]\times10^{-2}$
210 K	1.37 ± 0.03	3.99 ± 0.05	3.58 ± 0.06
10 K	1.57 ± 0.06	4.54 ± 0.07	4.64 ± 0.16
Ratio $\xi^{-1}_{10}/\xi^{-1}_{210}$	1.15 ± 0.03	1.14 ± 0.02	1.30 ± 0.04

***Table 4.3**: Inv Correlation lengths of the (2.25-ε,- 0.25+ε, 0) JT peak at 210 K and 10 K.*

Comparing the inverse correlation lengths at 210 K and 10 K shows there is a slight increase at low temperature accompanying the decrease in intensity and this differs from the behaviour observed in the 0.5 and 0.55 samples. This increase is largest in the *L* direction indicating at low temperature the Jahn-Teller order is more two dimensional in nature.

The (2.25-ε, -0.25+ε, 0) reflection was measured as a function of temperature in the temperature range 10 K – 300 K. Scans were taken along the *H*, *K* and *L* directions of reciprocal space using triple-axis geometry. In this experimental geometry the *H* direction corresponds to Q_z and the *L* direction to Q_x and in these two directions the resolution is high. The *K* direction is at approximately 90° to the Q_z direction and in this geometry the poorest resolution is in the *K* direction i.e. the χ direction. A comparison between the inverse correlation length of the (2, 0, 0) Bragg peak and the Jahn-Teller order revealed that the instrumental resolution was sufficient in the *H* and *L* directions to quantitatively determine changes in the inverse correlation length. .

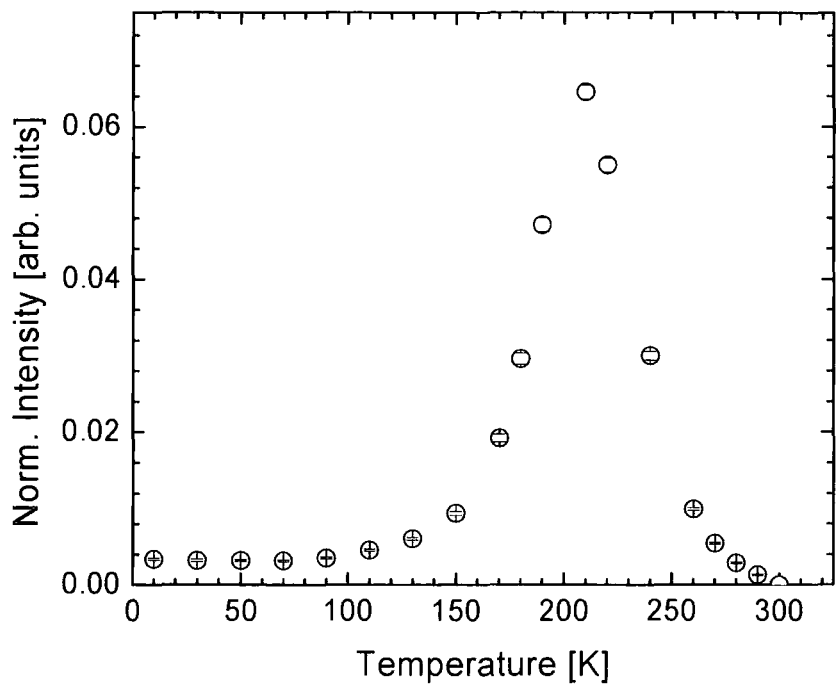

Figure 4.12: *Integrated intensity as a function of temperature in the H direction for the (2.25-ε, -0.25+ε, 0) JT order peak*

The integrated intensity in the *H* direction is shown as a function of temperature in Figure 4.12. On heating from 10 K the integrated intensity remains relatively constant with no increase in intensity in the range 10 – 110 K. As the temperature is increased above 110 K the integrated intensity begins to increase gradually up to 150 K. As the temperature is increased above 150 K there is a sharp increase in the integrated intensity and this continues before reaching a maximum at 210 K which is approximately 20 times greater than that at 10 K. This difference is significantly larger than the factor of ~ 6 observed in the lower doped samples. The intensity then decreases sharply as the temperature is increased above 210 K, and at 290 K it cannot be observed above background. The same behaviour is observed in the *K* and *L* directions and this is shown in Figure 4.13.

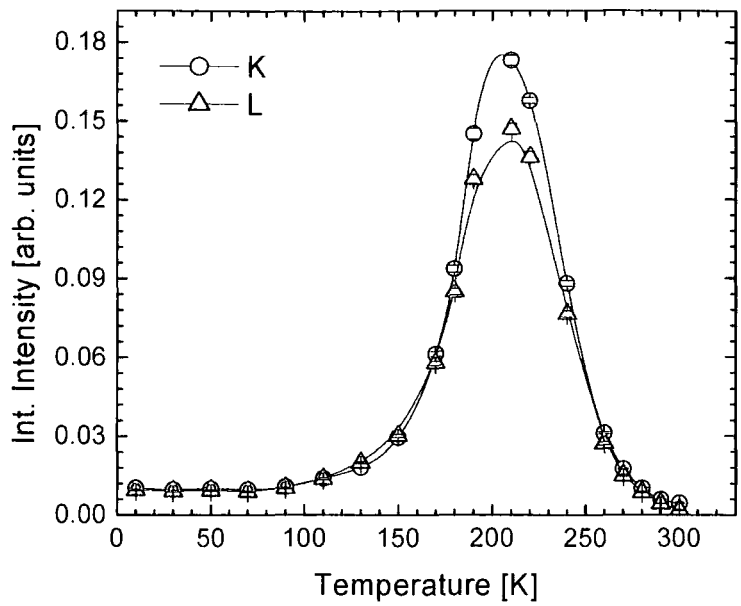

Figure 4.13: *Integrated intensity as a function of temperature in the K and L directions of the (2.25-ε, -0.25+ε, 0) JT order peak. The circles show the data along the K direction and the triangles along the L direction. Solid Lines are guide to the eye.*

We next discuss the behaviour of the incommensurability as a function of temperature. In the x = 0.5 and 0.55 samples there was no significant change in the position of the Jahn-Teller order with temperature. However, in the 0.475 sample in the low doped regime the Jahn-Teller order was measured to be slightly incommensurate with $\varepsilon = 0.004$. In the x = 0.6 sample a significantly larger variation in the incommensurability as a function of temperature was observed and significantly larger than observed in any bilayer manganite previously. The temperature dependence of the position in the H direction for the (2.25-ε, -0.25+ε, 0) peak is shown in Figure 4.14. The incommensurability was accurately calculated by measuring the position of the opposite reflection at (1.75+ε, 0.25-ε, 0) as a function of temperature and the (2, 0, 0) Bragg peak. Despite the inferior instrumental resolution in the K direction it was still possible to qualitatively measure the position of the peak as a function of temperature which is shown in Figure 4.15.

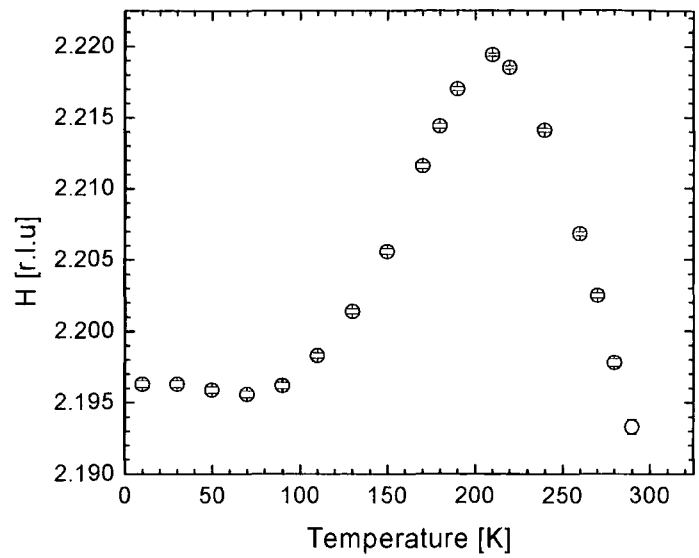

Figure 4.14: *Position of the (2.25-ε, -0.25+ε, 0) JT order peak as a function of temperature in the H direction*

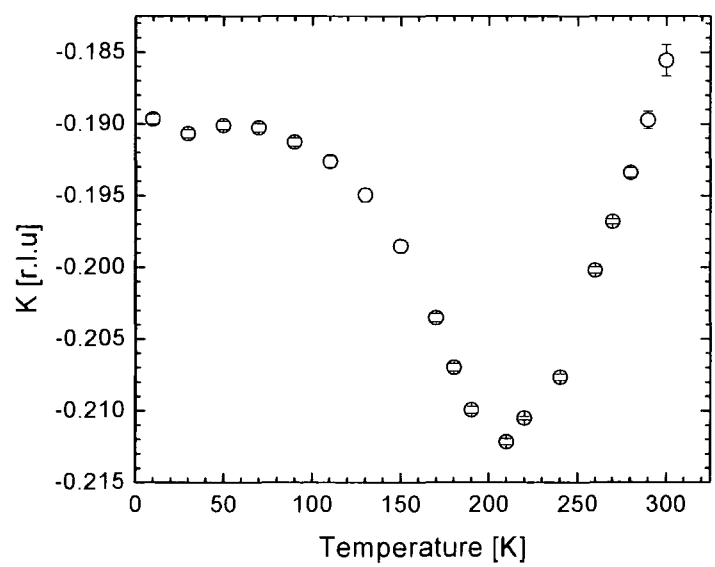

Figure 4.15: *Position of the (2.25-ε, -0.25+ε, 0) JT order peak as a function of temperature in the K direction*

At 10 K the Jahn-Teller order was measured to occur at an incommensurate modulation of (0.195, 0.195, 0). Referring to Figure 4.13 on heating there is no variation in the incommensurability in the temperature range 10 – 100 K. As the temperature is increased above 100 K the incommensurability begins to decrease. This decrease in the incommensurability continued, until maximising at a modulation of (0.218, 0.218, 0) at 210 K which is also the temperature where the intensity is at its maximum. As the temperature is increased above 210 K the incommensurability begins to decrease until the Jahn-Teller order disappears at 290 K. Figure 4.16 shows both the position and intensity of the (2.25-ε, -0.25+ε, 0) Jahn-Teller order reflection.

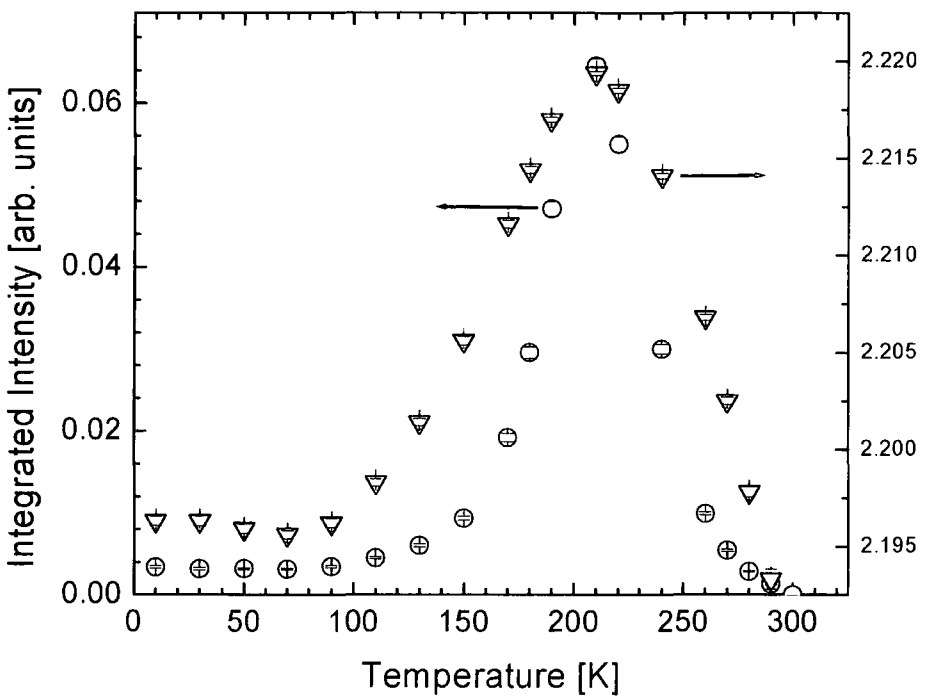

Figure 4.16: *Temperature dependence of the integrated intensity and position of the (2.25-ε, -0.25+ε, 0). The circles show the integrated intensity and the triangles show the position in the H direction.*

Comparing the data in Figure 4.16 a clear correlation between the integrated intensity and the position of the Jahn-Teller order can be determined. Below 100 K there is no change in either the intensity or the position. At 100 K the integrated intensity begins to increase whilst the incommensurability begins to decrease and this continues until 210 K. As the intensity decreases above 210 K the incommensurability also increases. From these observations we postulate that, as the intensity is increasing, the Jahn-Teller order is attempting to move towards the commensurate modulation of (0.25, 0.25, 0). This is the most stable configuration for the Jahn-Teller/Charge order because it is commensurate with the lattice. Possible reasons for this behaviour will be discussed in section 4.4.

The inverse correlation length was measured as a function of temperature in the *H, K* and *L* directions. As discussed previously the highest experimental resolution was in the *H* direction and measurements on the (2, 0, 0) Bragg peak determined that the instrumental resolution was sufficient to obtain quantitative measurements in the *H* and *L* directions but it is possible to obtain qualitative measurements in the *K* direction.. The variation of the inverse correlation length in the *H* direction with temperature is shown in Figure 4.17 and those in the *K* and *L* directions in Figure 4.18. As the temperature was increased from 10 – 100 K there was no change in the inverse correlation length. As the temperature is increased in the region 100 – 150 K there is a slight increase in the inverse correlation length observed in all three directions. This increase corresponds to the region in which the intensity begins to increase and the incommensurability begins to decrease. A possible explanation for this is that the initial movement of the Jahn-Teller order from the fixed position in the low temperature region causes a slight destabilisation of the Jahn-Teller order. As the temperature is increased above 150 K there is a decrease in the inverse correlation length and this occurs at the point where the integrated intensity begins to increase at a greater rate. The inverse correlation length continues to decrease until reaching a minimum at approximately 210 K –the point where the integrated intensity maximises and incommensurability is minimised. Above 210 K the inverse correlation length increases as the Jahn-Teller order becomes weaker and this continues until the Jahn-Teller order disappears.

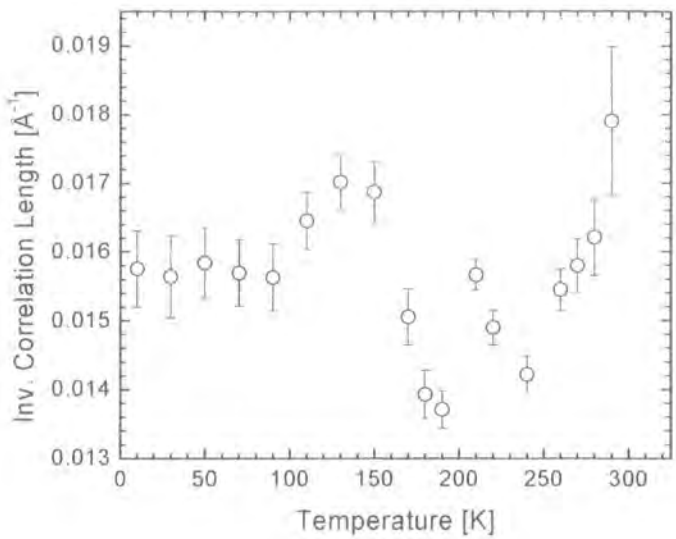

Figure 4.17: *Inverse correlation length as a function of temperature in the H direction for the (2.25-ε, -0.25+ε, 0) JT order peak.*

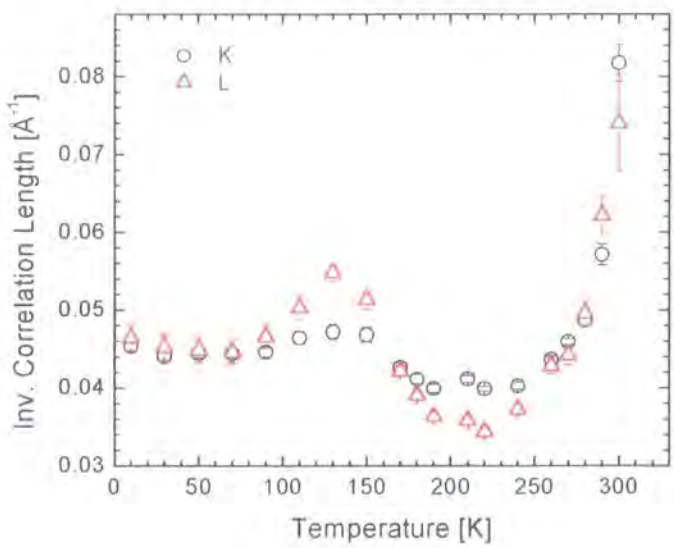

Figure 4.18: *Inverse correlation length as a function of temperature in the K and L directions for the (2.25-ε, -0.25+ε, 0) JT order peak which are represented by circles and triangles respectively.*

To summarise, the Jahn-Teller order in the x = 0.6 sample shows a clear change in behaviour from the x = 0.5 and 0.55 samples. The most significant difference is the fact that the Jahn-Teller order is incommensurate at all temperature and the magnitude of the incommensurability varies with temperature. At low temperatures the Jahn-Teller order is weak, poorly correlated and the incommensurability is large. As the temperature is increased above 100 K the Jahn-Teller order becomes stronger, more correlated and moves towards the commensurate wavevector with the intensity and position maximising at 210 K. Above 210 K the intensity decreased and the Jahn-Teller order became more incommensurate before disappearing at 290 K – a significantly higher temperature than in the x = 0.5 and x = 0.55 samples. A possible model will be described in conjunction with the charge order in section 4.4.

Charge Order

The charge order was found to be extremely weak and could only be observed in the temperature range 150 - 250 K – corresponding to the region where the Jahn-Teller order is strong. At 210 K the charge order was located at an incommensurate modulation of approximately (0.43, 0.43, 0) which, as expected, is double the modulation of the Jahn-Teller order at that temperature. The strongest charge order peak was observed at a position of (1.57, -0.43, 0). The charge order was extremely weak with an intensity approximately 200 times weaker than the corresponding Jahn-Teller peak. This is significantly weaker than the lower doped samples where the charge order is only a factor of 30 times weaker. The peak was scanned in the *H*, *K* and *L* directions at 210 K to obtain the inverse correlation lengths and these values are shown in Table 4.4

	H [Å^{-1}]×10^{-2}	K [Å^{-1}]×10^{-2}	L [Å^{-1}]×10^{-2}
210 K	2.04 ± 0.10	3.86 ± 0.10	8.36 ± 0.40

***Table 4.4**: Inverse Correlation lengths of the (1.57, -0.43, 0) CO peak at 210 K.*

The measurements of the charge order revealed it to be two dimensional in nature with a greater inverse correlation length in the *L* direction i.e. between the MnO_2 planes, than in the *H* and *K* directions.

The (1.5+2ε, -0.5+2ε, 0) charge order peak was measured as a function of temperature in the temperature range 150 – 250 K. At each temperature scans were carried out in the *H*, *K* and *L* directions and fitted to provide measurements of the intensity, position and inverse correlation length. The integrated intensity in the *H*, *K* and *L* directions is shown in Figure 4.19.

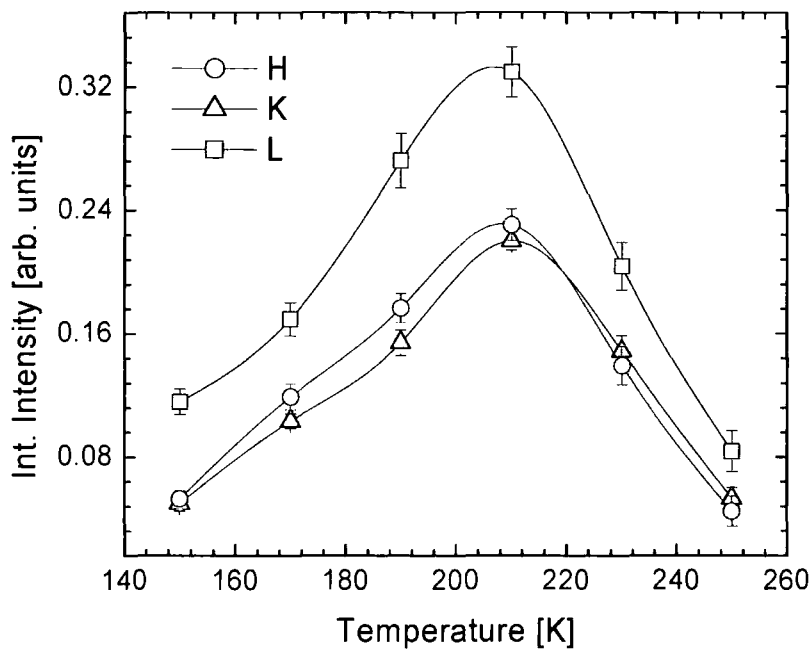

***Figure 4.19**: Integrated intensity as a function of temperature for the CO peak in the H, K and L directions. Solid lines are guides to the eye and error bars were obtained from the fits.*

The integrated intensity of the charge order reflection clearly maximises at 210 K which is the same temperature as for the Jahn-Teller order. Below 150 K and above 250 K the charge order could not be observed above background. The inverse correlation

length shows no change in the temperature range over which the charge order is observable. Due to the limited temperature range over which the charge order was observable it was not possible to determine the full behaviour of the incommensurability. The position in the *H* direction is shown in Figure 4.20.

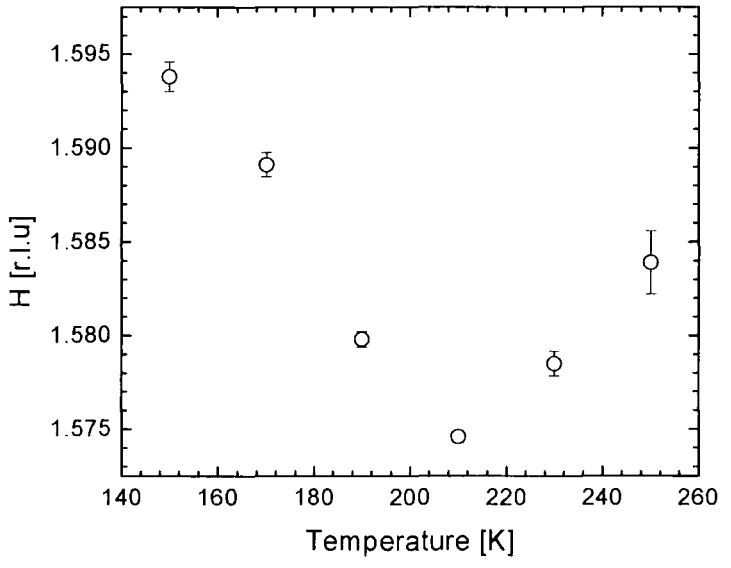

Figure 4.20: *Position of the (1.5+2ε, -0.5+2ε, 0) CO peak as a function of temperature.*

Even in this small temperature range there is a significant change in the position of the charge order peak. Similar to the Jahn-Teller order peak moving towards the commensurate modulation of (0.25, 0.25, 0) we observed that the charge order is moving towards the stable commensurate modulation of (0.5, 0.5, 0) in the range 140 - 210 K. The existence of the Jahn-Teller order in the low temperature regime is evidence that the charge order exists in this region but it is too weak to be observed by us. Using the position of the Jahn-Teller order we calculate that the charge order exists at a modulation of approximately (0.4, 0.4, 0) in the low temperature regime and therefore it can be determined that the charge order shows a change in position double that of the Jahn-Teller order. The charge order is similar to that in the x = 0.475 system in that it can only be observed in the high temperature regime. The results of the charge and Jahn-Teller order will now be discussed and a possible model suggested.

4.4 Discussion of the 0.6 Results

The temperature dependence of the integrated intensity, inverse correlation length and position is summarised in Figure 4.21. There are four clear regions for the Jahn-Teller ordering. In region I between 10 and 100 K the Jahn-Teller ordering is weak and poorly correlated. It is observed at a modulation of (0.195, 0.195, 0) which is close to a modulation of (0.2, 0.2, 0) expected from the ratio of Mn^{3+} to Mn^{4+} ions in the x = 0.6 system and the modulation measured by Li[4]. In this region the charge order is too weak to be observed and in this respect it is similar to the low temperature regime in the x = 0.475 doped sample in which the charge order is also too weak to be observed. In region II between 100 and 150 K the integrated intensity begins to increase - clear evidence of an increase in the elongation of the Mn - O bonds in the Mn^{3+} octahedra. Consistent with the lower doped samples the Jahn-Teller order begins to increase at the point where the intensity of the magnetic order begins to decrease. In this region the incommensurability starts to decrease towards the commensurate position of (0.25, 0.25, 0) in both the H and K directions. This initial movement appears to cause a destabilisation in the Jahn-Teller order evidenced by the increase in the inverse correlation length in this region. It is possible that there is competition between the state favoured by the doping level which maximises the distance between Mn^{3+} ions by coulombic repulsion and the commensurate checkerboard state which is the most stable pattern for the Jahn-Teller/charge order. As the temperature is increased into region III at 150 K there is a decrease in the inverse correlation length indicative that as the position of the Jahn-Teller approaches the commensurate modulation there is a stabilisation of the Jahn-Teller ordering. At 150 K there is also an associated increase in the gradient of the integrated intensity. The commensurability continues to increase with the intensity until both maximise at 210 K corresponding to the magnetic ordering temperature T_N. This was confirmed by SQUID magnetisation measurements by S. Giblin at University of Durham which are shown in Figure 4.22.

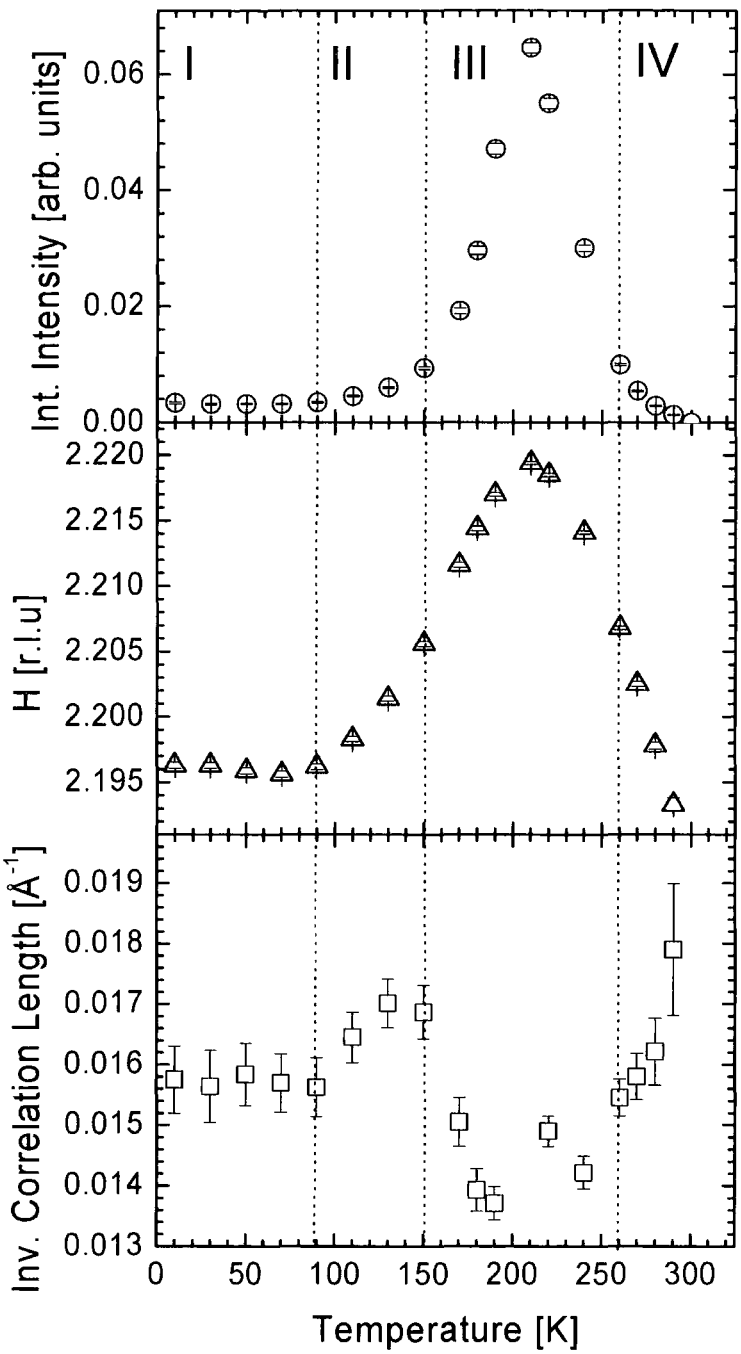

Figure 4.21: *Integrated intensity, position and inverse correlation length measured in the H direction of the (2.25-ε, -0.25+ε, 0) JT order peak as a function of temperature.*

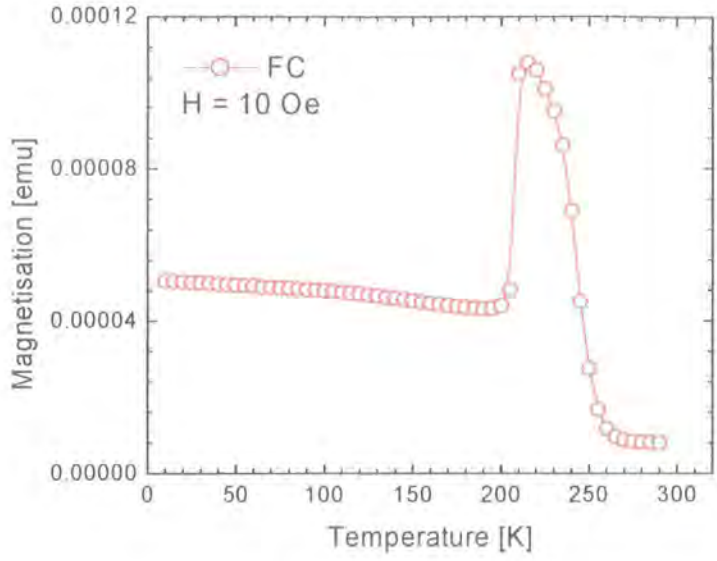

Figure 4.22: *Field cooled magnetisation data from the $x = 0.60$ sample under a field of 10 Oe. The red line is guide to the eye. These measurements give T_N as approximately 215 K.*

Above 210 K the intensity begins to decrease and this is accompanied by a decrease in the position and the inverse correlation length. This continues into region IV where the Jahn-Teller order is again weak, poorly correlated and is a large distance away from the commensurate position and above 290 K the JT order cannot be observed which agrees with the transition temperature of 280 K reported by Li *et al.*[4] and measurements by Dho *et al.*[1]

At its maximum the intensity of the JT order is similar to that observed in the lower doped systems. However, the decrease in intensity of the JT order from the high to low temperature regions is significantly larger than that in the lower doped systems. As discussed in the previous chapter the JT order superlattice reflections arise from the movement of the Mn^{4+} ions caused by the elongation of the Mn-O bonds associated with the cooperative Jahn-Teller distortion. In the low temperature regime the elongation of the Mn-O bonds decreases resulting in a decrease in the intensity of the JT order in the low temperature regime. In the $x = 0.60$ sample it is possible that the decrease in the Mn-O bond length is greater than in the lower doped systems but a decrease by a factor of 5

compared to the lower doped systems seems unlikely. However, in the x = 0.60 system there is an increase in the separation of the Mn^{3+} and hence, a decrease in the number of Mn^{3+} ions per unit cell and this combined with the decrease in the JT distortion could account for the greater intensity difference observed than in the lower doped samples.

The charge order could only be observed in region III between 150 and 250 K. Thus, the x = 0.60 system is similar to the x = 0.475 system in that the charge order can only be observed in the high temperature regime and not in the low temperature regime. The charge order in the x = 0.60 system was extremely weak in comparison with the lower doped systems. The charge order reflection is due to the electron density difference between the Mn^{3+} and Mn^{4+} ions; obviously the maximum intensity would occur when there is a 1:1 ratio of the two species and hence, an alternating pattern of Mn^{3+} and Mn^{4+} ions *i.e.* that observed in the half doped system. In the x = 0.6 system there are more Mn^{4+} ions than Mn^{3+} ions and the checkerboard pattern does not form even at 210 K where the intensity is at its maximum. The separation between the Mn^{3+} ions is larger than in the x = 0.5 system and hence, the charge density difference between Mn sites is smaller than that in the 0.5 system. As the Mn^{3+} ions move closer together the charge density difference between Mn sites increases and hence, the integrated intensity increases but because it never reaches the stable checkerboard configuration the intensity is significantly less than that in the x = 0.50 and 0.55 systems.

The change in the commensurability of the Jahn-Teller order is the largest observed in any bilayer manganite system. In the x = 0.475 sample a small incommensurability was observed of ε = 0.004 in the low temperature regime which suggested a long range modulation. In the three dimensional perovskite $Pr_{0.5}Ca_xSr_{0.5-x}MnO_3$ a small incommensurability is observed [7] and it was suggested that it was caused by the quasi-periodic defects known as discommensurations. However, the effect is so small the discommensurations could be separated by lengths approaching the domain size and the deviations could be attributed to domain boundaries. This is clearly not the case in the 0.60 sample in which the incommensurability is significantly larger with $\varepsilon \sim 0.05$ in the low temperature regime, we therefore postulate that the resulting pattern is caused by discommensurations in the charge order pattern. In the x = 0.6 doping level the ratio of Mn^{3+} to Mn^{4+} ions is 2:3 this corresponds to a modulation of (0.2, 0.2, 0) for the JT

ordering and (0.4, 0.4, 0) for the CO pattern which is in approximate agreement with the measurements of the JT ordering at low temperature. A proposed schematic of the arrangement in one dimension at low temperature is shown in Figure 4.23.

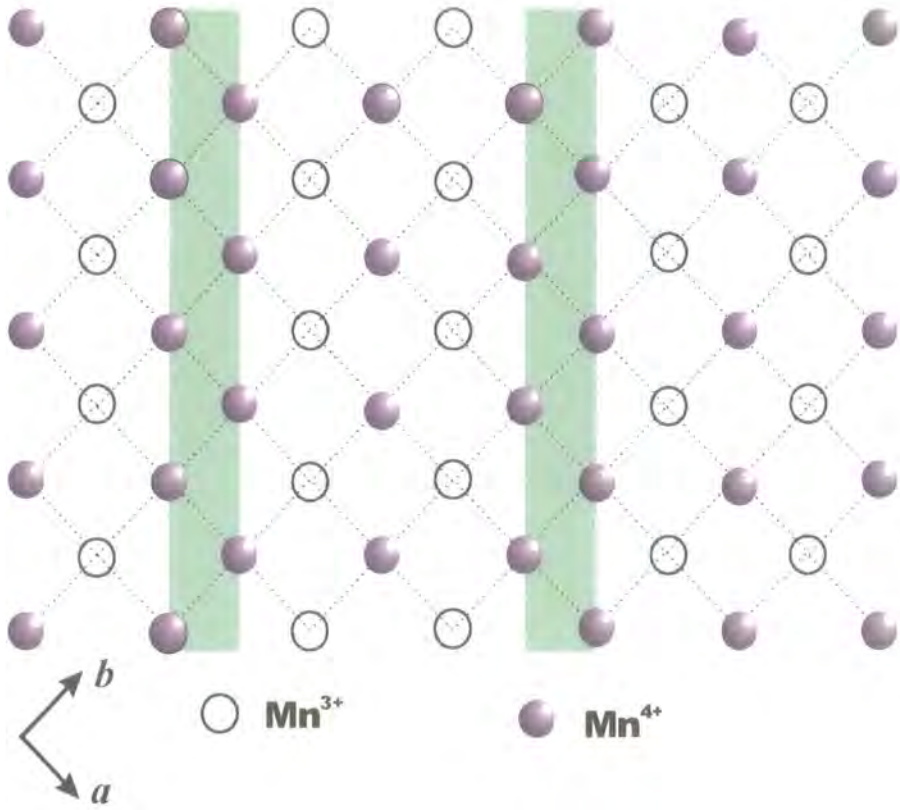

Figure 4.23: *Proposed schematic of the charge order pattern in the x = 0.6 sample with two Mn^{3+} ions for every three Mn^{4+} ions.*

In the model proposed there are regions of the checkerboard order separated by a discommensurations shown by the shaded regions at regular intervals giving a modulation of (0.2, 0.2, 0) at low temperature. It is not possible to show a quantitative model of the JTO/CO state as the commensurability increases because the Jahn-Teller and charge order exist at incommensurate wavevectors. In the above model we propose there is a reorganisation of the holes which results in an increase in the separation between the discommensurations and hence, an increase in the commensurability. Figure

4.16 provides strong evidence that it is the increase in the Jahn-Teller distortion that drives the increase in the wavevector towards the commensurate position.

The charge ordering temperature of 290 K is higher than that in the 0.55, 0.5 and 0.475 systems and it is an indication that the charge/Jahn-Teller ordered state is thermally more stable than in the lower doped samples. This is in agreement with the transport data reported by Dho *et al.* [1] where they report an increase in the charge ordering temperature in the x = 0.6 sample in comparison with the lower doped samples and the electron diffraction measurements by Li *et al.*[4]. This disagrees with the powder diffraction measurements by Mitchell *et al.*[3] who report the same behaviour in the x = 0.6 system as that in the 0.5 system with the intensity maximising at 160 K. It is possible that the there is a mix of two phases in the powder data and because the checkerboard pattern is the most stable configuration for the charge order it is this that is observed.

To summarise, there is a clear change in behaviour between the 0.55 and 0.60 samples. The 0.55 shows the same behaviour as the 0.5 system but in the 0.6 system the charge and Jahn-Teller order exist at incommensurate wavevectors and the position varies as a function of temperature. In the low temperature region below 100 K the Jahn-Teller order is weak, poorly correlated and the incommensurability is large and in addition the charge order is too weak to be observed. Between 150 K and 250 K the Jahn-Teller order is strong, well correlated and the incommensurability is smaller and the charge order can be observed. The position of the Jahn-Teller order is directly related to the magnitude of the Jahn-Teller distortion with the modulation moving closer to commensurate the stronger the Jahn-Teller order becomes. As in the x = 0.475 system the onset of the *A*-type antiferromagnetic order causes a much greater destabilisation in the charge order than in the x = 0.5 and 0.55 systems. This is presumably due to the stabilisation effect from the interaction with the lattice that occurs at the commensurate position that is absent in the incommensurate x = 0.60 system.

4.5 Conclusions

In summary high energy x-ray scattering has been used to study the Jahn-Teller and charge order in the bilayer manganite with x = 0.55 and x = 0.60.

There are significant differences between the ordered states in the 0.55 and 0.60 systems In the x = 0.55 doped system the Jahn-Teller order and the charge order exhibits the same behaviour as in the 0.50 doped system despite the fact that there is no longer a 1:1 ratio of Mn^{3+} to Mn^{4+} ions. The charge order is observed in the low temperature regime and there is no decrease in the correlation of the Jahn-Teller or charge order that accompanies the decrease in the intensity. In the 0.60 system there is a significant difference in the ordered state and the Jahn-Teller and charge order are not observed at commensurate wavevectors. This is a result of the fact there are 50 % more Mn^{4+} ions than Mn^{3+} ions which means that the stable checkerboard pattern cannot form and a model is proposed in which there are discommensurations in the charge order pattern. The position of the Jahn-Teller and charge order is not constant as a function of temperature and the position is directly linked to the intensity of the Jahn-Teller ordering. Between 10 – 100 K the Jahn-Teller order is weak and the distance from the commensurate position is large. The increase of the Jahn-Teller order from 100 - 210 K directly matches the increase in the position towards the commensurate (0.25, 0.25, 0) position. In the model proposed this occurs by a reorganisation of the holes resulting in an increase in the separation of the discommensurations and hence, an increase in the wavevector of the Jahn-Teller order. Unlike the x = 0.55 system the 0.60 system can be divided into low, intermediate and high temperature regions; in the low temperature region the Jahn-Teller order is weak, poorly correlated and the incommensurability is large. In the region from 150 – 250 K the Jahn-Teller order is intense, well correlated and the size of the incommensurability is small. The charge order cannot be observed in the low temperature regime and even in the intermediate regime it is very weak because the optimum checkerboard pattern does not form. Above 250 K the Jahn-Teller order is again weak and poorly correlated and above 290 K there is no long range Jahn-Teller order. The observation of the Jahn-Teller order below 150 K and above 250 K is evidence that the system is charge ordered it is just too weak to be observed. The results

demonstrate that the most stable configuration for the JTO/CO is the commensurate checkerboard pattern.

4.6 Future Work

The x = 0.575 system will be studied in order to determine the behaviour of the charge and Jahn-Teller order at a doping level between the 0.55 and 0.60 systems. High resolution TEM measurements would allow measurements of the charge distribution of the 0.60 sample in the high and low temperature regimes and compare the validity of the predicted discommensuration model.

The bi-layer system has been successfully studied using single crystal x-ray diffraction in the doping regime $0.475 < x < 0.60$ and the next stage of the study will involve single crystal experiments in the doping regime $x > 0.62$. These measurements will allow an accurate phase diagram of the bi-layer system to be determined as a function of temperature and doping and allow any differences between the Ling and Dho measurements to be reconciled.

4.7 References

1 J. Dho, W. S. Kim, H. S. Choi, *et al.*, Journal of Physics - Condensed Matter **13**, 3655 (2001).

2 C. D. Ling, J. E. Millburn, J. F. Mitchell, *et al.*, Physical Review B **62**, 15095 (2000).

3 J. F. Mitchell, C. D. Ling, J. E. Millburn, *et al.*, Applied Physics A-Materials Science and Processing **74**, S1776 (2002).

4 J. Q. Li, L. Dong, L. H. Liu, *et al.*, Physical Review B **64**, 174413 (2001).

5 R. Kajimoto, H. Yoshizawa, H. Kawano, *et al.*, Physical Review B-Condensed Matter **60**, 9506 (1999).

6 S. B. Wilkins, P. D. Spencer, T. A. W. Beale, *et al.*, Physical Review B **67**, 205110 (2003).

7 Z. Jirak, F. Damay, M. Hervieu, *et al.*, Physical Review B **61**, 1181 (2000).

Chapter 5

Charge Glass Ordering in $La_{2-x}Sr_xNiO_4$ for x = 0.20, 0.225 and 0.25

5.1 Introduction

The nickelate system $La_{2-x}Sr_xNiO_4$ has attracted great interest and has been studied extensively due to its structural similarity with the high T_C cuprate system $La_{2-x}Sr_xCuO_4$. The general introduction to the nickelate system is discussed in Chapter 2. X-ray and neutron techniques have demonstrated that in the nickelate system the charge order state is strongest and most stable in the commensurate doped x = 1/3 system. As the doping is decreased away from this value the charge order becomes weaker and less correlated and there is a decrease in the charge order temperature. Ghazi *et al.* reported that in the 0.30 and 0.275 doped systems the charge order was present and is still strong and well correlated but weaker than in the 0.33 system and as the temperature was increased the charge order wavevector moved towards the stable 0.33 position.[1, 2] In this chapter the behaviour of the 0.20, 0.225 and 0.25 doped systems will be studied to provide a complete understanding of the behaviour of charge ordered state in the doping region $0.20 \leq x \leq 0.33$. The x = 0.20 has previously been studied with neutron diffraction by Sachan[3] and the x = 0.225 composition has been studied with neutrons by Tranquada[4] and high energy X-rays of 100 keV which provided bulk measurements of the system by Vigilante *et al.*[5] These studies reported the presence of weak, diffuse incommensurate charge stripes i.e. the charge order existed in a charge glass which is a clear contrast with the intense well correlated charge stripes with $x > 0.275$. By comparing the results from this study with those earlier studies it was hoped that it would be possible to gain a better understanding of charge ordering in the low doped nickelates. Of particular interest is the comparison between the bulk measurements of the 0.225 system by Vigilante *et al.* and

the near surface measurements from this study. The same 0.33 sample studied by Ghazi *et al.* at 12 keV was studied using energies of 130 keV to obtain bulk measurements of the system.[6, 7] There was a considerable difference reported in the properties of the charge order in the bulk compared to that at the surface. In the bulk the charge order was found to exist in a charge glass with an inverse correlation length approximately eight times greater than that measured at the surface where the charge order was highly correlated. It was postulated that the reason for this difference was that the charge stripes were pinned at the surface resulting in a stabilisation of the charge order pattern. In this study, by comparing our measurements with those at high energy on the 0.225 sample, it will be possible to determine if similar behaviour occurs in the lower doped nickelates.

The previous x-ray studies of the 0.33, 0.30 and 0.275 compositions with x-rays showed clear differences from the neutron studies. The neutron measurements showed that on heating the intensity of the charge order decreased gradually whereas the x-ray measurements showed an initial increase in the charge order intensity on heating. Ghazi *et al.* suggest possible reasons but no definite explanation has been given for this difference. X-rays are more sensitive to the charge order than neutrons because they scatter directly from the charge density and hence, higher resolution and intensity measurements are possible. No previous studies have been carried out on the 0.25 sample using any technique. Measurements on this sample will provide information on the charge order state in an intermediate region between the charge glass state in the low doped nickelates and the highly correlated charge order observed in the 0.275 doping and above.

5.2 Experimental procedure

High resolution x-ray scattering results were performed at the XMaS beamline at the European Synchrotron Radiation Facility (ESRF) in Grenoble and this has been discussed in Chapter 2.

In this study an incident photon energy of 1 Å (12.4 keV) was utilised which is close to the peak flux of the beamline and utilising an energy of 12.4 keV allowed a larger sample volume to be probed. A Ge (1, 1, 1) crystal was utilised as an analyser to provide high resolution triple axis measurements. High quality of crystals of $La_{2-x}Sr_xNiO_4$ with x = 0.25, 0.225 and 0.20 were grown at the University of Oxford using the floating zone technique. The doping in the three crystals was measured using electron probe microanalysis (EPMA) and they were determined as x =0.25 ± 0.010, x = 0.225 ± 0.010 and x = 0.20 ± 0.010

The crystal structure is tetragonal with the *I4/mmm* space group but for comparison with previous work the samples were indexed with the *F4/mmm* setting with lattice parameters $a \sim b$ = 5.4145 Å and c = 12.715 Å and this structure is shown in Figure 5.1. The crystals were pre-aligned on the laboratory diffractometer and cut with the <1, 0, 1> direction surface normal The crystals were mounted in a displex cryostat with the <1, 0, 1> and <0, 1, 0> directions in the scattering plane and cooled to a base temperature of approximately 12 K. A search was then carried out around the (4, 0, 4) (or (4, 0, -4)) Bragg peak for each sample. Reflections with the wavevector (2ε, 0, 1) were located around the (4, 0, 4) in each sample with ε = 0.25 in the 0.20 doped sample, ε = 0.28 in the 0.225 sample and ε = 0.279 in the 0.25 doped sample. The larger than expected commensurability value in the 0.225 sample was revealed to be due to excess oxygen doping which was measured as δ = 0.02 ± 0.01 by thermo-gravimetric analysis (TGA). The oxygen doping in the 0.20 and 0.25 samples was measured as δ = 0.00 ± 0.01 and from TGA measurements.

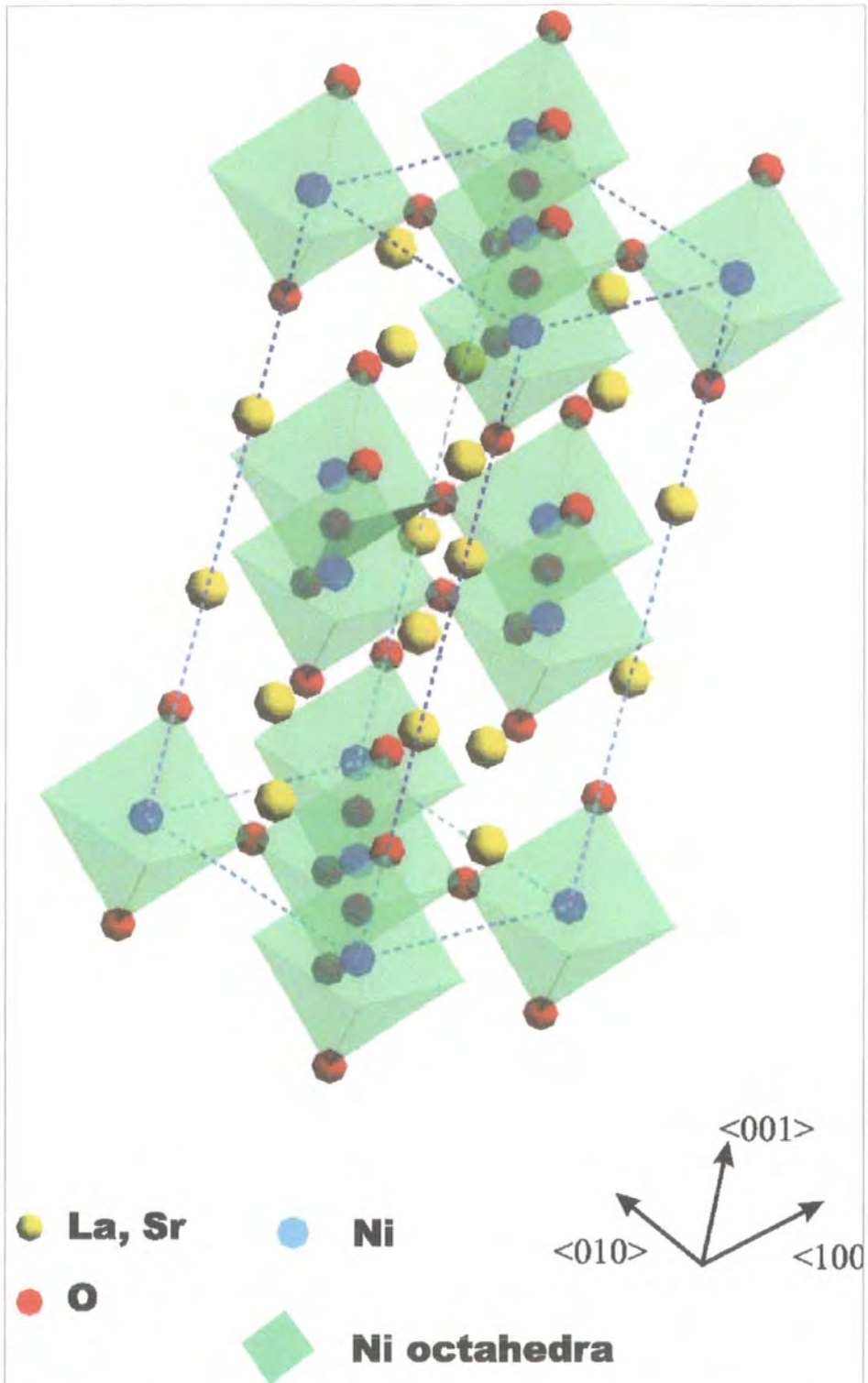

***Figure 5.1**: Crystal structure of the layered nickelate $La_{2-x}Sr_xNiO_4$*

5.3 Results

5.3.1 x = 0.20

The sample was aligned and a UB matrix obtained using the (4, 0, -4) and (4, 2 -4) as the *or0* and *or1* reflections respectively. The sample had a rocking curve width of approximately 0.02° which is very high quality for a transition metal oxide. Scans were carried out on the (4, 0, -4) Bragg peak in the *H*, *K* and *L* reciprocal space directions in this orientation and this gave the inverse correlation lengths of the Bragg peak as of 0.0020 $Å^{-1}$ in *H*, 0.0018 $Å^{-1}$ in *K* and 0.0047 $Å^{-1}$ in *L*.

The sample was cooled to base temperature of 10 K and a search was carried out around the (4, 0, -4) Bragg peak. Satellites which we attribute to charge ordering were located at position of (2ε, 0, 1) with ε = 0.255 at 10 K. The strongest of these reflections were located at (4.5, 0, -5), (4.5, 0, -3) and the (4, 0.5, -5). The strongest charge order reflection was the (4.5, 0, -3) reflection which had an intensity of only ~ 200 counts per second at 10 K which is very weak compared to the charge stripes in the x = 0.33 compound which were ~ 23,000 cps at base temperature. Scans were carried out in the *H*, *K* and *L* – the three principal directions of reciprocal space on the charge order reflections at base temperature and the data was fitted. The scans for the charge ordering and the associated fits in the three directions for the (4.5, 0, -3) reflection are shown in Figure 5.2 and as a comparison the scans for the (4, 0, -4) Bragg peak in the *H*, *K* and *L* directions are also shown. The charge order was found to fit a Lorentzian squared lineshape in all three reciprocal space directions.

Clearly the charge order is considerably broader and hence, less correlated in all directions than the crystal lattice. In the *H* and *K* directions the charge order was ~ 20 times less correlated than the crystal structure and in the in the *L* direction the charge order is ~ 50 times less correlated than the Bragg peak. These measurements are clearly indicative of the 2-D nature of the charge order present. This two dimensional nature is consistent with the charge ordering observed in the higher doped 0.275 – 0.33 samples.

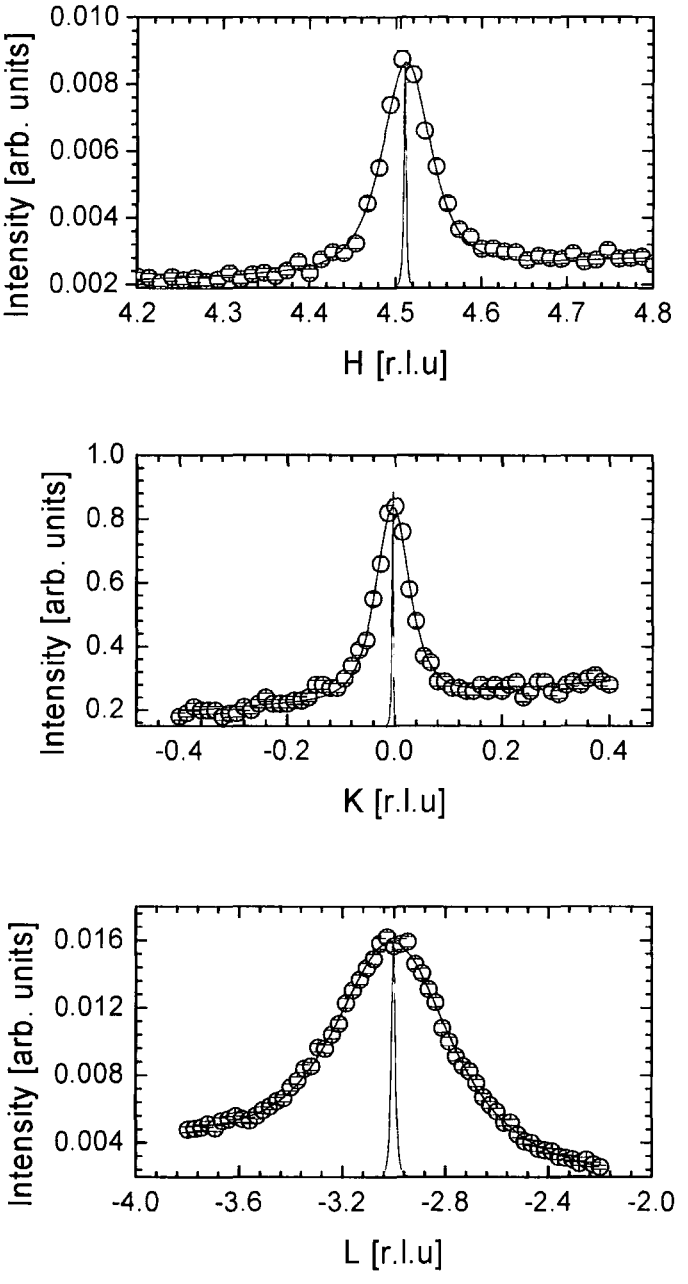

***Figure 5.2**: Scans through H, K and L directions of the (4.5, 0, -3) charge order peak. The black line is the fit to the experimental data using a Lorentzian squared lineshape and a linear background. The red line shows the corresponding scans of the (4, 0, -4) Bragg peak.*

However, unlike the higher doped samples the charge order is not only poorly correlated between planes but it was found to be poorly correlated within the planes as well. Table 6.1 shows a comparison of the inverse correlation lengths at 20 K for the 0.33 and 0.20 samples. As a comparison, the inverse correlation lengths of the (4, 0, -4) Bragg peak are also shown.

	H [Å^{-1}] × 10^{-3}	K [Å^{-1}] × 10^{-3}	L [Å^{-1}] × 10^{-3}
0.33	6.10 ± 0.07	2.66 ± 0.03	54.2 ± 0.4
0.20	41.8 ± 1.2	46.7 ± 1.3	209 ± 8
Bragg (4, 0, -4)	2.00 ± 0.04	1.80 ± 0.02	4.70 ± 0.10

***Table 5.1**: Inverse correlation lengths of the charge order in the 0.20 and 0.33 samples calculated from the fits at 20 K. As a comparison the inverse correlation length of the Bragg peak is also shown.*

The inverse correlation length ξ^{-1} was calculated using the equation

$$\xi^{-1} = \kappa \times \left(\frac{2\pi}{d} \right) \qquad [5.1]$$

where κ is the half width at half maximum of the peak and d is the Bragg plane spacing in the direction normal the scattering vector.

The table clearly shows that the charge order in the 0.20 doped sample is significantly less correlated than that in the 0.33 doped system in all directions. To summarise in contrast to the charge order in the 0.33 doped system where the charge stripes are intense and well correlated the charge order in a charge glass state characterised by weak, short range ordered and incommensurate charge stripes. The observation of a charge glass is in agreement with the neutron diffraction results on the 0.20 composition reported by Sachan *et al.* It should be noted that the charge order was also significantly weaker and less correlated than that reported in the 0.30 and 0.275 samples. This is indicative that the further the doping is decreased from the commensurate 0.33 doping the weaker and less stable the charge ordering becomes.

The charge ordering reflection (4.5, 0, -3) was measured as a function of temperature with scans being carried out in *H*, *K* and *L* at each temperature. The behaviour of the integrated intensity in the *H* direction for the (4.5, 0, -3) is shown in Figure 5.3. As the temperature was increased from 10 K the integrated intensity increased and reached a maximum at 50 K. As the temperature was increased further the charge order began to decrease in intensity and by 130 K the charge stripe melting was complete and only critical scattering was observable. Above 160 K no intensity from the charge ordering was observed above background.

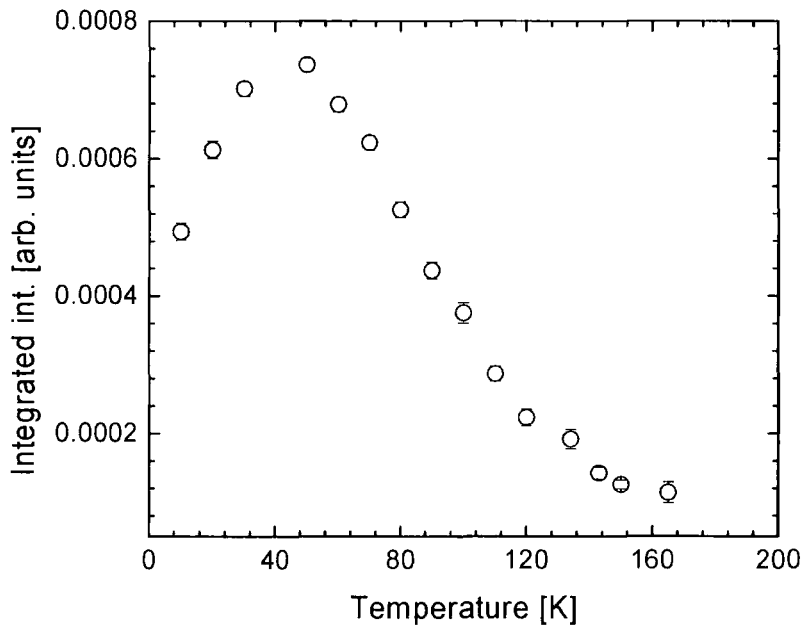

***Figure 5.3**: Temperature dependence of the integrated intensity of the (4.5, 0, -3) peak.*

The initial increase in intensity between 10 – 50 K was not observed in the neutron measurements on the 0.20 sample by Sachan *et al.* but it is consistent with the behaviour reported by Ghazi *et. al.* for the x-ray measurements on the 0.33, 0.30 and 0.275 systems where an initial increase in the integrated intensity with temperature was observed. Possible reasons for this will be discussed later in the Chapter but the initial increase in intensity is a indicative of an increase in the charge density contrast between hole rich and hole poor areas. As the temperature is increased above 50 K the holes gain thermal

energy allowing them to overcome the interactions with the lattice which fix them on the charge stripe. This lowers the hole concentration on the charge stripes and as a result the integrated intensity decreases.

The inverse correlation length for the (4.5, 0, -3) reflection is shown in Figure 5.4 in the *H* and *K* directions and that of the *L* direction in Figure 5.5.

In the temperature region 10 – 60 K the inverse correlation length decreases indicating the charge ordering is becoming more correlated as it is increasing in intensity. The intensity starts to decrease at 60 K but the inverse correlation remains almost constant until 80 K. At 80K, which corresponds to the magnetic ordering temperature T_N the inverse correlation lengths begin to increase as the charge order is no longer stabilised by the magnetic order. These increases continue until the charge order is no longer observable at 160 K for the (4.5, 0, -3) reflection

By measuring the position of the charge peak in the *H* direction the behaviour of the incommensurability can be determined. The temperature dependence of the incommensurability is shown in Figure 5.6.

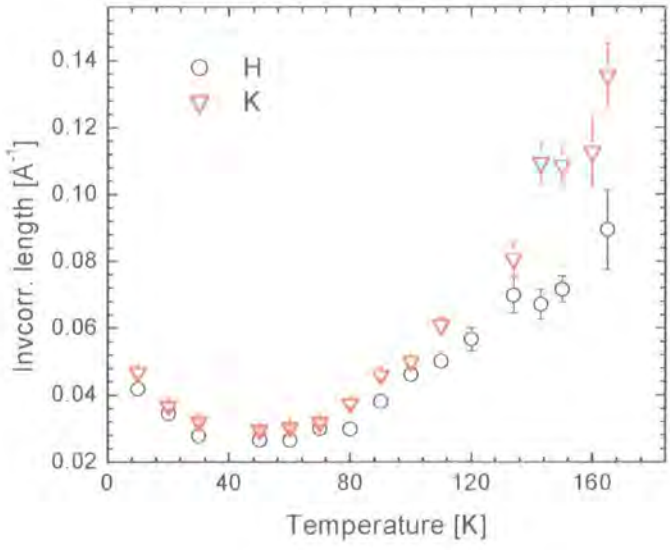

***Figure 5.4**: Temperature dependence of the inverse correlation length in the H, K directions for $La_{2-x}Sr_xNiO_4$ with $x = 0.2$*

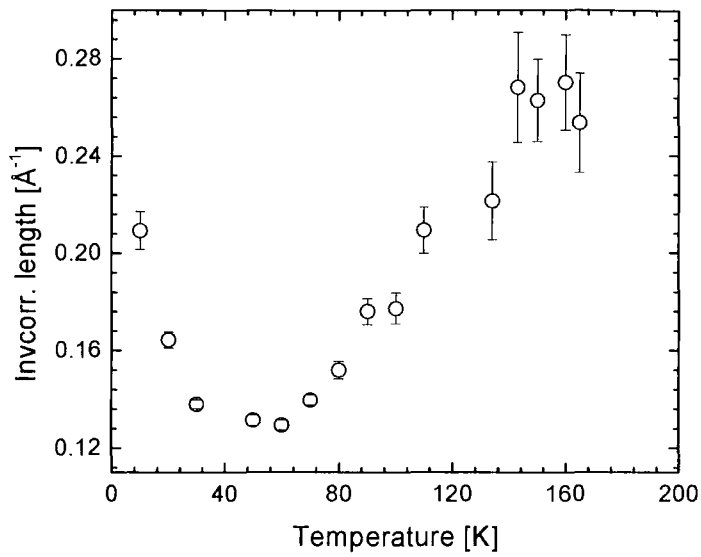

***Figure 5.5**: Temperature dependence of the inverse correlation length in the L direction for $La_{2-x}Sr_xNiO_4$ with x = 0.2*

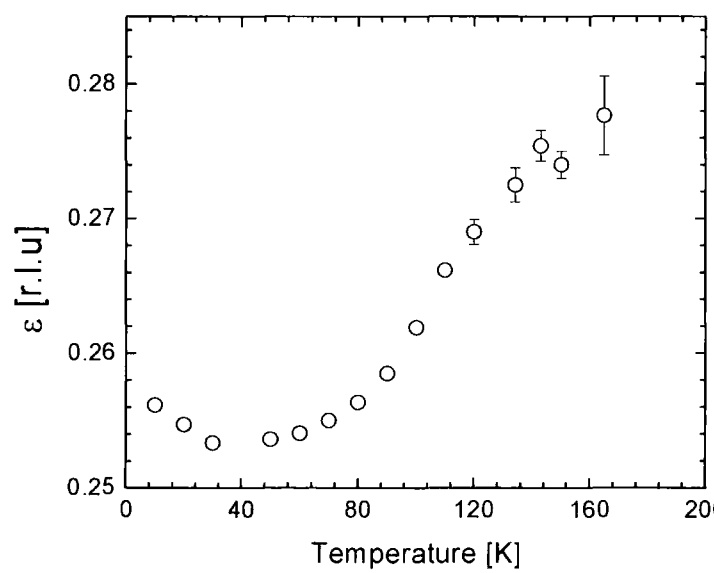

***Figure 5.6:** Temperature dependence of the commensurability for the (4.5, 0, -3) reflection for $La_{2-x}Sr_xNiO_4$ with x = 0.2*

Initially the incommensurability decreases towards from 0.255 at 10 K to $\varepsilon = 0.25$ i.e. the charge stripes move further apart to minimise the Coulomb repulsion. As the charge stripes gain more thermal energy they can overcome the Coulomb repulsion and move towards the stable ε = 1/3 position. There appears to be no stabilisation at the next commensurate value of ε = 0.25 and the 0.33 position is still the most stable configuration for the charge order.

The results for the integrated intensity, inverse correlation length and commensurability are summarised in Figure 5.7. Consistent with the behaviour observed in higher doped samples the charge ordering can be divided into 4 clear regions. In region I at 10 K the charge ordering is relatively strong, has a relatively small inverse correlation length and exists at a position with $\varepsilon = 0.255$. As the temperature is increased there is an increase in the integrated intensity of the charge stripe superlattice peaks. This is we believe evidence of an increase in the charge density between hole rich and hole poor stripes. It is postulated that the reason for this behaviour is the effect of the spin exchange interactions. At low temperatures the effect of the exchange interactions is strong, and this favours a uniform charge distribution across the charge stripe. This lowers the contrast in the charge density between the stripes and hence, the integrated intensity. The spin exchange interactions compete with the effects of Coulombic repulsion which seeks to maximise the distance between the charges. As the temperature is increased the holes gain more thermal energy and overcome the spin exchange interactions and to minimise Coulombic repulsion the holes attempt to maximise the distance between them. This has the effect of increasing the charge density and hence, the integrated intensity. This was the same behaviour as observed in the 0.30 and 0.275 doping levels by Ghazi *et al.* In region I the commensurability shows a clear decrease and the inverse correlation length shows a decrease - evidence that the charge order is becoming more correlated. This behaviour was not observed in the 0.275 and 0.30 samples and the reason for this difference will be discussed later. The charge order enters region II at 50 K and as the temperature is increased the charge stripes gain more thermal energy and this enables them to overcome the Coulomb repulsion and move towards the favoured $\varepsilon = 1/3$ value and thus the incommensurability wavevector increases.

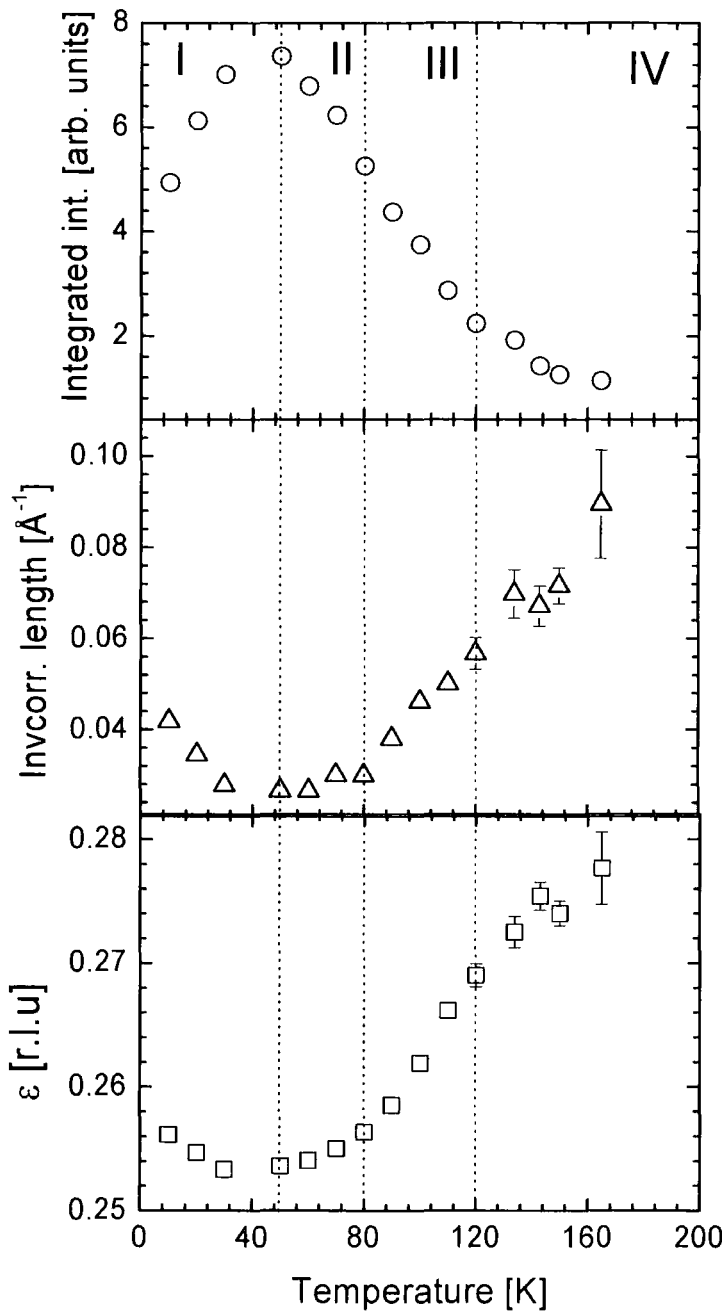

***Figure 5.7**: Integrated intensity, inverse correlation length and the incommensurate wavevector of the (4.5, 0, -3) charge order peak in the H direction. Unless shown the error bars are smaller than the data points*

This increase in commensurability was also observed in the 0.275 and 0.30 samples by Ghazi. From this it is evident that the $\varepsilon = 0.33$ is still the stable position for the charge ordering with no stabilisation at the commensurate position of $\varepsilon = 0.25$.

There is a decrease in the integrated intensity as the temperature is increased into region II. As the temperature is increased the holes gain thermal energy allowing them to overcome the interactions with the lattice which fix them on the charge stripe. This lowers the hole concentration on the charge stripes and as a result the integrated intensity decreases. The boundary of regions II and III at 80 K corresponds to the spin ordering temperature T_N. The charge stripes are no longer stabilised by the spin stripes and coupled with the increased thermal energy begin to vibrate and due to this there is a sharp increase in the inverse correlation length. In region III there is a continuation of the decrease in integrated intensity and increase in the incommensurability as the holes continue to gain thermal energy. In region IV at 120 K only critical scattering exists and this is very weak, virtually uncorrelated, and ε continues to move towards the 0.33 position. The charge ordering disappears before ε reaches the stable 1/3 value. Overall the charge order in the 0.20 doped system shows similar behaviour to that observed in the 0.275 and 0.30 samples. However, the charge order state is less stable than in the higher doped samples because it is further away from the commensurate 0.33 doping level. It should be noted that the behaviour of the charge order in the K and L directions with respect to the intensity and inverse correlation length was the same as that in the H direction.

When comparing the results with the neutron diffraction study by Sachan *et al.* there are clear differences in the results observed. Firstly, the integrated intensity in the neutron measurements shows a gradual increase in intensity in contrast to the x-ray measurements where an initial increase in intensity was observed with a maxima at 50 K. This difference in behaviour between neutron and x-ray measurements has been observed by Ghazi *et al.* and the reason for this discrepancy is undetermined. Secondly, the inverse correlation length shows an initial decrease in the x-ray measurements that was not observed in the neutron measurements. At 10 K the inverse correlation length calculated from the x-ray measurements is 0.042 ± 0.001 $Å^{-1}$ and using the HWHM from the neutron measurements the inverse correlation length at 10 K is estimated as 0.044 $Å^{-1}$ i.e.

they are approximately equal. However, we observe a decrease in the inverse correlation length in region I whereas no change was observed in the neutron study before it began to increase at approximately 80 K which is the same temperature as observed in the x-ray measurements. We postulate an explanation could be the greater resolution available from the x-ray measurements. The increased resolution of the x-ray measurements may also account for the difference in the commensurability results. We observed a decrease in the commensurability from 0.255 to 0.25 in region I whereas in the neutron study the commensurability is reported as remaining at 0.25 before increasing and the resolution may not have been great enough to observe this in the neutron study. A further large point of interest is the similarity in the inverse correlation lengths between the neutron and x-ray measurements. The neutron measurements probe the bulk of the sample and the similarity in the inverse correlation length suggests that the charge order exists in a similar state in the bulk and at the surface *i.e.* it is a charge glass in the bulk but it appears that there is no stabilisation of the charge order at the surface. A note of caution should be added because of the lower resolution using neutrons but comparing the results in the 0.225 sample at high energy with the results of this study should give a definite comparison between charge stripes in the bulk and at the surface.

5.3.2 $x = 0.225$

The 0.225 sample was mounted with the <101> direction surface normal and the <010> direction corresponding to the beam direction. The sample was aligned with the (4, 0, 4) and (4, 2, 4) reflections as the *or0* and *or1* reflections and had a rocking curve width of 0.02°. Scans were carried out on the (4, 0, 4) Bragg peak gave the inverse correlation lengths as 0.00132 $Å^{-1}$ in H, 0.000445 $Å^{-1}$ in K and 0.00303 $Å^{-1}$ in L.

The sample was cooled to 12 K and a search carried out around the (4, 0, 4) Bragg peak. Charge order peaks were located at modulations of (2ε, 0, 1) with the incommensurability ε = 0.28 at base temperature. This incommensurability is larger than the expected ε = 0.275 measured in the neutron and high energy x-ray measurements and is actually slightly greater than in the 0.25 sample. This occurs due to an excess in the oxygen doping, the hole concentration is given by the relationship $n_h = x + 2\delta$ where δ is the excess oxygen doping. The hole concentration $n_h \sim \varepsilon$ but as discussed previously there is deviation from this rule as the doping is decreased away from 0.33. For this reason the incommensurability is higher than expected. Scans in the H, K and L reciprocal space directions were carried out on the (4.56, 0, 5) charge order peak and these are shown in Figure 5.8 with the scans on the (4, 0, 4) Bragg peak shown as a comparison. The charge order was stronger than in the 0.20 sample with an intensity of approximately 5000 cps at 12 K. Similarly to the 0.20 sample the charge order was fitted to a Lorentzian squared lineshape in the 3 directions. From these measurements it can be seen that similar to the 0.20 sample, the charge order is far less correlated than crystal structure and is two-dimensional in nature. The charge order in the 0.225 sample was approximately a factor of 1.5 more correlated than the 0.20 sample, further evidence that the charge ordered state becomes more stable as the doping is increased towards x = 0.33. However, the charge order in the 0.225 sample, like the 0.20 sample, exists in a weak and diffuse state *i.e.* a charge glass. The (4.56, 0, 5) charge order peak was measured as a function of temperature in the H, K and L directions. From these measurements the integrated intensity, inverse correlation length and incommensurability of the charge ordering were determined as a function of temperature as they were for the x = 0.20 sample.

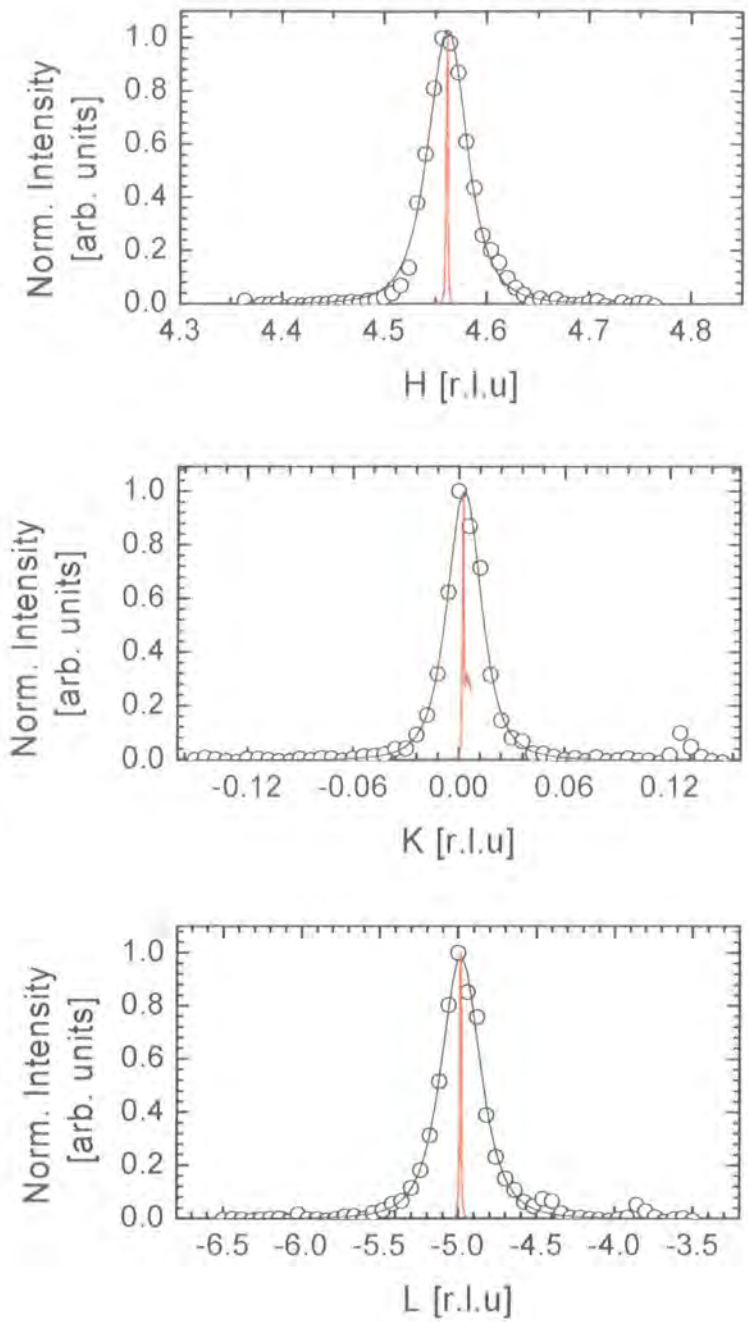

***Figure 5.8**: Scans through H, K and l. directions of the (4.56, 0, 5) charge stripe peak. The black line is the fit to the experimental data using a Lorentzian squared lineshape. The red line shows the corresponding scans of the (4, 0, 4) Bragg peak.*

The integrated intensity, inverse correlation length and incommensurability are shown in Figure 5.9. The charge order in the 0.225 sample can again be divided into 4 clear regions just as it was in the 0.20 sample. The charge ordering in the 0.225 sample is more stable and hence, the integrated intensity begins to decrease at a higher temperature than in the 0.25 system (60 K compared to 50 K in the 0.20 system). As the temperature is increased further the charge order behaves in the same way as observed in the 0.20 system but because the charge order is more stable it shows a higher charge order temperature.

The neutron measurements by Tranquada *et al.* [4] showed no increase in the integrated intensity on heating from base temperature in contrast to our measurements in which a large increase in integrated intensity was observed as shown in Figure 5.9 in region I. It could be argued that the initial increase in the low temperature region is due to a surface effects in the nickelates However, an increase in the integrated intensity was observed in the 100 keV high energy x-ray measurements by Vigliante *et al.*[5] so it is not a surface effect but it is an effect that x-rays are sensitive and neutrons are not. The comparison of the results for the 0.20 sample with the previous neutron work suggested that there was no difference in the degree of correlation for the charge order between the surface and the bulk which contrasts with that observed for the 0.33 sample. A comparison between the high energy x-ray results and our measurements will give an accurate comparison of the bulk and surface qualities of the charge order in the 0.225 system. The inverse correlation length in the H direction was estimated from the HWHM of the high x-ray energy measurements as approximately 0.03 $Å^{-1}$ (it should be noted that this was the same value as in the neutron study) and this is very close to the value in out surface measurements of 0.029 ± 0.001 $Å^{-1}$, indicative of the charge order existing in a similar state in both the bulk and at the surface. The inverse correlation length measured in the bulk of the 0.33 sample by Wilkins[7] was 0.028 $Å^{-1}$ - virtually the same as that measured in the 0.225 sample. From this we postulate that in the doping region 0.20 - 0.33 the charge order exists in a poorly correlated charge glass state in the bulk and there appears to be no variation in the correlation in the bulk with doping. In the 0.33 sample the charge order is stabilised at the surface due to a pinning effect.

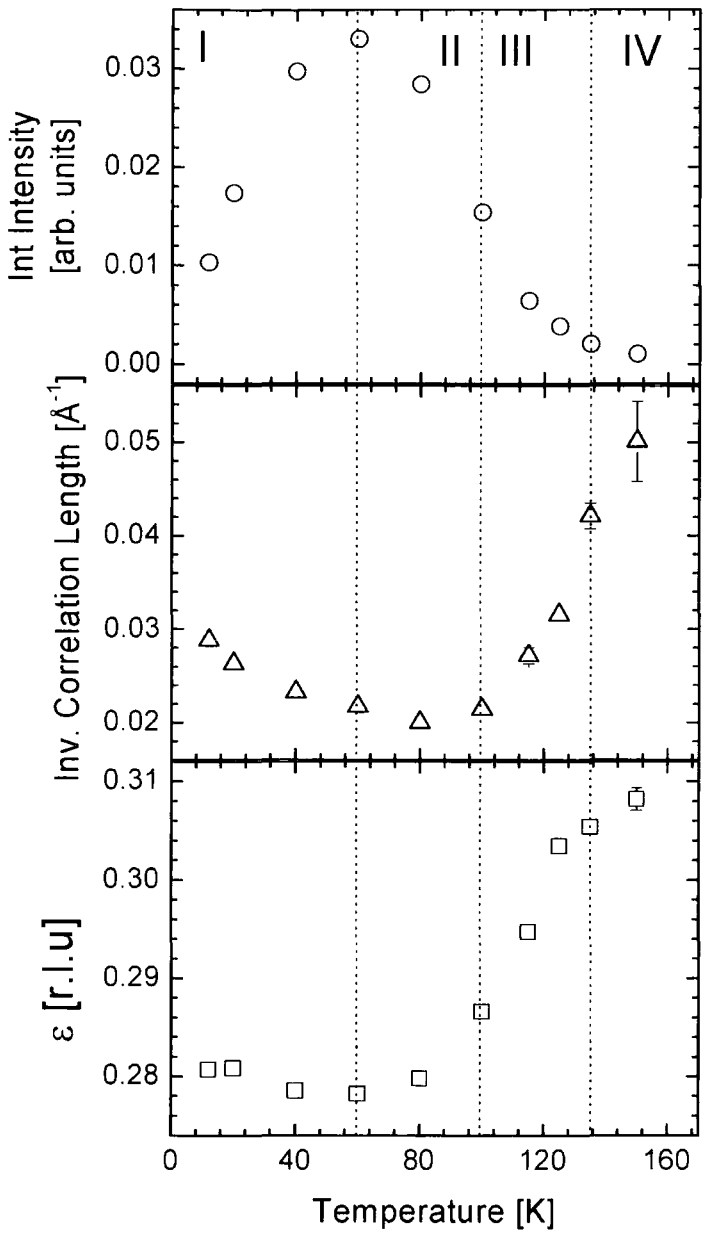

***Figure 5.9**: Integrated Intensity, inverse correlation length and incommensurability of the (4.56, 0, 5) charge order peak in the H direction. Unless shown the error bars are smaller than the data points*

However, as the doping is decreased away from this stable value the degree of stabilisation at the surface decreases until in the 0.225 and 0.20 samples the charge order exists in a charge glass in both the bulk and surface with no difference in the degree of correlation in the bulk and at the surface.

To summarise we have shown that the charge order exists in a charge glass state in the 0.20 and 0.225 doped nickelates. The charge ordering is especially weak in the 0.20 doped sample where the strongest peak is just 200 cps. When the results for the 0.225 sample are compared with the high energy x-ray scattering results they provide evidence that the charge stripes in the bulk and at the surface exist in the same state. This is a clear contrast with the measurements on the 0.33 doped system where there is a dramatic difference between the charge order in the bulk and at the surface. We have shown a clear difference in the charge order state in the 0.225 and 0.20 samples compared to the 0.275 - 0.33 region where the charge order is intense and well correlated. The 0.25 sample was studied to provide information on the charge order in the regime between the 0.225 and 0.275 samples in order to complete the systematic study of the entire doping region.

5.3.3 $x = 0.25$

The 0.25 sample was mounted with the <101> direction surface normal and <010> direction down the beam. This was the same experimental geometry as used for all other doping levels. The sample was aligned with the (4, 0, 4) and (4, 2, 4) reflections as the *or0* and *or1* reflections and had a rocking curve width of 0.03°. Scans carried out on the (4, 0, 4) Bragg peak gave the inverse correlation lengths of the Bragg peak as of 0.0017 $Å^{-1}$ in H, 0.0007 $Å^{-1}$ in K and 0.0046 $Å^{-1}$ in L.

The sample was mounted on the diffractometer in a displex cryostat and cooled to a base temperature of approximately 12 K. A search was carried out around the (4, 0, 4) Bragg peak and satellites were located at modulations of (2ε, 0, 1) with ε = 0.279 at base temperature. The strongest peak occurred at the (4.56, 0, 5) position in reciprocal space and it had an intensity of approximately 6000 cps at 12 K. This is weaker than the charge ordering observed in the systems with x = 0.275 and above but stronger than in the 0.225 and 0.20 samples. The charge ordering was scanned along the H, K and L directions of reciprocal space and was observed to fit the Lorentzian squared lineshape in the H, K and L directions. These fits are shown in Figure 5.10 and as a comparison the resolution scans for the (4, 0, 4) Bragg peak are also shown.

A comparison of the inverse correlation lengths is shown in Table 5.2 The charge order in the 0.25 doped sample as expected is more correlated than that in the lower doped samples. However, it is significantly less correlated than in the 0.33 system and, while it is less glassy than the low doped samples, it does not exist in the highly correlated state observed in the 0.275 doping levels and above.

	H [$Å^{-1}$] × 10^{-3}	K [$Å^{-1}$] × 10^{-3}	L [$Å^{-1}$] × 10^{-3}
0.33	6.10 ± 0.07	2.66 ± 0.03	54.2 ± 0.4
0.25	18.2 ± 0.2	14.7 ± 0.3	66.4 ± 0.7
0.225	28.8 ± 0.7	14.5 ± 0.4	79.1 ± 4.2
0.20	41.8 ± 1.2	46.7 ± 1.3	209 ± 8

***Table 5.2**: Inverse correlation length at 20 K for the 0.2, 0.225, 0.25 and 0.33 samples*

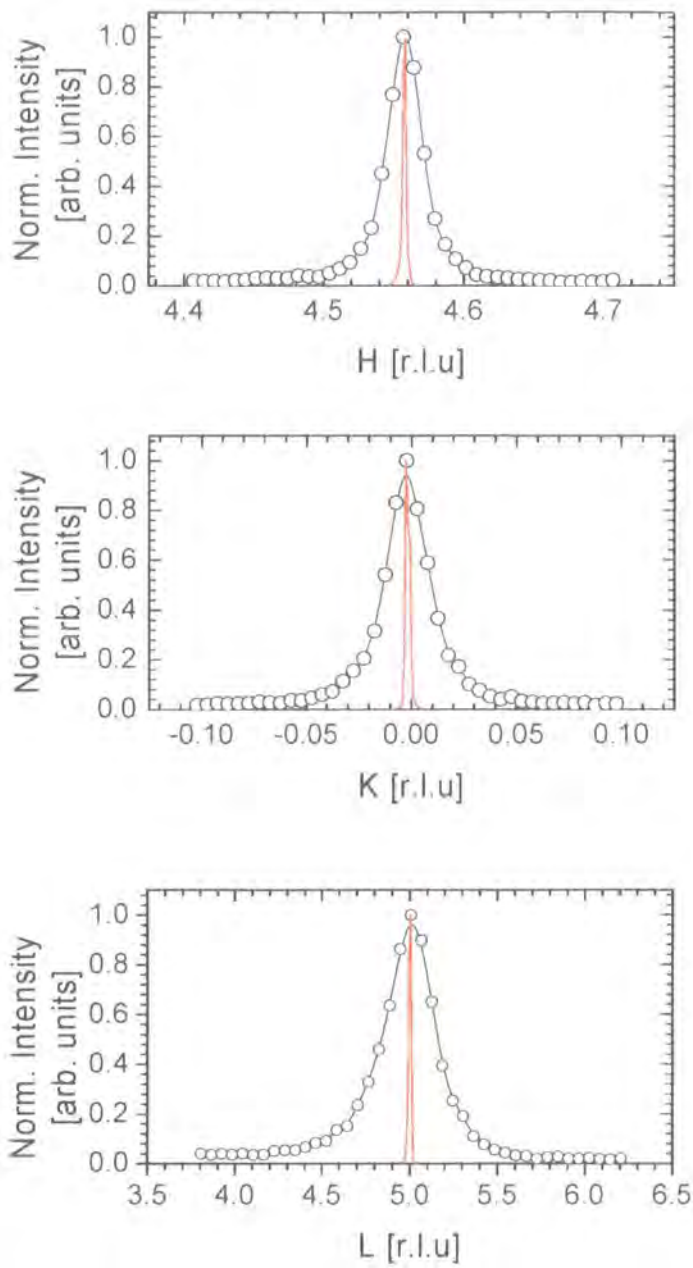

***Figure 5.10**: Scans through H, K and L directions of the (4.56, 0, 5) charge order peak. The black line is the fit to the experimental data using the Lorentzian squared lineshape. The red line shows the corresponding scans of the (4, 0, 4) Bragg peak.*

The intensity, inverse correlation length and commensurability of the (4.56, 0, 5) charge order reflection was measured as a function of temperature in the *H*, *K* and *L* directions. The results of the integrated intensity, inverse correlation and in the *H* direction are shown in Figure 5.11. In line with the other samples the charge order has four clear regions and behaves in the same way as described for the 0.225 and 0.20 doped samples. As the doping is nearer to 0.33 it displays a higher charge ordering temperature than the lower doped samples.

5.4 Discussion

In this section we refer to the results from the thesis of Dr. M. Ghazi for the 0.33, 0.30 and 0.275 samples. In all samples from 0.20 to 0.33 there is an initial increase in the integrated intensity as the temperature is increased. This behaviour is indicative of an increase in the contrast between the charge stripes. We postulate a possible reason for this is the influence of the spin exchange interactions. At low temperatures the effect of the exchange interactions is strong, and this favours a uniform charge distribution across the charge stripe. This lowers the contrast in the charge density between the stripes and hence, the integrated intensity. The spin exchange interactions compete with the effects of Coulombic repulsion which seeks to maximise the distance between the charge. As the temperature is increased the holes gain more thermal energy and overcome the spin exchange interactions and to minimise Coulombic repulsion the holes attempt to maximise the distance between them. This increases the contrast in the charge density between the hole rich and hole poor regions and hence the x-ray scattering intensity increases. Our measurements of the integrated intensity showed a considerable difference when compared with the neutron scattering results where the integrated intensity stayed constant on heating and then showed a gradual decrease in intensity. This is in clear contrast to our results where an increase in intensity is seen. We can offer no definite explanation for the discrepancy between the neutron and x-ray techniques. Both techniques are sensitive to long range correlations in the electron density. X-rays scatter directly off the electrons and are more sensitive to small variations in the charge density than neutrons which are primarily sensitive to the nuclear positions which input directly

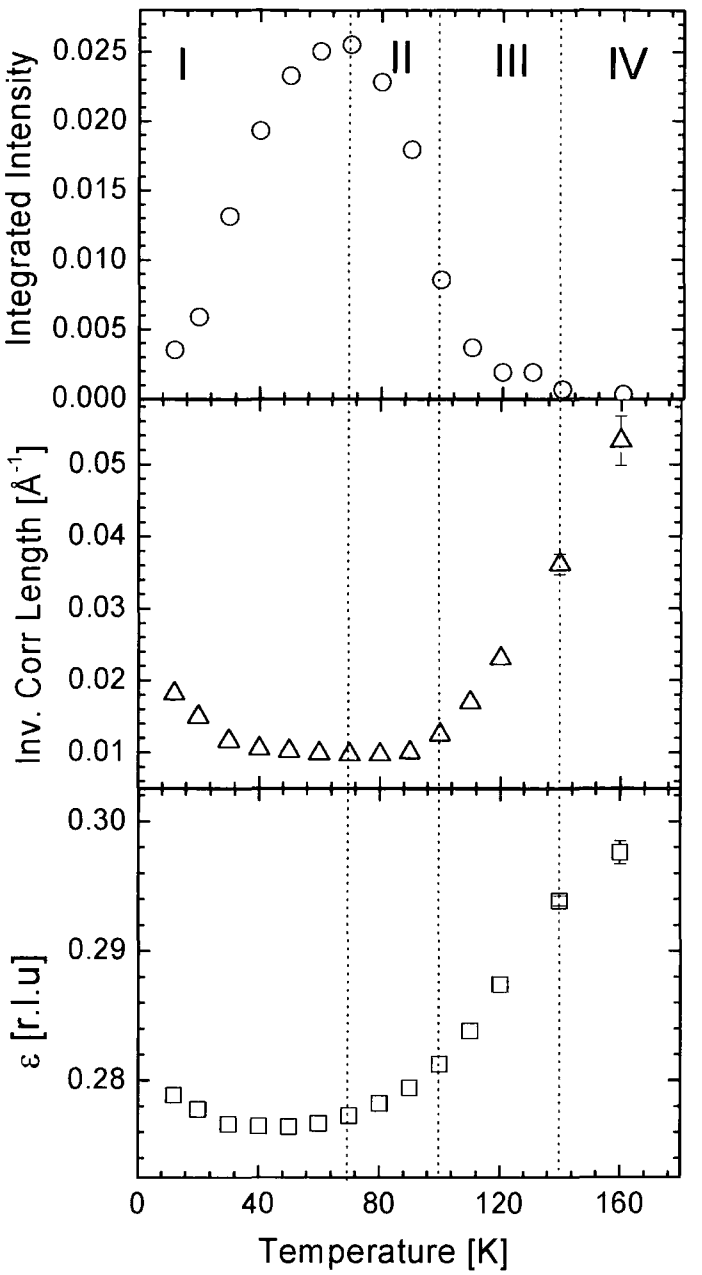

***Figure 5.11**: Integrated intensity, inverse correlation length and incommensurability of the (4.56, 0, 5) charge order peak in the H direction. Unless shown the error bars are smaller than the data points*

into the neutron scattering factor. However, neutron scattering will also reflect distortions in the electron density and hence, both techniques would be expected to show similar results with respect to the integrated intensity. The neutron and x-ray diffraction techniques probe different timescales. The stripe order is presumed to be dynamic in nature and because the electrons are significantly lighter than the nuclei they move much greater distances and have a considerably faster timescale. Both techniques see a time average of a large number of almost instantaneous scattering events. It is therefore possible that the lower intensity observed at low temperatures with the x-ray measurements is due to the larger dynamic excursions of the electrons. Secondly x-rays scatter directly off the charge density whereas the neutrons scatter from structural modulations associated with the charge order. It is possible that x-rays are measuring changes in the charge distribution on the stripes that the neutron measurements are not sensitive enough to observe. These explanations are only suggestions and further study is required to clarify this discrepancy.

When comparing the behaviour of the commensurability with temperature we refer the reader to Figure 5.12 which shows the temperature dependence of the commensurability in the x = 0.33, 0.30, 0.275, 0.25 and 0.20 samples. The results from the 0.225 sample have been omitted due to the excess oxygen doping. In the x = 0.33 system there is a small change in the incommensurability as it tends towards the ε = 1/3 value and when it reaches this position a stabilisation of the charge order pattern occurs. In all the lower doped samples the change in position is much more significant as the charge order tries to move towards the stable position of 1/3. However, the charge order in all samples disappears before the stable position is reached. In the 0.20 doped sample the charge order is very close to the next commensurate value of ε = 0.25 but there appears to be no stabilisation of the charge order pattern at this position. In all the samples with the exception of the 1/3 doped system the inverse correlation length shows a sharp increase in the inverse correlation length above T_N because long range order cannot exist in the absence of magnetic order. In the 0.33 sample the charge order is stabilised by the interactions between the lattice and the charge order state even above T_N.

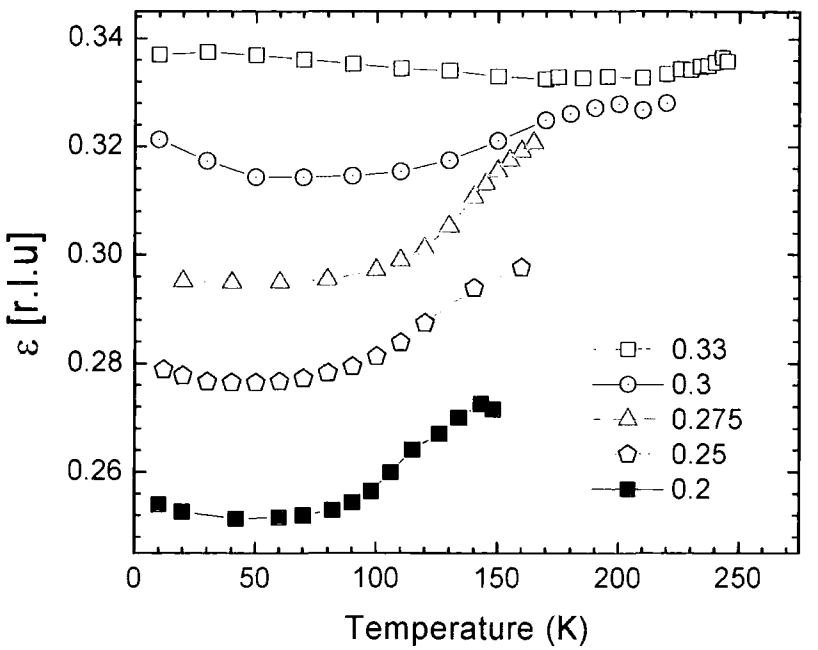

***Figure 5.12**: Commensurability as a function of temperature in the 0.20, 0.25, 0.275, 0.30 and 0.33 samples*

The low doped samples show virtually the same behavior as the high doped samples with four clearly identifiable regions. However, in region I of the low doped samples there is actually a decrease in both the incommensurability and inverse correlation length not observed in the 0.30 and 0.275 samples. A possible explanation for this involves the interplay between the spin exchange interactions, Coulomb repulsion and the stabilisation effect that occurs at ε = 0.33. At low temperatures the spin exchange interactions compete with the effect of the Coulomb interactions. As the temperature is increased the holes gain enough thermal energy to overcome the spin exchange interactions and Coulomb interactions have a greater effect. The Coulomb repulsion is minimised firstly by increasing the distance between the charge stripes which would explain the decrease in the commensurability and secondly by the charge stripes straightening which would cause a decrease in the inverse correlation length. This is not observed in the higher

doped samples because the charge order is closer to the stable 0.33 position and the stabilising effect overcomes the effect of the Coulomb repulsion.

Finally the inverse correlation length for all doping levels studied is shown in Table 5.3

	H [Å^{-1}] × 10^{-3}	K [Å^{-1}] × 10^{-3}	L [Å^{-1}] × 10^{-3}
0.20	41.8 ± 1.2	46.7 ± 1.3	209 ± 8
0.225	28.8 ± 0.7	14.5 ± 0.4	79.1 ± 4.2
0.25	18.2 ± 0.2	14.7 ± 0.3	66.4 ± 0.7
0.275	8.01 ± 0.14	4.89 ± 0.04	24.7 ± 0.3
0.30	7.56 ± 0.08	4.69 ± 0.09	18.8 ± 0.4
0.333	6.10 ± 0.07	2.66 ± 0.03	54.2 ± 0.4

***Table 5.3**: A comparison of the inverse correlation lengths at 20 K for the doping region from $0.20 \leq x \leq 0.33$ including the results from Ghazi* [2]

The results clearly demonstrate that in the 0.20 and 0.225 doped samples the charge order exists in a charge glass characterized by weak diffuse charge stripes. Whereas the charge order in the 0.275 doped systems and above exists in a well correlated intense state. The charge order in the 0.25 can be characterized as existing in an intermediate state between the two regimes.

5.5 Conclusions

In the nickelate system we have shown that the charge order in the 0.20 and 0.225 samples is weak, incommensurate and poorly correlated i.e. it exists in a charge glass. This differed from the intense, highly correlated charge order observed in the 0.275 doping level and above. The charge order in the 0.25 system was found to exist in a state between the charge glass in the lower doped systems and the highly correlated state in the higher doped levels. The study showed that as the doping was increased from 0.20 towards 0.33 the charge order became more intense and stable. The commensurability showed the same behaviour as in the higher doped samples with it moving towards the

stable 0.33 position and no stabilisation was observed at the next commensurate position of 0.25.

The comparison with the high energy results from the 0.225 sample and those in the 0.33 sample strongly suggests that the charge order in the bulk with respect to the inverse correlation length exists in the same state in the doping region 0.20 - 0.33. The charge order is pinned at the surface in the nickelates but as the doping is decreased from 0.33 the stabilisation of the charge order at the surface decreases until in the 0.225 doped sample and below it exists in a charge glass in the bulk and at the surface.

In this chapter the charge order in the doping region 0.20 – 0.33 has been investigated and characterised. The charge order is shown to be only stabilised at the commensurate position of 0.33 with no stabilisation at the commensurate position of 0.25. The next stage of the study will be to investigate the charge order in the doping region $0.33 \leq x \leq 0.50$ and to determine if a similar stabilising effect occurs at the commensurate doping of 0.5.

5.6 References

1 M. E. Ghazi, P. D. Spencer, S. B. Wilkins, *et al.*, Physical Review B submitted (2003).

2 Ghazi M.E, " *High-Resolution X-ray scattering studies of Charge Ordering in Highly Correlated Electron Systems"* PhD Thesis Department of Physics University of Durham, (2002).

3 V. Sachan, D. J. Buttrey, J. M. Tranquada, *et al.*, Physical Review B Condensed Matter **51**, 12742 (1995).

4 J. M. Tranquada, D. J. Buttrey, and V. Sachan, Physical Review B Condensed Matter **54**, 12318 (1996).

5 A. Vigliante, M. von Zimmermann, J. R. Schneider, *et al.*, Physical Review B **56**, 8248 (1997).

6 P. D. Hatton, M. E. Ghazi, S. B. Wilkins, *et al.*, Physica B **318**, 289 (2002).

7 S. B. Wilkins, "*Charge and Spin Correlations in Transition Metal Oxides"* PhD Thesis Department of Physics University of Durham, (2002).

Chapter 6

Stripe And Checkerboard Charge Order in the High doped Nickelates

6.1 Introduction

In the previous chapter the behaviour of the charge stripe ordering in the low doped nickelates with x = 0.20, 225 and 0.25 was discussed. The results showed that in this doping regime the charge stripe order existed in a charge stripe glass which is characterised by weak, diffuse, incommensurate charge stripes. It was clearly demonstrated that the further the doping level was away from the stable 0.33 level the lower the charge ordering temperature and the weaker the charge order. No stabilisation was observed to occur at the commensurate position of ε = 0.25 and the commensurability tended towards the 0.33 position just as it did in the 0.30 and 0.275 samples. The doping region $0.33 \leq x \leq 0.5$ has not been studied as intensively and until now there have been no x-ray measurements carried out in this doping regime. In this chapter we discuss the behaviour of the charge stripes in the doping region $0.33 \leq x \leq 0.5$ and report the first x-ray measurements of the charge order in this doping region.

Yoshizawa *et al.* have studied the nickelate system using neutron diffraction experiments in the doping regime $0.289 < x < 0.50$.[1] Their results are displayed in Figure 2.28 which show that as the doping is increased from x = 1/3 the charge ordering temperature decreases just as it did when decreasing the doping from 0.33. This is consistent with the x-ray results obtained by Du,[2] Ghazi *et al* [3] and described in the previous chapter for the doping levels of $0.20 < x < 0.33$. As shown in the lower panel of Figure 2.28 the incommensurability deviates from the $\varepsilon = n_h$ law as the doping is moved away from x = 0.33. Yoshizawa *et al.* postulated that this was due to the stripe order favouring the 1/3 doped state and they refer to this as the "commensurability effect". Neutron diffraction studies on dopings of x = 0.289 and x = 0.39 by Kajimoto *et al.*

reported that the commensurability moved towards the stable 0.33 position on heating for doping levels above and below $x = 0.33$.[4] This again, is consistent with the x-ray scattering results on the lower doped materials which also report the commensurability tending towards $\varepsilon = 0.33$ on heating. The results demonstrated that the charge order pattern is stabilised at the commensurate position of $\varepsilon = 1/3$ due to the coupling between the charge order and the lattice. The next commensurate charge order configuration occurs in the half doped system and one might expect the charge order pattern to be stabilised at this doping level. However, the doping region for $x > 0.33$ has been much less extensively studied than the doping levels of 0.33 and below, and indeed no x-ray measurements have been carried out in this doping regime. Recently, Kajimoto *et al.* carried out a neutron diffraction study on the charge order in the $La_{2-x}Sr_xNiO_4$ and $Nd_{2-x}Sr_xNiO_4$ systems.[5] The study showed evidence of incommensurate charge stripe order in the $La_{2-x}Sr_xNiO_4$ system up to a doping level of $x = 0.5$ and in the Nd doped system up to a doping level of $x = 0.7$. In the half doped system there are equal numbers of Ni^{2+} and Ni^{3+} ions and the most stable charge order configuration would be expected to be the checkerboard charge order pattern as observed in the half doped cobaltate and manganite systems. However, at low temperatures the charge order was observed to exist in an incommensurate stripe order phase with $\varepsilon = 0.44$ even in the half doped system. Kajimoto *et al.*, reported that the commensurability of the stripe order tended towards $\varepsilon = 0.44$ and even in the 0.7 doping level the wavevector was observed at this position. The dependence of the charge ordering temperature with doping is shown in Figure 6.1 and in the lower panel the behaviour of the commensurability with doping. In the half-doped $La_{1.5}Sr_{0.5}NiO_4$ system Kajimoto *et al.*, report the rearrangement of the charge order pattern from an incommensurate stripe phase at low temperatures to a checkerboard pattern with $\varepsilon = 0.5$ at high temperatures. At 10 K they observed both the stripe and checkerboard charge order but the stripe order pattern dominated. As the temperature was decreased the stripe order decreased in intensity while the checkerboard charge order increased in intensity. This continued until 180 K when the stripe order could no longer be observed above the background, and at approximately 200 K the intensity of the checkerboard pattern maximised.

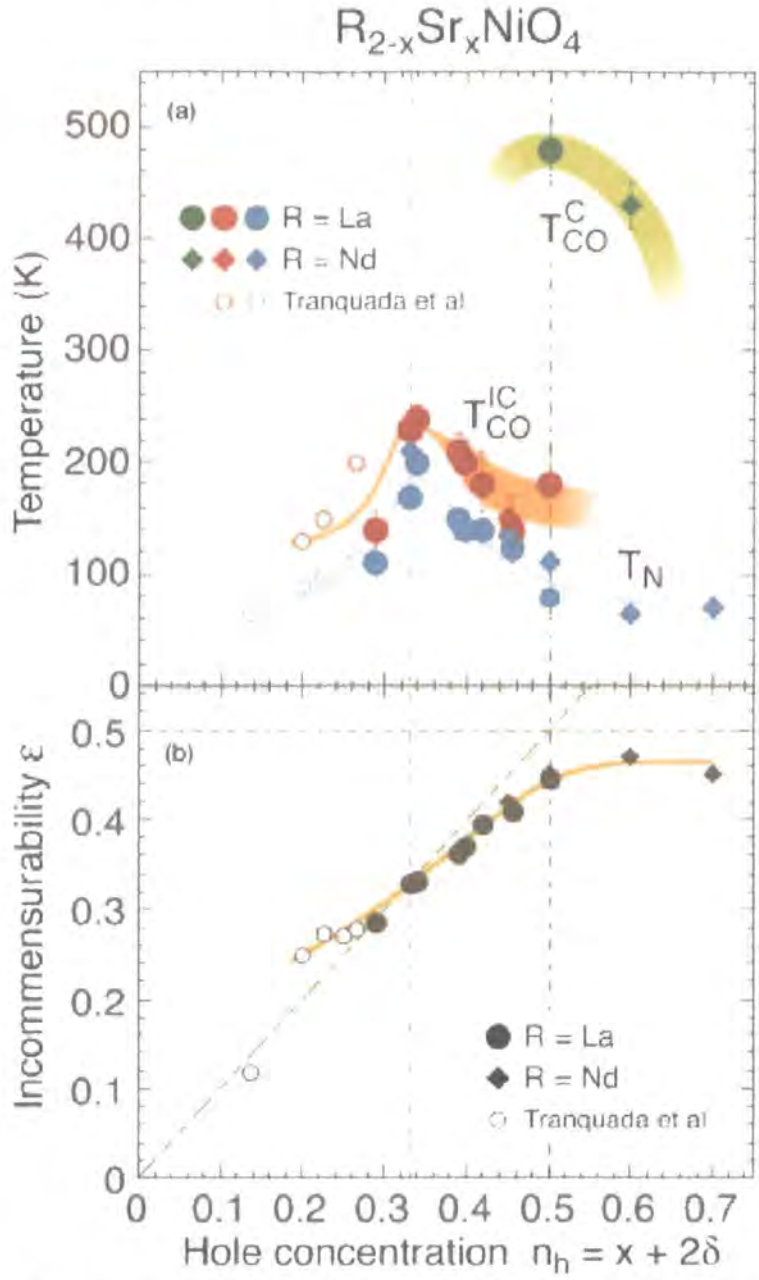

***Figure 6.1**: Hole concentration dependence of the transition temperatures T_{CO}^{IC}, T_{CO}^{C} and T_N (top). Hole concentration dependence of the incommensurability ε (bottom). The circles denote the La doped system and the diamonds the Nd doped system*

The checkerboard order was found to be thermally very stable and showed a transition temperature of 480 K. This is significantly higher than the charge ordering temperature

of 240 K observed in the 0.33 doped nickelate which previously showed the highest charge ordering temperature in the nickelate system, and this dramatic difference is illustrated in the upper panel of Figure 6.1. Optical measurements by Yamamoto *et al.*[6] measured an ordering temperature of ~ 400 K and also measured a decrease in the optical gap at 180 K which was attributed to the stripe ordering. Resistivity data obtained from the sample showed two changes in the slope at 180 K and 480 K. It was postulated that the anomalies could correspond to a two step process in the charge localisation and might be indicative of the formation of two different types of charge order. At low temperature the incommensurate stripe order pattern is favoured over the checkerboard pattern which is favoured at high temperatures. This was attributed to the stronger spin exchange interactions in Ni^{2+}-Ni^{2+} bonds present in the stripe pattern which are stronger than Ni^{3+}-Ni^{2+} bonds in the checkerboard pattern. Therefore, the stripe order state is energetically favoured at low temperatures due to the larger energy gain from the spin exchange interactions. Their measurements of the charge order found that there was virtually no correlation between the planes and the charge order was only poorly correlated within the plane – a charge glass similar to that in the half doped cobaltate and the 0.2 doped nickelate.

No x-ray measurements have been carried out on the nickelate system in the doping region $x > 0.33$. X-rays are much more sensitive to the charge order than neutron techniques and should in theory allow higher intensity and higher resolution. Earlier x-ray measurements by Ghazi *et al.* showed clear differences in the results obtained with x-rays compared to those obtained with neutrons. In this chapter the results obtained on the 0.40, 0.48 and 0.50 samples will be reported. Using the superior resolution available with x-ray measurements we intended to measure the transition of the 0.5 system from the stripe ordered phase to the checkerboard phase. By studying a 0.48 doped sample it would be possible to investigate the doping range over which the checkerboard charge order was observed and if it also displayed the checkerboard state. Finally the behaviour of the charge order commensurability will be measured in the three samples, in the 0.48 sample it would be of interest to investigate if the charge order still tends towards the stable $\varepsilon = 1/3$ position or if it shows a different behaviour. It should be noted that no measurements of either type have been carried out on the 0.48 composition.

6.2 Experimental Procedure

The crystals were grown at the University of Oxford using the floating zone method which has been described previously. The doping in the three samples was measured as x =0.40 ± 0.01, x = 0.48 ± 0.01 and x = 0.50 ± 0.01 using EPMA. The excess oxygen content was measured as δ = 0.00 ± 0.01 in each of the three samples using TGA.

The experiments were carried out on the XMaS beamline in Grenoble, France which has also been described previously. The system was indexed with the *I4/mmm* setting but to be consistent with previous measurements the *F4/mmm* setting with lattice parameters $a \sim b$ = 5.4145 Å and c = 12.715 Å, and this setting was used to allow comparison with earlier studies. The 0.40 and 0.48 samples were mounted on the 6-circle 11-axis Huber diffractometer and cooled using a closed cycle displex cryostat without a scatter shield which allowed a temperature range of 15 – 300 K to be accessed. An x-ray wavelength of 1 Å was used which is close to the peak flux of the beamline and allowed a larger volume of reciprocal space to be accessed. The 0.40 and 0.48 samples had been pre-aligned using the D3 laboratory diffractometer and cut so that the <101> direction was surface normal. All flight paths were evacuated to minimise air absorption and maximise intensity. A single bounce Ge(111) crystal was utilised as an analyser crystal to provide high resolution triple axis measurements.

6.3 Results for x = 0.40

The 0.40 sample was aligned with the <101> direction normal to the scattering plane and the <010> direction down the beam. The sample was aligned and the UB matrix calculated using the (4, 0, 4) and (6, 2, 6) as the *or0* and *or1* reflections respectively. The sample was cooled to base temperature which was approximately 13 K. The rocking curve width of the sample was 0.025° which is very good quality for a transition metal oxide. Scans were carried out on the (4, 0, 4) in the H, K and L directions of reciprocal space. This gave an inverse correlation length of the Bragg peak of 0.0019 $Å^{-1}$ in the H direction, 0.0013 $Å^{-1}$ along K and 0.0045 $Å^{-1}$ along L.

A search for charge stripe order was carried out around the (4, 0, 4) and (2, 0, 2) Bragg peaks. Satellites attributed to the charge stripe order were located at modulations of (0.715, 0, 1) which corresponds to an incommensurability of ε = 0.357. This incommensurability, ε, was lower than the hole doping, n_h, and this observation is consistent with the neutron results where there is a deviation from the $n_h = \varepsilon$ law as x is increased from 0.33. The strongest charge order peak occurred at (4.715, 0, 5) and this peak was measured as a function of temperature in order to determine the integrated intensity, inverse correlation length and incommensurability as a function of temperature. At 12 K scans were carried out in the H, K and L directions of reciprocal space on the (4.71, 0, 5) charge stripe peak and these scans are shown in Figure 6.2. In the H and L directions the peak shape was found to fit a Lorentzian squared peak profile and in the K direction the peak was fitted to two Lorentzian squared peaks. The charge stripe order was significantly broader than the Bragg peaks which is consistent with the charge ordered state seen in the lowered doped nickelates. The charge order had similar inverse correlation lengths in the H and K directions but the inverse correlation length was significantly larger in the L direction, indicative of the two dimensional nature of the charge stripe order which again was consistent with the lower doped nickelates. A comparison with the results from Ghazi *et al.* shows the charge order in the 0.40 system is similar to that in the 0.30 and 0.275 systems i.e. intense, well correlated and slightly incommensurate, but weaker than in the 0.33 sample.

The integrated intensity, inverse correlation length and incommensurability were measured as function of temperature for the (4.71, 0, 5) charge stripe peak. The integrated intensity is shown in Figure 6.3. Initially, the intensity increased on heating, maximising at 70 K, this was the behaviour observed in the lower doped systems. This is attributed to an increase in the contrast of the charge density between charge stripes. The intensity remained approximately constant in the region 70 K -110 K but on further heating showed a gradual decrease until 180 K where only critical charge fluctuations were present and at 220 K the charge ordering was not observable above the background.

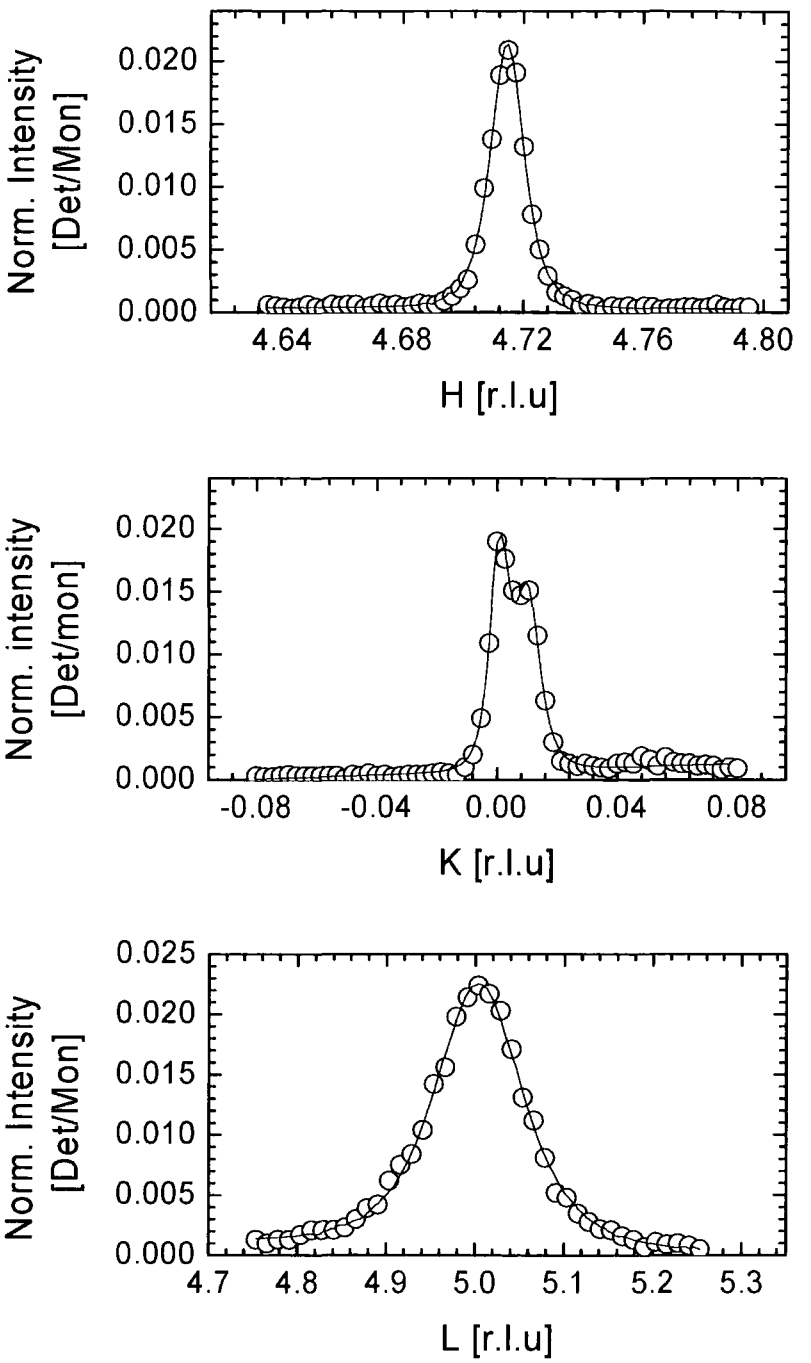

***Figure 6.2**: Scans through H, K and L directions of the (4.715, 0,5) charge order peak at 12 K. The black line is the fit to the experimental data using Lorentzian squared lineshapes.*

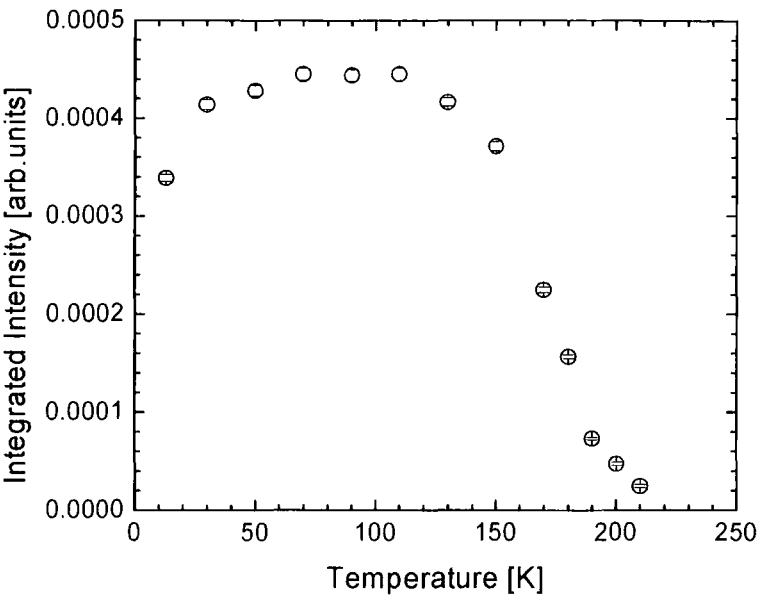

Figure 6.3: *Integrated intensity as a function of temperature for the (4.71, 0, 5) charge order peak in the H direction.*

The temperature dependence of the inverse correlation length is shown in Figure 6.4 and it can be seen that there is no change in the inverse correlation length below a temperature of 150 K. There is no change in the inverse correlation length during the initial increase in integrated intensity or at 110 K where the integrated intensity begins to decrease, this shows there is no change in the stripe correlation despite the change in the contrast of the charge stripes. The neutron study by Kajimoto *et al.* of the 0.39 doped system determined the magnetic ordering temperature, T_N, as 150 K and above this temperature they report a sharp increase in the inverse correlation length. This is in agreement with our data where above 150 K there is a sharp increase in the inverse correlation length. This demonstrates that the spin order stabilises the charge order pattern. The incommensurability is shown in Figure 6.5, the position of the (4, 0, 4) Bragg peak was measured to allow the change in position to be corrected for thermal expansion. At base temperature the incommensurability was measured to be 0.3574. From 12 – 110 K the incommensurability gradually decreased towards $\varepsilon = 0.33$.

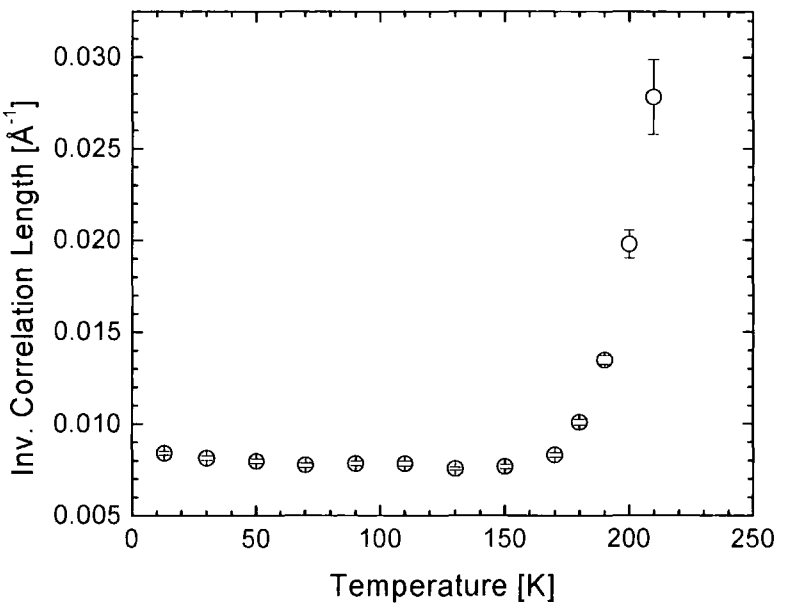

Figure 6.4: *Temperature dependence of the inverse correlation length for the (4.71, 0, 5) charge order peak*

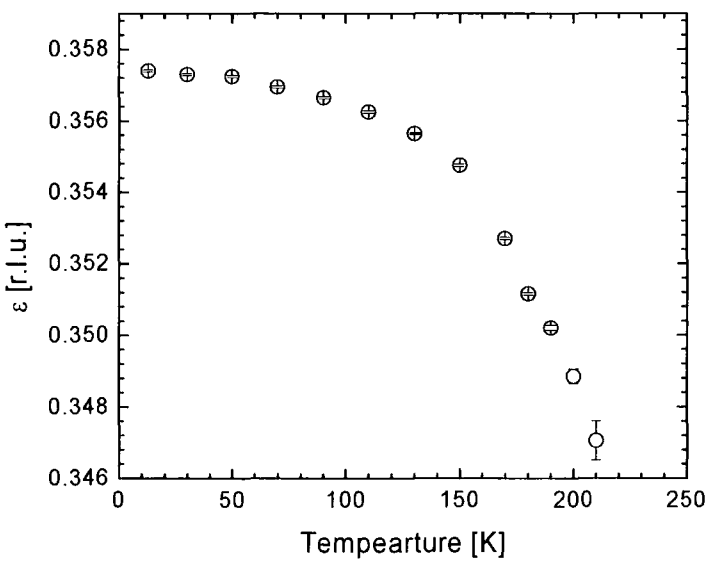

Figure 6.5: *Commensurability of the 0.40 doped sample as a function of temperature.*

At 110 K the incommensurability begins to decrease more sharply, and at T_N there is a further increase in the gradient and the incommensurability continues to decrease towards $\varepsilon = 0.33$ but the charge order disappears before reaching the stable $\varepsilon = 0.33$ position.

The results for the charge order reflection are summarised in Figure 6.6 which shows the temperature dependence of the inverse correlation length, incommensurability and integrated intensity. Consistent with the charge ordering in the lower doped systems the charge stripe order can be divided into four separate regions. In region I at a temperature of 12 K the charge stripes are strong, well correlated and are incommensurate with $\varepsilon = 0.3574$. As the temperature was increased there was an increase in the integrated intensity consistent with an increase of the charge density contrast. We postulate a possible reason for this is the influence of the spin exchange interactions. A possible mechanism has been described in the previous Chapter. To summarise, the intensity increases because the holes gain more thermal energy enabling them to overcome the spin exchange interactions which favour a uniform charge density on the charge stripe. As a result there is an increase in the contrast between the hole-rich and hole-poor regions as Coulombic interactions start to dominate and the integrated intensity increases. This behaviour is consistent with that reported in the lower doped systems with x-ray measurements in the previous Chapter. In region I there is no change in the inverse correlation of the charge order but there is a very small decrease in the incommensurability and it appears that the charge order is moving towards the stable value of $\varepsilon = 0.33$ as in the lower doped samples. This decrease in region I was not observed in the neutron study[4] and a possible explanation for this difference may be the that higher resolution available with x-ray measurements allows the small change to be measured. As the temperature is increased in region II the holes gain thermal energy allowing them to overcome the interactions with the lattice that fix them to the charge stripe. This lowers the hole concentration on the charge stripes and as a result the integrated intensity decreases. In region II there is no change in the inverse correlation length indicating that there is no change in the degree of stripe correlation. In region II the commensurability continues to decrease towards $\varepsilon = 0.33$ but in region II there is an increase in the gradient.

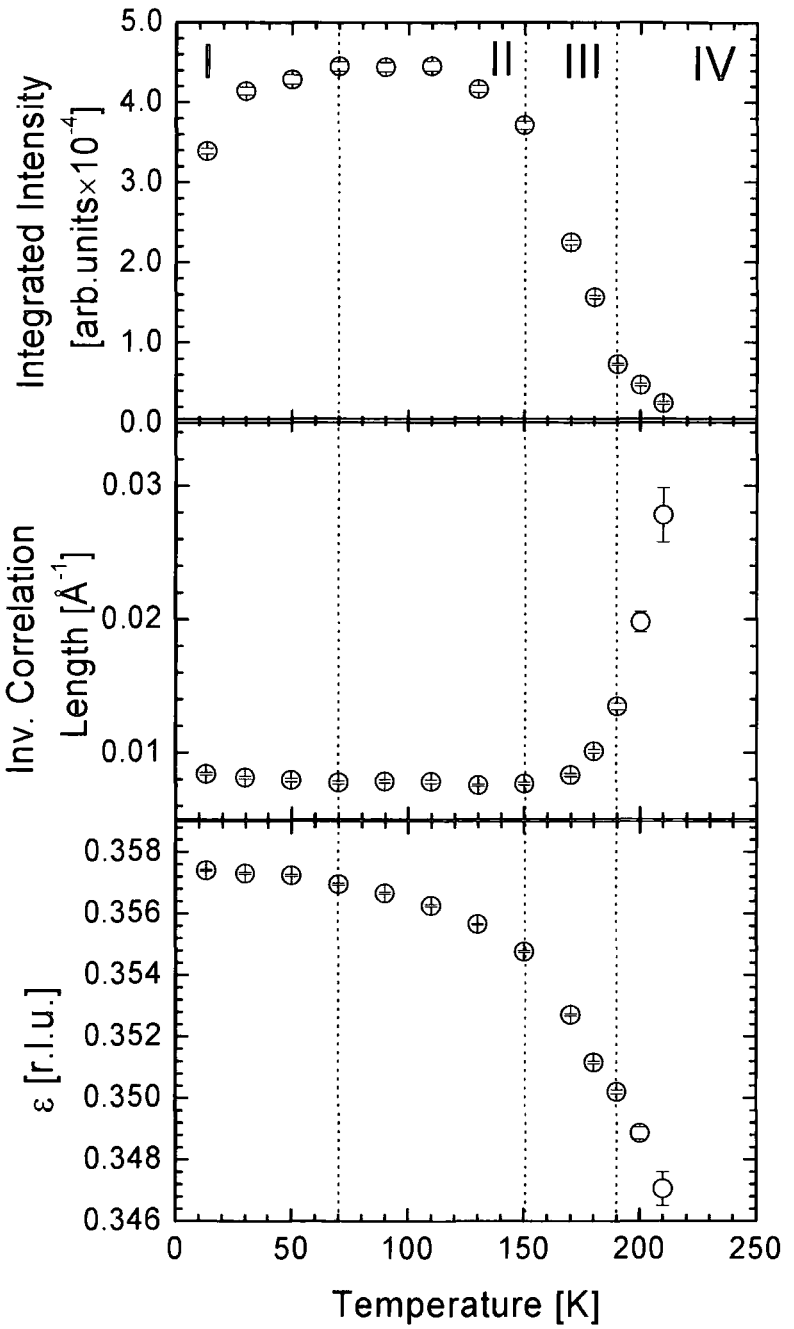

***Figure 6.6**: Integrated intensity, inverse correlation length and the incommensurability of the (4.71, 0, 5) charge order peak in the H direction. Unless shown, the error bars are smaller than the data points*

The boundary of regions II and III at 150 K corresponds to the spin ordering temperature T_N. The charge stripes are no longer stabilised by the spin stripes and coupled with the increased thermal energy they begin to vibrate, it is believed that due to this there is a sharp increase in the inverse correlation length. In region III there is a continuation in the decrease of the integrated intensity and another increase in the rate of movement towards the commensurate position as the holes continue to gain more thermal energy. In region IV above 180 K only critical scattering exists which is very weak, virtually uncorrelated and in this region ε continues to approach 0.33. The charge ordering disappears before ε reaches the stable 1/3 position. Comparing with the neutron results from Kajimoto *et al*[4]. we find that the results are very similar except for the initial increase in the intensity observed in our results and the slight decrease in the commensurability in Region I. Possible explanations for the difference in the behaviour of the intensity have been discussed in the previous chapter.

To summarise, the charge ordering in the 0.40 doped system shows the same behaviour as in the lower doped samples with the commensurability tending towards 0.33 as the temperature is increased. This is indicative that the 0.33 position is also the most stable configuration for charge order in the 0.40 doped system with no evidence for it stabilising at any other value. The charge stripe order in the 0.40 doped sample is very similar that observed in the 0.30 and 0.275 doped systems. Table 6.1 shows the inverse correlation lengths of the 0.40, and those of the 0.30 and 0.275 taken from Ghazi to illustrate the similarities between the charge order in these systems. The charge order in the 0.4 system is strong, well correlated and slightly incommensurate. However, in the 0.40 system the incommensurability decreases towards 0.33, as opposed to the increase in the $x = 0.33$ and 0.275 systems.

x	H [Å^{-1}] $\times 10^{-3}$	K [Å^{-1}] $\times 10^{-3}$	L [Å^{-1}] $\times 10^{-3}$
0.40	7.97 ± 0.12	4.32 ± 0.15	30.1 ± 0.5
0.275	8.01 ± 0.14	4.89 ± 0.04	24.7 ± 0.3
0.30	7.56 ± 0.08	4.69 ± 0.09	18.8 ± 0.4

***Table 6.1**: Inverse correlation lengths of the x = 0.40, 0.30 and 0.275 samples at 20 K*

Similar to the x = 0.30 and 0.275 systems the charge stripes are weaker and less correlated than in the x = 0.33 system and it displays a lower charge ordering temperature of 210 K compared to 240 K in the x = 0.33 system. A question that needs to be answered is whether the 0.33 position is the favoured position for the charge order for *all* doping levels in the regime $0.33 < x < 0.5$, or is there a point where the $\varepsilon = 0.5$ position becomes the stable configuration for the charge order.

6.4 Results for $x = 0.48$

By studying the x = 0.48 system it was intended to determine whether the charge order still favoured the ε = 0.33 position or if it favours the ε = 0.5 position. It was also intended to determine if it showed the rearrangement of the checkerboard and stripe charge order. The x = 0.48 sample was pre-aligned and cut so the <101> direction was surface normal and it was mounted so the <010> direction corresponded to the beam direction. The sample was aligned utilising the (4, 0, 4) and (6, 2, 6) reflections as the *or0* and *or1* reflections respectively. The sample was of good quality with a rocking curve width of 0.04°. Resolution scans carried out on the (4, 0, 4) Bragg peak gave the inverse correlation lengths as 0.0032 $Å^{-1}$ in H, 0.0045 $Å^{-1}$ in K and 0.0063 $Å^{-1}$ in L. The sample was cooled to base temperature of 12 K and a search carried out for charge order at the expected stripe and checkerboard positions. No evidence of checkerboard charge order was observed but incommensurate charge order was observed at a modulation of (0.83, 0, 1) corresponding an incommensurability of ε = 0.415. A search for checkerboard order was carried out at 200 K which corresponded to the temperature where the checkerboard charge order was expected from the literature to be at its maximum intensity. However, no checkerboard order was discovered, and from this we concluded that the 0.48 sample does not display checkerboard charge order.

The strongest charge order peak was observed at (4.84, 0, 5) and this was measured as a function of temperature to determine the inverse correlation length, incommensurability and integrated intensity. The peak was scanned in the H, K and L directions at 12 K which are shown in Figure 6.7. The charge stripe ordering was fitted to a Lorentzian squared lineshape in the H, K and L directions.

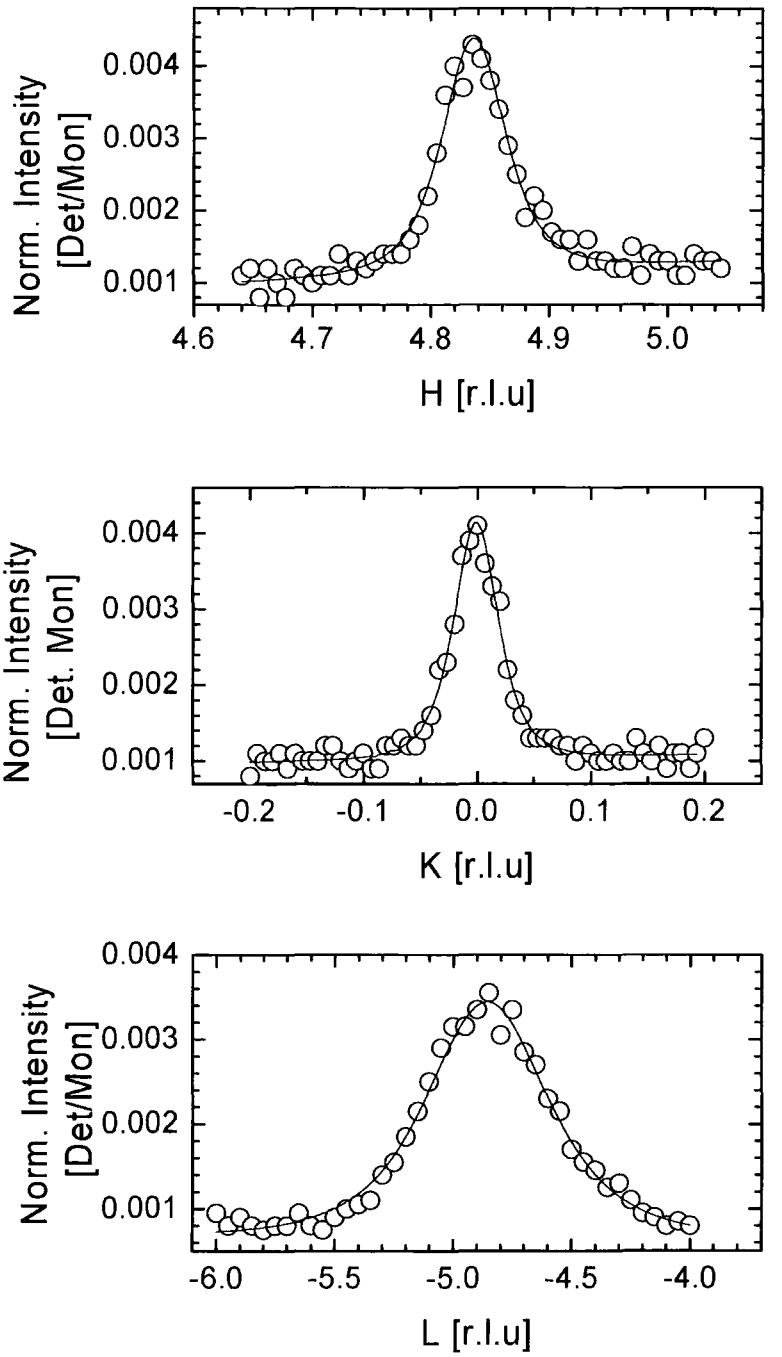

***Figure 6.7**: Scans through H, K and L directions of the (4.84, 0,-5) charge order peak at 12 K. The solid line is a fit to the experimental data using a Lorentzian squared lineshape.*

In the *H* and *K* directions the charge ordering showed similar inverse correlation lengths. In the *L* direction the inverse correlation length was significantly larger – demonstrating the two dimensional nature of the charge stripe order. The charge stripes were significantly broader than the Bragg peaks in all directions, with the structure having an inverse correlation length ~ 12 times sharper in the *H* and *K* directions than the charge and ~ 30 times sharper than the charge in the *L* direction. The charge stripes were weak, poorly correlated in all directions and exist in a charge stripe glass very similar to that observed in the $x = 0.20$ system. A comparison of the inverse correlation lengths of the stripe order in the $x = 0.48$ and 0.20 doped systems is shown in Table 6.2.

x	H [Å^{-1}] $\times 10^{-2}$	K[Å^{-1}] $\times 10^{-2}$	L[Å^{-1}] $\times 10^{-2}$
0.20	4.18 ± 0.12	4.67 ± 0.13	20.9 ± 0.8
0.48	3.24 ± 0.09	4.58 ± 0.05	16.7 ± 6.9

***Table 6.2**: Inverse Correlation lengths of the x = 0.20 and 0.48 samples at 20 K.*

In both systems the stripes are poorly correlated in all directions and exist in a charge glass state. The charge stripes also are very weak in both systems typically a few hundred counts per second compared to thousands of counts per second in the $x = 0.275$, 0.30, 0.33 and 0.40 systems. The doping levels in both systems are approximately the same distance away from the 0.33 doping and they show similar intensity and inverse correlation lengths; evidence that the dependence of the stability of the charge order with doping is the same whether the doping is decreased or increased from 0.33

The temperature dependence of the integrated intensity, inverse correlation length and commensurability in the *H* direction is shown in Figure 6.8. The intensity shows similar behaviour to the lower doped samples with an initial increase in intensity between 10 and 50 K. On further heating the integrated intensity begins to decrease and above 150 K it cannot be observed above the background. The inverse correlation length shows an initial decrease on heating, clear evidence of the charge order becoming more correlated. Above 90 K the inverse correlation length begins to increase sharply and continues to do so until the charge order cannot be observed above the background.

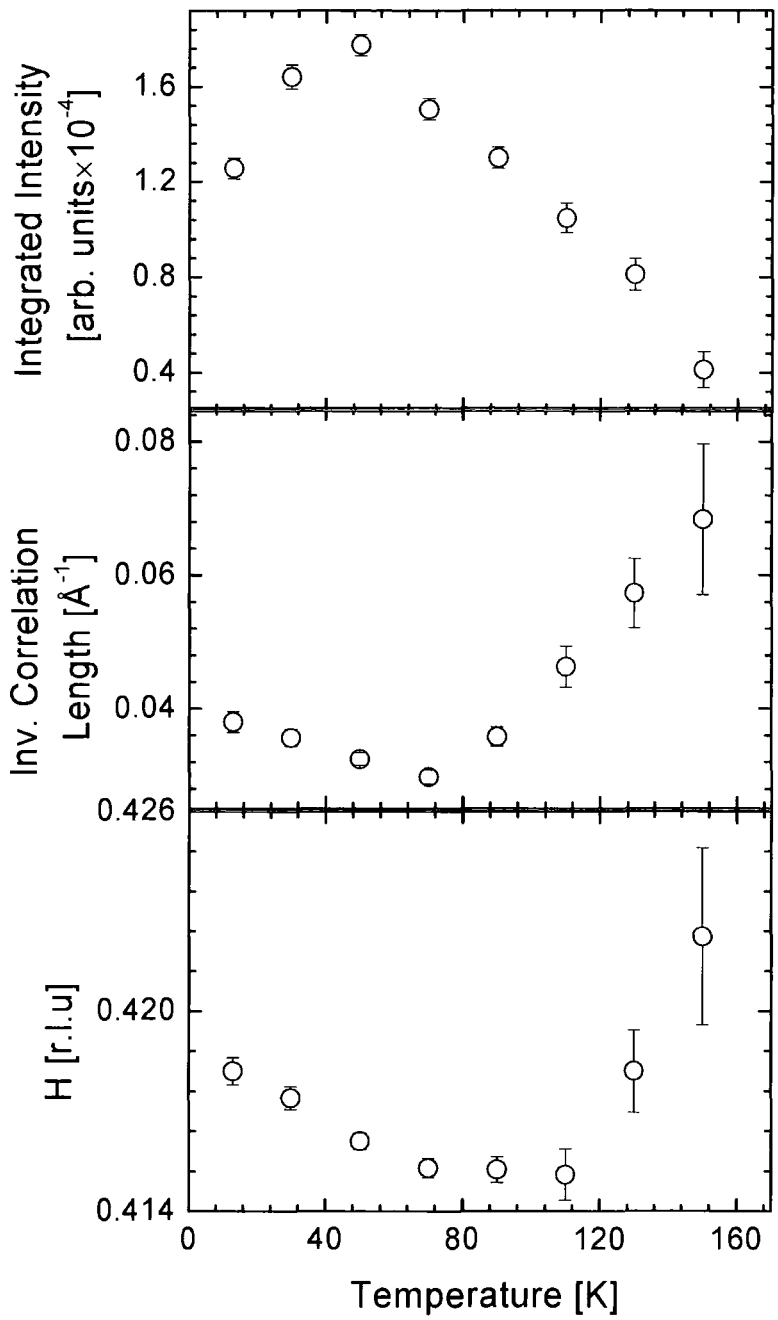

***Figure 6.8**: Integrated intensity, inverse correlation length and incommensurability of the (4.84, 0, 5) charge order peak in the H direction. Unless shown the error bars are smaller than the data points.*

Magnetization measurements carried out on the sample determined the magnetic ordering temperature, T_N, as approximately 90 K. The sharp increase in inverse correlation length above this temperature is expected due to the absence of the spin order stabilizing the charge order pattern. The charge order in the $x = 0.48$ system shows a lower transition temperature than in the $x = 0.40$ system presumably because the charge order state is less stable and hence, less thermal energy is required to overcome the interaction between the holes and the lattice that fix them to the charge stripe. The temperature dependence of the integrated intensity and inverse correlation length are qualitatively the same as observed in the lower doped systems. However, the commensurability demonstrates clearly different behaviour from the lower doped systems and this is shown in the bottom panel of Figure 6.8. The incommensurability initially decreases on heating and reaches a minimum value of $\varepsilon = 0.415$ at 90 K. At 90 K the incommensurability begins to increase and continues to increase until it disappears at 150 K with an incommensurability of $\varepsilon = 0.423$. A possible reason for the initial decrease in the commensurability is the influence of Coulomb repulsion where by the stripes will seek to maximise the distance between each other, causing the charge stripes to move further apart. Above 90 K the commensurability begins to increase as the charge stripes gain enough thermal energy to overcome Coulomb repulsion and move closer together. Whether the commensurability is moving towards $\varepsilon = 0.44$ or 0.5 cannot be determined because the charge order disappears before it reaches a stable position. However, the charge order is not moving towards the $\varepsilon = 0.33$ position and hence, is showing a clear change in behaviour from the lower doped systems. This result suggests that in the $x = 0.48$ doped system the $\varepsilon = 0.33$ position is not the most stable position for the charge order as the doping level of $x = 0.5$ is approached the charge order state enters a new regime. To summarise, the charge order in the $x = 0.48$ sample exists in a charge glass state. The charge shows the same behaviour with respect to the integrated intensity and inverse correlation length as the lower doped samples. However, in the $x = 0.48$ doped system the commensurability does not move towards $\varepsilon = 0.33$ indicating that $\varepsilon = 0.33$ is not the most stable position for charge order in the $x = 0.48$ sample. The absence of the checkerboard charge order in this doping level indicates that the checkerboard pattern can only exist in a doping range near to $x = 0.5$ at least on the low doping side of 0.5.

6.5 $x = 0.50$

The x = 0.5 doped sample was mounted in a displex cryofurnace. This allowed a temperature range from 50 – 800 K to be accessed which would be required to fully measure the checkerboard and stripe order. The same experimental setup was utilised to study the crystal as for the x = 0.40 and 0.48 samples. The crystal was aligned with the <101> direction normal to the scattering plane and the <010> down the beam direction. The sample was aligned and the UB matrix calculated from the (4, 0, -4) and (6, 2, -6) reflections as the *or0* and *or1* reflections respectively. A search was carried out around the (4, 0, -4) Bragg peak for charge stripe order and checkerboard charge order at 55 K. No evidence of checkerboard charge order was observed but a satellite was observed at (4.88, 0, -5) which was attributed to the stripe ordering with (2ε, 0, 1) with $\varepsilon = 0.44$. The sample was then warmed to 200 K and a search carried out for the checkerboard type charge order. A peak was observed at (5, 0, -5) position and this is at the expected checkerboard type charge order position (2ε, 0, 1) with $\varepsilon = 0.5$. No evidence of charge order was observed at the (4.88, 0, -5) position at 200 K so there is clearly a transition between the two charge ordered states.

Both the checkerboard and stripe order and stripe charge order were scanned in the three principal directions of reciprocal space at their most intense points – 200 K and 55 K respectively. Table 6.3 shows the inverse correlation lengths for the Bragg peak and the charge and stripe order and the ratios of the Bragg peak to the stripe and charge order.

	H [Å^{-1}]×10^{-2}	K [Å^{-1}] ×10^{-2}	L [Å^{-1}] ×10^{-2}
Stripe Order 55 K	5.33 ± 0.33	3.66 ± 0.25	38.8 ± 2.1
Check. Order 200 K	4.43 ± 0.36	4.58 ± 0.27	41.9 ± 4.5
(4, 0, -4) Bragg	0.165 ± 0.003	0.222 ± 0.009	0.382 ± 0.006
Stripe/Bragg	32.3 ± 2.1	16.5 ± 1.3	101 ± 6
Check/Bragg	26.9 ± 2.2	20.6 ± 1.5	110 ± 12

***Table 6.3**: Inverse correlation lengths measured on the (4.88,0,-5) at 55 K stripe order and the (5, 0, -5) checkerboard type charge order at 200 K. The inverse correlation length of the (4,0,-4) Bragg peak is also shown and the ratio of the inverse correlation lengths of the two types of charge order to the Bragg peak.*

In both regimes the charge order was very weak, typically tens of counts per second and there was no clear difference in maximum intensity between the two states. From Table 6.3 it can be determined that the charge order is poorly correlated in all directions and two dimensional in nature in both regimes that is the charge order exists in a charge glass. There is virtually no correlation between the planes with the charge order in both regimes being approximately 100 times less correlated than the crystal structure in the L direction. A comparison of the inverse correlation lengths between the stripe and checkerboard states reveals that there is virtually no change in the inverse correlation length beyond error in any direction between the stripe and checkerboard regimes. We conclude from this that the rearrangement of the charge from an incommensurate stripe pattern to a commensurate checkerboard pattern is not accompanied by an increase in the correlation length or in the intensity of the charge ordered state. It should be noted that the charge order in the $x = 0.5$ sample was weaker and less correlated than the $x = 0.48$ sample and from this it is concluded that with respect to the intensity and inverse correlation length there is no stabilisation of the charge ordered state.

The observation of a charge glass at high and low temperatures is in agreement with the neutron diffraction measurements. In the neutron diffraction study by Kajimoto *et al.*[5] they report the observation of both the stripe and checkerboard at low temperature but in the x-ray measurements the coexistence of the stripe and checkerboard order at 55 K was not observed. A possible explanation for this difference is that the neutrons were measuring the bulk and hence, were sensitive to more than one charge ordered domain and therefore measured a mixture of the stripe and checkerboard phases. X-rays with an energy of 12 keV are only sensitive to the near-surface qualities and this means that only one charge ordered domain may be measured.

The H direction of reciprocal space was scanned as a function of temperature to determine the mechanism by which the charge order pattern is rearranged from an incommensurate stripe order pattern to a commensurate checkerboard pattern and a schematic of the two states is shown in Figure 6.9. Specifically to determine whether there was a gradual increase in the commensurability from 0.44 to 0.5 or if the checkerboard and stripe ordering existed separately. The evolution of the charge order is shown in Figure 6.10 at a series of temperatures between 55 K and 225 K.

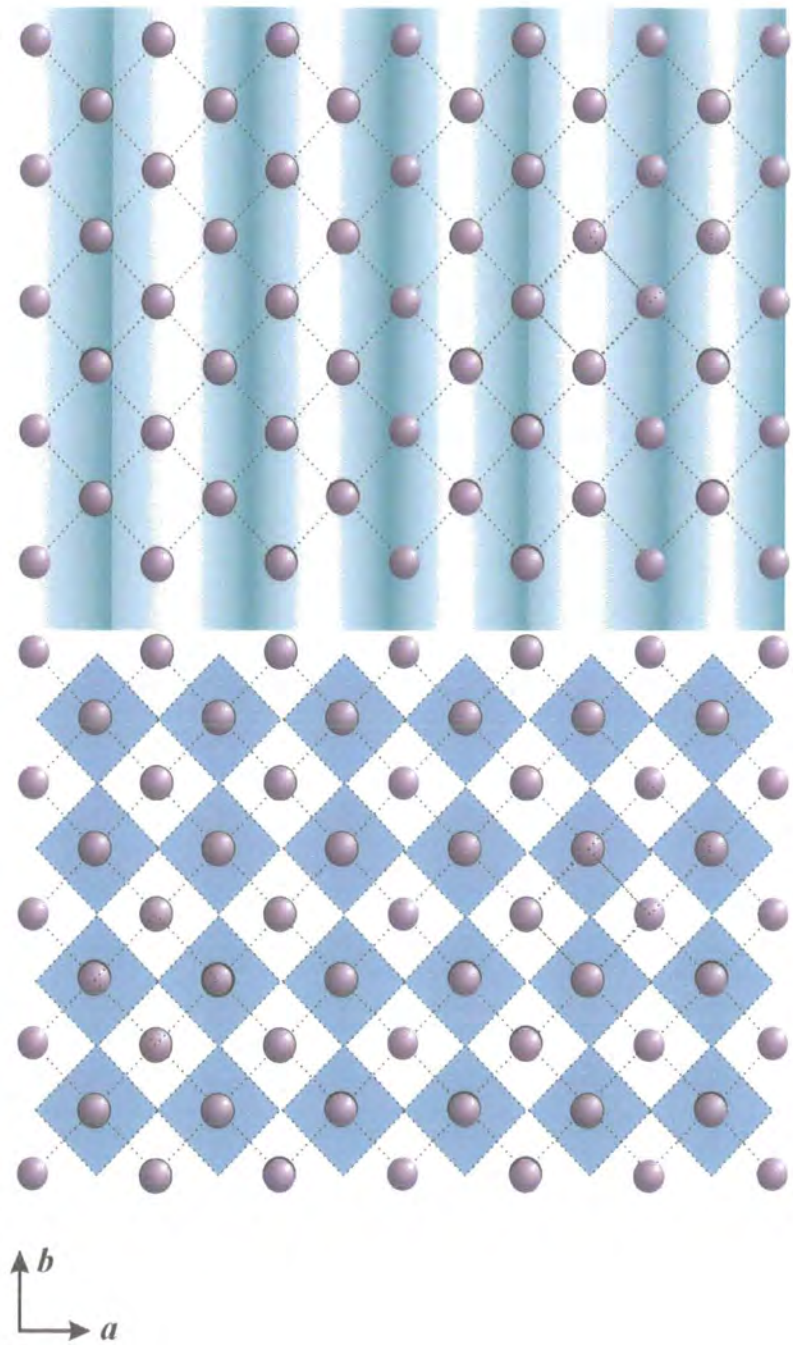

***Figure 6.9**: A possible schematic of the stripe order at a modulation of $\varepsilon = 0.44$ (top panel) and the checkerboard charge order with $\varepsilon = 0.5$. The blue shaded areas show the areas where the hole density is located. In the checkerboard pattern the holes are located on Ni sites giving an alternating Ni^{2+}/Ni^{3+} pattern. In the stripe pattern not all the holes are located on Ni sites giving an incommensurate pattern*

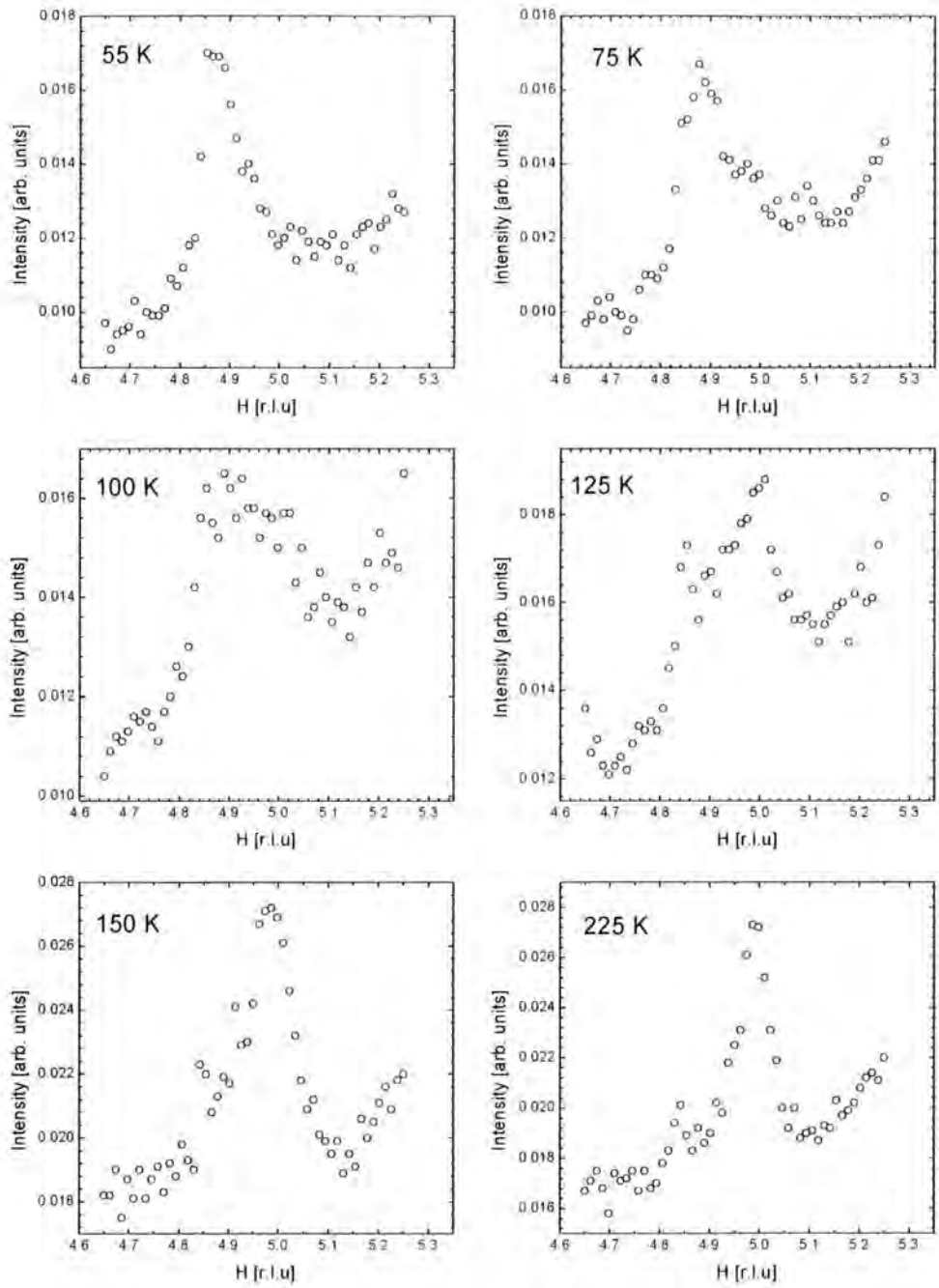

***Figure 6.10**: Scans in the H direction as a function of temperature in the range 55 – 225K.*

At 55 K only the stripe order is observed at a modulation corresponding to a commensurability of $\varepsilon = 0.44$ with no evidence of the presence of the checkerboard order. As the temperature is increased to 75 K the stripe order weakens and broadens but there is no change in the commensurability from $\varepsilon = 0.44$ and the checkerboard order is not observed. At 100 K an additional shoulder to the peak appears at the (5, 0, -5) position and we postulate that this is due to the appearance of the checkerboard order. However, this scan cannot be resolved into two separate peaks. At 125 K both the stripe and checkerboard order are observable at their respective positions but the checkerboard order is now stronger than the stripe order. It should be noted that the stripe order still shows a commensurability of $\varepsilon = 0.44$ i.e. there is no change in commensurability observed for the stripe order. At 150 K only the checkerboard order is clearly observable, however, there appears to be a shoulder on the peak that could be attributed to the stripe order. At 225 K there is no evidence for the stripe order pattern and only the checkerboard charge order is observed and appears to be sharper i.e. more correlated than at 150 K. Figure 6.11 shows the scans taken at 225 K, 125 K and 55 K in greater detail and the respective positions of the stripe and checkerboard order are highlighted with red and blue dotted lines respectively. Possible models for the charge order in the low and high temperature regimes and the rearrangement of the charge order will be discussed in section 6.6

The checkerboard charge order was measured as a function of temperature in the H direction in the temperature range 150 – 440 K. It was not possible to accurately measure the checkerboard order below this temperature because it could not be resolved. From these measurements the temperature dependence of the integrated intensity, inverse correlation length and commensurability were determined. The integrated intensity as a function of temperature is shown in Figure 6.12. The error bars shown were obtained from the errors on the peak fits. The inverse correlation length as a function of temperature is shown in Figure 6.13 and the error bars are obtained from the errors on the fits.

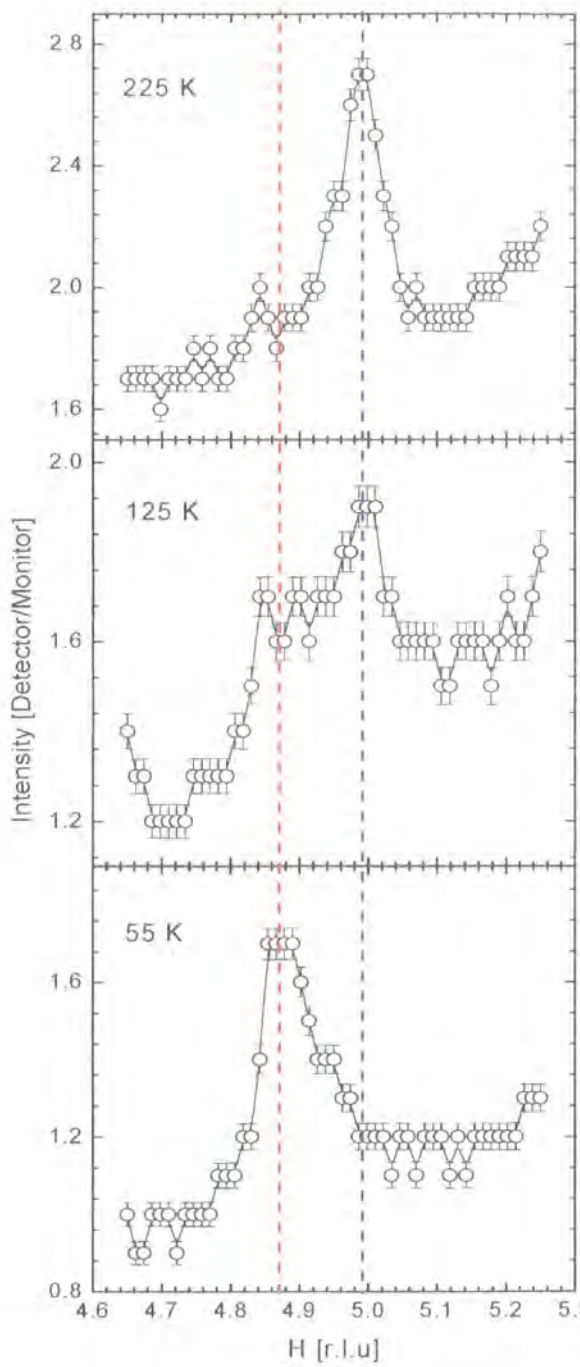

Figure 6.11: *Scans of the charge order at 225 K, 125 K and 55 K. The positions of the stripe and checkerboard order are outlined by the red and blue lines respectively.*

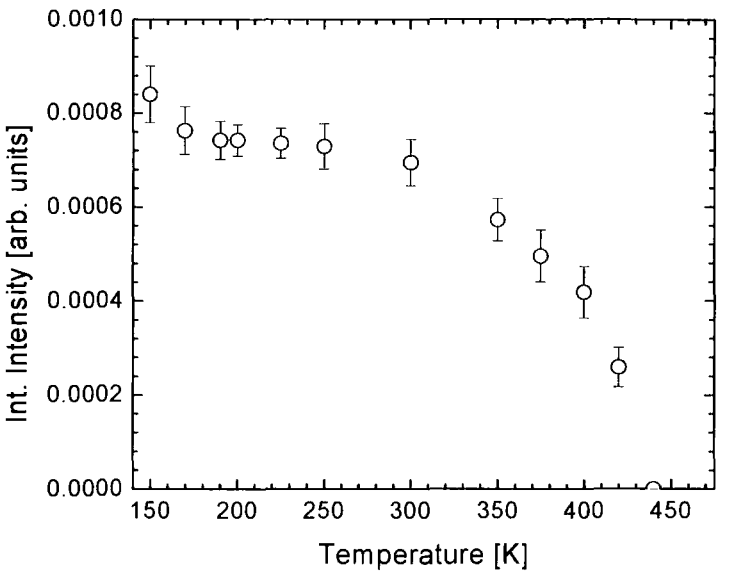

Figure 6.12: *Integrated intensity as a function of temperature of the (5, 0, -5) checkerboard charge order peak.*

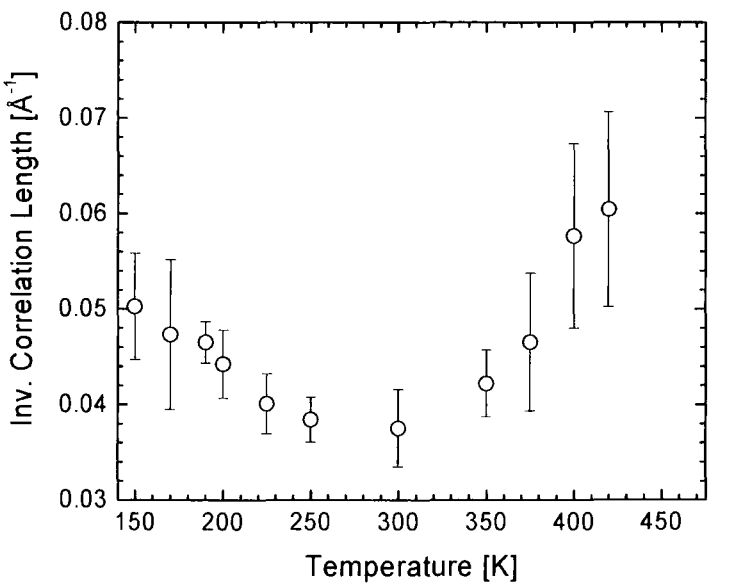

Figure 6.13: *Inverse correlation length as a function of temperature of the (5, 0, -5) checkerboard charge order peak*

Referring to the data in Figures 6.12 and 6.13 the integrated intensity remains constant in the temperature range 150 – 250 K, however the inverse correlation length of the charge order in this temperature range shows a decrease indicating a stabilisation of the charge ordered state. As the temperature is increased above 300 K the integrated intensity begins to decrease and this is accompanied by an increase in the inverse correlation length of the charge order which continues until the charge order cannot be observed above background at 440 K. This transition temperature is relatively close to that reported by Kajimoto *et al.* of 480 K but the behaviour of the inverse correlation length is not reported in the neutron study.

Despite the weak and diffuse nature of the charge order in the $x = 0.5$ system the checkerboard pattern is thermally stable as demonstrated by the transition temperature of 440 K which is significantly higher than that reported in the $x = 0.33$ system of 240 K. The checkerboard charge order pattern is very similar to that observed in the half doped cobaltate by Zaliznyak *et al.* [7] in which the charge order exists in a two dimensional charge glass with a transition temperature of over 800 K.

6.6 Discussion

If only the charge order is considered the most stable configuration is the checkerboard order pattern and this begs the question as to why the incommensurate stripe order phase is favoured at low temperatures. Referring to the bottom panel of Figure 6.1 it has been shown that there is a deviation from the $n_h = \varepsilon$ law as the doping is moved away from $n_h = 0.33$ and this deviation increases as the doping is moved away from 0.33. This occurs because the stripe order favours the stable $\varepsilon = 0.33$ position where the charge and spin stripes coincide i.e. "a commensurability effect". For this reason the commensurability of the charge and spin stripe order are observed at $\varepsilon = 0.44$ which is lower than expected from the doping, but consistent with the neutron measurements. We postulate that in the half doped system there are two competing effects. The first favours the commensurate 0.33 position because that is where the charge and spin stripes coincide, which stabilises the stripe pattern. The second effect is that of

Coulomb interactions which favours the checkerboard pattern with $\varepsilon = 0.5$ and is observed in the isostructural layered cobaltates and manganites.

In the lower doped levels we have shown the stripe order is stabilised by the magnetic order with a significant increase in the inverse correlation length observed in all doping levels above T_N. The neutron measurements by Freeman *et al.*[8] and Kajimoto *et al.*[5] determined T_N as 80 K and it is above this temperature that the stripe order weakens considerably and the checkerboard charge order first appears. We suggest from this that the presence of the spin order at low temperatures stabilises the incommensurate stripe pattern. Kajimoto *et al.* suggest a model in which a discommensuration which contains 1 hole per 1.5 unit cells is introduced into the checkerboard charge order pattern at low temperatures and as shown in Figure 6.14.

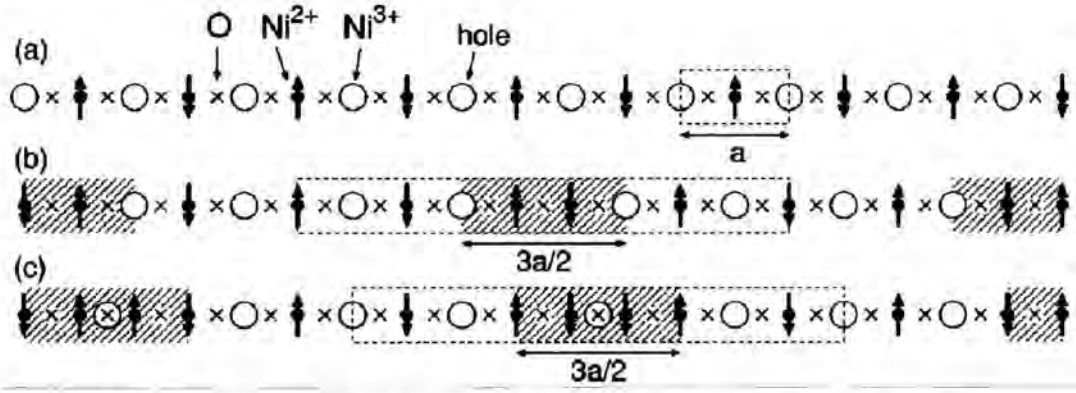

***Figure 6.14**: The Kajimoto model of the charge ordering along the 1, 0, 0 direction for (a) the checkerboard pattern and for the incommensurate charge order in (b) and (c). The charge order unit cell is shown by the dashed lines. The discommensuration is shown by the shaded region. The holes in the discommensuration are located on the metal sites in (b) and the oxygen sites in (c). Taken from Kajimoto et al.*[5]

This introduces Ni^{2+}- Ni^{2+} bonds and Ni^{2+}-hole-Ni^{2+} bonds into the charge order pattern. The energy gain from the spin exchange interactions between these bonds is expected to be significantly larger than that of the Ni^{3+}- Ni^{2+} bonds which are the only bonds in the checkerboard pattern and hence, the spin exchange interactions favour the stripe state. However, there are two problems with this model. The first is that the model does not conserve charge at the commensurate/incommensurate boundary. Secondly, this

would produce spin peaks at a modulation of (0.5, 0, 0) and this is not observed experimentally in either the studies by Freeman *et al.* or by Kajimoto *et al.*. Boothroyd[9] suggested a model in which the charge mainly sits on the Ni sites but occasionally jumps to the oxygen sites, introducing a discommensuration into the charge order pattern as shown in Figure 6.15.

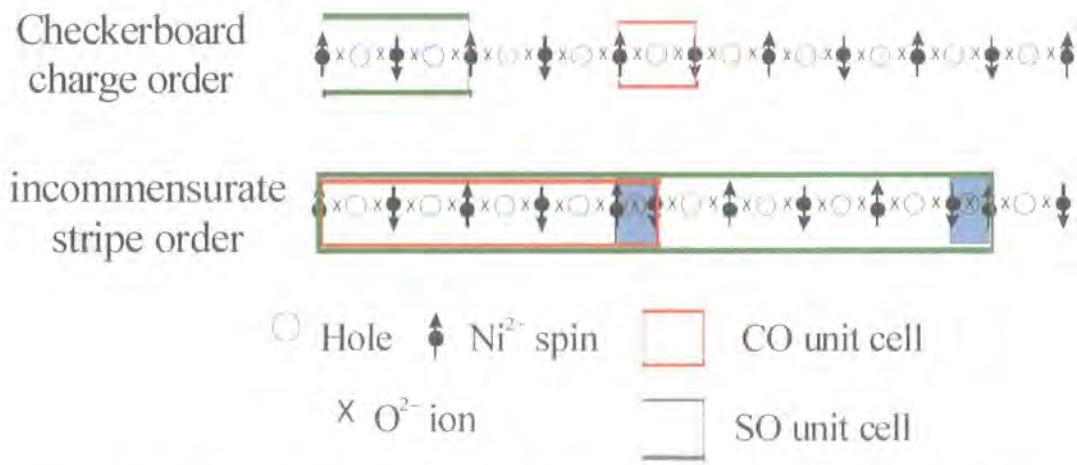

Figure 6.15: *Proposed schematic of the charge order and spin order in the checkerboard and stripe order phases. The position of the discommensuration is shown by the blue shaded regions. The CO unit cell is shown by the red outline and the spin order unit cell is shown by the green outline. In the incommensurate pattern the hole concentration averages 0.44 (4/9) per unit cell.*

In this model there is no commensurate/incommensurate boundary in the charge order pattern and hence, charge is conserved. However, in this model Ni^{2+}-hole-Ni^{2+} bonds are present and the energy gain associated with the spin exchange interactions in these bonds favours an incommensurate pattern. As required in the model above, the average hole concentration per unit cell is 0.44. A recent TEM study on $La_{1.725}Sr_{0.275}NiO_4$ by Li *et al.*[10] provided evidence that the charges can relocate to the oxygen sites in the nickelate system. Li *et al.* reported that while most of the holes were located on the Ni sites there were small regions in which the holes were also found on the oxygen sites and this suggests that the model postulated above is a viable one. In theory, TEM measurements on the half doped system may determine if this model is accurate but in this

incommensurate phase there is a delicate balance between the Coulomb repulsion, antiferromagnetic exchange interactions and the local lattice distortions.

Below T_N the spin exchange interactions dominate and hence, the stripe order phase dominates. As the temperature is increased above T_N the spin exchange interactions weaken and in addition the holes gain thermal energy and can overcome the spin exchange interactions and begin to relocate to the checkerboard position. This is in line with the observed results because the checkerboard pattern is not observed below T_N. As the temperature is increased further an increasing number of holes move to the checkerboard position until at 150 K all holes are located at the checkerboard position. The checkerboard order shows a decrease in inverse correlation length between 150 K and 225 K and a possible explanation is that the there may still be some competition between the stripe and checkerboard phases. The checkerboard charge order pattern is stabilised by the interaction with the lattice at the commensurate position resulting in the charge being thermally very stable. As the temperature is increased above 300 K the integrated intensity begins to decrease and the inverse correlation length begins to increase as the holes acquire sufficient thermal energy to overcome the interactions that fix them to the lattice and as a result the integrated intensity and correlation begins to decrease. By 440 K the charge order cannot be observed above background. The charge order in the x = 0.5 system is very weak and diffuse in comparison to the x = 0.33 system and we postulate that it is the coincidence of the charge and spin order that stabilises the charge order pattern accounting for the small inverse correlation length in the x = 0.33 system. As the doping is moved away from x =0.33 the charge and spin positions diverge and hence, in the x = 0.5 system only weak diffuse charge order is observed.

To summarise, we suggest that at low temperatures the stripe order pattern is stabilised by the spin stripe order and the associated spin exchange interactions. The most stable configuration for the stripe order is at ε = 0.33 where the charge and spin stripes coincide and as a result of this effect the stripe order is observed at lower wavevector than expected of the doping with ε = 0.44. At high temperatures the holes have acquired sufficient thermal energy to overcome the effects of the spin exchange interactions and the checkerboard pattern dominates.

6.7 Review of the Charge Ordering in the Nickelates

Finally we review the behaviour of the charge ordering in $La_{2-x}Sr_xNiO_4$ in the doping region $0.2 \leq x \leq 0.5$. For this discussion the results published in the thesis of M. E Ghazi which focussed on the 0.33, 0.30 and 0.275 samples will be included. Table 6.4 shows the inverse correlation for samples in the doping region $0.20 < x < 0.50$ in the *H, K, L* directions at 20 K unless specified and as a comparison the Bragg peak inverse correlation length of for the (4, 0, 4) Bragg peak is also shown. The comparison is valid because all of the crystals were of a similar quality and grown in a similar method. As the doping moves away from $x = 0.33$, in either direction, the inverse correlation length increases indicating the charge order is becoming less correlated away from this commensurate value. The charge ordering is most stable in the $x = 0.33$ sample. This is attributed to firstly, the charge and spin ordering coinciding at the same point in reciprocal space, and secondly the stabilising effect of the coupling between the charge order and the lattice at a commensurate value. In the $0.275 < x < 0.40$ regime the charge ordering exists in strong, well correlated state with relatively high charge ordering and spin ordering temperatures but lower than in the 0.33 sample.

X	*H* [Å^{-1}]×10^{-3}	*K* [Å^{-1}]×10^{-3}	*L* [Å^{-1}]×10^{-3}
0.20	41.8 ± 1.2	46.7 ± 1.3	209 ± 8
0.225	28.8 ± 0.7	14.5 ± 0.4	79.1 ± 4.2
0.25	18.2 ± 0.2	14.7 ± 0.3	66.4 ± 0.7
0.275	8.01 ± 0.14	4.89 ± 0.04	24.7 ± 0.3
0.30	7.56 ± 0.08	4.69 ± 0.09	18.8 ± 0.4
0.333	6.10 ± 0.07	2.66 ± 0.03	54.2 ± 0.4
0.40	7.97 ± 0.12	4.32 ± 0.15	30.1 ± 0.5
0.48	32.4 ± 0.9	45.8 ± 0.5	167 ± 7
0.50 stripe (50K)	53.3 ± 3.3	36.6 ± 2.5	388 ± 21
0.50 check (200K)	46.6 ± 5.0	45.8 ± 2.7	418 ± 45
Bragg	1.89 ± 0.04	1.39 ± 0.02	4.01 ± 0.01

Table 6.4 *Inverse correlation length of the charge order in doping levels $0.2 \leq x \leq 0.5$. Unless specified all measurements carried out at 20 K*

However, the charge ordering is incommensurate in these samples and the incommensurability changes with temperature. As the temperature is increased the charge stripes gain more thermal energy enabling them to overcome coulomb repulsion and move towards the commensurate value of $\varepsilon = 1/3$. For doping levels of $x < 0.275$ and $x > 0.40$ the charge ordering is weak, poorly correlated and incommensurate - the charge ordering exists in a charge glass state. It should be noted that in the $x = 0.50$ sample there is no stabilisation of the charge ordered state with respect to the intensity and inverse correlation length. In fact the charge ordering is actually less correlated then in the 0.48 sample i.e. it is following the trend that the charge ordered state is weaker the greater the divergence from the $x = 0.33$ doping level. To illustrate this Figure 6.16 shows the inverse correlation length in the H direction as a function of doping. All measurements were made at 20 K with the exception of the 0.5 sample which was made at 50 K.

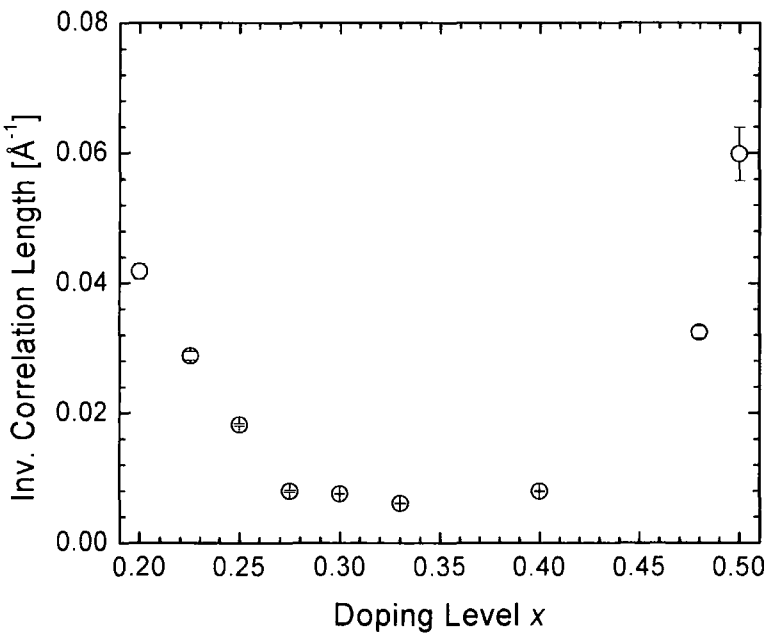

Figure 6.16: *Variation of the inverse correlation length in the H direction as a function of doping at 20 K. (Exception is the 0.5 measurement which was made at 50 K)*

Secondly, the behaviour of the commensurability is discussed. The temperature dependence of the commensurability is shown for all samples in Figure 6.17.

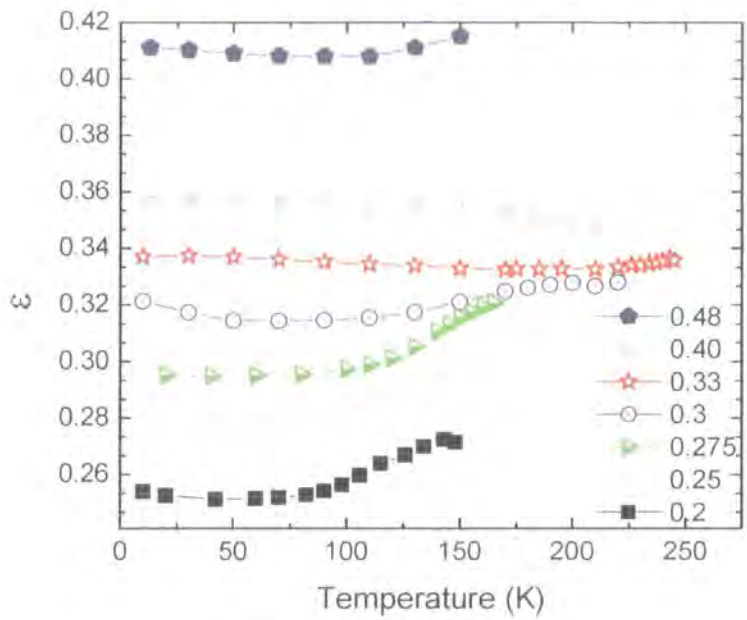

***Figure 6.17**: Commensurability in the nickelate system as a function of temperature in the doping region 0.20 – 0.48.*

In the x = 0.20, 0.225, 0.25, 0.275 and 0.30 samples the commensurability tends towards the stable 0.33 value but in each system it disappears before it can reach the stable ε = 0.33 position. It should be noted that the same effect (although to a much smaller degree) was observed by Ghazi *et al.* in the x = 0.33 sample with a stabilisation in the charge order pattern when it reached the commensurate position. In the x = 0.40 doped sample the charge order occurred at a position with ε > 0.33 but on heating the charge order also moved towards the commensurate position of ε = 0.33. However, in x = 0.48 the commensurability does not follow the pattern of the charge order moving towards 0.33; instead it actually increases slightly with temperature. At this doping level it is possible that the 0.33 position is not the most stable configuration for the charge in this doping level. We postulate that the charge order is on boundary of the charge stripe

state and the checkerboard charge order state and as the holes gain more thermal energy they attempt to move towards the stable $\varepsilon = 0.5$ position. The charge order in the $x = 0.48$ doped sample disappears before the stable checkerboard pattern can form.

6.8 Conclusions

The results have shown that as the doping moves away, in either direction, from $x = 0.33$ the charge ordering becomes weaker, less correlated and incommensurate. In the $x = 0.40$ sample the charge stripe order is intense and well correlated and shows similar properties to the $x = 0.30$ and 0.275 systems and the commensurability displayed a movement towards the stable $\varepsilon = 0.33$ configuration as in the lower doped samples. The charge stripe order in the $x = 0.48$ system existed in a charge stripe glass similar to the x = 0.20 doped system which is characterised by weak, poorly correlated charge stripes and displayed a similar charge ordering temperature. However, the commensurability does not tend towards $\varepsilon = 0.33$ with temperature and it is postulated that the charge ordering is entering a new regime It should be noted no evidence of checkerboard charge order was observed in the $x = 0.48$ doped sample indicating the critical concentration for checkerboard charge order is very close to a doping level of 1/2

In the $x = 0.5$ system the stripe order dominates at low temperatures and checkerboard charge order dominates at high temperatures in agreement with neutron measurements. This most likely occurs because the spin ordering favours the stripe order phase because the spin exchange interactions stabilise the incommensurate stripe order. Evidence for this is that above the spin ordering temperature of 80 K the stripe order collapses and the charge order begins to rearrange itself into the checkerboard pattern which is the most stable configuration for charge ordering alone. There was no difference in the correlation length or the intensity of the two charge states within the plane, or between planes. The commensurability of the stripe order does not increase from $\varepsilon = 0.44$ to 0.5 instead above T_N the holes begin to move from the stripe to the checkerboard position and there is a region in which the two states co-exist. The checkerboard state is very stable thermally but there is no increase in correlation with respect to the lower doped samples and in fact

the charge order is less correlated than in the 0.48 sample. This follows the expected behaviour with the charge order becoming less correlated the greater the divergence from a doping of $\varepsilon = 0.33$.

Questions still remain as to why the stripe order favours a modulation of $\varepsilon = 0.44$ and levels off at this value. In theory high resolution TEM analysis of the half doped system should allow a better understanding of the charge ordered pattern and may explain why the stripe order favours a modulation of $\varepsilon = 0.44$. What is clear is that in the half-doped system there is delicate balance between Coulomb repulsion, antiferromagnetic exchange, and local lattice distortions.

6.9 References

1 H. Yoshizawa, T. Kakeshita, R. Kajimoto, *et al.*, Physical Review B **61**, R854 (2000)

2 C.-H. Du, M. E. Ghazi, Y. Su, *et al.*, Physical Review Letters **84**, 3911 (2000).

3 M. E. Ghazi, P. D. Spencer, S. B. Wilkins, *et al.*, Physical Review B submitted (2004).

4 R. Kajimoto, T. Kakeshita, H. Yoshizawa, *et al.*, Physical Review B **64**, 144432 (2001).

5 R. Kajimoto, K. Ishizaka, H. Yoshizawa, *et al.*, Physical Review B **67**, 014511 (2003).

6 K. Yamamoto, K. Ishizaka, E. Saitoh, *et al.*, Physical Review B **67**, 014414 (2003).

7 I. A. Zaliznyak, J. P. Hill, J. M. Tranquada, *et al.*, Physical Review Letters **85**, 4353 (2000).

8 P. G. Freeman, A. Boothroyd, D. Prabhakaran, *et al.*, Physical Review B **66**, 212405 (2002).

9 A. Boothroyd, (Personal Communication).

10 J. Li, Y. Zhu, J. M. Tranquada, *et al.*, Physical Review B **67**, 012404 (2003).

Chapter 7

Soft x-ray Diffraction study of Magnetic Ordering in Holmium

7.1 Introduction

The usual technique for the determination of magnetic structures and correlations is single crystal neutron diffraction. Due to the associated magnetic moment and high penetration of neutrons they provide highly accurate information on the magnitude and direction of complex spin arrangements. X-rays interact with the magnetic moments but the interaction is typically 10^{-8} times weaker than the charge scattering. For this reason the majority of studies on the magnetic structure within systems were carried out using neutron diffraction techniques.

However, in 1972 de Bergevin and Brunel demonstrated that x-ray diffraction could be used to observe magnetic order effects in the cubic antiferromagnet NiO using a copper x-ray tube[1]. They observed very weak reflections at a modulation of (½, ½, ½) associated with the magnetic order which were observed to disappear at the Néel temperature. The development of synchrotron sources in the 1970s and 1980s meant that very intense photon fluxes became available. This intensity combined with the polarisation and tunability available meant that synchrotron sources were ideal for the study of magnetic order. This has enabled the magnetic structure in a variety of systems to be probed using resonant x-ray magnetic diffraction. By tuning the incoming x-ray energy to absorption edges that directly probe the bands where the magnetic ordering occurs there are huge resonant enhancements in the scattered intensity. The first system to be studied using the resonant x-ray magnetic scattering technique was the rare-earth element holmium (Ho). Gibbs *et al.* reported a 50 fold enhancement of the scattered intensity from the magnetic order at the Ho L_{III} edge[2]. This confirmed that the resonant enhancement could make studies of the magnetic order viable with x-ray diffraction. The technique has been successful in studying magnetic order especially in the lanthanides

and actinides where a resonant enhancement of 6 orders of magnitude has been reported in UAs by McWhan *et al.*[3, 4] at the U *M* edges.

Holmium is a rare earth metal and has a hexagonal closed packed structure with lattice parameters of $a = b = 3.57$Å and $c = 5.61$ Å. In the ground state there are 10 electrons in the $4f$ shell and three electrons in the $5d$ and $6s$ levels and it has a large magnetic moment of approximately 10 μ_B per atom. The first detailed studies of the magnetic structure of holmium as a function of temperature and magnetic field were carried out in the 1960s by Koehler *et al.* [5, 6] using neutron diffraction. It was reported that below the Néel temperature of ~ 133 K holmium orders antiferromagnetically with a near perfect spiral spin structure. The magnetic moments form ferromagnetic sheets within the basal planes and magnetic reflections along the hexagonal c-axis result from a gradual rotation of the magnetic moments from layer to layer and a schematic of this is shown in Figure 7.1.

These magnetic peaks split symmetrically around the (0, 0, L) Bragg peaks consistent with a spiral modulation. As the temperature is decreased from 133 K the magnetic modulation wavevector decreases from $\tau \sim 0.3$ to $\tau = 1/6$ at 20 K. At a T_C of approximately 20 K the system undergoes a first order phase transition into a conical spiral phase with a ferromagnetic component directed along the c-axis and this structure was also confirmed in later neutron studies by Felcher[7] and Pechan[8]. Despite the weak interaction between x-rays and the magnetic structure the large magnetic moment in holmium made it a very attractive system to study with x-ray diffraction. In 1985 Gibbs *et al.*[9] reported the successful observation of the magnetic order in holmium with non-resonant x-ray scattering at a synchrotron source. They compared the results with neutron scattering data on the same sample and determined that the x-ray and neutron measurements were in agreement with respect to the temperature dependence of the position and intensity. In addition the x-ray measurements provided significantly greater resolution allowing very small changes in the wavevector to be measured revealing previously unobserved behaviour in the modulation of the magnetic order reflections. A paper published by Blume [10] suggested that interesting magnetic effects could occur near to an absorption edge. The success of the non-resonant experiment led to the study of holmium using resonant x-ray scattering.

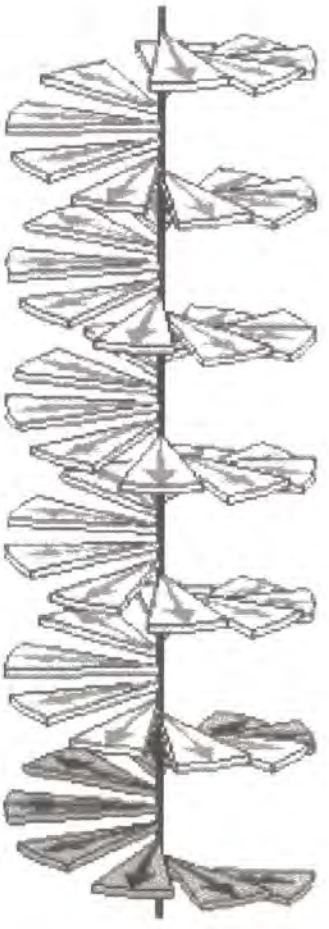

***Figure 7.1**: Schematic of the helical magnetic order in Holmium. The moments lie in planes normal to the c-axis and the relative orientations are shown by the arrows. The shaded parts illustrate the magnetic unit cell taken from* [11]

In 1988 Gibbs *et al.*[2] carried out resonant x-ray scattering measurements of the magnetic order at the Ho *L* edges which occur in the 8 – 10 keV range. They reported a fiftyfold resonant enhancement in the scattered intensity around the Ho L_{III} edge which occurs at 8.067 keV for the (0, 0, 2+τ) magnetic reflection where τ is the magnetic spiral wavevector. The observation of the 2nd, 3rd and 4th resonant integer harmonics at positions of 2+2τ, 2+3τ and 2+4τ was also reported which were not observed off resonance.[2, 12] These resonances originate from the excitation of an electron from a core level to either an unfilled atomic shell or narrow band above the Fermi level; the excited

state then decays with the emission of a photon. The magnitude of the resonance is dependent on the overlap between the initial state and excited state wavefunctions and the coupling between these states is controlled by optical selection rules. This is discussed for holmium by Hannon *et al.*[13] in which the resonant enhancement is due to multipole transitions, specifically the electric dipole and quadrupole transitions in holmium. A dipole transition involves a change in the orbital angular momentum of $\Delta l = \pm 1$ and for a quadrupole transition a change in the orbital angular momentum of $\Delta l = \pm 2$. The coupling between the initial and final states is therefore weaker in a quadrupole transition giving a transition rate that is significantly lower than that for a dipole transition. Therefore, the associated resonant enhancement is significantly smaller than that associated with a dipole transition to the same state. At the Ho L_{III} edge the dominant contributions to the resonant scattering are electric dipole transitions (E1) from the $2p$ to $5d$ states and quadrupole transitions (E2) from the $2p$ to $4f$ states. In holmium it is the $4f$ levels that are magnetically ordered but due to exchange interactions with the magnetic order in the $4f$ levels the $5d$ levels are weakly split by the magnetic order. The $4f$ states are probed at the Ho L edge but because it is a quadrupole transition, the resonant enhancement is of the same order of magnitude as the dipole transition to the $5d$ levels despite probing the levels where the magnetic ordering occurs. A much larger resonant enhancement would occur if the $4f$ levels were probed by a dipole transition and this will be discussed later in the chapter. Polarisation analysis carried out on the $(0, 0, 2+\tau)$ peak revealed the π polarised component to be significantly larger than the σ polarised component. There are only two harmonics associated with the dipole transition from the $2p - 5d$ levels and they occur at τ and 2τ whereas there are four harmonics associated with the quadrupole transition from the $2p - 4f$ levels at τ, 2τ, 3τ and 4τ. Analysis of the energy and polarisation dependence provided strong evidence that the data fitted the model of resonance exchange scattering.[12] This technique was applied to other rare earth systems including dysprosium (Dy)[14] and thulium (Tm)[15] and in each a similar resonant enhancement to that in holmium was reported at the respective L edges. The resonant enhancement available has also enabled the study of the magnetic order in thin films.

The electronic states in which the most significant resonant enhancements were predicted for those involving the 3*d* bands in the transition metals, the 4*f* bands in the lanthanides and the 5*f* states in the actinides because these are the states associated with the magnetism. UAs was studied at the M_{IV} and M_V edges of uranium which correspond to energies of approximately 3.7 keV and 3.5 keV respectively. A resonant enhancement of approximately seven orders of magnitude was observed at the M_{IV} edge and five orders of magnitude at the M_V edge and this allowed the magnetic structure of UAs to be investigated thoroughly. Similar resonant enhancements would be expected at the *L* edges of the transition metals and at the *M* edges of the rare-earth metals such as holmium. In a review paper by Vettier[16] an estimate is made of the resonant magnetic scattering in characteristic magnetic elements. In iron the scattering at the *L* edge is predicted to be 10% that of UAs at the uranium *M* edges. At the rare earth *M* edges the amplitude is predicted to be ten times larger than that at U *M* edges which is in agreement with the predictions by Hannon *et al.*[13]. However, only the actinide *M* edges that probe the 5*f* states in the actinides lie in the normal x-ray region. To probe the 3*d* bands in the transition metals and 4*f* bands in the lanthanides involves transitions at the *L* edges in the metal oxides and *M* edges of the lanthanides and these transitions occur in the soft region of the x-ray spectrum i.e. at energies of < 2 keV. There are 2 main problems associated with carrying out diffraction in this energy region. The first is that below 2 keV the absorption of x-rays is significant and hence, it is highly surface sensitive. Therefore sample surfaces must be of an extremely high quality and the experiments must be performed with the sample and diffractometer in a high vacuum. The second and most significant limitation is that at soft x-ray energies the size of the Ewald sphere is very small and hence, the volume of reciprocal space that can be accessed is extremely limited. Because of this limitation the technique can only access reflections with a large *d*-spacing. For example around the Mn L_{III} edge reflections with a *d* spacing of less than 9.7 Å cannot be accessed. Experiments carried out by Hase *et al.* [17] on metallic spin valves in layered thin films were successful in probing the magnetic alignment. However, it is only very recently that the technique has been successfully utilised on bulk single crystals at soft x-ray energies.

Wilkins *et al.*[18] carried out the first successful soft x-ray diffraction experiment on a single crystal of $La_{1.05}Sr_{1.95}Mn_2O_7$. The bi-layer manganite system has a very long *c*-axis of ~ 20 Å and hence, even at the Mn L_{II} and L_{III} edges which correspond to energies of 640 eV and 652 eV respectively it was possible to access the (0, 0, 2) Bragg reflection. The (0,0,2) reflection was scanned as a function of energy around the Mn L_{II} and L_{III} edges and a significant resonant enhancement was observed. The magnitude of the enhancement suggested that it could be possible to observe phenomena that only scattered very weakly away from resonance. This led to the investigation of the crystallographically forbidden (001) antiferromagnetic spin peak. The (001) reflection was not observed off resonance but became very intense due to the resonant enhancement as shown in Figure 7.2. In addition scans carried out in the θ–2θ direction gave a quantitative estimate of the inverse correlation. The inverse correlation length was calculated to be approximately half that observed on the same sample at 12.4 keV. This demonstrated that the technique was not particularly surface sensitive and the x-rays were in fact penetrating many unit cells.

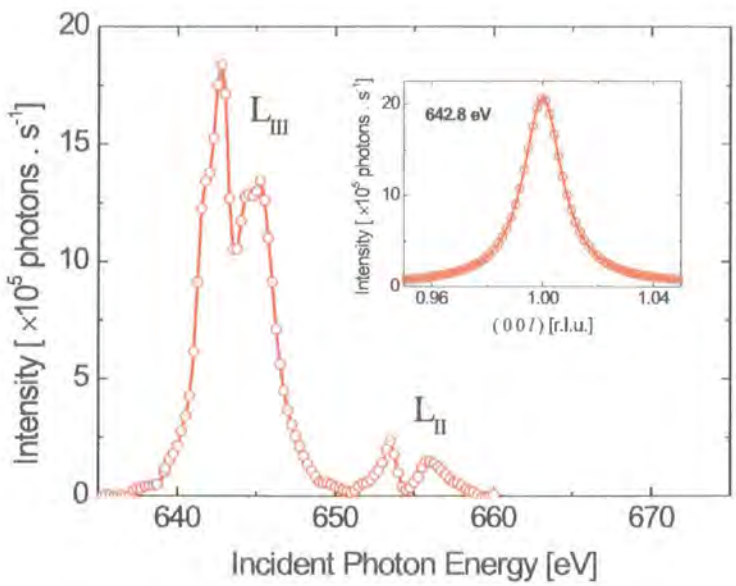

Figure 7.2: *Energy scan at constant wavevector through the (001) antiferromagnetic peak at 83 K. The inset shows a through the peak in the L direction at 642.8 eV.*[18]

In this chapter a soft x-ray study of magnetic order in holmium at the M_{IV} and M_V edges is discussed. The resonant enhancement at the Ho $M_{IV,V}$ edges is predicted to be significantly larger than that than observed at the Ho L_{III} edge. The transition that occurs at the M edge is a dipole (E1) transition from the $3d - 4f$ levels whereas at the L_{III} edge the two transitions are a dipole transition from the $2p - 5d$ levels and a quadrupole (E2) transition from the $2p - 4f$ levels. The $5d$ levels are not magnetically ordered but are instead split weakly by exchange interactions with the magnetic moments in the $4f$ levels. The magnitude of the magnetic scattering is related to the size of the exchange splitting and clearly, the exchange splitting will be significantly larger in the $4f$ levels where the magnetic ordering occurs than in the weakly polarised $5d$ levels. At the M edge the $4f$ orbitals are probed directly and hence, one is sensitive to the large exchange splitting within the $4f$ levels. This coupled with the larger overlap integral between the $3d$ and $4f$ levels than that between the $2p$ and $5d$ levels means that a significantly larger resonance is expected at the Ho $M_{IV,V}$ edges than that observed at the Ho L_{III} edge. The quadrupole (E2) transition from the $2p - 4f$ levels at the L_{III} edge does probe the $4f$ levels However, due to the nature of the quadrupole transition the transition rate is much lower than that of the dipole transition and hence, the resonant enhancement is similar to that of the transition into the $5d$ level.

While no Bragg peaks can be accessed in the Ewald sphere at the holmium $M_{IV,V}$ edges it is possible to access the long period magnetic order and Langehine *et al.*[19] reported the observation of the magnetic order at the M_V edge in an ultrathin holmium film. Holmium is the prototypical system for the study of magnetic order using resonant x-ray scattering. It has been studied in extensively using both resonant and non-resonant x-ray diffraction and neutron diffraction techniques and its properties are well known. By carrying out the experiment at soft x-ray energies it was hoped to determine the validity of the soft x-ray scattering technique by comparison with earlier results. In the next section the theory of resonant x-ray exchange scattering is discussed and this is followed by the experimental procedure, results and conclusions.

7.2 Resonant x-ray exchange scattering

Following from the work by Hannon *et al.*[13] the total coherent scattering amplitude from a magnetic ion can be written as

$$f = f_0 + f' + if'' + f_{spin} \qquad [7.1]$$

where f_0 α Zr_0 and is the contribution from the Thomson charge scattering, f_{spin} is the non-resonant scattering from the magnetic interaction and f' and f'' are the anomalous scattering factors. Far from resonance f' and f'' only contribute terms that are proportional to the spin and orbital angular momentum and the total non-resonant magnetic scattering amplitude is given by [10, 20]

$$f_{non-res}^{(mag)} = ir_0\left(\frac{\hbar\omega}{mc^2}\right)f_D\left[\frac{1}{2}L(Q)\bullet A + S(Q)\bullet B\right] \qquad [7.2]$$

where $L(Q)$ and $S(Q)$ are the Fourier Transforms of the orbital and spin densities respectively and f_D is the Debeye-Waller factor and Q is the momentum transfer. $\boldsymbol{A}$ and $\boldsymbol{B}$ are defined as

$$A = 2(1-\hat{k}\cdot\hat{k}')(\hat{\varepsilon}'\cdot\hat{\varepsilon}) - (\hat{k}\times\hat{\varepsilon})(\hat{k}\cdot\hat{\varepsilon}') + (\hat{k}'\times\hat{\varepsilon}')(\hat{k}'\cdot\hat{\varepsilon})$$

$$B = (\hat{\varepsilon}'\times\hat{\varepsilon}) + (\hat{k}'\times\hat{\varepsilon}')(\hat{k}'\cdot\hat{\varepsilon}) - (\hat{k}\times\hat{\varepsilon})(\hat{k}\cdot\hat{\varepsilon}') - (\hat{k}'\times\hat{\varepsilon}')\times(\hat{k}\times\hat{\varepsilon})$$

where $\hat{\varepsilon}$ and $\hat{\varepsilon}'$ are the incident and scattered polarization wavevectors respectively and $\hat{k}$ and $\hat{k}'$ are the incident and scattered wavevectors respectively. It should be noted that the non-resonant magnetic scattering is weaker than the charge scattering by a factor $\hbar\omega/mc^2$ in comparison with the charge scattering. In the normal x-ray region, between 3 and 10 keV, the associated scattering factor is weaker by a factor of 1/60 in comparison with the charge scattering from one electron giving an intensity that is ~ 3000 times weaker than that associated with the charge scattering. In addition magnetic scattering only occurs from unpaired electrons and this number is small even in the strongest

magnetic systems. For these reasons the non-resonant magnetic scattering is very small in comparison with the charge scattering.

As an absorption edge is approached the contribution of the anomalous scattering factors increases and this resonant contribution from the d resonance is given by [13]

$$f_{EL}(\omega)=\left(\frac{4\pi}{|k|}\right)f_D\sum_{M=-L}^{L}\left[\hat{\varepsilon}'^{*}\cdot Y_{LM}(\hat{k}')Y_{LM}^{*}(\hat{k})\cdot\hat{\varepsilon}\right]F_{LM}(\omega) \qquad \textbf{[7.3]}$$

where $Y_{LM}(\hat{k})$ are the vector spherical harmonics. The strength of the resonance is determined by the term F_{LM} which is dependent on the atomic properties and the equation for this term is given by:-

$$F_{LM}(\omega)=\sum_{\alpha,\eta}\frac{\left[P_\alpha P_\alpha(\eta)\Gamma_x(\alpha M\eta;EL)/\Gamma(\eta)\right]}{\left[x(\alpha,\eta)-i\right]} \qquad \textbf{[7.4]}$$

where η is the excited state, α is the initial state, P_α is the probability of the ion existing in the initial state and $P_\alpha(\eta)$ is the probability of a transition from the initial sate to the final state η. Γ_x/Γ is the ratio of the partial linewidth of the excited state due to a pure electric dipole radiative decay and that including all processes (e.g. Auger decay). Finally, the x term is the deviation from the resonance condition in units of the half width and is given by $x = (E_\eta - E_\alpha - \hbar\omega)/(\Gamma/2)$. This form of the scattering amplitude is valid in any isotropic system in which the symmetry is broken by the magnetic moment.

If the term in equation 7.3 is evaluated for the dipole transition that occurs in holmium at the L_{III} edge corresponding to the $2p_{3/2}$ — $5d_{1/2}$ the vector spherical harmonic terms can be written as follows. For $L = 1$ $M = \pm 1$

$$\left[\hat{\varepsilon}'\cdot Y_{1\pm1}(\hat{k}')Y_{1\pm1}^{*}(\hat{k})\cdot\hat{\varepsilon}\right]=\left(\frac{3}{16\pi}\right)\left[\hat{\varepsilon}'\cdot\hat{\varepsilon}\mp i(\hat{\varepsilon}'\times\hat{\varepsilon})\cdot\hat{z}_n-(\hat{\varepsilon}'\cdot\hat{z}')(\hat{\varepsilon}\cdot\hat{z}_n)\right] \qquad \textbf{[7.5]}$$

and for $L = 1$, $M = 0$

$$\left[\hat{\varepsilon}'\cdot Y_{10}(\hat{k}')Y_{10}^{*}(\hat{k})\cdot\hat{\varepsilon}\right]=\left(\frac{3}{8\pi}\right)\left[(\hat{\varepsilon}'\cdot\hat{z}')(\hat{\varepsilon}\cdot\hat{z}_n)\right] \qquad \textbf{[7.6]}$$

where $\hat{z}_n$ is a unit vector corresponding to the direction of the magnetic moment of the nth ion. Combining these terms gives the resonant scattering amplitude associated with the anomalous scattering factors.

$$f_{nE1}^{XRES} = \left[(\hat{\varepsilon}' \cdot \hat{\varepsilon})F^{(0)} - i(\hat{\varepsilon}' \times \hat{\varepsilon}) \cdot \hat{z}_n F^{(1)} + (\hat{\varepsilon}' \cdot \hat{z}_n')(\hat{\varepsilon} \cdot \hat{z}_n)F^{(2)}\right] \qquad [7.7]$$

where

$$F^{(0)} = (3/4k)\left[F_{11} + F_{1-1}\right] \qquad [7.8]$$

$$F^{(1)} = (3/4k)\left[F_{11} - F_{1-1}\right] \qquad [7.9]$$

$$F^{(2)} = (3/4k)\left[2F_{10} - F_{11} - F_{1-1}\right] \qquad [7.10]$$

The first term of [7.7] has no dependence on the magnetic moment and only contributes to the overall charge scattering. For incommensurate antiferromagnetically ordered systems the second term contributes to the first order magnetic satellites and the third term to the second order magnetic satellites. The second term is proportional to the magnetic moment and the third term contains two powers of the magnetic moment. The amplitude is dependent on the overlap between the initial and final states which therefore makes it possible to observe magnetic scattering from very weak magnetic moments.
In the paper by Hill and McMorrow [21] the dipole operator in equation. 7.7 is evaluated as a 2 × 2 matrix where the polarization states are either parallel or perpendicular to the scattering plane as defined in Figure 7.3. From this it can be determined that there are four possible scattering configurations for the incident and scattered polarisation given by:-

$$\begin{pmatrix} \sigma-\sigma' & \pi-\sigma' \\ \sigma-\pi' & \pi-\pi' \end{pmatrix} \qquad [7.11]$$

The first term only connects states in which there is no change in polarisation *i.e.* $\hat{\varepsilon}_\perp \rightarrow \hat{\varepsilon}'_\perp$ $(\sigma-\sigma)$ scattering and $\hat{\varepsilon}_\parallel \rightarrow \hat{\varepsilon}'_\parallel$ $(\pi-\pi)$ scattering. Therefore the matrix is diagonal with $\hat{\varepsilon}_\perp \cdot \hat{\varepsilon}'_\perp = 1$ and $\hat{\varepsilon}_\parallel \cdot \hat{\varepsilon}'_\parallel = \cos 2\theta = \hat{k} \cdot \hat{k}'$ giving

$$\hat{\varepsilon}' \cdot \hat{\varepsilon} = \begin{pmatrix} 1 & 0 \\ 0 & \hat{k}' \cdot \hat{k} \end{pmatrix} \qquad [7.12]$$

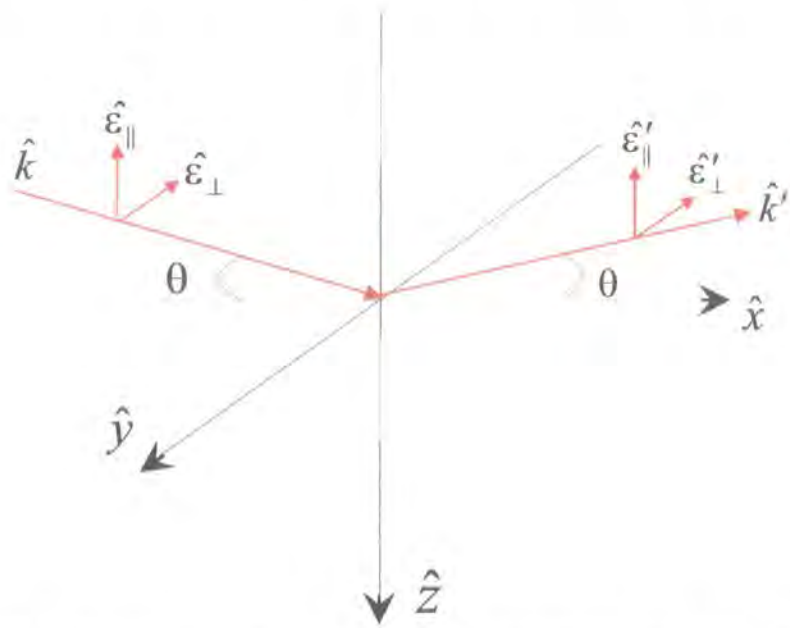

Figure 7.3: *Co-ordinate system used for calculating the polarisation dependence*

The second term allows π–π scattering and σ–π scattering but σ–σ scattering is forbidden. The resulting matrix is

$$(\hat{\varepsilon}' \times \hat{\varepsilon}) \cdot \hat{z}_n = \begin{pmatrix} 0 & \hat{k} \\ -\hat{k}' & \hat{k}' \times \hat{k} \end{pmatrix} \cdot \hat{z}_n \qquad [7.13]$$

The off-diagonal elements are $\hat{\varepsilon}'_{\parallel} \times \hat{\varepsilon}_{\perp} = -\hat{k}'$ and $\hat{\varepsilon}'_{\perp} \times \hat{\varepsilon}_{\parallel} = \hat{k}$. The matrix for the third term can also be obtained by a similar method to give the expression:-

$$f_{\delta\delta'}^{XRES} = F^{(0)} \begin{pmatrix} 1 & 0 \\ 0 & \hat{k}' \cdot \hat{k} \end{pmatrix} - iF^{(1)} \begin{pmatrix} 0 & \hat{k} \cdot \hat{z}_n \\ -\hat{k}' \cdot \hat{z}_n & (\hat{k}' \times \hat{k}) \cdot \hat{z}_n \end{pmatrix}$$

$$+ \left\{ \frac{F^{(2)}}{[1-(\hat{k}' \cdot \hat{k})^2]} \right\} \times \begin{pmatrix} [(\hat{k}' \times \hat{k}) \cdot \hat{z}_n]^2 & [\hat{k}' \cdot z_n - (\hat{k} \cdot \hat{k}')\hat{k} \cdot z_n](\hat{k}' \times \hat{k}) \cdot \hat{z}_n \\ [(\hat{k} \cdot \hat{k}')\hat{k}' \cdot \hat{z}_n - \hat{k} \cdot \hat{z}_n](\hat{k}' \times \hat{k}) \cdot \hat{z}_n & (\hat{k} \cdot \hat{k}')[(\hat{k} \cdot \hat{z}_n)^2 + (\hat{k}' \cdot \hat{z}_n)^2] \\ & -[1+(\hat{k} \cdot \hat{k}')^2](\hat{k} \cdot \hat{z}_n)(\hat{k}' \cdot \hat{z}_n) \end{pmatrix}$$

[7.14]

The vectors are resolved into their separate components along the $\hat{x}, \hat{y}, \hat{z}$ directions as defined in Figure 7.2. By this the resonant dipole scattering amplitude given by Hill [21] is

$$f_{nE1}^{XRES} = F^{(0)}\begin{pmatrix} 1 & 0 \\ 0 & \cos 2\theta \end{pmatrix} - iF^{(1)}\begin{pmatrix} 0 & z_1\cos\theta + z_3\sin\theta \\ z_3\sin\theta - z_1\sin\theta & -z_2\sin 2\theta \end{pmatrix} + F^{(2)}\begin{pmatrix} z_2^2 & -z_2(z_1\sin\theta - z_3\cos\theta) \\ z_2(z_1\sin\theta + z_3\cos\theta) & -\cos^2\theta(z_1^2\tan^2\theta + z_3^2) \end{pmatrix} \quad [7.15]$$

In synchrotron experiments the incident beam is σ polarised and hence, only the σ–σ' and σ–π' components need to be considered when calculating the resonant scattering cross-sections. The first term contributes to the charge scattering only and for σ–σ' scattering the amplitude of the first term is unity. The second and third terms give the polarisation dependences of the first and second order harmonic satellites i.e. the τ and 2τ. harmonics.

The cross-section due to the quadrupole transition was calculated in a similar way to that for the dipole transition by Hill and McMorrow. For the quadrupole transition there are thirteen distinct terms and hence, a significantly more complex equation. The calculations determined that there are contributions to not only the first and second harmonics but to the third order and fourth order harmonics which was in agreement with the results at the Ho L_{III} edge. The transitions at the Ho M_{IV} and M_V edges are predicted to be dipole transitions and hence, only the τ and 2τ reflections are expected.

7.3 Beamline 5U1

The 5U.1 beamline is situated on the undulator at the synchrotron source (SRS) Daresbury UK. The 5U.1 beamline was originally designed as a soft x-ray spectroscopy beamline and it provides monochromatic photons over an energy range of 60 - 1500 eV. It should be noted that above 1300 eV there is a considerable decrease in the flux on the beamline. This energy range allows the L edges in the $3d$ elements to be accessed, the N

edges in many of the actinides and the *M* edges in the rare earth elements such as holmium and dysprosium. The 5U.1 undulator beamline consists of a one metre long, ten-period, variable gap, permanent magnet undulator followed by an entrance-slitless plane grating monochromator (PGM). This has a minimum gap of 42 mm which gives a fundamental energy occurs at 60 eV with the harmonic radiation being emitted up to an energy of 2 keV.

A schematic of the optical layout is shown in Figure 7.4

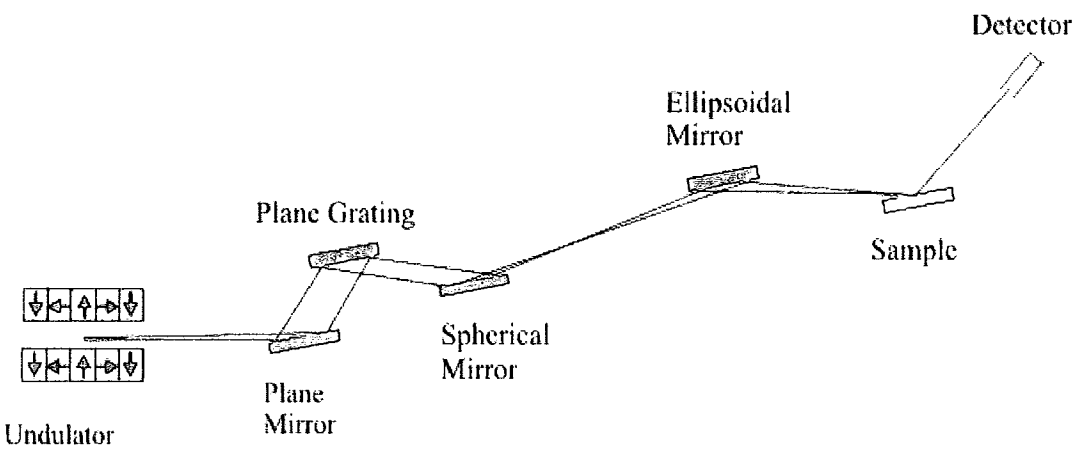

***Figure 7.4**: Schematic of the optical layout on station 5U.1*

After the undulator the first optical element is a 250 mm long, platinum coated CVD SiC plane mirror. The power incident on the mirror is 100 W and it is therefore water cooled. The diffraction grating has an ion-etched laminar profile with 1200 lines/mm and the substrate material is graphite with a platinum coated CVD-SiC surface. The beam from the grating is focused by a platinum coated fused silica spherical mirror. It has a radius of curvature of 307 m and operates at a glancing angle of incidence of 2.07. The large radius of the focusing mirror means the resolution in principal is limited by the size of the electron beam in the storage ring – source size and secondly the exit slit size. By selecting a suitable exit slit size it is possible the use the monochromator at the resolution limit imposed by the source size. The final optical element is an ellipsoidal mirror which is used to refocus the x-rays on to the sample.

The flux of the beamline is not constant with energy and the maximum flux is obtained at 200 eV and as the energy increased there is a gradual decrease in photon flux and above 1300 eV there is a significant decrease in the flux. In addition the energy resolution ΔE/E of the grating and hence, the beamline is dependent on the energy. The energy resolution as a function of energy is shown in Figure 7.5

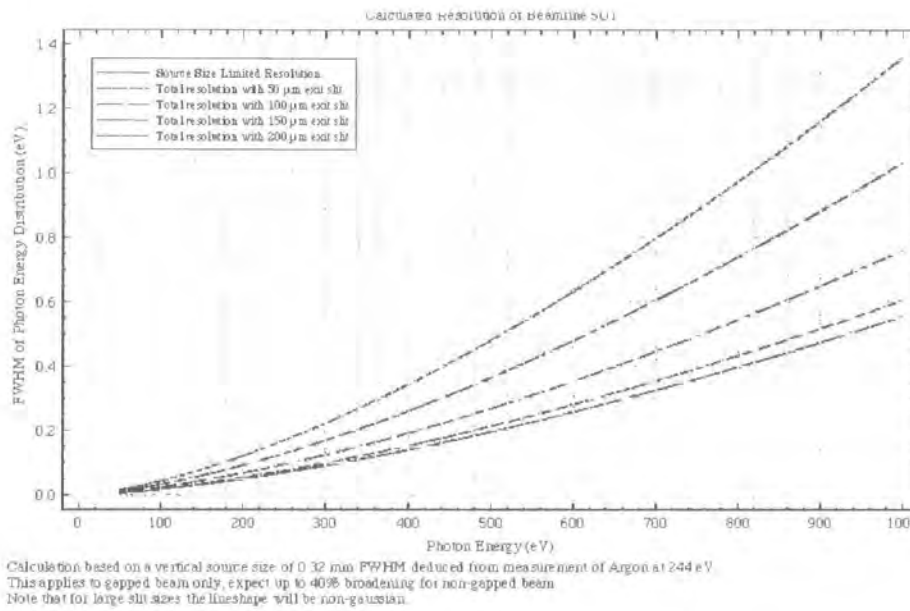

Figure 7.5: *Energy resolution, ΔE/E, as a function of energy for various exit slit sizes. Taken from the 5U.1 webpage on the Daresbury website.*[22]

The beamline was designed to allow many experimental chambers to be attached to the end of the beamline. For our experiments the phenomena we study occur at low temperatures so we required a diffractometer that could firstly be used at soft x-ray energies which meant that at high vacuum was required and secondly, could be cooled to low temperatures. Dr M. Roper modified the in-vacuum soft x-ray diffractometer so it could be cooled to a base temperature of 83 K and a picture of the diffractometer is shown in Figure 7.6.

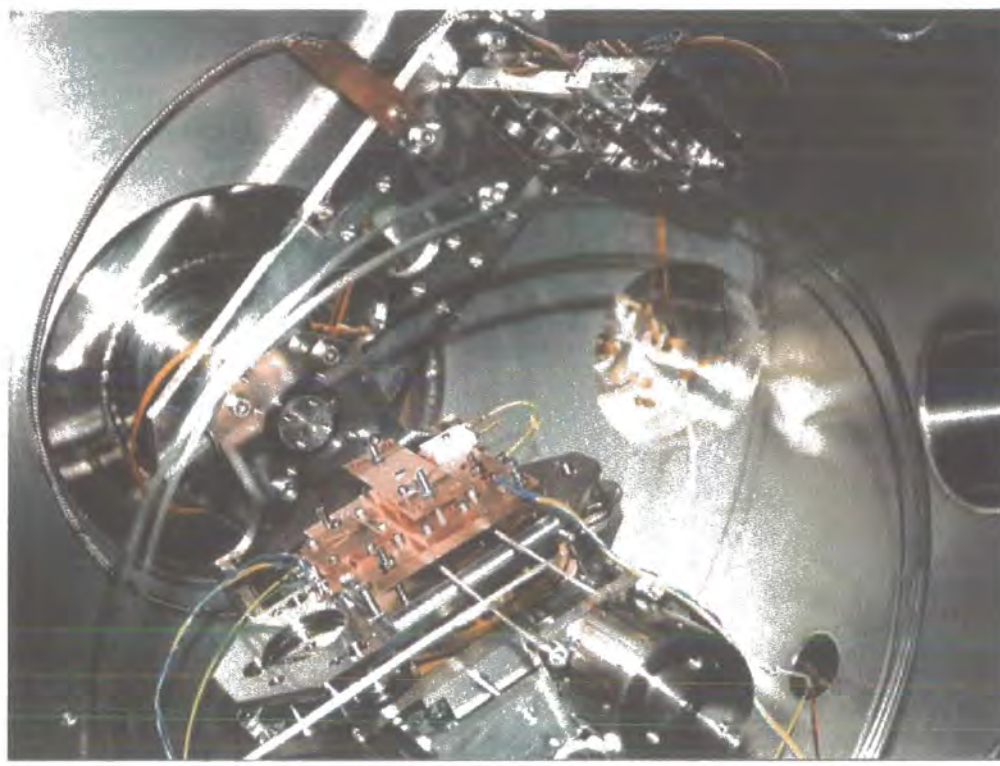

Figure 7.6: *Picture of the 5U.1 soft x-ray diffractometer*

The sample stage was cooled by the use of a copper heat exchanger which was attached to 0.5mm stainless steel tubes in which liquid nitrogen was passed through. Nitrogen from a pressurized Dewar was re-liquefied by passing it through an exchange coil in a bath of liquid nitrogen. The re-liquefied gas/liquid mixture was passed through the 0.5 mm steel tubes which were connected to the diffractometer by a UHV compatible flange and through contact with the copper heat exchanger cooled the sample stage. The nitrogen was exhausted to the atmosphere after being passed through the system. A film heater was connected to the copper heat exchanger and the temperature was controlled with the use of a Lakeshore temperature controller. The sample was measured with silicon diodes and the temperature stability was measured to be approximately ± 0.05 K. The scattered x-rays are detected by the measurement of the drain current from a silicon p-i-n diode. The current output is fed into a current to voltage amplifier and the voltage output from this is input into a voltage to frequency converter. The frequency output is proportional to the incident photon flux and this is counted by a counter on the beamline.

The diffractometer is a 2 circle diffractometer with motion in the θ and 2θ directions only. The sample mount has been designed so that it can be manually adjusted over a small range in the χ direction to allow the sample to be aligned. Due to this it is essential that the crystals are cut extremely accurately. The sample is aligned on the centre of rotation by use of a laser. The laser is designed so that it can be moved to be coincident with the incoming x-ray beam. Firstly, this allows the crystal to be placed on the centre of rotation and secondly, this allows χ to be adjusted so that the crystal is flat and therefore diffracts in the plane of the detector.

7.4 Experimental Procedure

A high quality holmium crystal grown at the University of Birmingham was mounted in the diffractometer with the <0, 0, 1> direction surface normal and the <1, 0, 0> direction corresponding to the incident beam. The holmium crystal was indexed in the *P63/mmc* hexagonal space group with $a = b = 3.57$ Å and $c = 5.61$ Å. The sample had been pre-aligned on the D3 diffractometer and the surface had been polished with 1 μm diamond paste before etching the surface with a solution of 25 % nitric acid, 25% acetic acid and 50 % methanol followed by a methanol watch. This ensured the surface was of a high quality which was vital for measurements at soft energies.

To determine the position of the absorption edges drain current measurements were performed. The drain current is a measurement of the photoelectron emission caused by the absorbed x-rays and at an absorption edge there is a significant increase in absorption and subsequent emission of electrons. By measuring the current passing through an earthed wire attached to the sample the absorption edge position can be determined. To enable these measurements to be carried out it was necessary electrically insulate the sample using GE varnish and a thin piece of paper. This ensures there is no electrical contact between the sample and the copper mount but still allows a good thermal contact. A wire was attached to the sample using conductive silver epoxy which was attached to an ammeter.

7.5 Results

The sample was cooled to base temperature which was approximately 85 K for the soft x-ray diffractometer. Initially a drain current scan was carried out to confirm the positions of the Ho M_V and M_{IV} edges. This is shown in Figure 7.7 and it confirmed the positions of the Ho M_V and M_{IV} edges as 1350 eV and 1391 eV respectively.

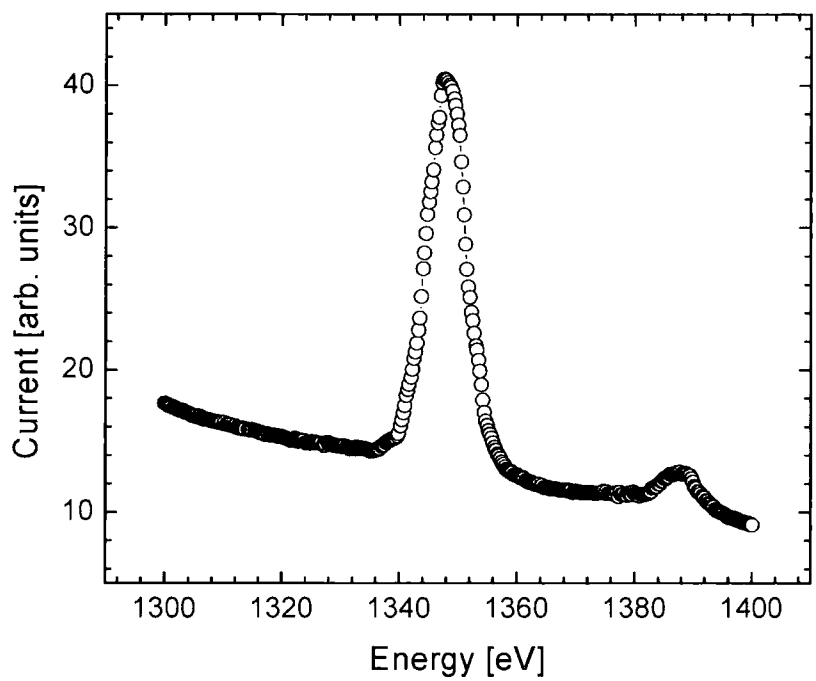

Figure 7.7: *Drain current measurement on holmium as a function of energy at 85K.*

At the Ho M_{IV} and M_V edges the small radius of the Ewald sphere means that no Bragg reflections can be accessed and the only reflections that can be accessed are those associated with long range modulations of the magnetic spiral. However, this did not cause any problems as the crystal had been pre-aligned so that the <0, 0, 1> direction (*i.e.* the same direction as the orientation of the magnetic order) was virtually surface normal.

The energy was tuned to the M_{IV} and M_V edges as calculated from the drain current measurements and a search was carried out for the reflections associated with the magnetic order at the τ, 2τ, 3τ and 4τ positions. No evidence of the magnetic order was observed of any modulation at the M_{IV} edge. However, at the M_V edge a very intense peak was observed at a 2θ angle of 23.95° and a weaker peak at a 2θ angle of 49.08°. A scan performed above T_N confirmed that the reflections originated from the magnetic order. These 2θ angles were calculated to give modulations of (0, 0, 0.255) and (0, 0, 0.510) respectively which are close to the modulations predicted from the earlier L edge experiments for the τ and 2τ and a more detailed comparison will be made later in the section. However, no evidence of the 3τ and 4τ harmonics was observed at the M_V edge. The transition occurring at the M_V edge corresponds to a dipole transition from the $3d_{5/2}$ – $4f_{7/2}$ level. As discussed in section 7.2 the resonant exchange magnetic scattering associated with dipole transition only results in harmonics at the τ and 2τ positions not the 3τ and 4τ positions, which is consistent with the results observed. Away from the M_V edge the τ and 2τ reflections could not be observed above background. The exit slit was reduced in size to 30 μm to maximise the energy resolution ($\Delta E/E$) and at 85 K an energy scan was carried out on the (0, 0, τ) reflection at a constant wavevector to ensure that the θ and 2θ angles were changed so that the peak was not moved off during the scan. The energy scan of the τ reflection is shown in Figure 7.8 and it is normalised to the monitor. The (0, 0, 2τ) reflection was scanned using the same method and the energy scan is shown in Figure 7.9.

Firstly the energy dependence of the (0, 0, τ) reflection is discussed. The reflection could not be observed off resonance and as the energy is increased towards the M_V edge there was a dramatic increase in the scattered intensity which maximised at 1340 eV. As the energy is increased above 1340 eV the intensity rapidly decreased before minimising at 1350 eV. As the energy was increased the intensity increases before showing a second maxima at 1360 eV and then decreased above this energy. When discussing this behaviour the reader is referred to the drain current measurements in Figure 7.7. The drain current is a measure of the absorption, and the drain current began to increase at 1340 eV and maximised at 1350 eV.

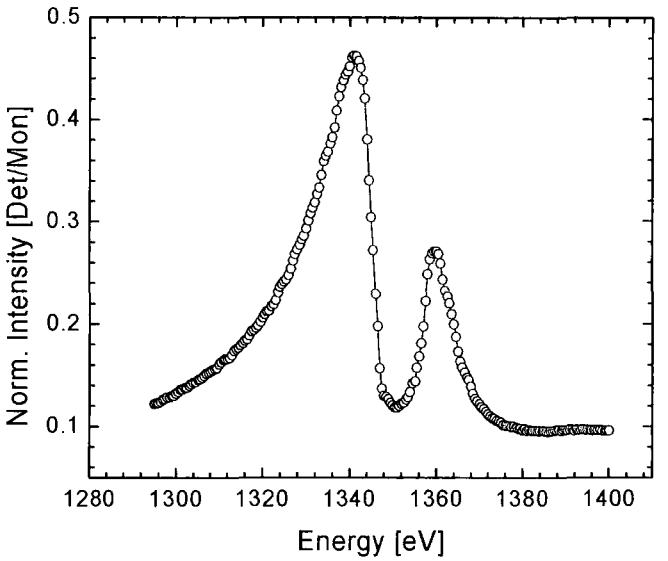

Figure 7.8: *Energy scan at constant wavevector through the (0, 0, τ) magnetic order reflection. The energy scan was taken in high resolution mode with a 30 μm slit.*

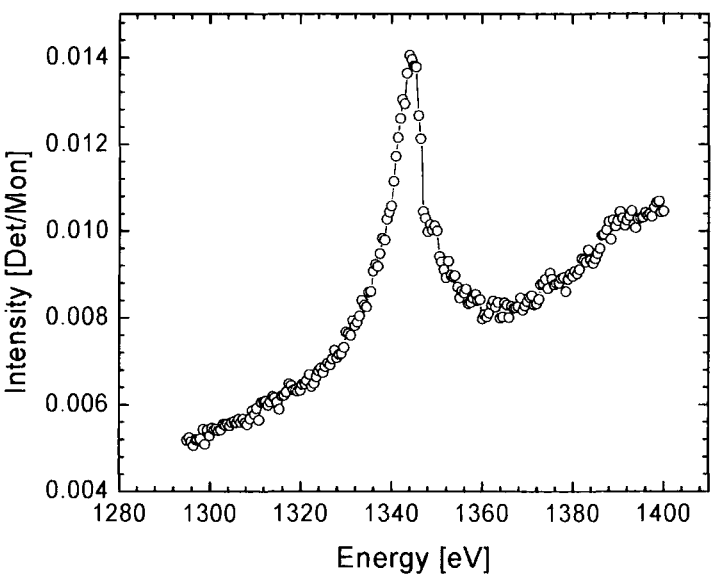

Figure 7.9: *Energy scan at constant wavevector through the (0, 0, 2τ) magnetic order reflection. The energy scan was taken in high resolution mode with a 30 μm slit.*

This increase in the drain current began at 1340 eV and this corresponds exactly with the energy where the intensity began to decrease. The drain current reached a maximum at 1350 eV, which was the energy where the intensity minimised. When the absorption decreases above 1350 eV there is a corresponding increase in the intensity with it maximising at 1360 eV. From this data it is concluded that the two peaks observed are not in fact separate resonances but occur due to the significant increase in absorption at M_V edge. Attempting to correct for the absorption introduced significant error into the energy scans and did not give an accurate energy profile. If the absorption could be accurately corrected for, it is postulated that an energy resonance would be observed to maximise at 1350 eV.

The (0, 0, 2τ) magnetic order reflection was significantly weaker than the first order reflection and also could not be observed off resonance. As the energy was increased towards the M_V edge there was a resonant enhancement in the intensity and the scattered intensity maximises at 1345 eV before decreasing above this energy. The behaviour of the first order reflection showed that the absorption at the M_V edge is considerable and if absorption could be accurately corrected for the second order reflection would also show a maximum in intensity at 1350 eV. The intensities of the first and second order reflections maximise at slightly different energies – 1340 eV and 1345 eV respectively and the effects of the absorption do not appear to be as significant in the 2τ energy scan. A possible explanation for this is that the first order reflection occurs at a lower angle and therefore at a more glancing angle than the second order reflection. While the same sample volume is probed at both positions the incident beam is sensitive to a larger surface area at the τ position than the 2τ position resulting in a smaller sample thickness penetrated. Therefore, there is a greater sensitivity to the effects of the absorption at the τ position than at the 2τ position

The x-ray absorption at the Ho M_V edge is clearly significant and the question that arises from this is how surface sensitive the technique is at the Ho M_V edge. The scattering factors at the holmium M edges are not known, which means that the absorption cannot be calculated accurately. However, resonant x-ray studies by Helgesen[23] and Thurston[24] have measured the correlation of the magnetic order and reported it to show a correlation very close to that of the lattice and therefore

measurements of the inverse correlation length should give an estimate of the penetration depth. The inverse correlation length in the L direction of the τ and 2τ reflections was measured at the energies where the intensity of each maximised i.e. at 1340 eV and 1345 eV respectively. The first and second order reflections were fitted to Gaussian lineshapes and the inverse correlation length was calculated from the fits to the data. Table 8.1 shows the inverse correlation lengths of the reflections and as a comparison the inverse correlation length measured at the L_{III} edge by Thurston *et al.*[24]

	Inverse correlation length [Å^{-1}]
τ	0.0158 ± 0.0004
2τ	0.0171 ± 0.0007
τ at L_{III} edge	0.0006

Table 7.1: *Inverse correlation length of the first and second order reflections at 85 K at 1340 eV and 1345 eV respectively. As a comparison the inverse correlation length calculated from the data measured by Thurston et al.[24] at the L_{III} edge is shown.*

Calculating the correlation lengths for a Gaussian lineshape gave the penetration depths as approximately 105 Å and 98 Å respectively from the τ and 2τ measurements which is approximately 17 unit cells in the L direction. These values indicate that the measurements are near surface sensitive, but only the first 3 Å can be considered to be truly surface sensitive. At this penetration depth the electronic and magnetic properties behave as they would in the bulk and hence, the measurements are representative of the bulk. The 2τ reflection appears to be slightly less correlated than the τ reflection but the second order reflection was measured at a slightly higher energy and referring the reader to Figure 7.7 we postulate that this is due to the higher absorption at 1345 eV. A comparison with the inverse correlation length calculated from Thurston *et al.*[24] determined that the penetration depth at this energy is over twenty times smaller than the range over which the magnetic order is correlated. It was therefore very unlikely that any change in the inverse correlation length would be measured because at all temperatures the volume probed would be considerably smaller than the correlation of the magnetic order.

Due to the large absorption it was very difficult to estimate the magnitude of the resonant enhancement at the M_V edge. However, the intensity of the first order reflection at 1340 eV was a similar magnitude to that observed by Wilkins *et al*[18]. for the spin ordering in the bi-layer manganite and could not be observed off resonance. From this it is postulated that the resonant enhancement is a similar to that observed in the bi-layer manganite and hence, significantly larger than that observed at the L_{III} which is in agreement with the predictions by Hannon *et al.*[13]. To determine the exact resonant enhancement would require experimental values of the absorption which cannot be easily obtained at soft energies.

The integrated intensity, inverse correlation length and the wavevector as a function of temperature was measured for both the (0, 0, τ) and (0, 0, 2τ) reflections. Due to the diffractometer only having a base temperature of 85 K the temperature dependence could only be studied over a limited range but it could still be compared with the data taken from previous studies. The (0, 0, τ) reflection was measured at 1340 eV and the (0, 0, 2τ) reflection at 1345 eV, corresponding to the energies where the scattered intensity was observed to maximise.

The peaks were scanned in the Q_Z direction and the data fitted and from the fits the integrated intensity, position and inverse correlation length were determined. Firstly, the behaviour of the integrated intensity for both reflections is discussed. The first and second order reflections were measured at slightly different energies but any comparison should still be valid. Gibbs *et al.*[12] compared the intensity as a function of temperature both on and off-resonance for the first order reflection and confirmed that the scaling factor between the two intensities was the same at all temperatures i.e. the temperature dependence was independent of energy. The integrated intensity as a function of temperature for the (0, 0, τ) and (0, 0, 2τ) reflections is shown in Figures 7.10 and 7.11 respectively. The integrated intensity of the first order reflection shows a gradual decrease from 85 – 115 K and then shows a sharp increase above this temperature consistent with a first order transition which is in agreement with both the earlier neutron and x-ray work.

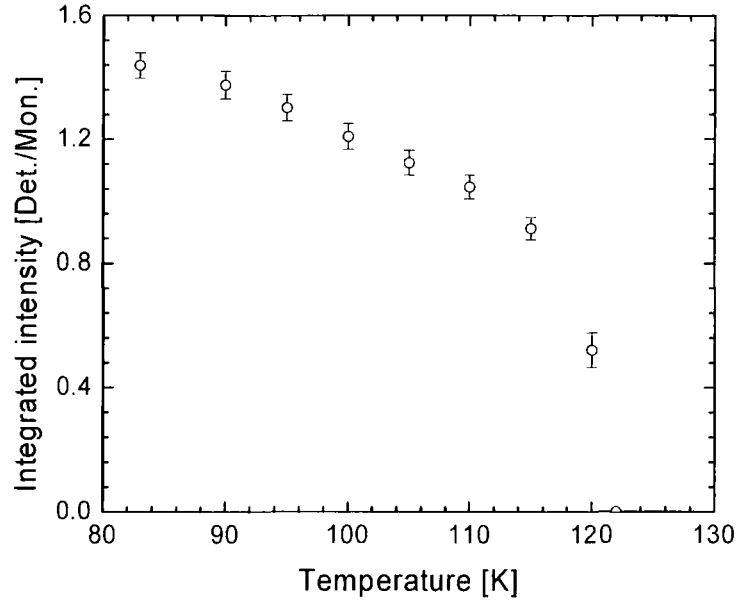

Figure 7.10: *Integrated intensity as a function of temperature for the (0, 0, τ) reflection*

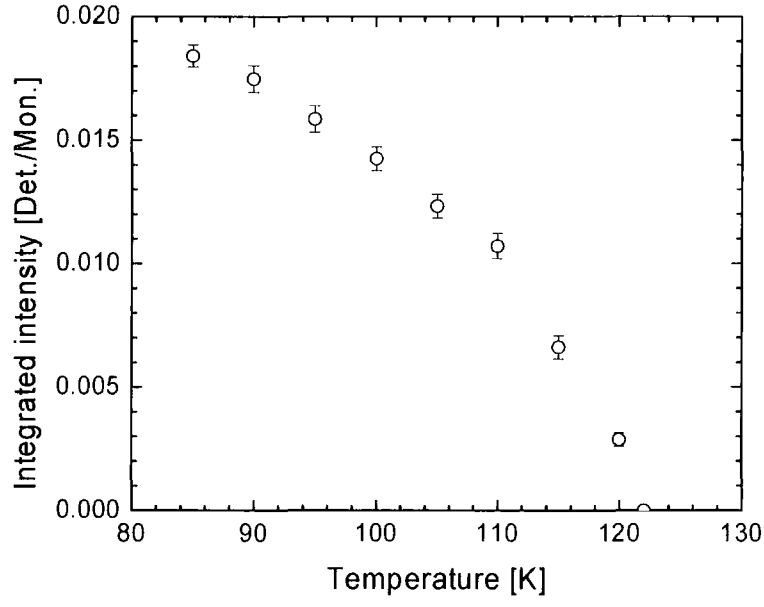

Figure 7.11: *Integrated intensity as a function of temperature for the (0, 0, 2τ) reflection*

From the data the transition temperature was estimated as approximately 122 K for both the τ and 2τ reflections as neither could be detected above background above this temperature. This is lower than the literature value in the earlier studies of 133 K and is probably due to an offset in the temperature between the sample surface and the sample stage and this offset is estimated to be 10 – 15 K. If the behaviour of the τ and 2τ reflections are compared it is clear that the integrated intensity of the second order reflection is decreasing at a greater rate than that of the first order reflection. This is in agreement with the L edge measurements by Helgesen *et al.*[23] which are shown in Figure 7.12.

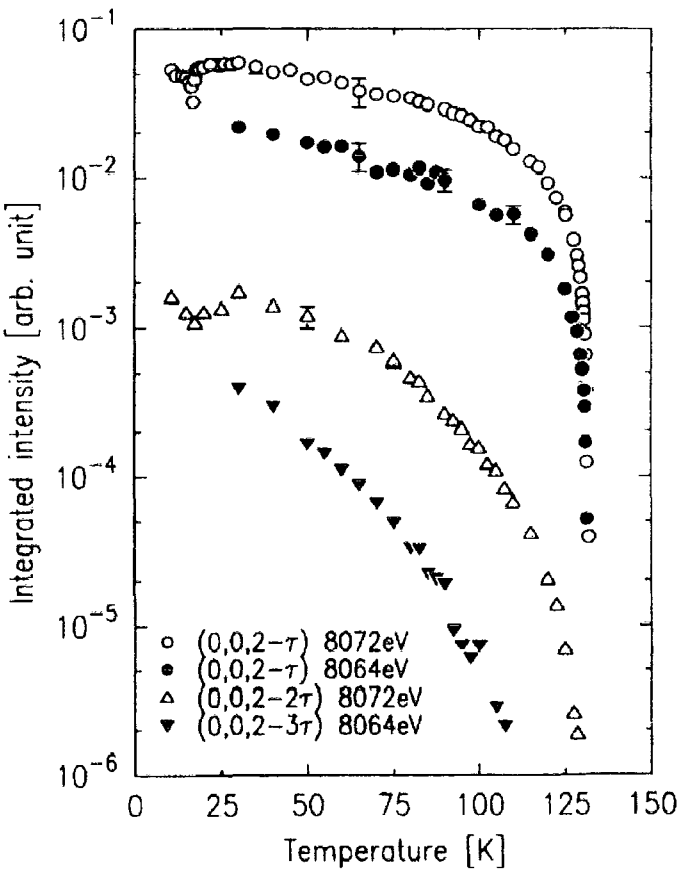

Figure 7.12: *Integrated intensity versus temperature for the first, second and third order harmonics at the Ho L_{III} edge measured by Helgesen et al.*[23]

To allow a better comparison, the intensity of both the first and second order reflections is shown on a logarithmic scale in Figure 7.13.

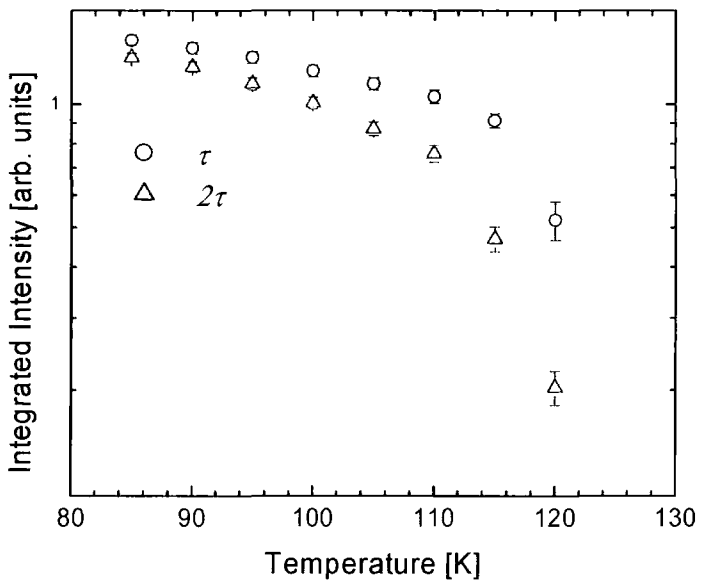

Figure 7.13: *Comparison of the intensity at the M_V edge for the τ (circles) and 2τ (triangles) reflections. The reflections have been scaled for an easier comparison.*

Even over the limited temperature range studied the behaviour of the integrated intensity appears in agreement with the L edge measurements, with the 2τ reflection showing a more rapid decrease in intensity. An exact comparison would require more data points but this comparison strongly suggests that the behaviour of the magnetic order at the M_V edge is approximately the same as that at the L_{III} edge.

The inverse correlation length of the τ and 2τ showed no change with temperature which is as expected because the inverse correlation length is determined by the sample volume probed not the degree of correlation of the magnetic order which remains significantly greater than the sample volume probed at all temperatures..

The position of both the first and second order reflections was measured as a function of temperature with the wavevector being obtained from the fits and the results are shown in Figures 7.14 and 7.15 respectively.

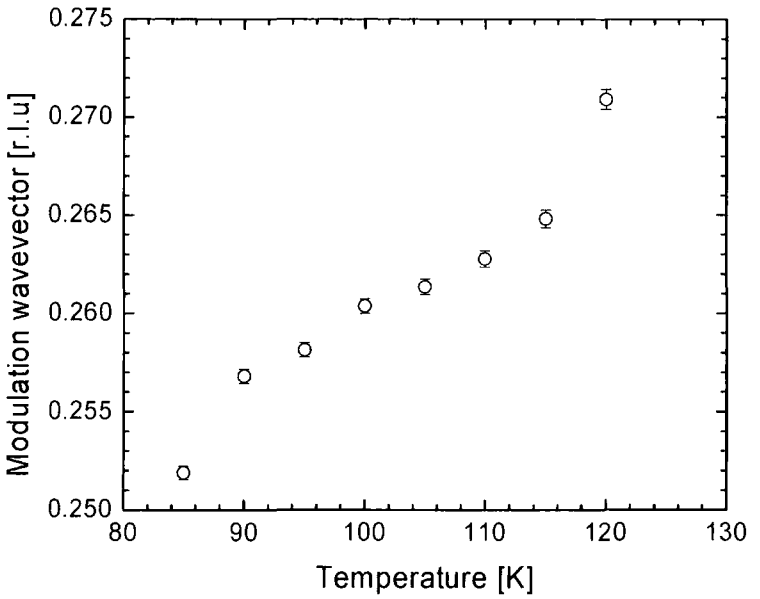

Figure 7.14: *Temperature dependence of the modulation of the (0, 0, τ) reflection.*

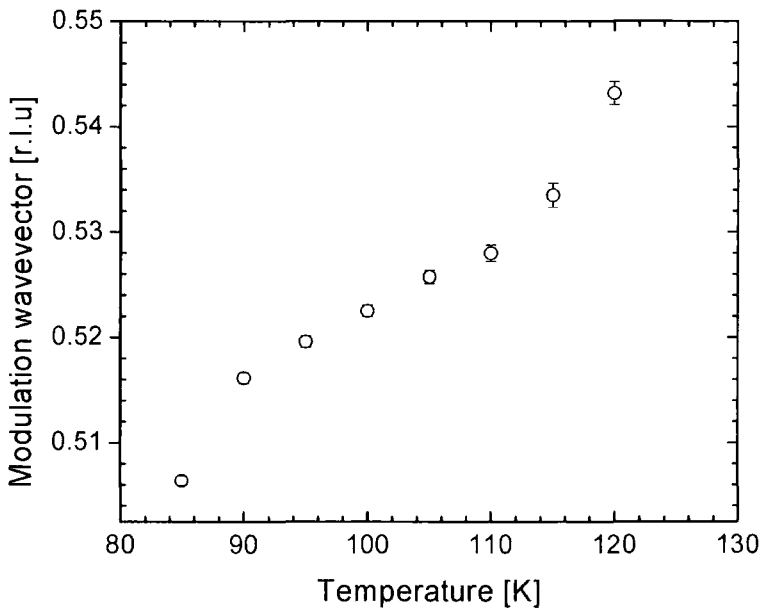

Figure 7.15: *Temperature dependence of the modulation of the (0, 0, 2τ) reflection.*

At 85 K the position of the first order reflection was calculated as (0, 0, 0.255). This was compared with the x-ray and neutron results from Gibbs *et al.*[9] and shown in Figure 7.16. The measurements of the wavevector at the *L* edge by Helgesen *et al.* were in agreement with those shown in Figure 7.16.

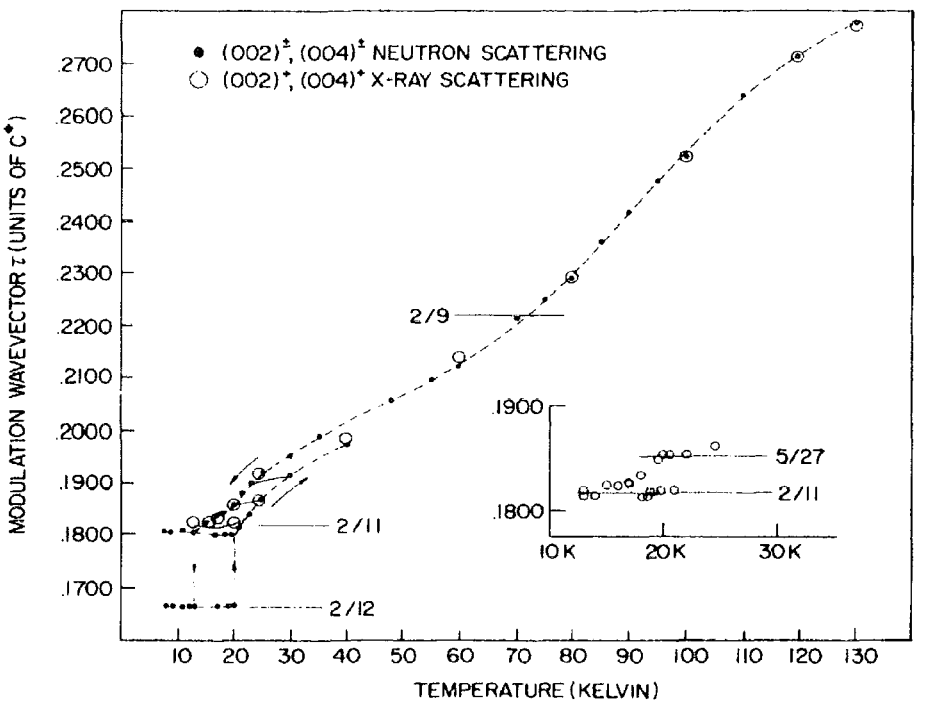

Figure 7.16: *Temperature dependence of the modulation of the magnetic order measured with x-ray (open circles) and neutron diffraction (closed circles) taken from Gibbs et al.*[9]

The comparison showed that the wavevector measured was slightly higher than expected because from the above figure the wavevector is predicted as approximately (0, 0, 0.24). However, from the temperature dependence it was determined that there was a temperature offset of 10 - 15 K and if this is considered the wavevector position is very close to that observed at 100 K by Gibbs *et al.*[9] As the temperature was increased the modulation wavevector of the magnetic order increased continuously and at 120 K just before the transition the modulation of the magnetic order was calculated as (0, 0, 0.275). This is in good agreement with Gibbs *et al.*[9] who measured the wavevector close to T_N to be $\tau = 0.28$. The second order reflection was observed at a modulation of (0, 0, 0.510)

at base temperature – double the modulation of the first order reflection and as expected the modulation changed by double the amount over the temperature range. The change in the wavevector is not linear with temperature and this is in agreement with the data in Figure 7.16, despite the limited temperature range over which the *M* edge study was conducted. This behaviour occurs due to the magnetic order favouring certain modulations that are commensurate with the lattice. However, this is most significant at temperatures below 80 K and hence, in this study the effect is not as apparent as it would be if studied across the whole temperature range of the magnetic order.

From these observations we have demonstrated that the magnetic order displays the same behaviour at the *M* edge as previously observed in the neutron and *L* edge resonant measurements. Due to the temperature limitation of the diffractometer it was obviously not possible to measure the dependence of the magnetic order throughout the entire antiferromagnetically ordered region. However, the results over the limited temperature range show that with respect to the behaviour of the integrated intensity and the wavevector modulation is in agreement with the best results measured using neutron and x-ray diffraction techniques. However, the large absorption meant that it was not possible to measure the behaviour of the inverse correlation length because the measurement was limited by the low penetration depth.

7.6 Conclusions

The study has shown that the soft x-ray scattering technique is suitable for the study of systems in which no Bragg peak is accessible within the Ewald sphere and that valid results can be obtained from this technique.

The comparison with the earlier neutron and resonant x-ray diffraction results determined that the soft x-ray technique measured the same results for the integrated intensity and the wavevector for the magnetic order as reported in earlier studies. However, due to the large absorption it was not possible to determine the temperature dependence of the inverse correlation length. This is a possible limitation of the technique but the calculated penetration depth of 100 Å is not considered especially

surface sensitive and the similarity of the measurements to the results of earlier studies on holmium reflects this. It should also be noted that the absorption measured in the bi-layer system by Wilkins *et al.*[18] was determined to be a factor of five times smaller at the Mn L_{III} edge and hence, less surface sensitive than in holmium.

As a result of the large absorption it is not possible to determine the exact size of the resonant enhancement. However, the magnitude of the scattering at the Ho M_V edge was similar to that observed for the magnetic order in the bi-layer manganite at the Mn *L* edge which was estimated to be ten times that of the corresponding charge scattering. From this observation we postulate that the resonant enhancement is similar and also similar to that observed at the actinide *M* edges. This is significantly larger than at the *L* edge and is in agreement with the predictions of Hannon *et al.* who predicted that the x-ray resonant exchange scattering is largest when the magnetically ordered 4*f* level is directly probed by a dipole transition.

7.7 Future Work

The study of the antiferromagnetic spiral phase in holmium could only be carried out over a limited temperature range due to the limitations of the diffractometer. However, it would be possible to measure the behaviour of the magnetic spiral in dysprosium which shows the same antiferromagnetic pattern between 90 and 180 K. This study has demonstrated that the soft x-ray technique can be utilised to study the rare earths in addition to the transition metal oxides and even with the high absorption is not particularly surface sensitive. The resonant x-ray scattering technique allows the magnetic order associated with different elements in a compound to be probed by tuning to a specific absorption edge. A system in which the behaviour of the magnetic order is still not fully understood is the RFe_4Al_8 system where R = Ho, Dy. By tuning to the Fe *L* edges and the Ho, Dy *M* edges it will be possible to investigate the magnetic sub-lattices associated with the different elements and obtain a better understanding of the system. Most importantly it can be used to directly probe the orbital order in the manganites which is discussed in Chapter 8.

7.8 References

1 F. de Begrevin and M. Brunel, Physical Letters **39A**, 141 (1972).
2 D. Gibbs, D. R. Harshman, E. D. Isaacs, *et al.*, Physical Review Letters **61**, 1241 (1988).
3 D. B. McWhan, C. Vettier, E. D. Isaacs, *et al.*, Physical Review B **42**, 6007 (1990).
4 E. D. Isaacs, D. B. McWhan, C. Peters, *et al.*, Physical Review Letters **62**, 1671 (1989).
5 W. C. Koehler, J. W. Cable, M. K. Wilkinson, *et al.*, Physical Review **151**, 414 (1966).
6 W. C. Koehler, J. W. Cable, H. R. Child, *et al.*, Physical Review **158**, 450 (1967).
7 G. P. Felcher, G. H. Lander, T. Arai, *et al.*, Physical Review B **13**, 3034 (1976).
8 M. J. Pechan and C. Stassis, Journal of Applied Physics **55**, 1900 (1984).
9 D. Gibbs, D. E. Moncton, K. L. D' Amico, *et al.*, Physical Review Letters **55**, 234 (1985).
10 M. Blume, Journal of Applied Physics **57**, 3615 (1985).
11 H. Ohsumi, Journal of the Physical of Japan **71**, 1732 (2002).
12 D. Gibbs, G. Grubel, D. R. Harshman, *et al.*, Physical Review B **43**, 5663 (1991).
13 J. P. Hannon, G. T. Trammell, M. Blume, *et al.*, Physical Review Letters **61**, 1245 (1988).
14 E. D. Isaacs, D. B. McWhan, D. P. Siddons, *et al.*, Physical Review B **40**, 9336 (1989).
15 J. Bohr, D. Gibbs, and K. Huang, Physical Review B **42**, 4322 (1990).
16 C. Vettier, Journal of Electron Spectroscopy and Related Phenomena **117-118**, 113 (2001).
17 T. P. A. Hase, I. Pape, B. K. Tanner, *et al.*, Physical Review B **61**, R3792 (2000).
18 S. B. Wilkins, P. D. Hatton, M. D. Roper, *et al.*, Physical Review Letters **90**, 187201 (2003).
19 C. Schussler-Langeheine, E. Weschke, A. Y. Grigoriev, *et al.*, Journal of Electron Spectroscopy and Related Phenomena **114-116**, 953-957 (2001).
20 M. Blume and D. Gibbs, Physical Review B **37**, 1779 (1988).
21 J. P. Hill and D. McMorrow, Acta Crystallographica A **52**, 236 (1996).
22 http://srs.dl.ac.uk/station/5U.1/#PHYDES.
23 G. Helgesen, J. P. Hill, T. Thurston, *et al.*, Physical Review B **50**, 2990 (1994).
24 T. Thurston, G. Helgesen, J. P. Hill, *et al.*, Physical Review B **49**, 15730 (1994).

Chapter 8

Direct Observation of Orbital Ordering in $La_{0.5}Sr_{1.5}MnO_4$ by Soft X-ray Diffraction

8.1 Introduction

The manganite systems have been studied greatly over the last decade in order to determine how the interplay between the charge, spin and orbital degrees of freedom is related to the electronic and physical properties. Through neutron, x-ray and electron diffraction techniques the charge and spin have been investigated thoroughly but until very recently it has not been possible to investigate the orbital degree of freedom. In the 1950s Goodenough[1] predicted that the half-doped perovskite manganites would be orbitally ordered. At low temperatures Goodenough predicted that at low temperatures the manganites would be charge ordered in an alternating pattern of Mn^{3+} and Mn^{4+} ions. This would be accompanied by an ordering of the $3d_{3z^2-r^2}$ orbitals on the Mn^{3+} ions in a zigzag pattern. While the charge and magnetic ordering and their effect on the structural properties have been thoroughly investigated through a large range of techniques, very little is known about the influence of the orbital ordering in the manganites. A resonant x-ray scattering study by Murakami *et al.*[2] reported a claim of the first direct observation of orbital ordering in the manganites. Murakami *et al.* carried out resonant x-ray scattering measurements using anomalous scattering around the manganese *K*-edge on $La_{0.5}Sr_{1.5}MnO_4$. At the manganese *K*-edge a reflection was observed at a modulation of (0.75, 0.75, 0) which was not observable away from the *K*-edge. In their paper they attributed this reflection to orbital ordering as it agreed with the modulation predicted by Goodenough and claimed that it was the first direct measurement of orbital order in the manganites. This technique was also used to study $LaMnO_3$[3], $Pr_{0.5}Ca_{0.5}MnO_3$[4],

$Nd_{0.5}Sr_{0.5}MnO_3$[5] and the bi-layer $LaSr_2Mn_2O_7$ [6]. Each of these systems showed similar behaviour to those observed in $La_{0.5}Sr_{1.5}MnO_4$ at the Mn *K*-edge. It was claimed that this technique was a direct probe of the orbital order in each system but this claim has been strongly debated. At the manganese *K*-edge the transition that occurs is from the $1s - 4p$ orbitals whereas the orbital ordering occurs in the $3d$ orbitals. In theoretical papers by Elfimov *et al.*[7] and Benafatto *et al.*[8] calculations were carried out that strongly suggested that the *K*-edge technique were not a direct measurement of orbital order and instead was a measurement of the associated Jahn-Teller modulation.

The theory proposed by Murakami *et al.* was that the Jahn-Teller / orbital ordering in the $3d$ orbitals causes the splitting in the empty $4p$ orbitals between the y and x, z components which is of magnitude Δ and this gives rise to reflections at forbidden positions on resonance with intensity proportional to Δ^2. In the studies by Murakami *et al.* on $La_{0.5}Sr_{1.5}MnO_4$ and $LaMnO_3$ they did not state the origin of the splitting, but they did suggest two possible mechanisms. The first was that the Jahn-Teller distortion of the oxygen octahedra around the Mn^{3+} ions that accompanies the charge/orbital ordering in which the long axis is always along the occupied $3d$ e_g orbital. The second mechanism proposed was that the splitting is caused by the Coulomb interaction between the $4p$ conduction band states and the orbitally ordered $3d$ orbitals. To summarise, in the first mechanism the splitting in the $4p$ orbital is caused by the Jahn – Teller (JT) distortion whereas in the second mechanism the splitting is caused by the orbital ordering. Benafatto *et al.* believed the first model to be correct and carried out calculations that showed intensity from the JT effect to be at least 100 times greater than that from the orbital ordering at the Mn *K*-edge. The calculations showed that the splitting in the $4p$ orbitals produced by the two mechanisms was significantly larger from the JT effect, then the Coulomb interaction and that the scattered intensity observed could only be explained by the effect of the JT distortion. For the $LaMnO_3$ system the relative weight of the two mechanisms was calculated and the scattered intensity was in favour of the Jahn-Teller effect by a ratio of 1:100. The magnitude of the JT distortion is smaller in $La_{0.5}Sr_{1.5}MnO_4$ but the calculations by Benafatto again showed that even a relatively small distortion would still produce significantly greater scattered intensity than the orbital ordering. From these calculations it was concluded that the *K*-edge experiments were far more

sensitive to the effects of the JT distortion than the orbital order and it was not possible to determine the effect due to the orbital order. Hence, the measurements at the manganese *K* edge are not a direct measurement of the orbital order in the manganites but an indirect effect associated with it.

Recently a theoretical paper by Castleton and Altarelli [9] proposed that carrying out the measurements at the manganese L_{II} and L_{III} edges at approximately 640 eV would be a direct probe of the orbital order. By tuning to these levels it was postulated that this would provide a direct probe of the orbital ordering because at these energies the 3*d* orbitals are being probed directly and it would, in theory, provide information on whether the ordering is due to direct orbital ordering or the cooperative Jahn-Teller effect. They carried out a series of calculations to predict the scattered intensity for $La_{0.5}Sr_{1.5}MnO_4$ at the Mn *L* edges and interpreted their results within a one electron model.

$La_{0.5}Sr_{1.5}MnO_4$ has a charge ordering transition of approximately 220 K and the charge ordering of the Mn^{3+}/Mn^{4+} sub-lattices is accompanied by orbital ordering i.e $T_{CO} = T_{OO} = 220$ K. The system antiferromagnetically orders at $T_N = 110$ K which was observed by neutron diffraction[10]. However, magnetic susceptibility measurements gave a higher antiferromagnetic transition temperature concurrent with the charge and orbital ordering temperature.[11] It is therefore probable that the in-plane magnetic order occurs at a temperature of $T_N(ab) = 220$ K and at $T_N(c)$ becomes fully three dimensional. This is consistent with the rod-like neutron scattering reported between T_N and T_{CO} reported by Sternlieb *et al.*[10] Goodenough demonstrated that the spin ordering is dependent on the ordering of the orbital degree of freedom and that a distinctive "herringbone" pattern is required in order to explain the observed antiferromagnetic ordering. The fact that three-dimensional ordering does not occur until 110 K does not disagree with the Goodenough spin model as spin interactions mediated by the orbital order in the model only produce a coupling with the *ab* plane. Figure 8.1 shows a schematic of the energy levels for one electron in the 3*d* shell of an $Mn^{3+}O_6$ octahedron taken from Castleton *et al.* There are four electrons in the 3*d* shell of the Mn^{3+} and in the absence of the crystal field they would occupy the same energy level. Hund's rule coupling on the Mn^{3+} sites is strong

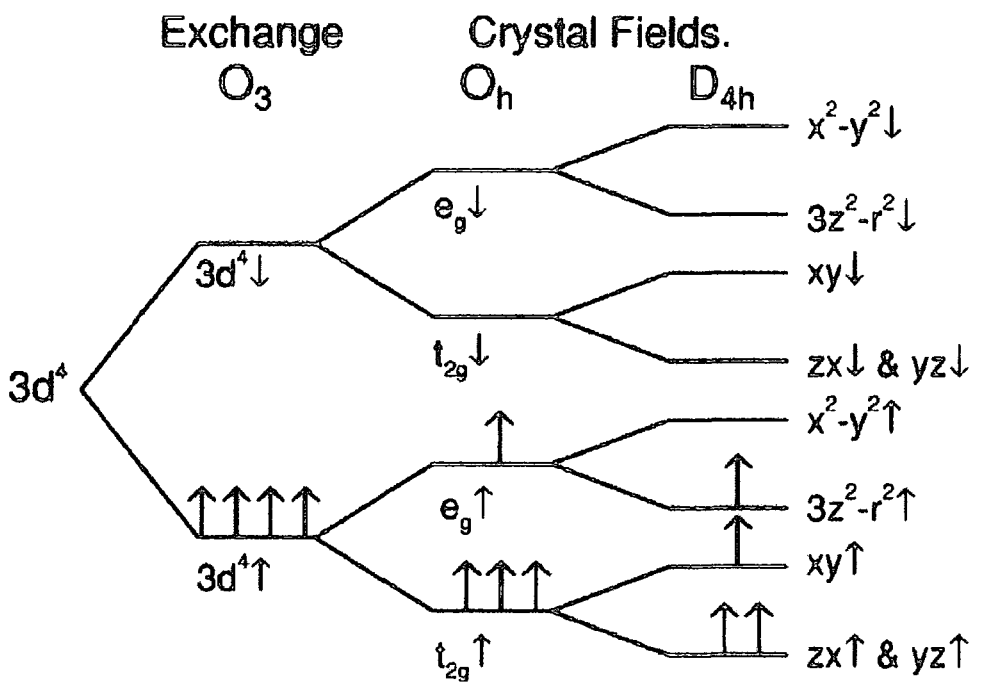

Figure 8.1: *Schematic of the 3d energy levels of a $Mn^{3+}O_6$ octahedron under the effect of the crystal field and Jahn-Teller distortion field taken from Castleton and Altarelli.* [9]

and the crystal field has a large cubic *(O_h)* component which causes a splitting into a $t_{2g}e_g$ configuration with three electrons occupying the t_{2g} and one electron in the e_g orbital. Both energy levels are degenerate and to lower the energy level this degeneracy is lifted by the effect of the Jahn-Teller distortion of the oxygen octahedra. This reduces the symmetry to D_{4h} which causes a splitting in the t_{2g} level and a splitting in the e_g level into two levels which are denoted as $3z^2\text{-}r^2\uparrow$ and $x^2 - y^2\uparrow$ respectively and it is the $3z^2\text{-}r^2\uparrow$ that is orbitally ordered. There are therefore two possible mechanisms for the orbital ordering. Firstly, it could arise as a result of the Jahn-Teller order that occurs at T_{CO} or alternatively it could arise from the spin ordering that occurs at $T_N(c)$. In the $LaMnO_3$ and $La_{0.5}Ca_{0.5}MnO_3$ manganites the magnitude of the Jahn-Teller distortions has been determined using crystallographic refinements of high resolution x-ray and neutron diffraction data. The size of the distortions varies between 7 – 12% which suggested that the Jahn-Teller mechanism may be important in these materials. However, in $La_{0.5}Sr_{1.5}MnO_4$ the MnO_6 octahedra show almost no distortion with a fractional change of

only approximately 1% in the Mn-O bond and for this reason it was suggested that principal mechanism was the Goodenough spin mechanism. The only technique that can distinguish between the Jahn-Teller order and orbital order is soft x-ray scattering at the Mn L edges. In the calculations by Castleton and Altarelli they predicted the spectrum shown in the upper panel of Figure 8.2 for $\delta = 1.000$. The largest scattered intensity occurred at the L_{III} edge and this was associated with transitions into the split $t_{2g}\downarrow$ level. The $t_{2g}\downarrow$ level is split by the Jahn-Teller distortion and hence, the intensity at the L_{III} edge is mainly associated with the Jahn-Teller ordering. The intensity at the L_{II} edge is associated with a transition into the empty $3d_{x^2-y^2}\uparrow$ orbital i.e. this is measure of the orbital order in the system.

Castleton and Altarelli predicted that it would be possible at the L edges to determine whether the scattering was due to the Jahn-Teller or orbital ordering or a combination of the two. In their calculations they gradually reduced the effects of the Jahn-Teller (JT) ordering on the calculated energy profile until just the scattering from the orbital order was present and this is shown in Figure 8.2. The contribution of the JT order was changed by use of the parameter δ, as $\delta \rightarrow 0$ the contribution of the JT order is gradually reduced and for $\delta < 0.25$ the JT effects are negligible and the effects of the orbital ordering dominate. The calculations determined that the only significant peak from the JT order occurred at the L_{III} edge, which is represented by the square icon. For $\delta < 0.5$ the intensity of this peak at the L_{III} edge shows no significant change in the intensity with δ. However, as δ is increased above 0.5 and the JT effects begin to dominate there is a dramatic increase in the scattered intensity of the peak at the L_{III} edge and from this it was concluded that the effects of the JT distortions dominate at the L_{III} edge. The peak at the L_{II} edge represented by the circle is due to the transition into the unoccupied $3d_{x^2-y^2}\uparrow$ level associated with the orbital order and would therefore, be observed even in the absence of any JT order. This is clearly seen in Figure 8.2 where the peak shows no significant change in intensity with the JT contribution and it was concluded that the effects of the orbital order dominate at the L_{II} edge. To summarise, the calculations suggested that any signal measured at the L_{III} edge would be caused by the Jahn-Teller distortions and that at the L_{II} by orbital ordering.

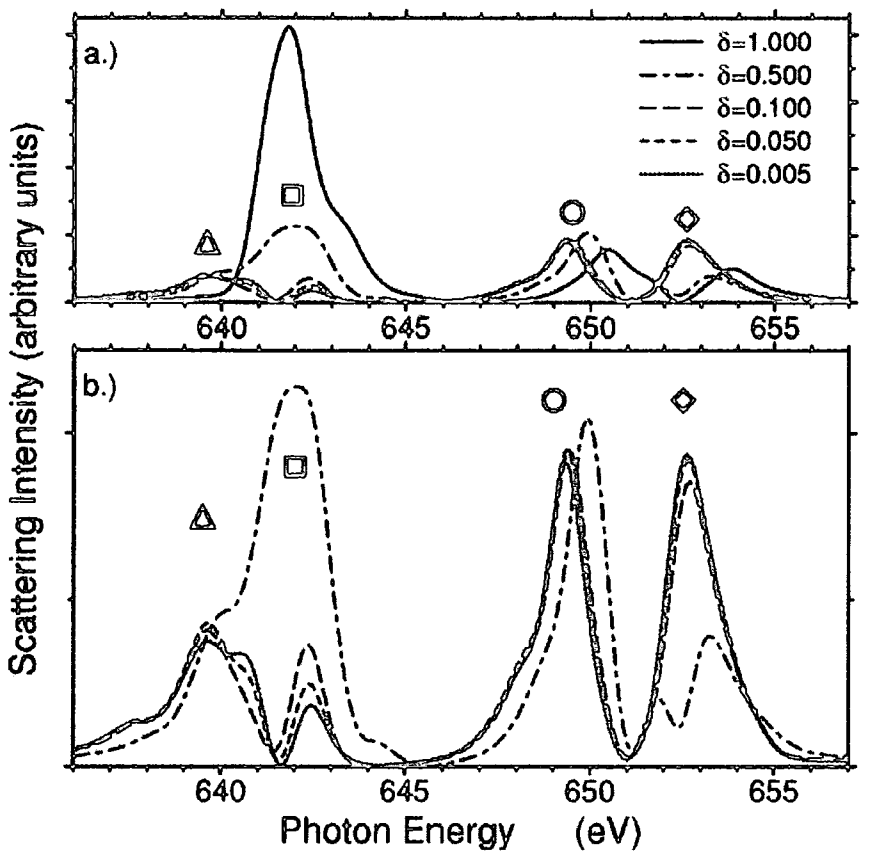

***Figure 8.2**: Calculated scattering at the Mn L edges for different contributions of the Jahn-Teller ordering with $\delta = 0$ being pure orbital ordering only and $\delta = 1.00$ strong JT. The lower panel shows the peak detail at lower δ values taken from Castleton and Altarelli* [9]

In addition the theoretical study suggested that it would be possible to obtain information about the nature of the orbital ordering pattern in the manganites. At the *K*-edge it is not possible to distinguish between the rod shaped $3x^2\text{-}y^2/3y^2\text{-}r^2$ ordering (which is the accepted pattern) and the $x^2\text{-}y^2/z^2\text{-}y^2$ ordering because both will have the same effect on the 4*p* levels. In the simulations carried out the $x^2\text{-}y^2$orbital was set as the occupied orbital and the difference in the calculated intensity around the Mn *L* edges is shown in Figure 8.3. It can be seen that there is a significant difference in the scattered intensity between the two orbitally ordered patterns. The upper panel shows the calculated results for the rod shaped orbital ordering which is characterised by strong contribution at the L_{III}

edge and two relatively weak peaks around the L_{II} edge. The lower panel shows the calculated results for the x^2-y^2/z^2-y^2 ordering pattern and this is characterised by a strong contribution at the L_{III} edge and an equally strong resonance at the L_{II} edge. Measurements performed at the Mn L_{II} and L_{III} edge would therefore confirm the nature of the orbital order pattern.

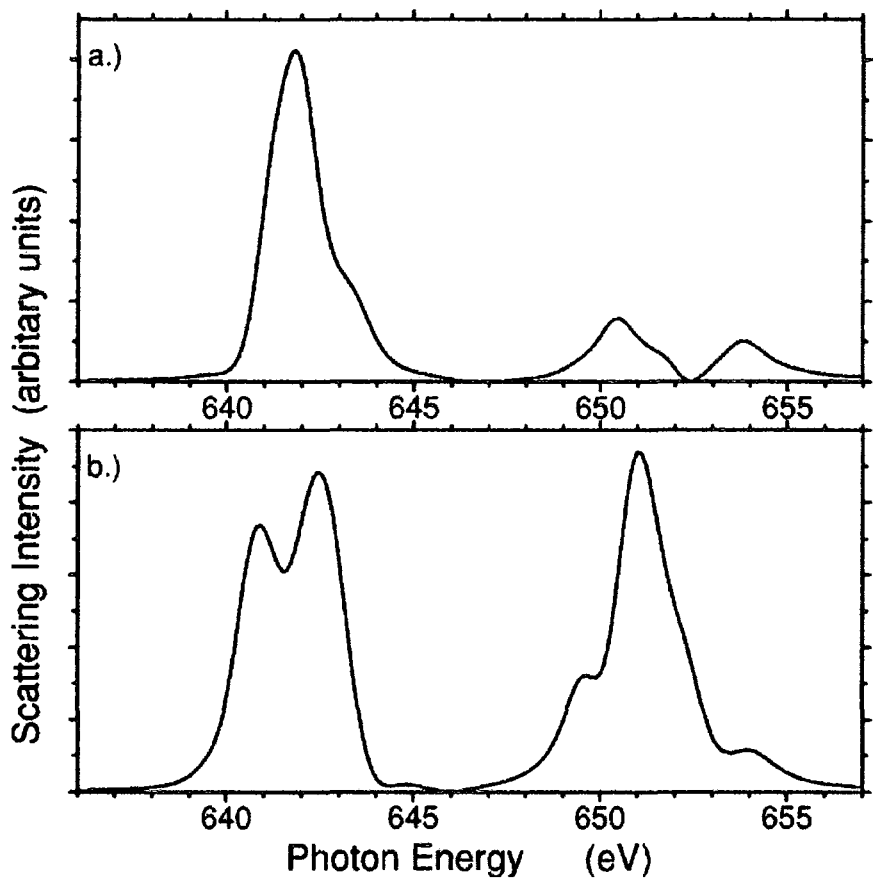

Figure 8.3: *Calculated intensity at the Mn L_{II} and L_{III} edges for the $3x^2$-y^2/$3y^2$-r^2 pattern (top panel) and the x^2-y^2/z^2-y^2 (bottom panel) taken from Castleton and Altarelli* [9]

Despite the small Ewald sphere at this energy it is possible to access the orbital order reflection at a modulation of (¼, ¼, 0), which has a Bragg angle of approximately 63° at the manganese L_{III} edge. Diffraction measurements at this energy are difficult due to the small size of the Ewald sphere and the large absorption effects. However, the experiment by Wilkins *et al.*[12] on the bi-layer manganite system showed that it was possible to carry

out soft x-ray diffraction at the manganese *L* edges and the experiment carried out in the previous chapter showed that it was also possible to carry out studies when no Bragg peak could be reached in the Ewald sphere. By using soft x-ray diffraction to study the Jahn-Teller/orbital order at the manganese *L* edges it would be possible to determine whether the resonances are caused by direct orbital ordering or by the Jahn-Teller distortions. From the measurements it will also be possible to identify the nature of orbital ordering present which is information that cannot be obtained at the Mn *K*-edge or using any other technique.

8.2 Experimental Procedure

A single crystal sample of $La_{0.5}Sr_{1.5}MnO_4$ was grown at the University of Oxford using the floating zone method. The doping was measured as $x = 0.50 \pm 0.01$ using EPMA and the excess oxygen as $\delta = 0.00 \pm 0.01$. The crystal was indexed using the *I4/mmm* setting with lattice parameters $a = b = 3.86$ Å and $c = 12.40$ Å and the unit cell is shown in Figure 8.4. The sample was pre-aligned and cut so that the <1, 1, 0> direction was surface normal and thus allowing the (¼, ¼, 0) reflection to be accessed when mounted on the soft diffractometer. It was essential that the surface was of a high quality and this was accomplished by polishing the crystal surface with 1 μm diamond paste. The sample was mounted on the two circle diffractometer in the <1, 1, 0> / <0, 0, 1> zone with the <0, 0, 1> direction corresponding to the incident beam direction and was aligned using the χ adjustment and a laser which had been mounted so that it could be adjusted to be coincident with the incoming x-ray beam. A 300 μm slit was mounted in front of the diode detector to improve the experimental resolution.

The diffractometer was evacuated and then cooled to a base temperature of approximately 85 K and a search carried out for the orbital order reflection around the manganese L_{III} and L_{II} edges that corresponded to energies of 639 eV and 652 eV respectively. At these energies the (0.25, 0.25, 0) orbital order reflection would occur at a 2θ angle of approximately 126° and searches were carried out around this position.

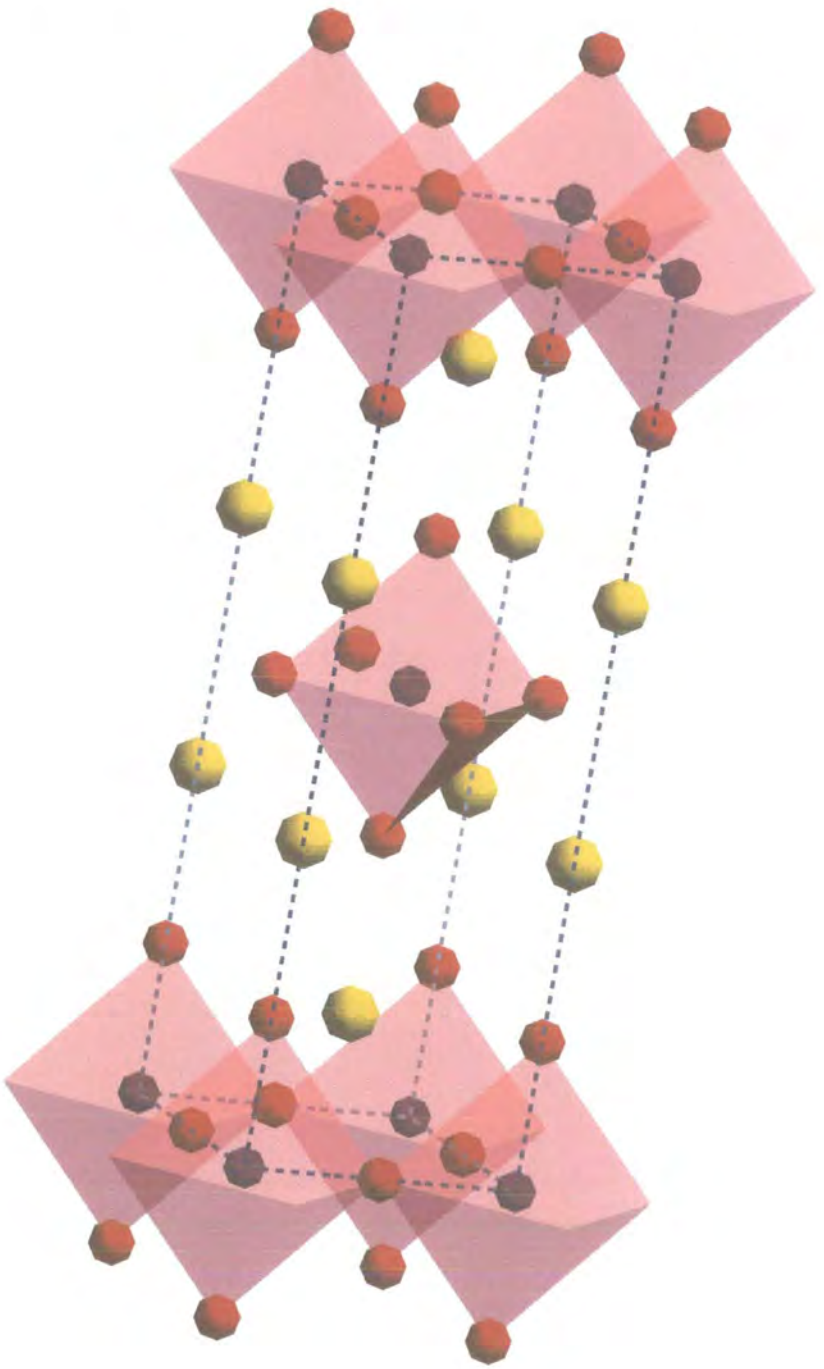

Figure 8.4: *Crystal structure of the $La_{0.5}Sr_{1.5}MnO_4$ system. The yellow balls show the La/Sr sites, the purple balls show the Mn ions and red balls represent the oxygen ions.*

8.3 Results

The search for the orbital order was initially carried out at the Mn L_{III} edge corresponding to an energy of 639 eV because the resonant enhancement was predicted to be greatest at this energy. A reflection was located at a 2θ angle corresponding to the expected modulation of (0.25, 0.25, 0) for the orbital order at the L_{III} edge. The (0.25, 0.25, 0) reflection was scanned as a function of energy at constant wavevector through the L_{II} and L_{III} edges at 85 K and this is shown in Figure 8.5. The exit slit was set to 30 μm so that the energy scan was carried out in high resolution mode which corresponded to a resolution of ΔE = 1 eV at the Mn L_{II} and L_{III} edges. By scanning at constant wavevector the angular positions are altered to ensure that throughout the scan the (0.25, 0.25, 0) peak is accessed.

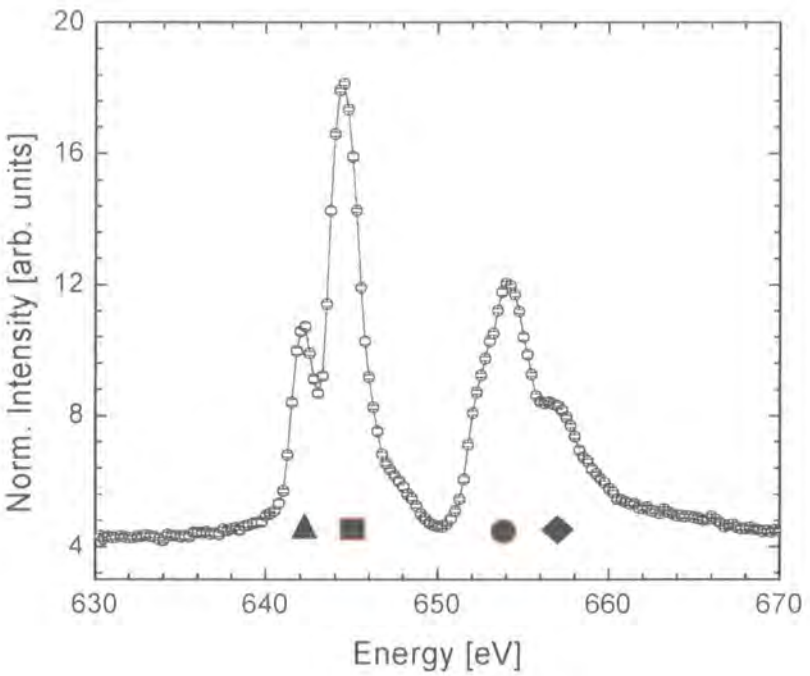

Figure 8.5: *Energy scan at constant wavevector of the (0.25, 0.25, 0) orbital order peak at 85 K between 630 – 670 eV. The symbols show the energies of the four major features as predicted in Figure 8.3*

In Figure 8.5 there is a clear resonant enhancement in the scattered intensity observed at both the L_{II} and L_{III} edges. There are four clear features in the energy scan which is in agreement with predictions by Castleton and Altarelli shown in Figure 8.2. These features were observed at energies of 641.4 eV and 643.6 eV at the L_{III} edge and at energies of 653.4eV and 656.2 eV at the L_{II} edge. The (0.25, 0.25, 0) reflection was scanned in the [110] (longitudinal) direction of reciprocal space at each of the four peaks in the energy spectrum at a temperature of 85 K. At each of the energies the data was found to fit a Lorentzian squared lineshape and the fits at the L_{III} and L_{II} edges are shown in Figures 8.6 and 8.7 respectively. It should be noted that the orbital order peak was significantly broader than the instrumental resolution.

From the fits the inverse correlation length ξ^{-1} was calculated using the equation :-

$$\xi^{-1} = \kappa \times \left(\frac{2\pi}{d} \right) \quad \textbf{[8.1]}$$

where κ is the half width at half maximum of the peak and d is Bragg plane spacing in the direction normal to the scattering vector. Table 8.1 shows the inverse correlation length at each of the four energy features and as a comparison the inverse correlation length of the Jahn-Teller and orbital order measured at the manganese K-edge is also shown.

Energy	Inverse correlation length $[Å^{-1}] \times 10^{-3}$
641.4 eV	2.98 ± 0.06
643.6 eV	3.10 ± 0.04
653.4 eV	2.60 ± 0.04
656.2 eV	2.60 ± 0.03
Orbital order K-edge at 6555 eV	1.98 ± 0.03
Jahn-Teller order K-edge at 6555 eV	2.22 ± 0.02

***Table 8.1**: Inverse correlation lengths of the four features in the energy scan at 85 K. As a comparison the inverse correlation lengths measured at the K-edge for the Jahn-Teller and orbital order are also shown.*

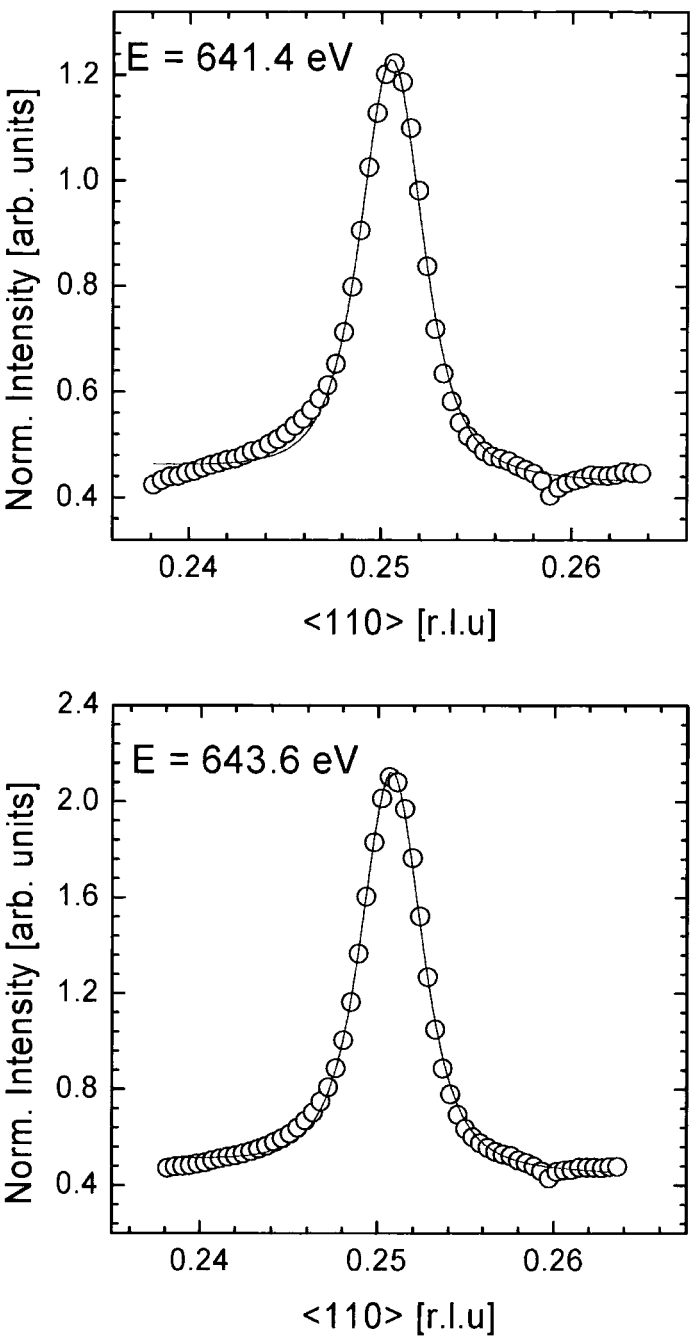

Figure 8.6: *Scan of the (0.25, 0.25, 0) at the L_{III} edge through the (110) direction. The blue lines show the Lorentzian squared fits*

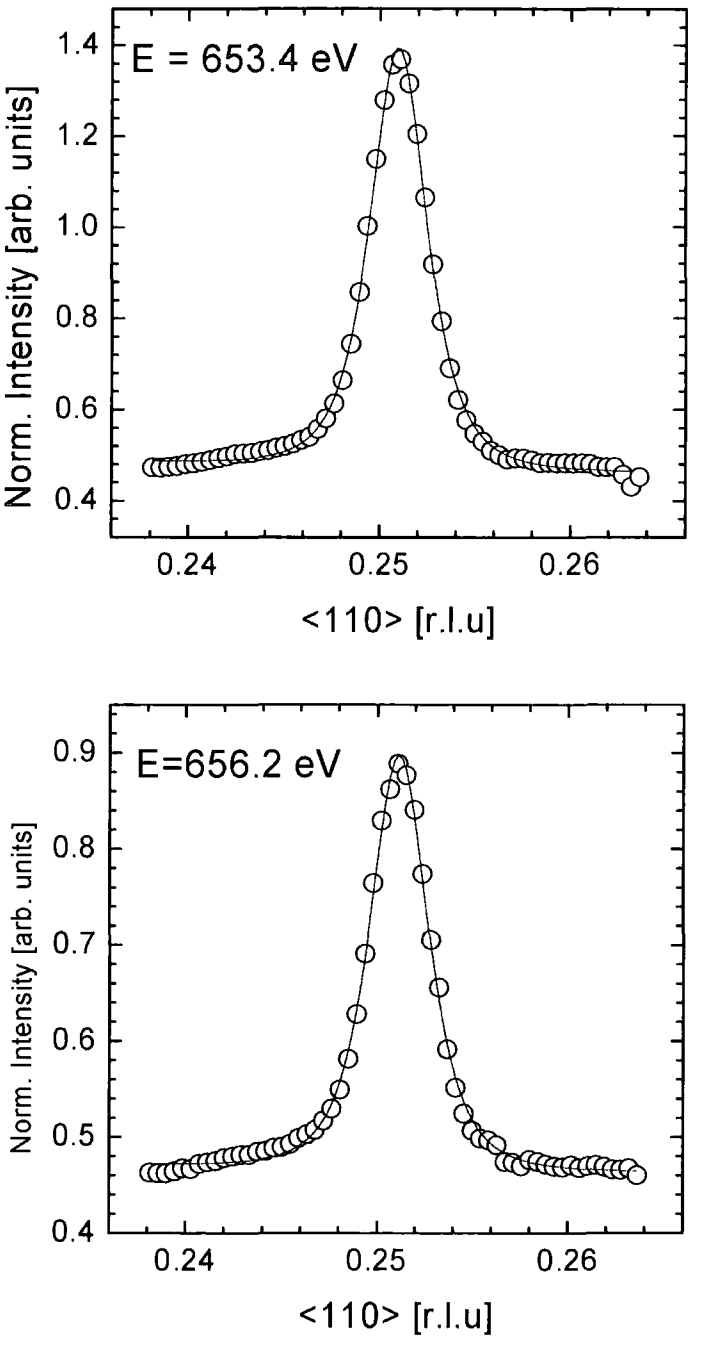

Figure 8.7: *Scan of the (0.25, 0.25, 0) at the L_{II} edge through the (110) direction. The blue lines show the Lorentzian squared fits*

One of the initial concerns about the soft x-ray scattering technique was the degree of surface sensitivity. In the initial work by Wilkins on the bi-layer manganite system it was found that the technique was not especially surface sensitive with an inverse correlation length measured at 900 eV on the (0, 0, 2) Bragg peak approximately half that at an energy of 12.4 keV. A comparison between the inverse correlation lengths of the orbital order at the *L* and *K* edges reveals only a relatively small difference in the inverse correlation lengths indicative that the soft x-ray technique is not especially surface sensitive and in $La_{0.5}Sr_{1.5}MnO_4$ penetrates many unit cells. The inverse correlation lengths of the peaks at the L_{III} edge are greater than those measured at the L_{II} edges and this will be discussed in greater detail later on in the Chapter.

As discussed in section 8.1 it was intended from these measurements to determine the nature and origin of the orbital order in the $La_{0.5}Sr_{1.5}MnO_4$ system and these properties can be obtained from the energy scan of the orbital order. Firstly we consider the nature of the orbital ordering. The calculations carried out were not based on experimental data and as a result there is not an exact match between the predictions and the energy scan experimentally observed. However, despite this it is still possible to clearly determine the nature and origin of the results observed. As discussed in section 8.1 at the *K* edge it is not possible to determine if the orbital ordering pattern is of the $3d_{3x^2-r^2}/3d_{3y^2-r^2}$ type or of the $3d_{x^2-z^2}/3d_{z^2-y^2}$ type. Figure 8.4 shows the two predicted patterns for the different types of orbital ordering. A comparison between our data and the predictions made by Castleton seems to suggest that it is the former pattern that occurs. Evidence for this is the larger intensity observed at the L_{III} edge compared to that at the L_{II} edge which is predicted for the $3d_{3x^2-r^2}/3d_{3y^2-r^2}$ type ordering but not for the $3d_{x^2-z^2}/3d_{z^2-y^2}$ type ordering where the scattered intensity is approximately equal at the two edges. However, when comparing the predictions with the results it is necessary to be cautious because the calculations by Castleton and Altarelli were purely theoretical and not based on any experimental data.

As discussed in section 8.1 the observed scattering could be associated with the Jahn-Teller distortions or the Goodenough orbital ordering. Figure 8.8 shows the energy spectra predicted by Castleton and Altarelli[9] with pure orbital ordering (δ= 0.005) shown in the top panel and strong Jahn-Teller contribution (δ=1.000) in the bottom panel.

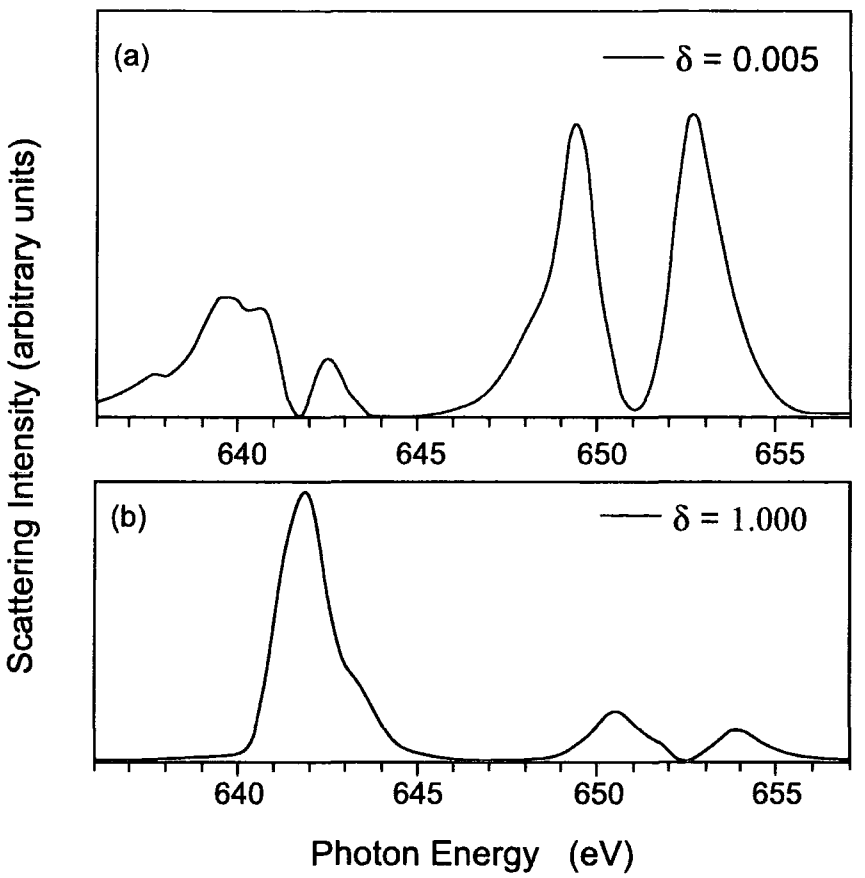

Figure 8.8: *Energy spectra predicted by Castleton and Altarelli[9] for $\delta = 0.005$ (pure orbital ordering) and $\delta = 1.000$ (strong Jahn-Teller ordering).*

For δ= 0.005 there is no Jahn-Teller ordering and the observed scattering is due to the pure orbital ordering only. In this regime only weak peaks are predicted at the L_{III} edge and the scattering at the L_{II} edge dominates and this remains true for $\delta < 0.25$. For the regime in which there is a mixture of Jahn-Teller and orbital ordering corresponding to

$0.25 < \delta < 0.75$ there is no significant change in the intensity of the peaks at the L_{II} edge but there is a significant increase in the intensity around the L_{III} edges. In the regime where the Jahn-Teller order dominates, corresponding to $\delta = 1.000$, the two peaks observed at the L_{III} edge dominate. Comparing the predictions with our measurements in Figure 8.5 shows that the co-operative Jahn-Teller order effect is clearly the dominant mechanism in the observed scattering. Evidence of this is the strong intensity observed at the L_{III} edge which is in agreement with the predictions of Castleton and Altarelli for a strong JT contribution as shown in the lower panel of Figure 8.8. However, there is also a significant resonance at the L_{II} edge which as discussed is only associated with the direct orbital ordering. It is concluded from this that there are two separate contributions to the observed scattering, the first from the Jahn-Teller distortions of the Mn^{3+} ions and the second from the Goodenough direct orbital ordering. Fitting of the experimental data will be needed to determine the exact contributions of the Jahn-Teller and orbital ordering. These results showed that even in $La_{0.5}Sr_{1.5}MnO_4$ which has relatively small Jahn-Teller distortions that the Jahn-Teller effect and not orbital ordering is the dominant mechanism but our results have shown that there is also a significant contribution from the direct orbital ordering.

The integrated intensity, inverse correlation length and position of the (0.25, 0.25, 0) orbital order reflection was measured as a function of temperature at each of the four features in the energy scan which corresponded to energies of 641.4 eV and 643.6 eV at the L_{III} edge and 653.4 eV and 656.2 eV at the L_{II} edge. This was carried out to determine if there was any difference in behaviour between firstly the peaks at the L_{III} and L_{II} edges, and secondly between the results at soft energies and those at the manganese *K*-edge. The temperature dependence of the integrated intensity of the two features at the L_{III} edge is shown in Figure 8.9 and for the two features at L_{II} edge in Figure 8.10.

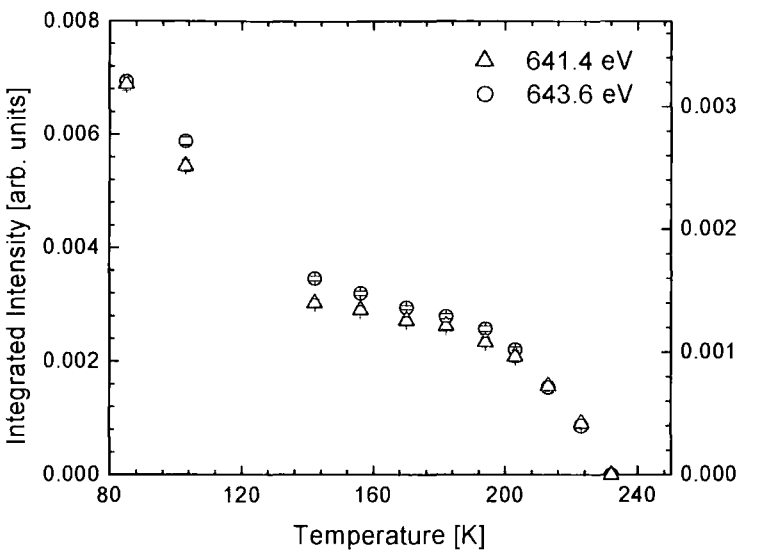

Figure 8.9: *Integrated intensity as a function of temperature for the (0.25, 0.25, 0) reflection for the two peaks at the L_{III} edge.*

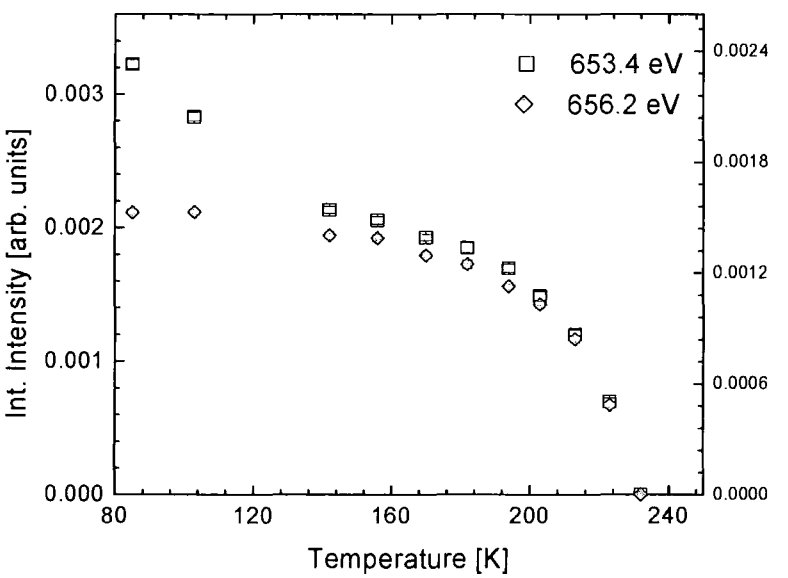

Figure 8.10: *Integrated intensity as a function of temperature for the (0.25, 0.25, 0) reflection for the two peaks at the L_{II} edge.*

In measurements at the *K*-edge by Murakami *et al.*[2] and Wilkins *et al.*[13] on heating from a base temperature of 10 K the integrated intensity shows a gradual decrease until the transition temperature at approximately 220 K. Clearly, the temperature dependence of the orbital order shows a significant difference at the Mn L_{III} and L_{II} edges than that observed at the Mn *K*-edge. Above 140 K there is a gradual decrease in the intensity of the orbital order at each of the four energy positions before disappearing at ~ 220 K and this is in agreement with the temperature dependence observed at the *K*-edge.

If we consider the L_{III} edge data as a measurement of the Jahn-Teller order and the L_{II} edge data as a measurement of the orbital order was can conclude that they show the same transition temperature. However, as the temperature is decreased below 140 K a significant increase in the integrated intensity was observed at the L_{III} and L_{II} edges that was not observed in the *K*-edge experiments. Referring to Figures 8.9 and 8.10 the increase in intensity is more significant at the L_{III} edge than that observed in the features at the L_{II} edge. Table 8.2 shows a comparison of the integrated intensity at 85 K and 140 K and this clearly demonstrates the larger increase in the intensity at the L_{III} edge and this can be observed in a comparison of the energy scans shown in Figure 8.11.

	641.4 eV (L_{III})	643.6 eV (L_{III})	653.4 eV (L_{II})	656.2 eV (L_{II})
85 K	3.19 ± 0.05	6.93 ± 0.08	3.23 ± 0.03	1.53 ± 0.02
140 K	1.40 ± 0.03	3.45 ± 0.04	2.13 ± 0.02	1.40 ± 0.02
I_{85}/I_{140}	2.28 ± 0.06	2.01 ± 0.03	1.52 ± 0.02	1.09 ± 0.02

Table 8.2: *Comparison of the integrated intensity at 85 K and 140 K. Errors are given by the fits.*

There is an increase at the L_{II} edge but this is significantly smaller especially at the second feature at 656.2 eV whereas the intensity at the L_{III} more than doubles from 140 to 85 K. It is concluded that the influence of the Jahn-Teller distortions becomes even more dominant at low temperatures. The different temperature dependence of the features at the L_{III} and L_{II} edges clearly shows that the Jahn-Teller distortions and Goodenough orbital ordering are separate from each other and behave in a different way with respect to temperature.

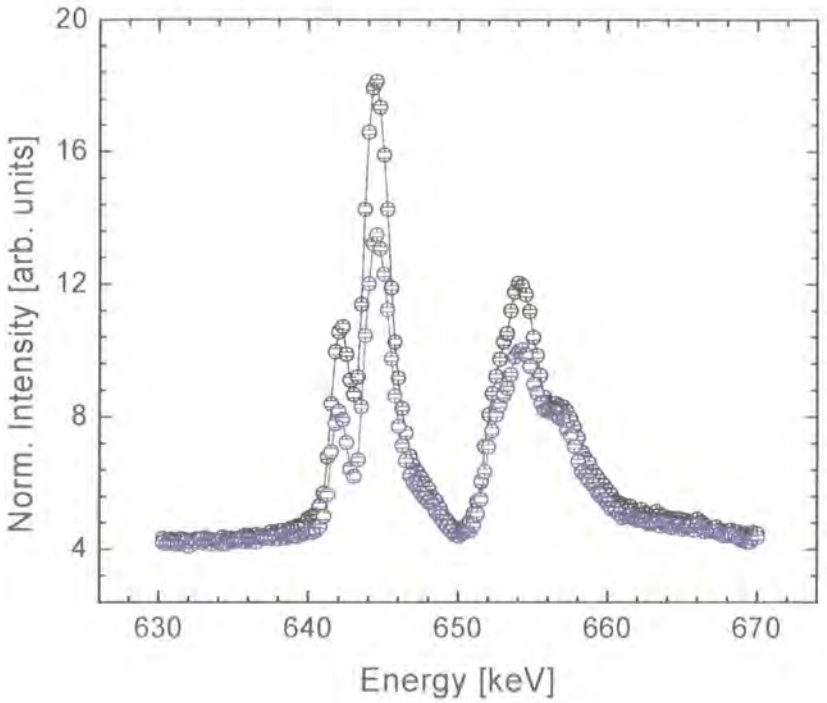

Figure 8.11: *High resolution energy scans performed at 85 K (black symbols) and 140 K (blue symbols). Lines are guide to the eye.*

The inverse correlation length was measured as a function of temperature at the L_{III} and L_{II} edges. This is shown in Figure 8.12 for the features at 643.6 eV and 653.4 eV *i.e.* the two strongest features at the L_{III} and L_{II} edges. The weaker features at the respective edges behave in the same way but they are not shown. There is a clear difference in the behaviour of the inverse correlation length with temperature of the scattering at the L_{III} edge and that at the L_{II} edge. At the L_{II} edge the inverse correlation length shows no significant change which is in agreement with the *K*-edge behaviour of the orbital order. However, at the L_{III} edge the inverse correlation length shows a sharp increase below 140 K *i.e.* it becomes less correlated and this accompanies the sharp increase in intensity of the peak associated with the Jahn-Teller distortions. There is clearly something significant occurring below 140 K that causes the observed increase in intensity and we postulate that this is the magnetic ordering.

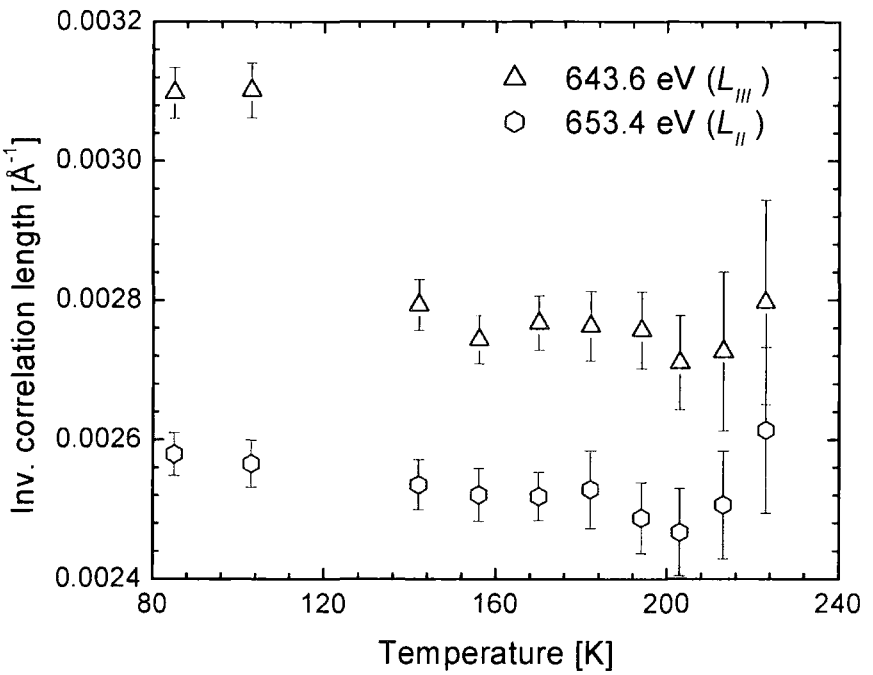

Figure 8.12: *Inverse correlation length as a function of temperature at the L_{III} and L_{II} edges for the (0.25, 0.25, 0) reflection. The red triangles show the signal at the L_{III} edge and the green circles the inverse correlation length at the L_{II} edge.*

The magnetic ordering temperature T_N is known to be approximately 110 – 160 K from earlier studies depending on the sample under study. It should be noted that no change in the inverse correlation length was observed at T_N in the earlier studies at the K edge. To determine the exact value of T_N in our sample, magnetisation measurements were carried out on SQUID at the University of Oxford. These results are shown in Figure 8.13 and from these results T_N was determined as approximately 120 K. This is evidence that it is indeed the influence of the magnetic ordering that causes the observed increase in intensity and inverse correlation length at the L_{III} edge. It is not known why the magnetic ordering causes this effect and why the onset of magnetic order has a more significant effect on the peak associated with the Jahn-Teller distortions than that associated with the direct orbital order, but this will be investigated in later work.

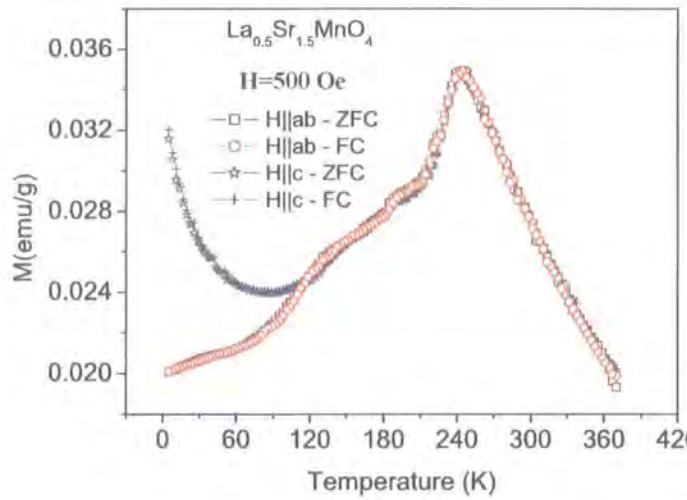

Figure 8.12: *Magnetisation measurements performed on $La_{0.5}Sr_{1.5}MnO_4$*

The relationship between the orbital and spin ordering will require a detailed temperature dependence of the orbital ordering especially around the magnetic transition temperature of 120 K. It is also possible to access the magnetic ordering reflection which occurs at a modulation of (0.25, 0.25, 0.5) and by a detailed measurement of this it may be possible to determine the relationship between the spin and orbital ordering to explain the observed results. There was no change in the intensity reported by Murakami *et al.*[2] at T_N at the *K* edge and a possible explanation for this is that the *K*-edge measurements are not a direct probe of the orbital ordering and hence, the technique is not sensitive to how the magnetic order affects the electronic structure of the 3*d* orbitals. What is evident from this study is that by utilising soft x-ray scattering at the Mn *L* edges considerably more information about the nature and mechanism of the orbital ordering is obtained than by the *K*-edge technique.

8.4 Conclusions and Future Work

This is the first experiment to utilise resonant soft x-ray scattering to probe the orbital ordering in the manganites. The measurements at the manganese *L* edges directly probe the orbital ordering and have provided information about both the electronic configuration and the mechanisms behind the orbital ordering. Recently the technique has also been used to successfully observe orbital and magnetic order in $Pr_{0.6}Ca_{0.4}MnO_3$ by Thomas *et al.*[14]

The orbital order energy scan provided conclusive evidence that it is the effect of the co-operative Jahn-Teller distortions that is the dominant mechanism behind the orbital ordering even in $La_{0.5}Sr_{1.5}MnO_4$ which is believed to only show a small Jahn-Teller distortion. It is highly probable that the Jahn-Teller order is a cause of the orbital order in all the manganites. The evidence for this is the large peak located at the L_{III} edge which was in line with the predictions by Castleton and Altarelli. However, significant intensity could only be observed at the L_{II} edge which is caused only by the direct Goodenough ordering. From this it is concluded that while the effects of the Jahn-Teller distortions dominate there is a significant contribution from the direct orbital order i.e. there are two contributions to the observed orbital ordering. Comparing the observed results with the predictions of Castleton and Altarelli suggested that the orbital ordering was the $3d_{3x^2-r^2}/3d_{3y^2-r^2}$ type. However, the predictions of Castleton and Altarelli were not based on experimental data and fitting of the experimental data will provide definite information about the orbital order pattern and the relative contributions of the Jahn-Teller and direct orbital ordering to the observed pattern.

At low temperatures there is a noticeable increase in the intensity in the features at the L_{III} and L_{II} edges. However, this increase is greater at the L_{III} edge and this shows that the effect of the Jahn-Teller distortions is even more dominant at low temperatures. The magnetic ordering is postulated to be the cause of this but this will require further investigation to determine the relationship between the magnetic and orbital order. This

will require a detailed temperature dependence of the orbital order at low temperatures. It is possible to access the (0.25, 0.25, 0.5) spin order reflection at the Mn *L* edges and by measuring this it will hopefully lead to an improved understanding of the interplay between the spin and orbital degrees of freedom.

This is the only technique available to directly probe the orbital degree of freedom. In the future the technique will be applied to the other manganite systems known to show orbital ordering at the Mn *K*-edge such as $Nd_{0.5}Sr_{0.5}MnO_3$, $Bi_{0.24}Ca_{0.76}MnO_3$ and $LaSr_2Mn_2O_7$. This will allow an understanding of the behaviour of the orbital order and Jahn-Teller order in different manganite systems to be determined and their relative contributions in different manganites. In theory the technique could also be used to probe the orbital degree of freedom in the 4*d* elements where recent experiments have suggested that Ca_2RuO_4[15] and $La_2Ru_4O_{10}$[16] ruthenate systems display some type of orbital order.

8.5 References

1 J. B. Goodenough, Physical Review **100**, 564 (1955).

2 Y. Murakami, H. Kawada, H. Kawata, *et al.*, Physical Review Letters **80**, 1932 (1998).

3 Y. Murakami, J. P. Hill, D. Gibbs, *et al.*, Physical Review Letters **81**, 582 (1998).

4 M. von Zimmermann, J. P. Hill, D. Gibbs, *et al.*, Physical Review Letters **83**, 4872 (1999).

5 K. Nakamura, T. Arima, A. Nakazawa, *et al.*, Physical Review B-Condensed Matter **60**, 2425 (1999).

6 Y. Wakabayashi, Y. MuraKami, I. Koyama, *et al.*, Journal of the Physical Society of Japan **69**, 2731 (2000).

7 I. S. Elfimov, V. I. Anisimov, and G. A. Sawatzky, Physical Review Letters **82**, 4264 (1999).

8 M. Benfatto, Y. Joly, and C. R. Natoli, Physical Review Letters **83**, 636 (1999).

9 C. W. M. Castleton and M. Altarelli, Physical Review B **62**, 1033 (2000).

10 B. J. Sternlieb, J. P. Hill, U. C. Wildgruber, *et al.*, Physical Review Letters **76**, 2169 (1996).

11 F. Damay, C. Martin, A. Maignan, *et al.*, Journal of Magnetisim and Magnetic Materials **183**, 143 (1998).

12 S. B. Wilkins, P. D. Hatton, M. D. Roper, *et al.*, Physical Review Letters **90**, 187201 (2003).

13 S. B. Wilkins, T. A. W. Beale, P. D. Spencer, *et al.*, Physical Review B **to be published** (2004).
14 K. J. Thomas, J. P. Hill, Y. J. Kim, *et al.*, cond-matt/0311553 (2003).
15 J. H. Jung, Z. Fang, J. P. He, *et al.*, Physical Review Letters **91**, 056403 (2003).
16 P. Khalifah, R. Osborn, Q. Huang, *et al.*, Science **297**, 2237 (2002).